Développement d'un calorimètre sans contact pour des systèmes isopériboliques millifluidiques : application aux écoulements diphasiques

Marta Romano Romano Mungaray

N° d'ordre : 4886

THÈSE

présentée à

L'UNIVERSITÉ DE BORDEAUX I

École doctorale des sciences chimiques

par Marta ROMANO

pour obtenir le grade de

Docteur

Spécialité : physique-chimie

Development of a non contact calorimeter in isoperibolic millifluidic systems using InfraRed Thermography

-

Applied to biphasic flows

Soutenue le 30 octobre 2013

Rapporteurs:

M.	Laurent Prat	Professeur
M.	Lounès Tadrist	Professeur

Membres du jury :

M.	Jean Christophe BATSALE	Professeur	Directeur de thèse
M.	Laurent Prat	Professeur	Rapporteur
M.	Lounès Tadrist	Professeur	Rapporteur
M.	Sebastien Righini	Industriel Solvay	Examinateur
M.	Mathieu Joanicot	Directeur scientifique Saint Gobain	Examinateur
Mme.	Cindy Hany	Industriel Solvay	Examinateur

Invités :

M.	Christophe PRADERE	Chargé de recherche	Co-directeur de thèse
M.	Jean TOUTAIN	Maître de conférence	Co-directeur de thèse

Remerciements

Voici la première page du manuscrit qui est aussi la denière page a rédiger... C'est ici que trois ans de thèse s'achèvent et qu'une autre vie commence. Comme le veut la tradition, je vais tenter de satisfaire au difficile exercice de la page des remerciements, peut-être une des tâches la plus ardue de ces années de thèse. Non qu'exprimer ma gratitude envers les personnes en qui j'ai trouvé un soutien soit un problème, la difficulté tient plutôt dans le fait de n'oublier personne. C'est pourquoi, je remercie par avance ceux dont le nom n'apparaît pas dans cette page et qui m'ont aidé d'une manière ou d'une autre.

J'ai effectué ma thèse entre le LOF et l'i2M-TREFLE, j'ai vécu une véritable garde alternée!!! C'est-à-dire, j'ai navigué entre les laboratoiress, j'avoue qu'au quotidien cela n'a pas toujours été facile. Mais c'est bien connu les grands défis nécessitent des grands efforts! La difficulté n'était pas due à la distance spatiale entre les laboratoires, mais plutôt à la différence des cultures scientifiques. De ce fait j'ai eu la chance de voyager entre deux mondes très différents et très complémentaires à la fois. Grâce à ce mélange scientifique je ne suis plus la même personne après l'échappée solitaire de la thèse...

Mes premiers remerciements s'adressent tout naturelement à mes encadrants de thèse. Une équipe magnifique au sein d'un laboratoire unique l'i2M-TREFLE: Christophe Pradere, Jean Christophe Batsale et Jean Toutain. Vous avez toujours été là pour m'orienter et pour me donner le goût de la recherche, mais surtout pour la partager avec bonne humeur !!!
Christophe, tu as toujours su me pousser à aller plus loin et tu n'as jamais accepté des arguments trop simplistes. Merci de m'avoir fait confiance et d'avoir pris le temps de suivre mes idées. J'ai été extrêmement sensible à tes qualités humaines d'écoute, de compréhension et de pédagogie tout au long de ce travail ... (désolée à la fin je n'avais plus ni la force ni l'envie de simplifier l'estimation du ρC_p $-\triangleright$ je te dois une..)
J.C. merci d'avoir été là pour nous apporter une bouée dans les moments où l'on se noyait dans les gouttes... Je suis très reconaissante du temps que tu as passé avec moi. Ca a été une aventure incroyable de travailler avec quelqu'un qui a autant d'expérience et autant d'envie de transmettre son savoir-faire.
Jean, merci pour ton sens rigoureux qui t'amène à accomplir tes idées sous la forme des programmes uniques et performants... ce que j'ai retenu plus particulirement de toi est le soin et la précision avec laquelle tu tiens à faire les choses... toujours aux petits oignons!
Vous avez eu beaucoup confiance en moi, plus que des encadrants, je crois avoir trouvé en vous des amis qui sont là aussi bien dans le travail que dans la vie. Je ne sais comment vous exprimer ma gratitude autrement qu'en vous promettant d'agir comme vous avec des ètudiants dans ma situation, si un jour l'occasion m'en est donnée!

Je souhaiterais remercier les membres de mon jury. Lounès Tadrist et à Laurent Prat davoir pris le temps de relire et de rapporter mon manuscrit mais aussi d'avoir apport des questions très intéréssante avec toute votre expertise. Merci à Sébastian Righini qui a pris le temps d'examiner le manuscrit avec un oeil insdutriel très objetif. J'adresserai un remerciement spécial Matthieu Joanicot qui est le fondateur du LOF et un des premiers à proposer des sujets tranverse comme celui là. Il a su partager les gouttes avec les thermiciens de Bordeaux et finalement il a bien accepté d'être acteur de la conclusion de ce sujet de recherche.

J'adresse un remerciement particulier à Patrick Maestro, ancien directeur du LoF, pour m'avoir accueilli au labortoire et m'avoir accordé sa confiance afin de mener le projet de thèse, mais aussi pour sa disponilibité, ses bons conseils et surtout pour sa bonne humeur. Je remercie toute l'équipe microchimie du LoF, tout particulirement je remercie Cindy Hany pour sa disponibilité, Flavie Sarrazin pour son amitié et sa patiente, et surtout pour m'avoir appris autant de choses à propos des gouttes mais aussi de la vie =). Je remercie Emmanuel Mignard pour ses conseils, son amitié et pour m'avoir invité à collaborer souvent dans ses projets. Un gran merci à Pierre Guillot pour ses bonnes idées et sa disponibilité. J'ai beaucoup apprecié partager avec vous mon quotidien!

À ces permanents qui trouvent toujours un peu de temps pour les étudiants. Merci à Max Chabert et Hugues Bodiguel pour ce beau stage microfluidique qui m'a ouvert les portes du LoF. Un ENORME merci à Jacques Leng pour ses conseils bienveillants ainsi que pour son temps, sa pédagogie et le partage de son savoir-faire avec des jeunes motivés!

Philippe Rivoal et Cyril Vidaillac je vous remercie pour vos encouragements, pour votre amitié et aussi pour

toutes les fois que vous m'avez déppanée avec quelque chose pour la manipe, ainsi que pour vos blagues!

A ceux qui ont partagé mon bureau et mon quotidien au LOF. Merci à Pierre, Flavie, Vincent, Nicolas, Laetitia A ceux qui se sont embarqués dans laventure la même année que moi Julien et Antonio, merci pour avoir partagé ces trois ans mais surtout les derniers mois difficiles. Ainsi j'adresse un grand remerciement à tout l'ensemble du LoF, pour ces petits et grands moments: ces après-midi des manipes où j'ai pu rigol avec les gens présents ou encore ces dicussions fantastiques devant la machine à café..

Ces remerciements seraient incomplets si je n'en adressais pas à l'ensemble de l'I2M-TREFLE, pour cet esprit de partage et de bonne humeur qui rempli les couloirs du batiment AMPT. Je remercie le gens de Thermoconcept, de Fahrenheit et tous les membres de l'équipe thermocinétique ainsi que de l'OTPI. Je remercie particulièrement Elena Palomo del Barrio de la Castilla de la Esquina pour sa bonne humeur et son avis toujours juste (ou pas..). Une petite pensée et un gran merci l'as du volant et de la manipe Alain Sommier. Je remercie également ceux qui ont partagé mon bureau et mon quotidien: Emmanuel, Anna, Maimouna, Regis, Marie, Alex, Fouzia.

À celles, qui ont fait pour moi le lourd travail administratif du côté LoF. Merci à Céline, Hélène, Elsa, Sylvie, Christiane. Merci Martine qui savait donner du bonheur à la vie. Et celles du côté I2M-TREFLE, Sylviane, Muriel et Sandrine.

Je remercie tout particulièment Flavio, Thierry, Uxying qui savent ce qu'est une garde alternée...

Surtout ce travail n'aurait pas pu se faire si des nombreuses personnes n'y avaient pas contribué : M. Barboteau et son équipe à l'atélier du CRPP, Dr. Le Bourdon pour les mesures de SIV au sein de l'ISM, Romain Guillaument pour avoir réalisé l'étude en 3D des gouttes, Alicia Ricci pour avoir testé le calorimètre au cours de son stage de licence. Egalement je remercie les deux endroits où j'ai pu évacuer le stress de mes journées le Bleu tenu par Mr et Mme Parfait, ainsi que à tout l'équipe du bar vin La parcelle où l'on se laisse emporter par une ambiance chaleureuse autour des cépages manignifiques!

Je remercie très chaleuresement mes amies Nora, Vincent, Ana, Dunia, Sylvain, Uxying, Carolina M., Roman K., Nicolas L. pour m'avoir guidé, écouté et encouragé durant ces années. A Mélanie d'avoir ajouté la dosequi manquait du francais à ces remercimenets!
Agradezco muy especialemente el amor incondicional y el apoyo de la familia. A mi mamá por haber sido la fuerza que no tiene fronteras, ni límites y que va mas haya de lo tangible, te amo con todas mis fuerzas. Papá me hubiera gustado que leyeras este manuscrito para que pudieras conocer a la química en la que me convertí... Este trabajo se lo dedico con todo mi amor a mi dos hermanos, espero que en estas páginas sientan el esfuerzo que representa para mí vivir lejos de ustedes.

Le plus FORT de mes remerciements est pour Christophe. Merci de m'avoir tenu la main jusqu'aux dernières lignes de ce mémoire. Merci d'être là tous les jours!

Contents

Introduction

Micro- and millifluidic droplet-based systems are recognized techniques for high-throughput screening platforms. In the field of chemistry, these platforms are used as tools for analysis, process intensification and data acquisition. The principal motivation for the development of adapted tools for online monitoring is profiting from these high-throughput screening platforms. Today, it is possible to perform classic reactions in smaller volumes, where both the yields and the productivity are increased. Therefore, it is essential to provide well-adapted tools for experimental data monitoring.

Chemical reaction characterization, in terms of kinetics and thermodynamics, is a key aspect of chemical science. Characterization techniques are used to the estimate crucial parameters for the development, design and security of processes. Typically, characterization approaches are based on classical spectroscopy techniques (UV-vis, Raman, etc.), which are well adapted to online kinetics monitoring, by measuring the concentration evolution as function of the time (conversion rate). However, many chemical or physical processes are associated with thermal phenomena and are therefore commonly characterized by calorimetric methods to obtain the associated thermodynamic data and kinetics.

In the case of a chemical reaction, the evolution of heat flux is reproducible and directly proportional to the reaction conversion rate. Thus, calorimetric measurements can deliver to kinetic and thermodynamic data. To achieve such quantification, the measurements are usually performed inside of insulated and confined chambers, under very specific conditions. Such estimations not only provide information regarding the chemical reaction but also with respect to the design parameters in terms of equipment dimensions, materials selection and safety aspects.

Chemical reaction characterization based on heat flux measurements is a widely used approach. Among the various techniques, several *in situ* calorimetric applications have been developed for both miniaturized and flow-based systems. However, despite the advertised promises, most of these *in situ* temperature measurement techniques are intrusive, are difficult to adapt and have been tested only on single-phase flows. Hence, these techniques are not suitable for use as flexible online analysis tools. From this point of view, the online and non-

contact calorimeter proposed in this study was designed to monitor reactions performed in two-phase flows. This online thermal analysis tool can perform thermodynamic and kinetics data acquisition.

Microfluidics has emerged as an interdisciplinary science and technology, influencing subject areas such as soft matter, chemical synthesis, biological analysis, optics and information technology. Moreover, thermal science has always played an important role in the study of chemical reactions and phase changes. From this point of view, calorimetry has become an important and commonly used technique for both of these scientific disciplines. Additionally, when chemical reactions and phase changes are performed under flow, the transport phenomena become increasingly relevant. This work, in which chemical reactions are performed in two-phase flows at the microscale, is located at the boundary of three important scientific domains, which include chemistry, thermal science and fluid mechanics, as schematized in figure 1.

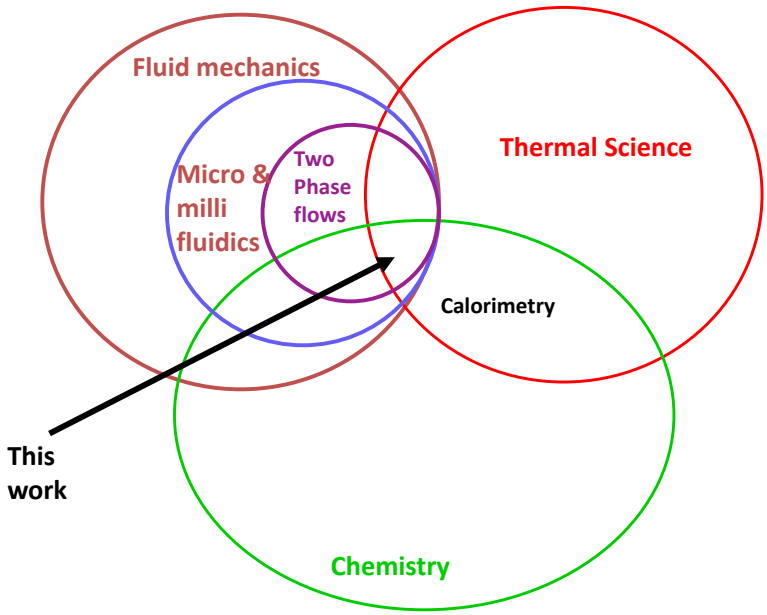

Figure 1: The location of this research work among the interdisciplinary fields

For reaction engineering purposes, the use of segmented flows, such as liquidliquid or liquidgas flows, in miniaturized devices has soared in recent years [1, 2, 3]. Furthermore, recent advances have been made in the study of biphasic flows for the cooling systems of miniaturized electronic devices toward the improvement of micro-heat exchangers. The first thermal studies of liquidgas segmented flows used numerical and analytical approaches [4, 5, 6]. Additionally, several experimental studies regarding the thermal effects and characterization of segmented liquidgas flows have been reported [7, 8, 9, 10, 11, 12]. These studies analyzed the influence of the length of the slugs to enhance the heat transfer in micro-channel heat sinks. In contrast, only one study on liquid-liquid thermal analysis has been reported [13].

As a result, very few studies on the thermal analysis of liquid−liquid flows, particularly with respect to the

development of parameter estimation methods, have been reported in the literature. This work is a pragmatic attempt to implement thermal estimation methods for liquid−liquid two-phase flows in miniaturized systems.

The main objective of this exploratory work in the field of thermal microfluidics is to develop new methods to determine the enthalpy and kinetics of chemical reactions under difficult experimental conditions. This work provides the first measurements of the temperature fields of liquid-liquid two-phase flows inside a millifluidic tubing-based isoperibolic chip and includes an estimation of the reaction heat flux and enthalpy. To achieve these estimations, our research has led to the development of:

- a non-contact droplet flow calorimeter,
- an experimental study related to the stability and periodicity of the flow,
- a quantitative thermal analysis,
- novel methods for identifying thermodynamic properties by using inverse processing methods,
- calorimeter validation for the characterization of a model reaction, and
- application to the characterization of two reactions,

This manuscript is composed of five chapters:

The first chapter is devoted to a survey of the state-of-the-art focused on the various microfluidic tools available, as well as the scientific background that justifies the main objectives of this work. First, we present the microfluidics and flow configurations for monophasic and biphasic conditions. Second, an overview of the recent developments in thermal metrology as adapted to miniaturized systems, namely, the application of infraRed thermography (IRT) to these systems, is presented.

The second chapter is devoted to a detailed description of the experimental set-up of the non-contact droplet flow isoperibolic calorimeter used to characterize the chemical reactions. The original concept of this device was based on a combination of InfraRed Thermography and a droplet flow running in an isoperibolic millifluidic system. The device was design for use without special lighting or particular insulation. The developed experimental assembly reveals that highly exothermic reactions can be studied safely.

The third chapter is an experimental investigation of the stability and periodicity of the flow. Here, the two-phase flow is characterized in terms of its velocity, periodicity and reproducibility. Two imaging techniques are used to study the biphasic droplet flows. The IRT technique allows for the measurement of temperature fields, while visible imaging is used to characterize the biphasic flow hydrodynamics. This very important characterization technique allows several hypotheses concerning the modeling of heat transfer to be established.

The fourth chapter is dedicated to quantitative thermal analysis, where the thermal effects present in this complex system are discussed and modeled. To provide a global overview of when both the hydrodynamic and thermal effects are coupled in a biphasic system, a three-dimensional (3D) numerical model is presented. Consequently, from this study, some hypotheses are assumed to simplify the thermal modeling process. As a result, three thermal models are presented. According to the proposed thermal analysis, two thermal scenarios are identified. These distinct approaches enable an estimation of the thermophysical properties, such as ρC_p, the dissipated heat source, and the reaction enthalpy and kinetics.

The fifth chapter is devoted to experimental validation in which the analytical models proposed in chapter four are compared to the experimental work. Thus, using a well-known reaction, the methodology for estimating the mixing kinetics of the reaction is verified by comparison with the thermal analysis. Finally, we show through two chemical applications that this novel non-intrusive calorimetry technique, based on millifluidic and IR thermography, is a convenient and powerful tool for the characterization of chemical reactions performed in a droplet flows.

Chapter 1

Introduction and theoretical background

Abstract

The study of microfluidic systems has emerged as an interdisciplinary science and technology field. The development of droplet microreactors has increased significantly in recent years. Microreactors are mainly applied as analytical tools for the acquisition of data from chemical reactions and molecules, materials synthesis and biological applications. Many spectroscopy-based analysis tools exist for the online monitoring of the evolution of such systems, particularly in terms of concentration evolution. In contrast, online tools for monitoring temperature evolution are uncommon and less developed. Nevertheless, temperature is a crucial parameter for the analysis and characterization of such systems. In this chapter, several thermal metrology techniques, as applied to miniaturized underflow systems, are analyzed to justify the development of a novel tool for the thermal characterization of droplet microreactors. Within the framework of this thesis, a new experimental method and theory is proposed to achieve the measurement of chemical enthalpy and kinetics.

1. Introduction and theoretical background

Microfluidics is the branch of fluid mechanics that addresses the behavior, precise control and manipulation of fluids that are geometrically constrained to a small scale, that is, typically a sub-millimeter scale. Because this science is widely developed, only multiphase systems are considered here. At this characteristic scale (μL), multiphase flows are an interesting and challenging branch of fluid mechanics because the usual dimensionless numbers and classical correlations possess very different orders of magnitude [14, 15].

The presentation of technical details and specific concepts regarding microfluidic applications is beyond the scope of this manuscript. However, to facilitate the understanding of the physical mechanisms that act in this configuration, a brief overview based on the key parameters, such as the hydrodynamics, transport phenomena and thermal metrology, as applied to miniaturized systems, is described.

1.1 Description of micro- and millifluidic systems

Micro- and millifluidic issues address fluid flows over small scales and pertain to the manipulation of small volumes of liquids or gases (commonly, from the femtoliter to microliter range) through miniaturized channels of varied geometrical shapes. The emergence of microfluidics in 1980 has led to a significant amount of studies concerning flows at small scales, as well as to the development of numerous techniques to understand the original devices.

The study of fluid flow at small scales enhanced the interest of classical areas of fluid dynamics, physics, chemistry and life sciences.

Thus, the rapid development of microfabrication techniques depended on significant advances in the microelectronics field. The most common microfabrication techniques were based on silicon and glass supports. Since microfluidics emerged, new techniques based on polydimethyl dimethylsiloxane (PDMS) and polymethyl methacrylate (PMMA) were successfully developed for the generation of microfluidic structures. These materials offered important advantages in terms of chip fabrication, rapid design, increased safety and simplicity of experimental protocols, in addition to low-cost techniques.

Afterward, miniaturized chips were again simplified by using commercial tubing as reactors. This versatile application of commercial tubes is the easiest way to work at small scales (diameters) and under a significant range of lengths and materials.

1.1.1 Single phase flow

The first studies at this reduced scale were performed in single-phase flows, for which fluid behavior was extensively studied. Numerous books and articles have been published [14, 15, 16]. To characterize the associated fluid behavior, the classical relations of fluid mechanics based on the influence of thermophysical properties are studied here.

The most current relation is the dimensionless Reynolds (Re) number. This value is currently used to find the relation between the magnitude of the inertial and viscous forces and is defined as:

$$Re = \frac{\rho \bar{U} d_h}{\mu} \tag{1.1}$$

where ρ is the mass density ($kg.m^{-3}$), $\bar{U}$ is the mean velocity of the flow ($m.s^{-1}$), d_h (m) is the hydraulic diameter, which is the characteristic length of the flow section, and μ is the viscosity of the fluid (Pa.s). Typically, at this flow scale, the Re number is lower than 100 and the flow regime can be considered laminar.

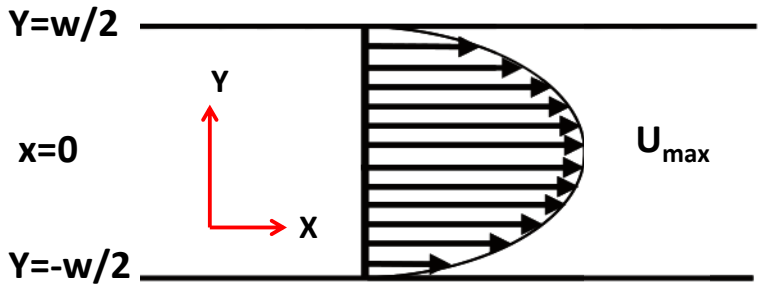

Figure 1.1: The Poiseuille velocity profile for a laminar flow of an incompressible Newtonian fluid

In this type of channel geometry, the velocity profile is parabolic and can be described by the Poiseuille law, as illustrated in figure 1.1. The laminar flow in such a round pipe can be presented as a bunch of straight layers of liquid, each having a velocity function of their radial distance from the center of the tube. Because this profile is parabolic and results from the no-slip condition, the maximum velocity (U_{max}) is at the center ($y = 0$), whereas the velocity is equal to zero at the wall boundaries ($y = \pm w/2$).

1.1.1.1 Incompressible liquids in co-flow

In such microfluidic flows, both diffusional and convective transports occur. For example, we consider a T−junction with two inlets and one outlet, with two miscible fluids A and B, as shown in figure 1.2. Here,

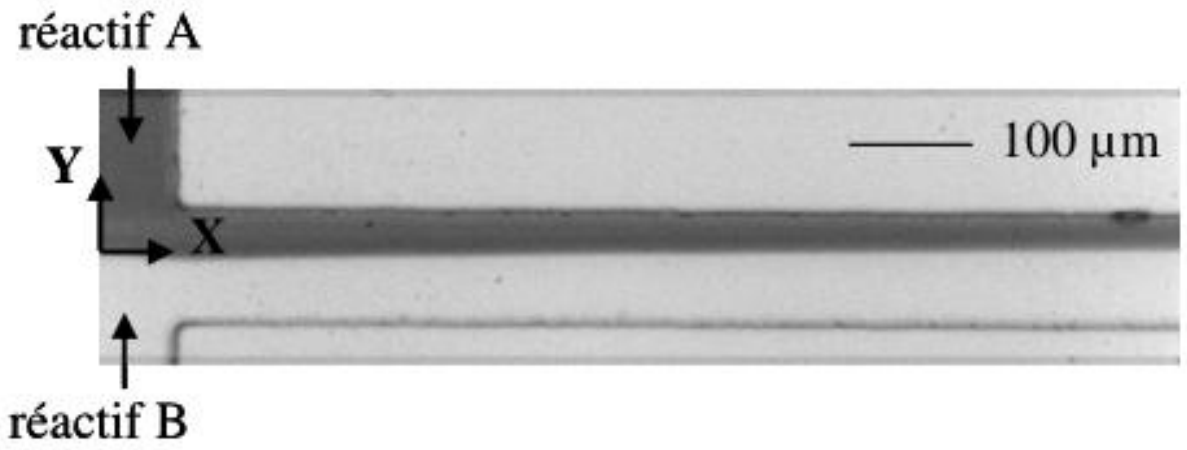

Figure 1.2: In reactive co-flow, the product formed at the interface is colorless, where w is the width of the channel [17]

the laminar flow induces the flow of both fluids along the same direction (x), due to molecular-diffusion induced mass transfer in the transverse (y) direction of the flow.

The mixture process is assumed to be dominated by diffusion. The limitation due to diffusion is well known in microfluidics and can be viewed as either a drawback or an opportunity. In this case, the opportunity is to design experimental conditions for studying the diffusion of solutes as a function of distance. In contrast, the drawbacks associated with diffusion in microfluidics are generally nontrivial. Due to low Reynolds numbers, it is difficult to mix solutions efficiently. The process of mixing, which includes dilutions, is central to most chemical and biochemical processes that occur in microfluidics.

1.1.1.2 Study of the mixing process in co-flow

Many studies concerning the observation and modeling of the interdiffusional zone in a T-shape junction have been published [18, 19, 20, 21]. In that case, the channel dimensions are defined according to the figure 1.3.

The length L represents the distance along the flow direction from the point of contact of the two solutions. The width of the channel is w, and the principal dimension of diffusion is d. As illustrated in figure 1.3, the asymmetric development of the interdiffusion region occurs due to the difference in the diffusion coefficients between the two species. The curvature of the inlets results in a smaller zone of zero flow at the intersection point of the two fluids.

This microfluidic device allowed an estimation of the coefficient of diffusion D ($m^2.s^{-1}$) between two fluids, according to the following relation:

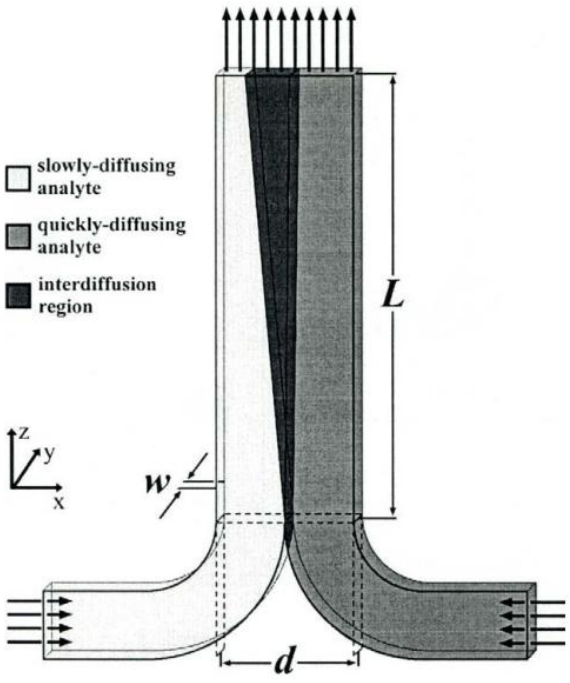

Figure 1.3: Co-flow T-junction interdiffusional mixer [20].

$$t_{diff} = \frac{e^2}{D} \quad with \quad e = \frac{d}{2} \tag{1.2}$$

Thus:

$$d^2 = 4.D.t_{diff} = 4.D\frac{x}{\overline{U}} \tag{1.3}$$

where e (m) is the half-width of the interdiffusional zone as function of the length of the channel d (m) crossed by the fluids flowing under a co-flow configuration. The diffusion length can be rewritten as function of mean velocity $\bar{U}$ $(m.s^{-1})$ during a given position of the channel x (m), as shown in equation 1.3. Many studies of interdiffusion coefficients have been published [14, 17, 19, 22].

Strook et al. [23] proposed a chaotic advective mixer in microchannels at low Reynolds numbers that was based on a passive method of mixing the streams of steady pressure driven flows. This method used bas-relief structures designed with basic microfabrication techniques directly onto the floor of the channel. As illustrated in figure 1.4, fluorescein dye was used to evidence the chaotic mixing measured with confocal imaging, revealing that the mixing length and time were significantly reduced.

Many methods were proposed in the literature [14, 15, 24], with the associated conclusions indicating that in co-flow, the mixing time and length are limited by diffusion. This limitation is a drawback for the kinetics of

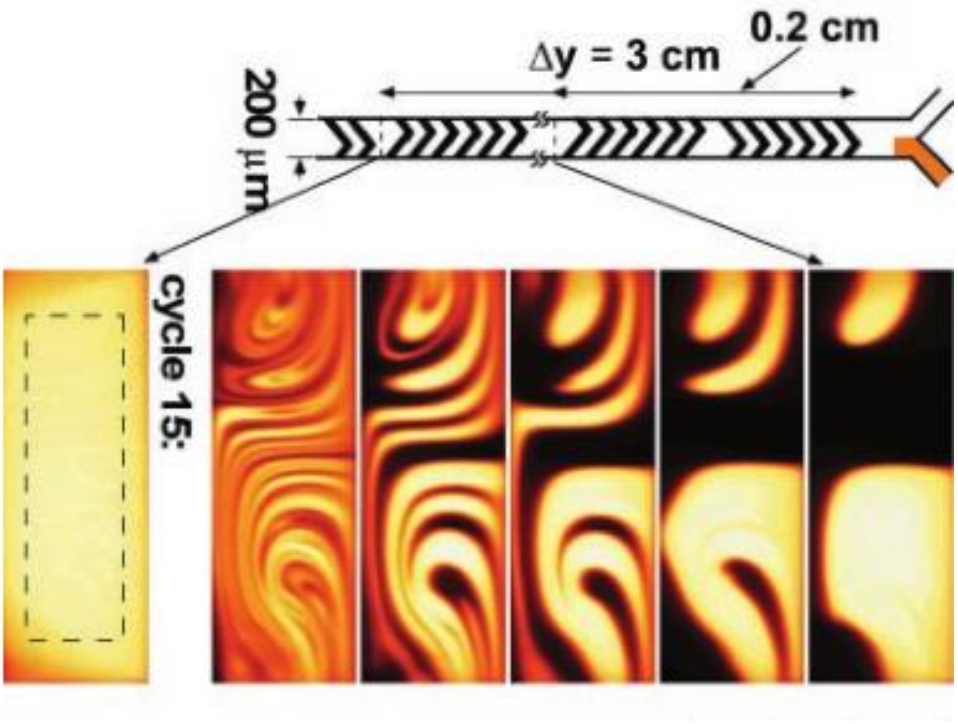

Figure 1.4: Confocal micrographs of the distribution of fluorescent molecules in the cross-section of the channels, demonstrating that chaotic advection decreases the mixing time [23].

chemical reactions. To increase advection and to improve the mixing time, one alternative is to use multiphase flows, segmented by bubbles or droplets and transported by a continuous phase.

1.1.2 Multiphase flows of two incompressible liquids

Multiphase flows that involve immiscible fluid systems are well known and have been studied for years. These flows exhibit a wide range of possible phase distributions. These transient flows lead to variations of many properties as functions of time, such as the pressure drop and concentration component contained in one fluid phase. Consequently, many applications, such as heat exchangers [8, 25], power dissipation in microelectronic devices [6], droplet-based microfluidics [26, 1] and emulsions [27], have been developed, based on such segmented flows. Moreover, micro- and millifluidics provide an excellent way to precisely control fluid flow. From this point of view, multiphase systems can be used to create original, calibrated and controlled flow patterns, such as droplets, bubbles or jets.

The dynamic behavior of these flows offers design challenges and provides unique opportunities to overcome the transport limitations in single-phase microflows.

1.1.2.1 Generation of segmented flows

The flow of immiscible fluids generally occurs in the form of a segmented flow. Consequently, the disperse phase flowing at the center of the channel is segmented into distinct slugs by a continuous phase. Generally, the continuous phase perfectly wets the wall, creating a liquid film that surrounds the disperse phase to avoid contact with the wall. Due to the flow field, the segmented flow increases interfacial deformation and promotes the natural growth of interfacial instabilities, without any local actuation. The droplet polydispersity in these streams can be as small as $1 - 3\%$ [28]. Droplet generation techniques must be sufficiently flexible to provide droplets of prescribed volumes at a given rate.

Research in this domain has led to the development of a variety of different droplet, bubble and slug generation techniques, such as co-axial injection, T junction, cross junction [29, 30] or flow focusing [31] capabilities. Additionally, the merging of technologies has enabled the integration of electrodes into microdevices to provide electrical control over droplet formation, where examples of these electrohydrodynamic (EHD) methods include dielectrophoresis (DEP) [32] and electrowetting on dielectric (EWOD) materials [33].

Baraud et al. [28] summarized the three main approaches, which are based on different physical mechanisms and are described by the flow field at the slug generation zone: (i) breakup in co-flowing streams (figure 1.5), (ii) breakup in cross-flowing streams (figure 1.6) and (iii) breakup in elongational strained flows (figure 1.7).

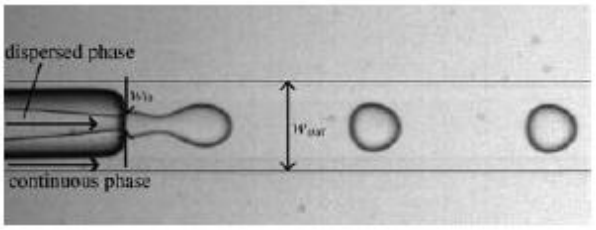

Figure 1.5: Droplet production in a co-axial injection device. The inner flow is produced by a thin, round capillary and then is inserted into a square exit capillary [28].

In the three proposed designs, the droplet formation mechanism is mainly governed by shear and interfacial forces; hence, a similar set of parameters governs the generation of segments, including channel geometry, flow rate, viscosity and surface tension. These parameters play critical roles in the control of droplet generation. More precisely, in miniaturized systems, flow instabilities provide passive ways to increase the interfacial area, e.g., by an unstable fluid interface that breaks down into droplets or bubbles. Because of the low Reynolds numbers that are often associated with microfluidic systems, viscous instabilities play an important role. However, at very high flow rates, inertial forces become significant [34]. Many variations of the basic flow focusing design have been developed to allow for highly complex and original applications [35, 36, 37]. Here, the co-axial injection technique used to generate segmented flows is described.

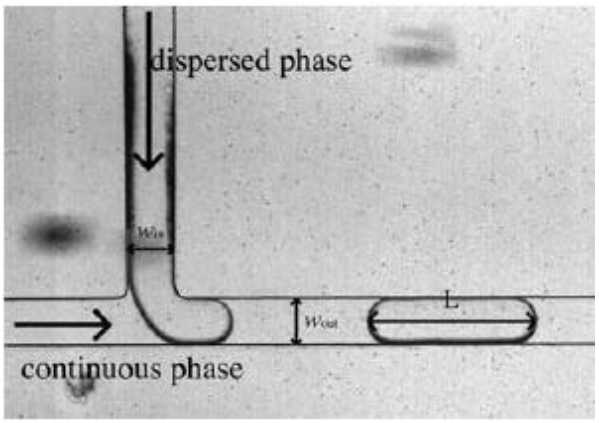

Figure 1.6: Droplet production in a T-junction. The dispersed phase and the carrier phase meet at 90 degrees in a T-shaped junction [28].

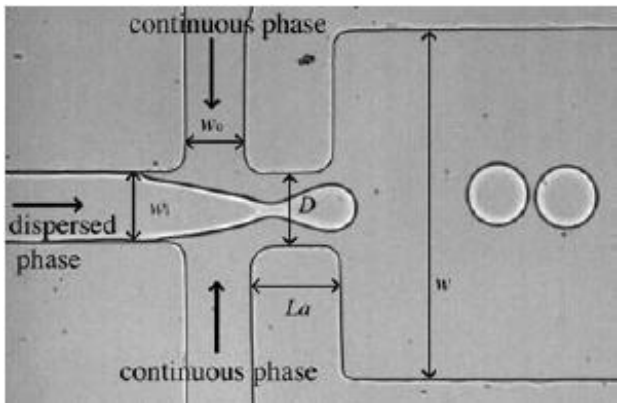

Figure 1.7: Droplet production in a flow-focusing device. The dispersed phase is squeezed by two counter streaming flows of the carrier phase, forcing drops to detach [28].

- **Co-axial injection device**

It is possible to generate different flow patterns in miniaturized devices. When two immiscible fluids flow through microchannels, monodisperse droplets or jets are obtained, depending on the flow rate ratio between the aqueous and oil phases. Guillot et al. [38] reported experimental data for liquid-liquid flows, showing that the confinement and shape of the geometry play a fundamental role. Additionally, the stability of the jet was analyzed in the framework of the lubrication approximation at low Reynolds number. The authors reported that in a cylindrical geometry, the jet remained continuous at high capillary numbers and broke down into droplets at lower flow rates, as illustrated in figure 1.8. The transition between the droplet and jet regimes was related to the absolute/convective transition of the Rayleigh-Plateau instability and reached remarkable agreement with the data .

Herrada et al. [39] reported simulation results concerning the phase transition of the jetting and dripping of a liquid flow-focused by a gas. A simultaneous influence of the jet and the meniscus as instability sources was

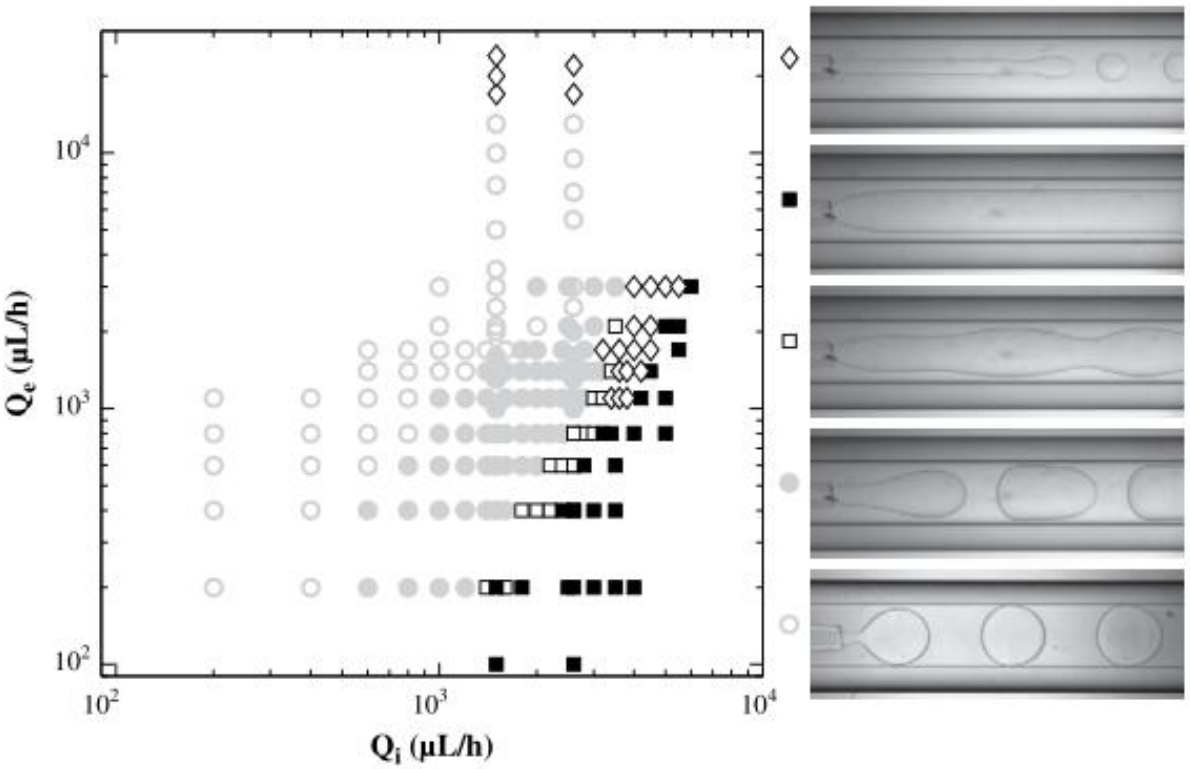

Figure 1.8: Map of the flow behavior in the (Q_e, Q_i) plane. The droplet regime includes droplets smaller than the capillary (o) and plug-like droplets (•) confined by this capillary. Jets are observed in various forms, including jets with visible peristaltic modulations convected downstream (□), wide straight jets that are stable throughout the 5-cm-long channel (■), and thin jets that break into droplets at a well defined location (◇) [38]

noted. Furthermore, many other works concerning flow regimes and patterns have been reported in the literature for liquid−gas and liquid−liquid systems [40, 41, 10, 3]. Recently, Marre et al. [42] performed the same strategy as that published by Guillot et al. to demonstrate that the possibility of generating stable millifluidic droplet flows of supercritical carbon dioxide and liquid water. These studies also revealed that many flow properties are preserved when scaling from the micro- to millifluidic regime and enable the generation of stable droplet flows [43].

Today, most reported flow regime measurements are carried out for a wide range of fluids and miniaturized channel geometries. In the future, it will be necessary to arrive at more general, dimensionless scaling arguments for the transition lines from one regime to other. Regardless, such studies have demonstrated the feasibility to generate different flow regimes in a controlled manner by carefully adjusting the flow rates and the properties of the external and internal fluids.

The co-axial injection technique allows for the generation of periodic monodisperse biphasic flows.

1.1.2.2 Hydrodynamics in segmented flows

At a constant total flow rate, the biphasic flow is displaced by simple translation in the channel. When this happens, segmented flow is generated at the same frequency; once the flow reaches the periodic established state, the segmented flow is regularly spaced and flows at a constant velocity. Thus, it is possible to apply the principal of space-time correspondence, e.g., a given position in the microfluidic circuit corresponds to a given time. Hence, in such systems, the following is true:

- The residence time of each droplet is well defined. In this case, the Residence Time Distribution (RTD) corresponds directly to the residence time, i.e., the average amount of time that a droplet spends in the microfluidic circuit, and is described as:

$$\tau = L/\bar{U}$$

  , where L (m) is the length of the channel and $\bar{U}$ $(m.s^{-1})$ is the mean velocity for the total flow rate.

- RTD is very narrow, and for a first approximation, RTD can be considered close to zero [44].

- Space-time correspondence suggests the possibility to obtain experimental space evolution as a function of time.

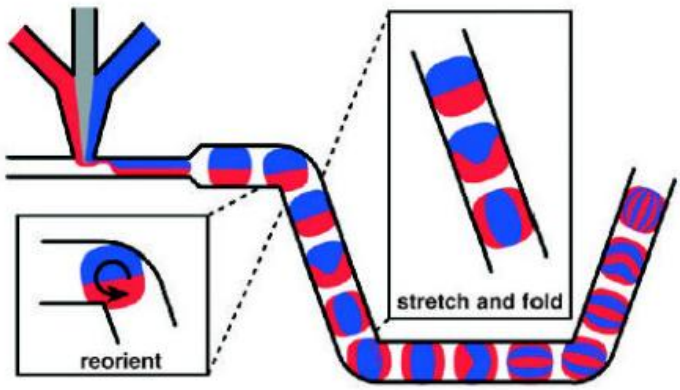

Figure 1.9: Mixing by chaotic advection in a plug moving through a winding channel. The interfaces between the red and blue fluids are reoriented, stretched, and folded as the plug moves through the corners and straight sections of the channel [45].

Song et al. [19] applied their previous studies concerning chaotic mixing in a single phase to droplet flows. As illustrated in figure 1.9, the authors experimentally observed that flow patterns within droplets (or plugs) act as the bakers transformation [1]. A scaling law to predict the mixing time in droplets was proposed based on experimental work. It was demonstrated that under favorable conditions, a sub-millisecond mixing time can be

[1] chaotic mixing has been described for a flow that reduces the striation length by stretching, folding, and reorienting the fluid in a manner similar to that of the bakers transformation

measured in microfluidic systems [45]. These results were complemented by numerical studies published by Muradoglu et al. [46], in which the effects on the quality of the mixing of various non-dimensional parameters were studied, and it was found that (i) the capillary number, (ii) the viscosity ratio between the phases and (iii) the relative size of the droplet compared to the average channel width were the most critical parameters influencing the mixing. Mixing was found to be weakly dependent on the Reynolds number.

Dogan et al. [47] numerically studied the chaotic mixing of miscible liquids for gas-segmented serpentine channels. The effects of various non-dimensional parameters on the quality of mixing were investigated, and the authors found that (i) the relative bubble size, (ii) the capillary number and (iii) the non-dimensional channel corrugation length were the most important parameters influencing the mixing behavior. A weak dependence of the mixing behavior on the Reynolds number was confirmed.

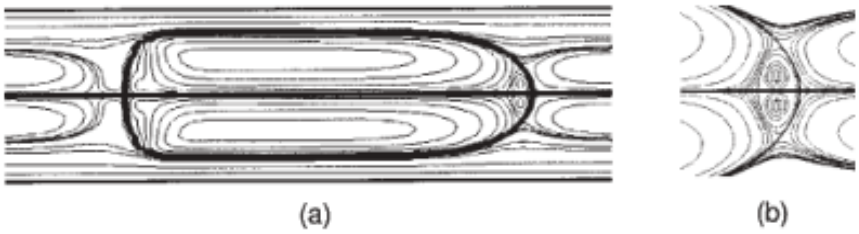

Figure 1.10: (a) Streamlines in the reference frame of the droplet obtained by two-dimensional computations; (b) A magnified perspective of the droplet head [48].

Sarrazin et al. [48] reported numerical simulations and experimental studies that determined the hydrodynamics of liquid−liquid flows. Micro-particle image velocimetry (PIV) measurements were used to compare the experimental velocity fields inside droplets using numerical simulations. The published results revealed the presence of internal zones at the front and back of the droplets in which mixing mainly arises from diffusion (figure 1.10. a). Moreover, a recirculation zone in the droplet head was clearly revealed (figure 1.10. b).

Additionally, it has been demonstrated [49] that in microchannels, the combination of viscous and non-viscous reagents enhances the mixing in droplets moving through the channel by providing a nearly ideal initial distribution of reagents within each droplet.

The use of biphasic flows addressed one of the most fundamental problems encountered in single-phase microfluidics by providing control over dispersion and mixing. As demonstrated, biphasic flows improve significantly the mixing time inside the droplets or plugs by recirculation, chaotic mixing and shearing between the phases or by a combination of such phenomena.

1.1.3 Applications of segmented flows on micro−millifluidics systems

Micro- and millifluidic gas−liquid and liquid−liquid systems allow more efficient heat and mass transfer because a high ratio of total surface area to volume is available. Moreover, segmented two-phase flows are especially attractive because of the enhancement of radial mixing in both phases as a result of reducing the axial dispersion, compared to that of a single phase. The occurrence of these phenomena in such complex flows was the motivating factor for the study of heat transfer systems and the analysis of chemical reactions and biological systems.

1.1.3.1 Heat transfer systems

Efficient heat transfer systems have provided significant advances to cooling systems in microelectronics [15], micro-heat exchangers [10] and lab-on-a-chip modules [16]. The latter examples are characterized as systems in which at least one dimension is less than a few millimeters. Certain scaling issues must be considered for miniaturized elements when developing metrology. Heat flux is a function of surface area, while heat capacity depends on volume. Moreover, thermal characteristic time scales in miniaturized systems evolve linearly with the length scale, resulting in a specific heat flux that shrinks linearly with decreasing dimension.

As a result, the high surface-to-volume ratio that characterizes micro- and millichannels is useful for enhancing heat exchange, through the dissipation or the accumulation of significant amounts of heat in segmented flows due to the relation that exists between the heat capacity and the engaged volumes [5]. Through experiments and optimization studies, Betz et al. [8] demonstrated that segmented flow enhances heat transfer by up to 140% in a microchannel heat sink. Gas−liquid systems without phase changes are an interesting option for heat transfer enhancement in compact heat exchangers. The presence of gas bubbles that separate liquid slugs induces recirculation inside the liquid phase, so that the overall wall heat transfer coefficient is increased with only a moderate penalty in terms of pressure drop. Further, such gas−liquid flows are rather stable, due to the absence of explosive boiling. The heat of vaporization is very high. It has been shown that a boiling flow can dissipate up to 10,000 $W.cm^{-2}$ of heat [50, 51, 52], which is 10 times more than that of a single-phase flow. Gas−liquid systems with phase changes, such as boiling flows, are attractive because they deliver high heat flux at the constant temperature of the phase change. However, such systems can be difficult to control due to backflow and instabilities [12]. Investigations concerning the control of instabilities and backflow, including nucleation sites [53] and inlet restrictions [51], have been reported. When water is the working fluid, one drawback of boiling flow is that the saturation temperature is higher than the operating temperature of most electronics; the proposed solution is to use refrigerants as working fluids because their respective boiling temperatures are

lower than that of water. However, refrigerants offer lower cooling capabilities due to their lower specific heat and heat of vaporization values.

1.1.3.2 Chemical reactors and biological systems

When studying chemical reactors and biological systems, the applications of biphasic flows are wide. As previously discussed, the dispersion and mixing inside that occurs inside droplets or slugs is controlled by chaotic convection and recirculation, which is driven by shear between the inner and external fluids. These conditions are necessary to achieve the study of such systems. Thus, underflow systems have the ability to translate reactive systems into miniaturized circuits and can afford the possibility to study these systems over time. Furthermore, as a result, it is also possible to develop statistical information concerning the observed phenomena.

Miniaturized two-phase flows are schematized in figure 1.11. Jensen et al. [2] classified reaction systems into three broad categories. This classification, as discussed below, can also be applied to biological systems.

1. Both phases participate in the chemical reaction.
2. Heterogeneous catalytic gas−liquid reactions ocurr.
3. The reactions are exclusively confined to one phase, where the second phase is a passive tool for achieving a desired phase distribution, typically used to improve either mixing or the dispersion characteristics.

We focus on reactions that are exclusively confined in one phase. Other applications are reported in the literature [3, 54, 55, 56, 57]. In such a case (i.e., confined reactions/phenomena), the number of parameters that can be studied inside a plug or droplet is infinite; that is, such studies are only limited by the imagination and/or technology.

- Reactions confined in one phase

Song et al.[1] developed several techniques for studying different types of reactions, performed in parallel and in series. As a result of these studies, the authors demonstrated that a wide range of reactions can be performed in droplet flows [58]. The performed reactions were classified into five categories:

1. Enzyme kinetics (see figure 1.12) and DNA [2] analysis
2. Protein crystallization
3. Synthesis of molecules

[2]DeoxyriboNucleic Acid (DNA) is a molecule that encodes the genetic instructions

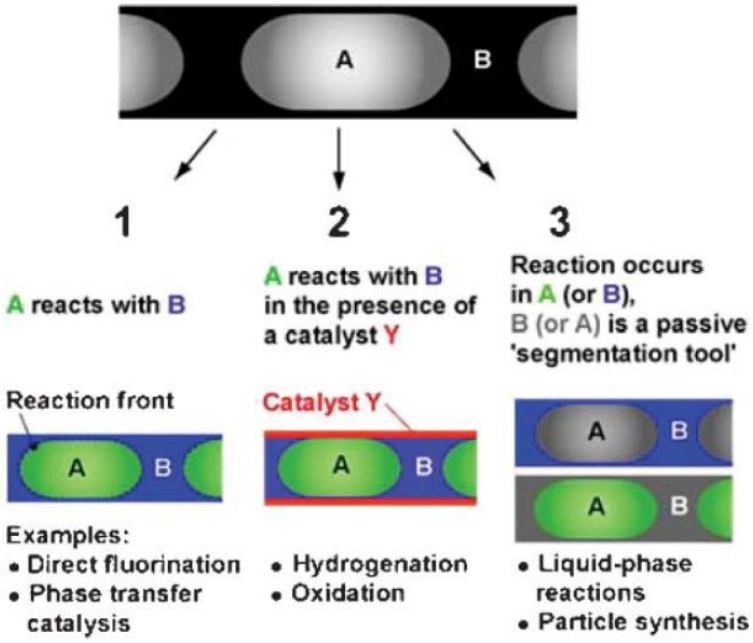

Figure 1.11: Multiphase systems used to perform reactions. The disperse phase (A) is shown in green, and the continuous phase (B) is colored blue. (1) Immiscible fluids, either a gasliquid mixture or two liquids, react with each other. (2) Immiscible fluids react with each other in the presence of a catalyst. (3) The reaction occurs only in one phase (either continuous or dispersed) [2].

4. Synthesis of nanoparticles, microparticles, and colloidal assemblies

5. Synthesis of reaction

Additionally, chemical droplet-based platforms have shown dimensional scaling benefits that have enabled the decrease of mixing reaction times based on the use of one-, two- or three-dimensional arrays [58]. Other researchers applied miniaturized systems to the production of hierarchically organized large emulsions (Figure 1.13) and particles with very good control of the size, shape and internal structures [59].

It was reported by Engl et al. [60] that considering the high modularity of millifluidic flows, it was possible to synthesize particles with strong control over the final object sizes, monodispersity and aspect ratio. An example is illustrated in figure 1.14, in which the polymerization of spherical and non-spherical particles, through the encapsulation of droplets or solid particles, is shown. A similar millifluidic tubing-based system was used to produce metallic microparticles; the authors demonstrated that it was possible to fabricate original and well-defined geometries [61].

The use of polymerization in high-throughput millifluidic platforms to perform kinetic measurements in the liquid phase is described in the literature [62], in addition to the chemical synthesis of slow reactions [63], the chemical synthesis at high pressure [42] and heterogeneous catalysis, especially for liquid/solid reactions [64].

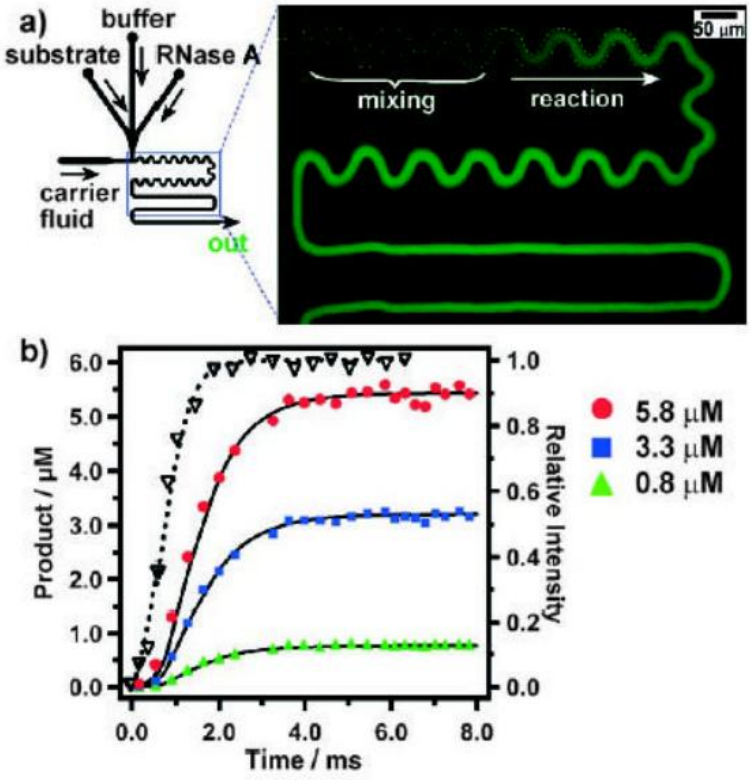

Figure 1.12: A microfluidic set for the enzyme kinetic analysis of droplet turnover on the millisecond timescale. a) Left: The experimental setup. Right: Fluorescence images, the intensity of the aqueous plugs and the carrier fluid moving through the microchannel. b) A graph of the experimental kinetic data for three substrate concentrations, where the calibration curve is plotted by ▽. The solid lines are fitted for reaction progress, including the explicit treatment of mixing. [45]

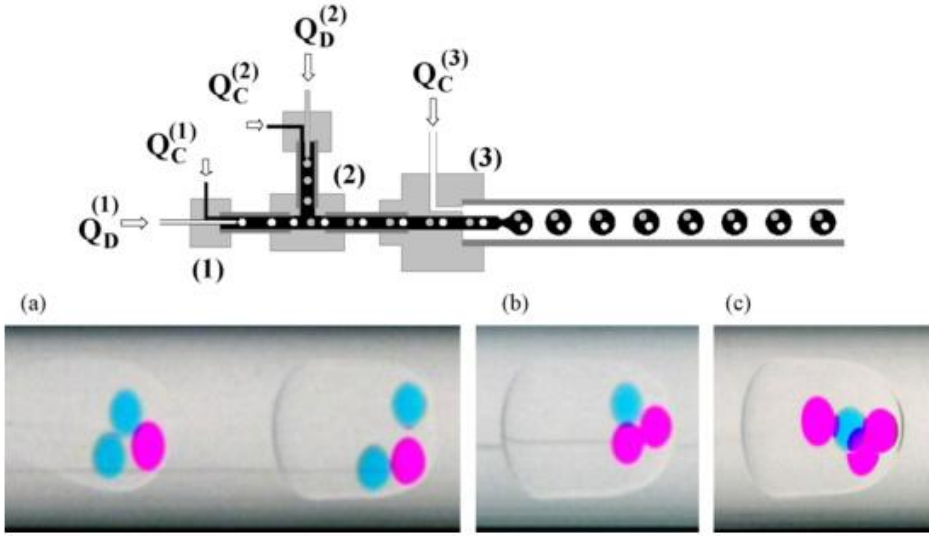

Figure 1.13: Millifluidic set-up used to fabricate double macro-emulsions with two types of internal droplets. The organic phase and continuous phases are respectively silicone oil and 95% (w/w) glycerol in water [59].

Only a subset of the applications of two-phase flow systems in micro- and millifluidic devices was presented; because of the very large number of applications in this research domain, it is impossible to mention all such applications.

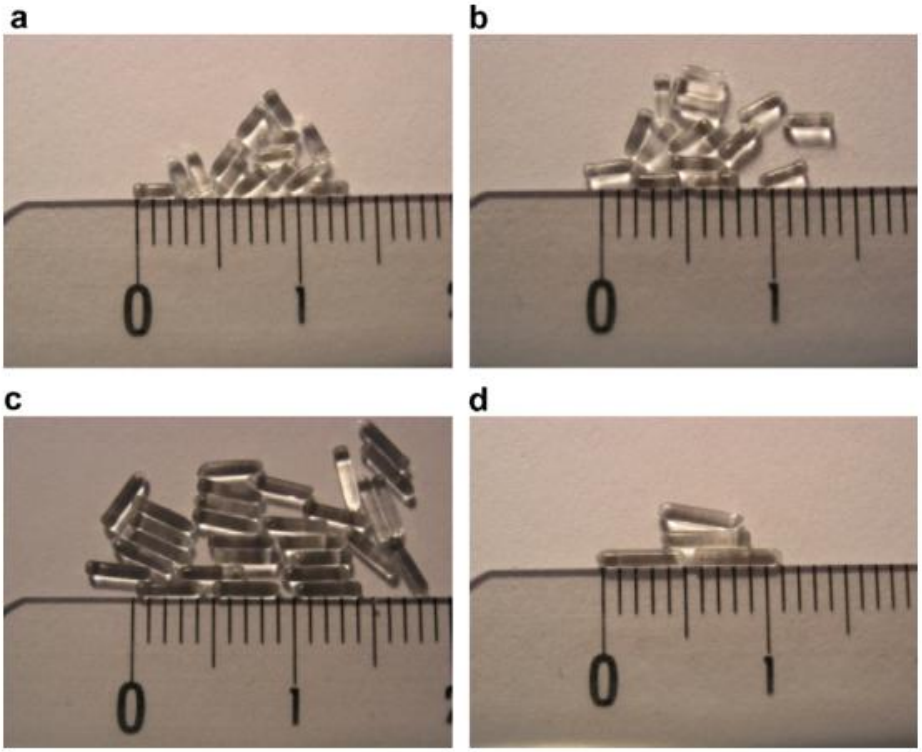

Figure 1.14: Rod-like particles obtained after polymerization in a millifluidic narrow tube [60].

Through these recently published examples, it is possible to note the diversity of issues that can be addressed by using miniaturized systems to understand physical phenomena, data acquisition and chemical synthesis. However, depending on (i) the speed of a reaction, (ii) chemical compatibility, (iii) chemical behavior and (iv) the availability of reagents, the scale of the miniaturized system plays a major role and must be defined.

1.1.4 Characteristic scale

The previous applications were performed in micro- and millifluidic systems. These miniaturized techniques have different orders of magnitude, as summarized in table 1.1. The differences are directly related to the scale size of the miniaturized systems. In this table, the inner diameter (d), the volume (V) of the reactor, the total flow rate (Q) and other characteristic values are reported.

- **Relevant differences**

Microfluidic devices require a specific microfabrication process. As a result, a collection of technologies is used in the fabrication of a microdevice. Accordingly, many processes must be performed, many of which are carried out in clean rooms. These processes typically include depositing a film, patterning the film with the desired micro-features, and removing (or etching) portions of the film. Additionally, microfabrication techniques offer

	<<micro>> droplets		<<milli>> droplets	macro
$\mathbf{d}_{reactor}$	50 μm	500 μm	1 mm	10 cm
$\mathbf{V}_{reactor}$	0.3 nL	0.3 μL	3 μL	250 mL
Q	0.1 mL.h^{-1}	1 mL.h^{-1}	10 mL.h^{-1}	
Surface/Volume	30000	3000	1500	1
Residence time	seconds	minutes	minutes - hours	hours
Mixing time	milliseconds	seconds	seconds - minutes	seconds
Reactions				
Fast	**++**	**+**	**-**	**-**
Slow	**-**	**+**	**++**	**++**
Exothermic	**++**	**++**	**++**	**-**
Sampling	**-**	**-**	**++**	**+**

Table 1.1: Comparison of three systems at different scales, including the respective order of magnitude of each, for microfluidics and millifluidics in which the drops are assumed to be spherical, and in batch, which corresponds to a half-filled flask measuring 10 cm in diameter.

the possibility of making any pattern or design at high precision. In contrast, millifluidic devices are fabricated by connecting plastic or glass capillary tubes to each with connectors, where the possible configurations vary greatly.

According to the specific nature of the chemistry that will be performed, the raw material (PDMS, glass, TEFLON) must be chosen in advance for microdevice fabrication. In contrast, for millifluidic set-ups, tubing selection is an easy task. Furthermore, world-wide suppliers, such as Upchurch Scientific, sell any length of tubing with a variety of choices of (sub)millimetric inner diameters with tolerances less than 5%. Versatile nuts and sleeves allow the use of tubing sizes that range from 360 μm to 1/16 or 1/8 inch outside diameter measurements within the same device. Thus, depending on the chosen diameters of these tubes, it is possible to assemble the tubes with inexpensive commercial ties or crosses, as well as design flow-focusing or simple T- junction patterns, as in microfluidics (cf. figure 1.5 and 1.6). However, the characteristic lengths tend to be one or two orders of magnitude higher than those used in microfluidics. Nevertheless, the associated Reynolds numbers remain low, i.e., approximately 1, and the flows are laminar; hence, it is easy to generate droplets in a rough millifluidic device.

Millifluidics are flexible tools, e.g., the raw materials are easily available, and the system can be partially or totally disassembled to modify the flow pathway. It is also possible to recycle some of the materials after the device has been used. The versatility of this technological approach is convenient and is one of the main advantages associated with millifluidics over microfluidic devices. Indeed, microfluidics are based on expensive microfabrication technologies that require significant knowledge and expertise. Although millifluidic devices do not require time consuming, expensive soft lithography or etching techniques for their fabrication, microfabrication offers the possibility to create a wide range of original and complex structures, which is not always possible when using millifluidic tubing devices.

⋙ **Summary of the millifluidics tubing based devices**

Considering the flexibility of millifluidics, this technology has become an adaptable and high-potential tool for process intensification and analysis, based on the following:

- An on-line tool to study underflow systems
- The possibility of studying a large range of reactions (fast and slow) and phenomena
- Low cost without requiring microfabration techniques or infrastructure
- The miniaturization of analytical tools
- A high-throughput platform
- The use of small volumes of reagents
- A high level of security

Finally, miniaturized scale technology must often be selected as a function of the phenomena or the type of system to be studied. In our study, we perform exo- and endothermic chemical reactions inside of droplets in liquid−liquid systems at rates varying from fast to slow. Additionally, it is important to note that millifluidic tubing-based devices provide more opportunities for boundary condition selection. For these reasons and according to the summarized characteristics in table 1.1, a millifluidic tubing-based system is applied in our study.

1.2 Thermal metrology of miniaturized underflow systems

MicroElectroMechanical Systems (MEMS) are miniaturized technological devices that generally involve coupled field behaviors, combining two or more energy domains, such as mechanical, electrical, optical or thermal energy. The thermal domain is arguably the most prevalent in MEMS devices, either by intentional design or undesirable coupling [65, 66]. MEMS applications involve elements that are on the order of at least several microns in scale, and traditional thermal analysis modeling techniques can be applied for their analysis. One application of MEMS consists of investigating the chemical reactions in fluid flow situations in miniaturized channels; in such devices, the temperature information is one of the most important parameters. Hence, thermal metrology development is highly important, including both the theoretical and practical aspects of such measurements.

Localized temperature microsensors were developed as the first chip reactor for microfluidic calorimetry, as proposed by Monk et al. [67] in 1968; the proposed under flow system was controlled by one thermopile.

Thirty years later, Kohler et al. [68] proposed a calorimeter based on the same principle as Monk et al. by integrating three high-sensitivity thin film thermopiles (thickness of 500 μm) to perform *in situ* temperature measurements of chemical reactions in single-phase flows. Additionally, other applications to monitor temperature information were developed, to study the processes of convective heat transfer. This study was achieved by integrating into the miniaturized system three K thermocouples measuring 50 μm in diameter, which also corresponds to the height of the channels [69]. The same methodology was applied by Baviere et al. [70] to study the hydrodynamics and the associated heat transfer in two-dimensional microchannels ranging from 200 to 700 μm in size by integrating four T thermocouples measuring 500 μm in diameter. The use of localized measurements (by thermopiles and thermocouples) allows for monitoring of the temperature evolution at several positions along the miniaturized channel.

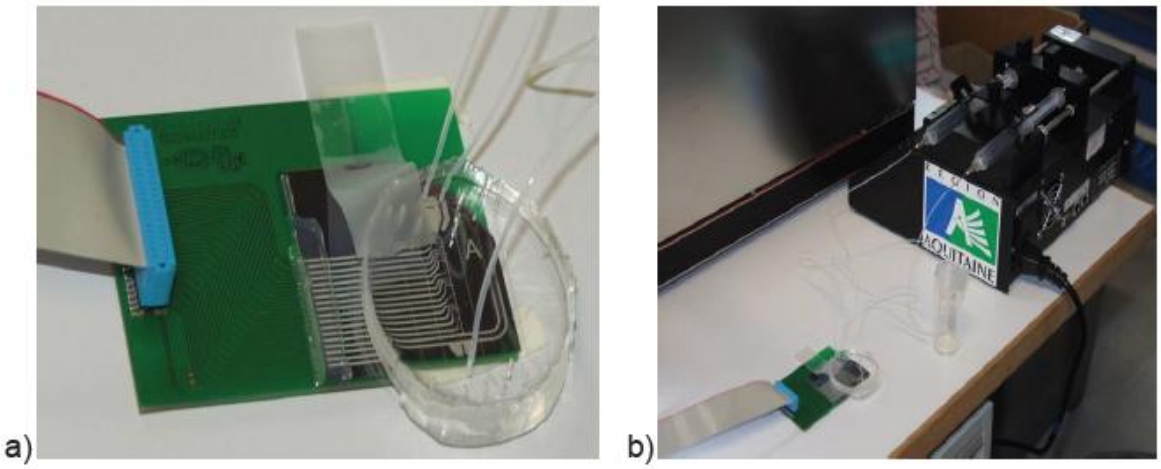

Figure 1.15: a) A microdevice composed of 16 polysilicon diodes, used as thermal sensors. b) A complete microfluidic experimental set [71].

Later, Marty et al. [71] designed and fabricated a microdevice composed of 16 polysilicon diodes as thermal sensors (see figure 1.15). These sensors demonstrated very good thermal sensitivities of 55 $mV.^{\circ}C^{-1}$ and were used to perform calorimetry experiments under the transient thermal regime for fast reactions. Later, thin-film technology proposed thinner films of less than 1 μm, which were appropriated for temperature measurements in microsized devices. By applying this novel technique [72], a thin film heat flux and temperature microsensor [73] were developed to ensure a sensitivity of approximately 37.8 $\mu V.K^{-1}$, which is close to those of a K-type wire thermocouple (40 $\mu V.K^{-1}$) . Both microdevices are composed of 40 thermal resistances. This original set-up was used to demonstrate that by increasing the number of local measurements of the temperature (the number of sensors), the temperature profile resolution along the channel was increased.

In contrast, Velve Casquillas et al. [74] fabricated a micro-device using a metallic substrate to detect reaction heat and to perform kinetic analysis in microreactors via temperature recording. The experimental device is

illustrated in figure 1.16. It should be noted that the electrodes are placed at the inlet and the outlet of the microchannel. Wang et al. [75] used a similar experimental set-up, operated in continuous flow, to measure reaction enthalpy by monitoring the temperatures from sensor chips placed at the inlet and the outlet of the millifluidic channel. The main drawback of such systems is that the measurements remain global and intrusive.

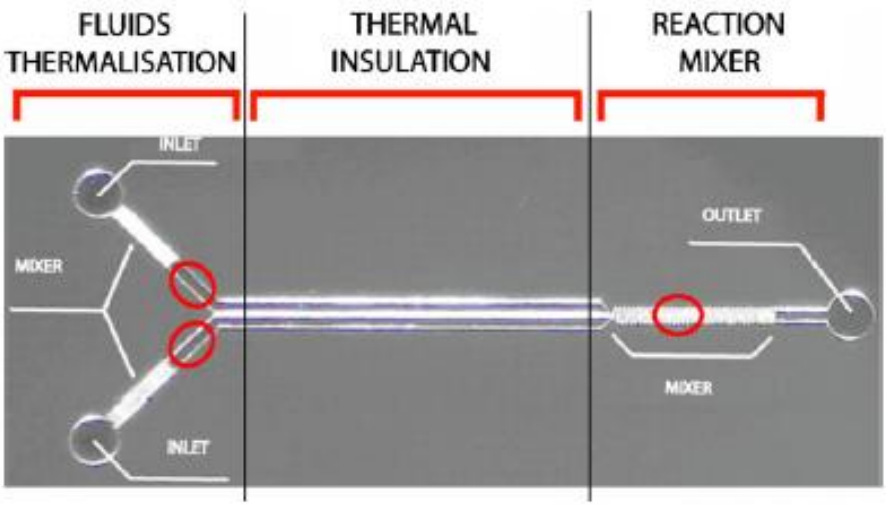

Figure 1.16: Fabricated microcalorimeter. The red circles indicate the location of the platinum electrodes used for monitoring the local temperature in the device [74].

The previously described metrology techniques used for temperature monitoring are *in situ* techniques. They are intrusive methods, e.g., the measuring technology is integrated inside the system, which may cause perturbations due to the sensor thickness. This may introduce a relative roughness at the microchannel surface with a magnitude of 0.2 to 2% of the channel height. Thin-film technology, it has been noted, tends to be a less intrusive technique [73, 72].

Some non-intrusive techniques have been adapted for miniaturized underflow systems. Hany et al. [76] proposed a technique to perform the global thermal analysis of a chemical reaction with a continuous microfluidic calorimeter, based on a thermopile (a Peltier element), by measuring the dissipated heat flux. In the same way, Schneider et al. [77] proposed a homemade micro-reactor that was combined with a commercial calorimeter (Calvet type) to estimate the global kinetics of the reaction.

Additionally, a local estimation of temperature fields was performed by Pradere et al. [78], who used infrared thermography (IRT) to measure temperature fields. The reported methodology used to process the temperature information led to estimations of the enthalpy and kinetics of chemical reactions under co-flow in microchannels.

The previously presented thermal metrology techniques are summarized in table 1.2. It is important to note that

	Sensor	Characteristic size	Measurement	Type of flow	References
INTRUSIVE	Micro thermopile (Flux)	500 μm thickness	Local	Single phase	[68, 67]
	Thermocouple (T)	50-500 μm diameter	Local	Single phase	[69, 70, 71]
	Diode/sensor (T)	450 μm thickness	Global	Single phase	[74, 75]
	Thin film micro sensor (T)	100- 300 nm	Local	Single phase	[73, 72]
NON INTRUSIVE	Thermopile (Flux)	2 cm	Global	Single and biphasic	[76, 77]
	IRT (T)	30 to 250 μm	Local Global	Single and biphasic phase	[78, 79]

Table 1.2: Summary of the thermal metrology techniques

most of the advances in metrology with respect to miniaturized underflow systems have been applied to chemical reaction characterization. Nevertheless, few of the previously mentioned systems performed calorimetry; those that did are summarized in table 1.3.

Literature	Flow range	Principle	Operation mode	Construction	Device
Monk et al. [67]	$ml.min^{-1}$	Heat balance	Isothermal	Twin chamber	Gold silver chip
Kohler et al. [68]	$\mu l.min^{-1}$	Heat accumulation	Isothermal	Single chamber	PDMS/Glass
Velve Casquillas et al. [74]	$\mu l.s^{-1}$	Heat accumulation	Adiabatic	Single chamber	PDMS/Si/glass chip
Luo et al. [75]	$ml.min^{-1}$	Heat compensation	Adiabatic	Single chamber	Teflon
Hany et al. [76]	$\mu l.min^{-1}$	Heat compensation	Isothermal	Twin chamber	PDMS/Si chip
Schneider et al. [77]	$\mu l.min^{-1}$	Heat compensation	Isothermal	Twin chamber	Alumina chip

Table 1.3: Miniaturize under flow calorimeters

Table 1.3 shows that calorimetry applications to the study of reactions have specific principles and operational modes; additionally, such applications are specifically constructed to determine the heat release rate for a given chemical process, as well as to track the global kinetics of reactions. Temperature is a crucial parameter for chemical reactions; accordingly, underflow calorimetry must be able to control the temperature set point to study the influence of temperature accurately.

It is important to note that most metrology techniques have been applied to single-phase flows in microfluidic systems. The resolution measurements have shown great advances from the micro−thermopiles through the

¨ thin film technology ¨ to the infrared images, as metrology has evolved from a mono-sensor to an image. In actuality, two thermal characterization attempts have been made for biphasic flows, both of which were carried out by using non-intrusive techniques. The first study was a local thermal analysis of a droplet flow in a microfluidic chip (PDMS/glass chip), performed by Pradere et al. [80] for the study of an acid-base chemical reaction. It was concluded that in such case, the thermal model used to achieve quantitative measurement was difficult because a number of parameters were necessary to develop a complete thermal description of the flow, the thermophysical properties and the chemical reaction (the heat source). Hence, the fields of Peclet (or velocity) were estimated by IRT experiments. The second exploration was achieved by Hany et al. [76], in which global measurement estimations of the dissipated heat of biphasic flows were performed.

Thermal measurements based on IRT is a suitable technique with high resolution for measuring the temperature fields of biphasic flows. The characteristic length of the system is limited by the associated wavelength (IR domain), which is approximately 10 μm. Nevertheless, even with an IR camera, the main difficulty remains the thermal modeling with respect to realizing inverse processing for chemical parameter estimation.

1.2.1 Infrared thermography and miniaturized systems

IRT is a versatile technology that can be applied in a wide range of domains and scales, ranging from macroscopic applications, such as building [81] and agriculture diagnostics [82], to the observation of miniaturized systems, such as electronic device characterization [83] or biological and chemical systems [84]. Thus, IRT offers the possibility to adapt the resolution as function of the miniaturized system size.

Underflow miniaturized systems were first studied by Mollman et al. [85]. Unfortunately, such pioneer work was only devoted to a qualitative analysis of the temperature fields. Moreover, many other IRT applications have been published based on this qualitative imaging approach, where the aim is to highlight the thermal phenomena that occur in several systems, such as chemical reactions [86], nanofluids in microfluidics [87], and the temperature distribution in miniaturized devices [88]. Generally, these phenomena are very difficult to observe and, hence, to measure.

Some studies have applied IRT information to the realization of quantitative analysis for parameter estimations. Rouizi et al. [89] applied inverse methods to IRT measurements to estimate the fluid bulk temperature distribution. Fudym et al. [90] developed an analytical two−temperature model for the convection-diffusion thermal modeling of a microfluidic chip. Additionally, the same technique developed by Pradere et al. [78] was applied to millifluidic isoperibolic reactors by Hany et al. [79] to estimate the enthalpy of single-phase reactive flows. Recently, Haber et al. [91] performed single-phase exothermic reactions inside microcapillaries at different flow rates using IRT; the investigators developed a quantitative on-line monitoring technique of the

axial temperature profiles within microreactors. Walsh et al. [7] demonstrated the feasibility of estimating the heat transfer properties of a gas−liquid flow.

Even if the measurement accuracy of the absolute temperature field is difficult due to poor knowledge of the radiative properties (spectral emissivity, transparency, etc.) of the investigated surface, the quantitative interpretation of such fields is possible by performing calibrations beforehand and developing heat transfer models.

Hence, thermography can play an important role in the thermal characterization of different microfluidic systems, which can further support related research and development work; additionally, thermography can aid in the control of system operation without modifying system performance. The wide application of IRT shows the possibility for its use in the monitoring of underflow systems with very good resolution. The applications reveal that the IRT method is a powerful tool for the quantitative characterization of such microsystems with respect to the following advantages.

Advantages:

- Non-intrusive and non-contact technique
- Fast, reliable and accurate output
- A large surface area can be scanned
- Presented in visual and digital form
- Requires very little skill for monitoring
- Quantitative analysis can be performed by applying thermal modeling

Disadvantages:

- Instrument cost is relatively high (although the price is expected to decrease)
- The high degree of knowledge and expertise required in thermal modeling and inverse processing

1.3 Conclusion

In this chapter, it was shown that two-phase millifluidic tubing-based systems are a suitable online tool for the study of underflow chemical reactions. The surface-to-volume ratio at millifluidic scales allow the enhancement of heat and mass transfer exchanges compared to batch reactors. Additionally, the small size of the device allows fast response times. The small quantities of products involved are relevant considerations with respect to the economy, environment, toxicity and security, especially for highly exothermic reactions.

Today, many tools exist for the online monitoring of chemical reaction evolution, in terms of concentration evolution, by using Raman or UV-visible spectroscopy. In contrast, online tools with the ability to monitor the temperature evolution of a reaction are uncommon and less developed.

Various thermal metrology techniques developed throughout the past 20 years were presented. Ultimately, most were intrusive and provided mono-sensor measurements of temperature. In the study of a biphasic flow, it is important to have excellent thermal measurement resolution, e.g., a two-phase flow may induce different thermal responses at two neighboring points due to the presence of two different media. For these reasons, it is important to choose a suitable technique for accurate temperature measurements. Additionally, when a chemical reaction is performed, the heat transfer must be accurately measured to precisely estimate the thermal parameters, as well as to deduce the heat flux dissipated by a heat source.

Thus, the quantitative interpretation of such measured temperature fields is only possible by performing calibration steps beforehand and developing heat transfer models.

The analysis of the existing thermal metrology techniques applied to miniaturized systems highlights two key points.

- Despite the promise of in situ temperature measurements techniques, such approaches are difficult to adapt to millifluidic tubing-based systems. Additionally, these intrusive techniques are not sufficiently compatible with online analysis tools.
- IR thermography is a non-intrusive and non-contact measurement technique. Each IR image provides a significant amount of thermal information. However, the calibration methodology and the thermal modeling approach for a two-phase flow in a millifluidic device has not yet been realized.

Based on the work already contributed to the literature, it appears that both the associated measurement techniques and thermal modeling approaches must be improved to better understand the online thermal analysis of chemical reactions in biphasic flows. The most important barrier to this type of quantitative analysis is our ability to propose a well-stated thermal modeling approach.

In this thesis work, we propose to characterize the chemical reactions inside droplet flows that occur in millifluidic reactors by applying IRT techniques. Thus, to achieve a quantitative interpretation of such temperature fields, a calibration protocol and heat transfer model will be developed.

Chapter 2

Development of the non-contact droplet flow calorimeter

Abstract

This chapter is devoted to a presentation of the experimental set-up of the non-contact droplet flow calorimeter developed for the characterization of chemical reactions. Each part of the complete device, from the reactor chamber to the regulation system, is presented in detail. The original device concept was based on a combination of infrared thermography with a droplet flow running in an isoperibolic millifluidic system. Thus, the resolution of the IRT technique allows local temperature measurements to be performed, while the isoperibolic boundary allows the heat transfer to be controlled (diffusion and convection). Additionally, the droplet flow ensures reaction intensification due to the surface-to-volume ratio, which promotes heat and mass transfer. The biphasic flow in such systems is generated and controlled by fluid injection at imposed flow rates. Furthermore, the combination of two imaging techniques (IRT and visible) is used to reinforce the understanding of the biphasic droplet flow. IR techniques allow for the measurement of temperature fields, while visible imaging characterizes the biphasic flow patterns. The developed experimental assembly reveals that highly exothermic reactions can be studied safely.

2.1 Introduction: Basis of the novel calorimetry design

The first miniaturized underflow isoperibolic calorimeter using infrared thermography was proposed and patented by Batsale et al. [92]. The feasibility of co-flow calorimetry was developed by Hany et al. [79]. The operating conditions are listed below.

- Criterion:
  - The temperature (T_s) of the surrounding is controlled and held constant.
  - The heat compensation principle is met by using a high power thermostat and fast control unit for T_s.
- Advantages:
  - With this configuration, the temperature of the surrounding remains constant, and the reaction temperature varied.
  - The diffusion heat losses around the channel are controlled.
  - Perfect knowledge of the heat transfer between the reaction chamber and the wall is assumed.

From this idea, the aim of this section is to describe the basis of the non-contact droplet flow calorimeter, which includes:

- Infrared thermography (IRT) and
- Droplet flow running under isoperibolic conditions.

This novel approach to calorimetry was developed in response to very precise specifications in the field of reactive and multiphase flow microfluidic devices. These specifications have been outlined as these fields have evolved. One of the most important specifications for the application of calorimetry to fluidics is the monitoring of data anywhere along the flow path (local measurement and estimation). Additionally, this technique must be flexible for adaptation to the constraints of industrial reactions/processes. Otherwise, such devices are not suitable for the study of industrial reactions. The final general specification concerns the type of chemical reactions to be performed in such a device.

2.1.1 Infrared thermography

The emission of a heat flux is based on heat transfer by thermal radiation. All bodies emit energy in the form of photons moving in a random direction, with random phase and frequency. When the radiated photons reach

another surface, they may either be absorbed (α), reflected (ρ) or transmitted (τ). The behavior of a surface impinged with incident radiation can be described and schematized as follow:

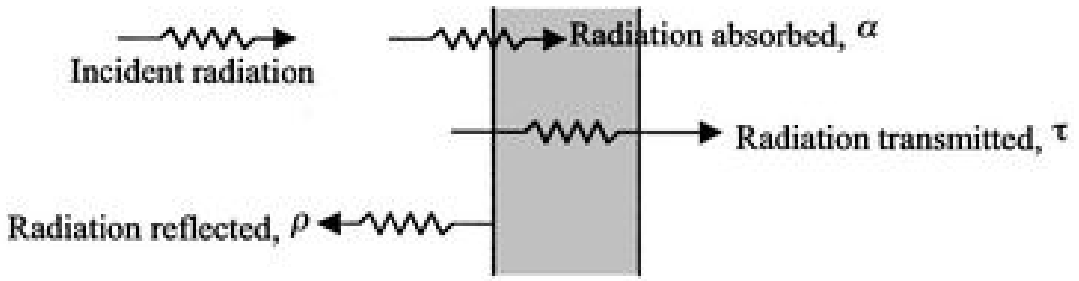

Figure 2.1: Radiation surface properties

More precisely:

- α=absorbance: the fraction of absorbed incident radiation,
- ρ= reflectance: the fraction of reflected incident radiation, and
- τ=transmittance: the fraction of transmitted incident radiation .

From energy considerations, the sum of these three coefficients is equal to unity $\alpha + \rho + \tau = 1$. Thus, reflective energy may be either diffuse or specular (mirror-like). Diffuse reflections are independent of the incident radiation angle. For specular reflections, the reflection angle is equal to the angle of incidence. However, the sketched processes in figure 2.1 are not always involved, particularly when speaking about the following bodies.

- Black body: no transmittance or reflectance, just absorbance. That is, $\tau = \rho = 0$ and α=1.
- Opaque body: none of the radiation that reaches the body is transmitted, although some may be reflected. That is, τ=0 and $\alpha + \rho$=1.
- Transparent body: transmission of all radiation that reaches the body. That is, τ=1 and $\alpha = \rho$=0.

The amount of radiation emitted by an object increases non-linearly with temperature; therefore, measuring the radiation variation allows access to the temperature. For a black body, the relationship approximation between the radiative heat flux and the temperature is defined as:

$$\Phi_r = \epsilon S \sigma_B (T^4 - T_a^4) \tag{2.1}$$

where Φ_r (W) is the radiative flux emitted by the observed body, σ_B is the Stefan Boltzmann constant ($5.6703x10^8$ $W.m^{-2}.K^{-4}$), ϵ is the emissivity, S (m^2) is the heat exchange surface of the body, T (K) is the temperature, and

T_a (K) is the room temperature. The radiative flux expressed in equation 2.1 is schematized in figure 2.2.

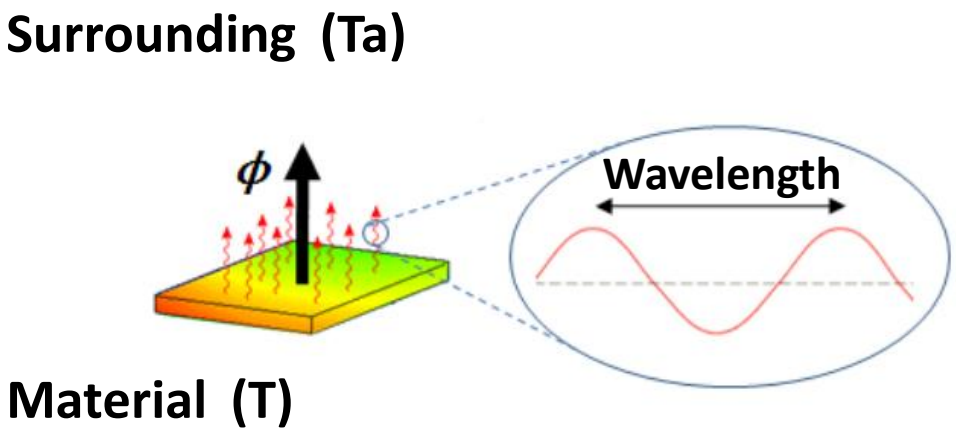

Figure 2.2: Schematic of radiative heat flux

To measure the absolute temperature of an object, perfect knowledge of the emissivity is necessary. Nevertheless, even if the measured temperature is only proportional to the absolute temperature, thermal processing can be applied and quantitative analysis can be performed. In practice, when measuring a heterogeneous material with different emissivities, it is easier to work with an emissivity ratio between the different materials/phases.

Infrared thermography (IRT) is a non-intrusive tool for the measurement of temperature fields. The principle of this imaging technique is based on the use of bolometric or quantic sensors that can detect the radiative heat flux emitted by a surface. That is, radiation is an electromagnetic wave classified in the infrared domain (from 1 to 1000 μm). Thus, infrared cameras are usually based on a focal plane array (FPA) that is sufficiently sensitive to measure radiation in the mid (3 to 14 μm)-wave infrared bands, denoted as MWIR.

2.1.2 Millifluidic isoperibolic chip: Droplet flow

The millifluidic isoperibolic chip is illustrated in figure 2.3. The chip is designed by using a bulk piece of brass for temperature and thermal control, while the flow set-up is realized using commercial TEFLON [1] small-size tubing and junctions. The bulk brass is thermally regulated by a Peltier module from -5 to 90 °C for accurate and controlled cooling and heating of the tubes, which are inserted into grooves engraved in the bulk brass. Because the TEFLON tube is a good thermal insulator (λ_T =0.25 $W.m^{-1}.K^{-1}$), and the bulk brass is a good thermal conductor (λ_P= 380 $W.m^{-1}.K^{-1}$), the boundary condition for the external diameter of the tubing is

[1] In terms of materials, it should be noted that polyyetragluoroethylene, perfluoroalkoxy and fluorinated ethylene propylene materials are also known as PTFE, PFA and FEP, respectively, and are otherwise simply called TEFLON materials

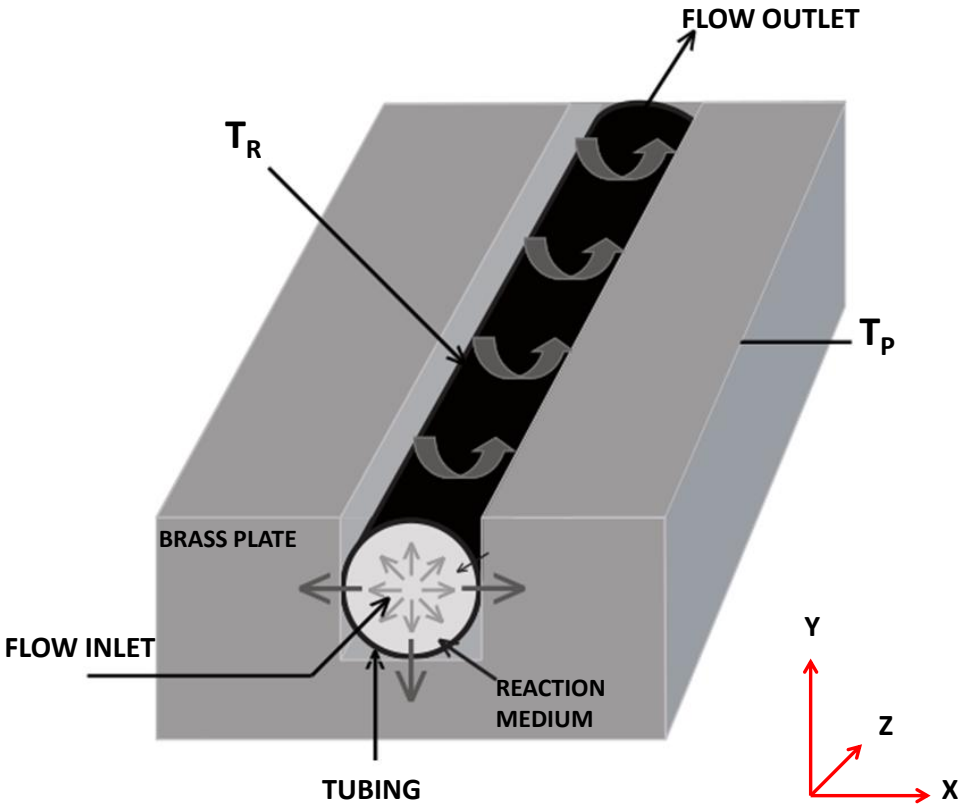

Figure 2.3: Schematic of the isoperibolic system

isoperibolic. Consequently, the temperature inside the chemical reactor (tubing or reaction media) results from the heat transfer coefficient between the imposed temperature of the bulk brass and the inner diameter of the tube.

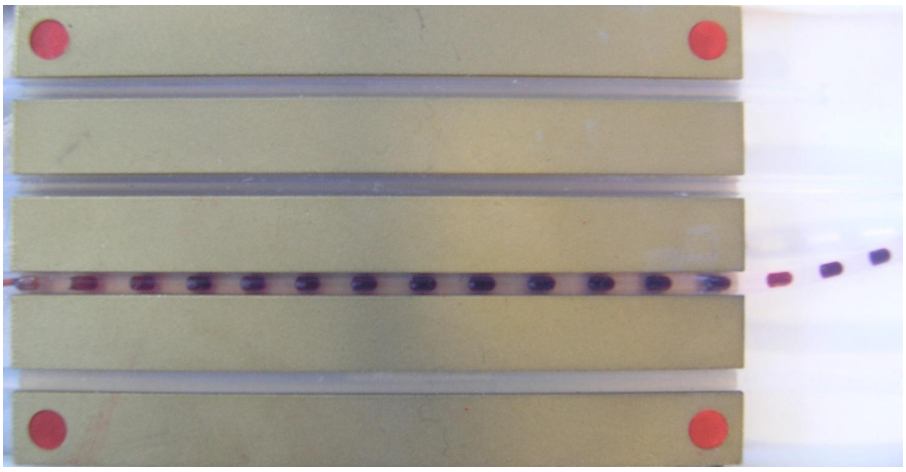

Figure 2.4: The millifluidic droplet-based system is composed of a brass chip and TEFLON tubing.

Figure 2.4 illustrates the reactor (tubing), in which the biphasic flow is performed by a high precision syringe pump, thus droplets are generated by the injection of different ratios of oil, which acts as the continuous phase, and an aqueous phase. This allows control of the hydrodynamic parameters, such as the total flow rate (i.e.,

droplet velocity), the droplet size and the volume fraction of oil and droplets. At the inlet of the tube, droplet generation is carried out by using smaller tubes to deliver the reactants. The main TEFLON tubing has an outer diameter of 3.17 mm and an inner diameter of 1.6 mm. The tubes used to supply the reagents have an outer diameter of 500 μm and an inner diameter of 250 μm. This design allows the initial and boundary conditions to be controlled.

In figure 2.5, which depicts a cross-sectional representation of the isoperibolic system, it should be noted that 3/4 of the tube is in contact with the brass plate, which induces the conduction heat losses.

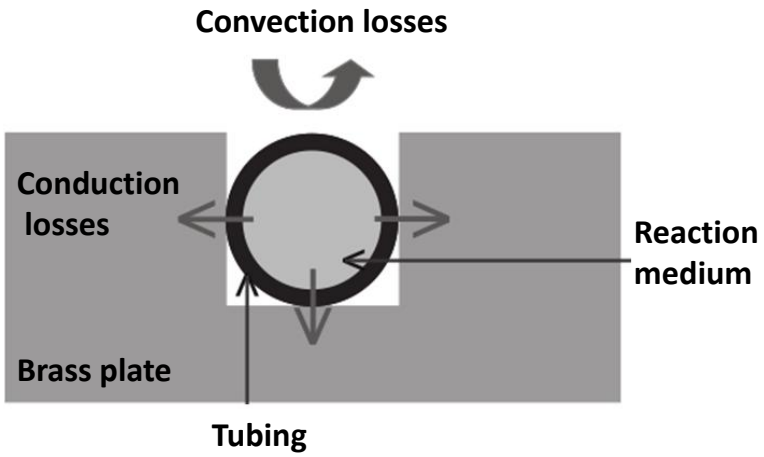

Figure 2.5: Cross-sectional representation of the isoperibolic system

The 1/4 (α) of the tube that is in contact with the ambient may have a heat exchange coefficient of approximately 10 $W.m^{-2}.K^{-1}$, which indicates that the thermal losses from this small section, if we consider e = 1mm and λ =0.1 $W.m^{-1}.K^{-1}$, are described by:

According to the representation 2.5, if we attempt to realize an energy balance in steady state by applying a heat source (ϕ, W) inside the tubing, the following expression is written:

$$\phi = hS\,(T_{tube} - T_a) + h_pS\,(T_{tube} - T_p) \tag{2.2}$$

Here, h ($W.m^{-2}.K^{-1}$) is the coefficient of heat loss due to convection with the surroundings through 1/4 of the tubing perimeter, whereas h_p ($W.m^{-2}.K^{-1}$) is the thermal resistance due to heat transfer by conduction through the thickness of the tubing (i.e., isoperibolic condition) within the 3/4 of the perimeter of the tubing, and S (m^2) is the heat exchange surface. Based on these configurations, the equation 2.2 can be rewritten as follows:

$$\phi = h\frac{1}{4}\pi dL(T_{tube} - T_a) + \frac{\lambda_{tube}}{e_{tube}}\frac{3}{4}\pi dL(T_{tube} - T_p) \tag{2.3}$$

where T_a (K) is the temperature of the surrounding, T_p (K) is the temperature of the brass chip, and d (m) the diameter. The calculation of the ratio R between the heat losses as a result of conduction and convection is performed as follows:

$$R = \frac{(1-\alpha)\pi dLh}{\alpha\pi dL\frac{\lambda}{e}} \quad with\alpha = 0.25 \quad R = \frac{1}{3}\frac{he}{\lambda} = \frac{1}{3}10^{-3} \tag{2.4}$$

The estimated value R= 3.3310^{-3} is smaller than unity, which allows us to neglect the convective heat losses compared to the conduction losses (i.e., the isoperibolic condition). For this reason, in further development, the system is considered completely isoperibolic (i.e., R is 1) and not otherwise (i.e., 1-α).

2.2 Design of the calorimeter

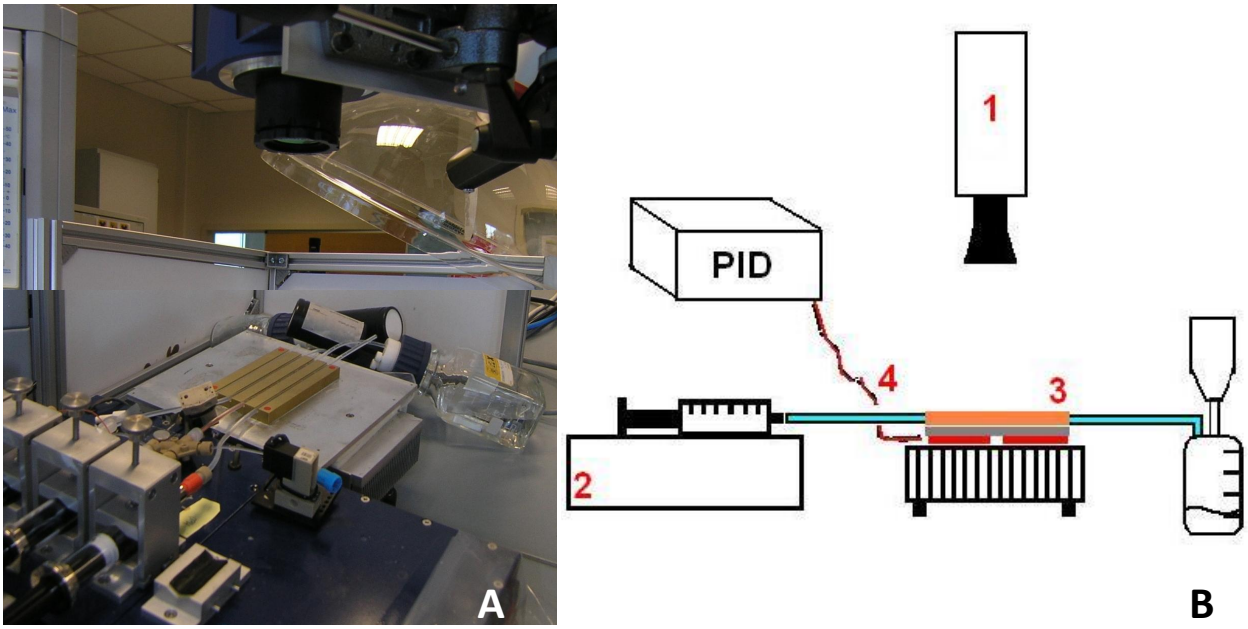

Figure 2.6: A. Picture of the experimental set-up. B. Outline of the experimental set-up, in which the 1) infrared or visible camera, 2) syringe pump, 3) isoperibolic set-up and 4) thermal regulation system are all displayed.

2.2.1 Infrared Camera

An infrared CEDIP camera (model JADE MWIR J550) is used for the temperature field measurements (highlighted by number 1 in figure 2.6.B). This camera has both linear and array In Sb detectors (FPA, Focal Plane

Array) and is built from 76,800 individual detectors (240 x 320 pixels), with an optimum wavelength ranging from 2.5 to 5.2 μm and a pitch of 30 μm. The IR objective lens is a MWIR with F/2 of 25 mm. With this objective, the spatial resolution of the temperature measured by each pixel of the sensor is approximately 250 μm. The scanning frequency can reach 1 kHz. The development of fast array detectors has enabled the construction of cameras capable of recording fast thermal processes, which justifies the need for a detector based on quantum well properties, such as the In Sb detector. To ensure optimum operating conditions, such detectors require the use of a cooling system to bring the temperature to -203°C (77 K), which is even lower than typical cooled detectors, which require a temperature of -196 °C (77 K) to operate. A Stirling engine is used to cool the quantum well detectors, which are currently the most sensitive infrared detectors, with a temperature resolution of 40 mK. For this reason, such detectors are mainly used in scientific research. Another characteristic feature of these detectors is the relatively high homogeneity of individual elements (pixels) in the array. Information on the basic features of photon detectors has been reported in the literature [93, 94].

2.2.2 Visible camera

The AVT Manta GigE Series with a monochrome CCD (Charge Coupled Device) sensor from Sony ICX445 was used for our experiments. The resolution of the CCD is 1296 x 964, the sensor measures 1/3" in size, and the pixel size is 3.75 μm. A visible objective of 16 mm from PENTAX (1/3 sensor size) is used, allowing for a spatial resolution of 4 μm. The acquisition rate of this camera is fixed to 30 fps (frames per second). This camera is controlled by home-made LabVIEW software, which gives us the possibility to perform subsampling acquisition to obtain fewer images if necessary. This software also allows us to obtain the timebase of the acquired images. Usually, the camera is located at block 1 in figure 2.6.B (this place is shared with the IR camera).

2.2.3 Syringe pump

This delivery system, i.e., the syringe pump, is characteristic of micro- and millifluidic applications. The syringe pump is used to generate controlled flows. In reactive chemical flows, such systems are used to master the incorporation and the delivery of a fixed flow rate of fluid into a channel solution. Using this injection system, laminar and pulsed streams can be generated in the range of milliliters or nanoliters per second. The syringe pumps are the neMESYS model from Cetoni and are suitable for the high-precision delivery of microvolumes. This device is very important for ensuring flow stability. On the one hand, it is important to control droplet generation; and on the other hand, it is also important to generate droplets with precise control of size and shape. When the flow of the fluids is controlled over the length of the chip, the spatial distribution can be

easily converted to a temporal distribution. In this case, when the droplets are in contact with the wall of the flowing section, it is possible to assume that the droplets are moving at the average velocity of the flow; thus, $t = d/\bar{U}$, where t (s) is the time in the observed point, d (mm) is the distance traveled and $\bar{U}$ $(m.s^{-1})$ is the droplet velocity (the placement of the syringe pump is highlighted by number 2 on figure 2.6.B)

2.2.4 Isoperibolic set-up

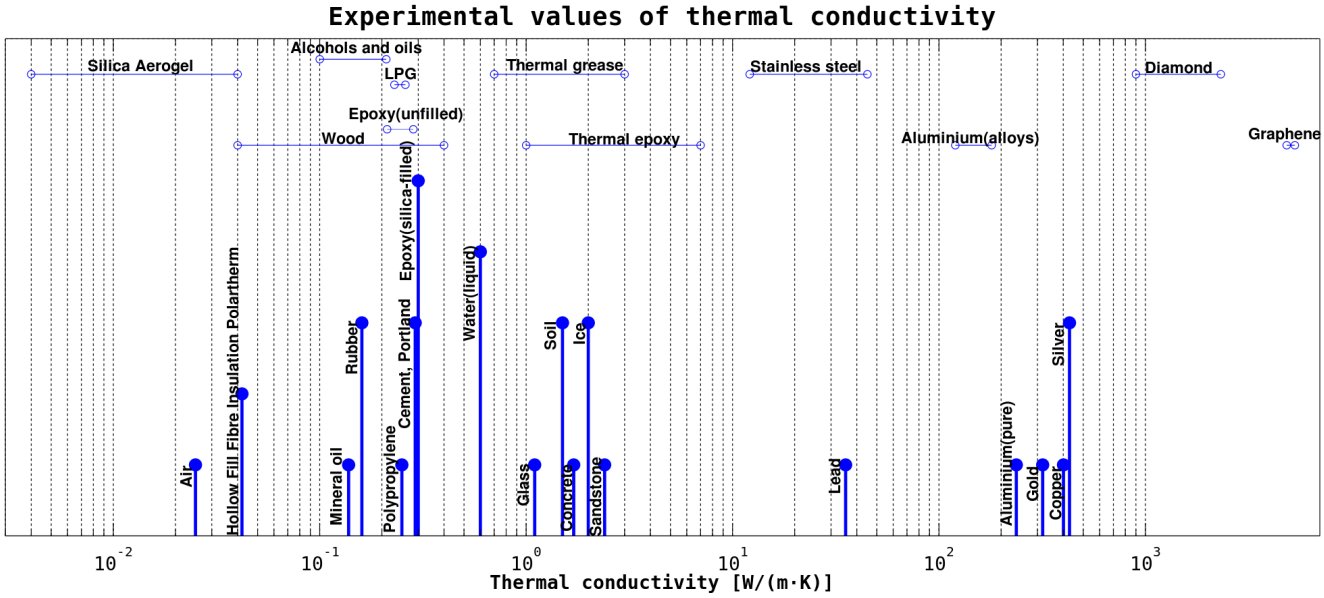

Figure 2.7: Experimental values of thermal conductivities [95]

As illustrated in figures 2.6.A and B, the original isoperibolic set-up is constructed of (i), a conductive bulk metallic piece (chip) and (ii) insulating tubing, in which the chemical reaction takes place. To ensure isoperibolic boundary conditions, it is crucial to identify a material with high thermal conductivity. As shown in figure 2.7 [95], the best commercial materials for this purpose are aluminum, gold, copper, silver and diamond. For cost reasons, gold, silver and diamond are excluded. Despite the poor thermal conductivity of aluminum, with a value of $\lambda = 220\ W.m^{-1}.K^{-1}$, the thermal capacity of aluminum is also insufficient; further, this material has a shiny mirror-like surface, which causes significant reflection problems. Some surface treatment can be carried out to reduce reflections, such as 1) polishing the surface, 2) painting the surface black, or 3) oxidizing the surface (anodizing). Nevertheless, with a thermal conductivity of $\lambda = 400\ W.m^{-1}.K^{-1}$, copper is the preferred choice. Brass has almost the same thermal conductivity, depending on the percentage of zinc. It is important to note that aluminum weighs less (ρ= 2,700 $kg.m^{-3}$) than brass (ρ= 8,600 $kg.m^{-3}$), although the heat capacity of aluminum is 900 $J.Kg^{-1}.K^{-1}$, and that of brass is 380 $J.Kg^{-1}.K^{-1}$. As a result, the thermal behavior responses of both materials will differ in terms of stability. Because the value for brass (i.e., ρC_p (3,26x10^6 $J.m^{-3}.K^{-1}$)) is higher than that of aluminum (ρC_p (2,43x10^6 $J.m^{-3}.K^{-1}$)), this will ensure that the bulk brass material will be less disturbed by surrounding temperature variations.

2.2.5 Spectral analysis of the tubing

Regarding the selection of tubing, it is important to satisfy three conditions:

1. The polymer chemical compatibility
2. The wettability
3. The transparency of the polymer materials in the wavelength range of the IR camera (2.5 - 5 μm)

The first can be easily established by using the supplier references tables, where the compatibility degree and the substances with which to avoid are reported. The second condition plays an important role during droplet generation. When the tubes are made of fluoro polymers, such as PTFE or PFA, their surfaces are usually hydrophobic. Consequently, a fluorinated oil will totally wet the wall. Concerning the third condition, it is important to know the degree of transparency of the tubes at the IR wavelength. Several tubes satisfying the chemical and wettability parameters selected for infrared spectroscopy characterization at the platform SIV [2] of the ISM [3]. Figure 2.8.A shows the transmittance spectra from 2 to 15 μm wavelength of three different materials, FEP (fluorinated ethylene propylene), PFA (perfluoroalkoxy) and TEFZEL (is a modified ETFE, ethylene tetratluoroethylene). In figure 2.8.B, only the results in the IR range of the camera are plotted.

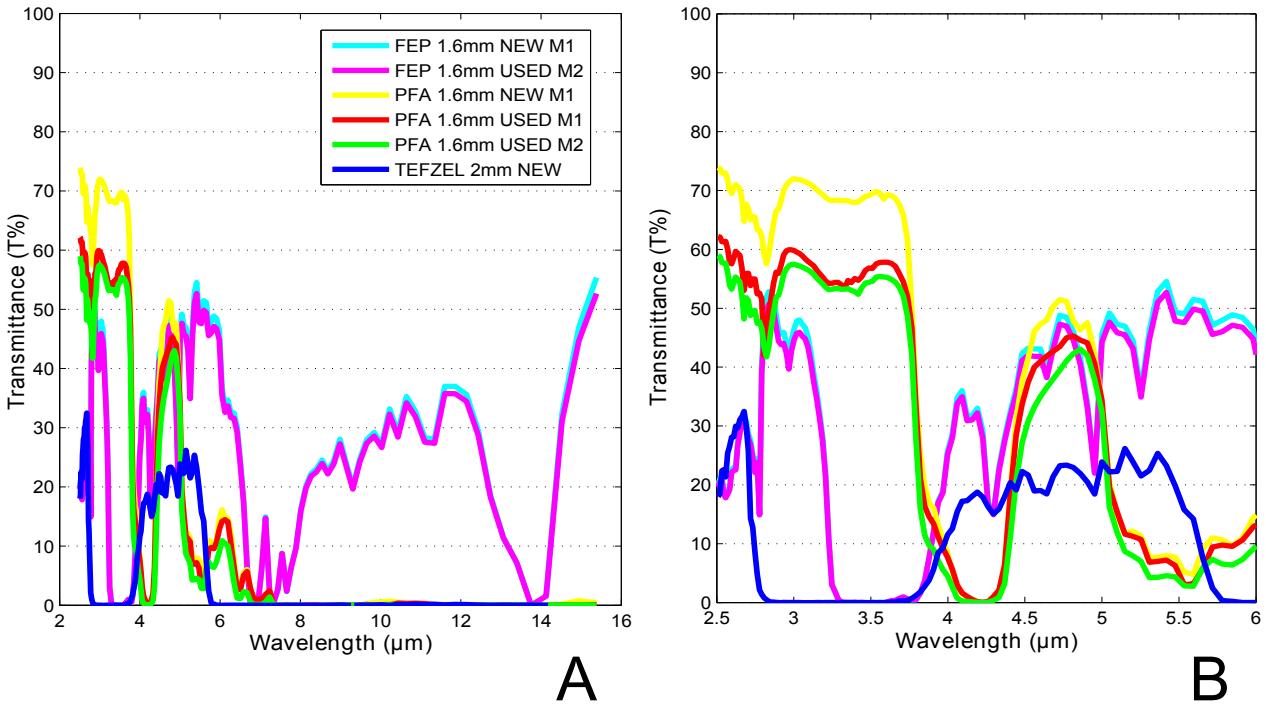

Figure 2.8: A. Infrared spectra of the selected tubes. B. A magnified presentation in the wavelength range of the infrared camera.

[2] SIV (Spectroscopie et Imagerie Vibrationnelle)
[3] ISM (Institut de Science Moleculaire, Bordeaux)

Another important point is the swelling behavior of the tubing when the fluorinated oil is injected. These parameters directly affect the degree of transmittance of the materials, as shown in figure 2.8.B. In this figure, the differences between the spectrum of new PFA tubing and used tubing are reported. The label *PFA used M1* means that the protocol of the measurement corresponds to 4 hours of oil flowing at several flow rates, ranging from 10 $mL.h^{-1}$ to 40 $mL.h^{-1}$. For the label of *PFA used M2*, the protocol represents more than 20 series of experiments, corresponding to 80 hours of various oil flow rates, ranging from 10 $mL.h^{-1}$ to 40 $mL.h^{-1}$. As shown in the spectra, no significant difference between *PFA used M1* and *PFA used M2* arises; it is worth noting that although *PFA used M1* is most likely saturated by oil, the transmittance remains unchanged. Regarding the other polymer FEP analyzed, we noticed that the transmittance spectra are quite similar, without significant changes between the new and used tube samples.

To summarize this spectral analysis, it is important to note that three materials can be used, including TEFZEL, FEP and PFA. Even if TEFZEL is more opaque to infrared, all of the tubing types are semi-transparent bodies. Nevertheless, PFA and FEP are significantly more compatible with our solvents. Moreover, the maximum recommended operating temperature for tubing is 100 °C.

Finally, to avoid transmittance variation during the experiments, two cycles of oil will be administered before any chemical reaction measurements are performed, to achieve the saturation level of the tubing.

2.2.6 Emissivity behavior of the biphasic media

To study the emissivity of the biphasic media, a simple experimental study was performed. In figure 2.9, the principle of the experiment is sketched. PFA tubing was filled with equal parts oil and water (colored blue); additionally, a second tube filled with air was placed in the next groove, as depicted in the visible image in figure 2.9.A. The initial temperature of the brass chip at $t = 0$ s was equal to the room temperature T_p=25°C. Then, the brass chip temperature was raised to T_p=35°C. In this transient study, three stationary phases were analyzed; by applying image analysis, their temperature profiles as functions of time were extracted to evidence the emissivity behavior when a thermal constraint is applied.

Figure 2.10 shows these profiles as functions of time. The observed temperatures are expressed in digital levels (DL). In this figure, it is important to note that due to the spatial thermal gradient, the intensities of the brass chip, the air tube and the biphasic media at $t = 0$ s are not the same, even when their initial temperatures are the same (see also figure 2.9.B). Then, when the temperature is varied to T_p=35°C at $t \geq 3$s, the dynamic response of each of medium is different because each has different thermophysical properties, as shown in figure 2.9.C. Finally, when the steady state is reached at $t = 60$s, the three phases are at the same temperature, i.e., the brass temperature T_p (see also figure2.9.C). At this time, the biphasic media reach the same temperature, so they also

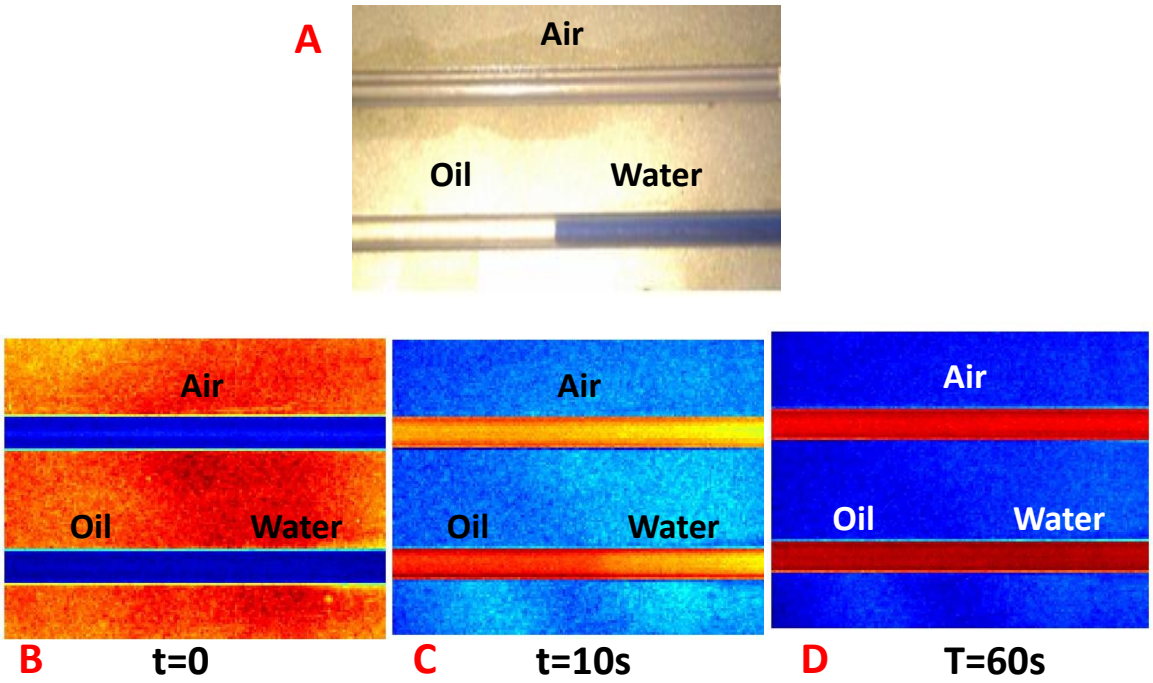

Figure 2.9: A. Visible image of the experiment in which one PFA tube was filled with equal parts oil and water (colored blue), and the second tube, with air. B. IR image of experiment at t = 0s C. B. IR image of the experiment at t = 10s D. IR image of the experiment at t = 60s

have the same emissivity (see figure2.10.B). In contrast, it can observed that for the same temperature, the tube containing air appears to be cooler than the tube containing biphasic media. Thus, it can be concluded that the water and oil mixture is more opaque than air, with an emissivity close to $\epsilon = 1$.

It is important to note that for further experiments, because the tubing is semi-transparent and the emissivity values of water and oil are the same, the measured temperature will integrate a portion of the tubing volume, although the thermal response will be representative of the thermal behavior of the biphasic media, which can be compared with an opaque body.

2.2.7 Thermal regulation system

The isoperibolic chip is thermally regulated with a PID system based on Peltier modules, which can achieve temperatures from -5 °C to 90 °C. This approach can achieve accurate and controlled cooling and heating of the tubes, which are inserted into grooves within the bulk brass. The placement is highlighted by number 4 in figure 2.6. According to the temperature operating condition, the power to be dissipated by the system will be calculated for a sandwich system of a brass chip and an aluminum plate. Using this double-layer composition, the aluminum plate acts as a dynamic distributor, which means that regarding the thermal properties, this material will deliver the heat dissipated by the Peltier modules more rapidly and homogeneously than the brass. The calculation of the dissipated power is reported in appendix A. Here, four Peltier modules are needed to

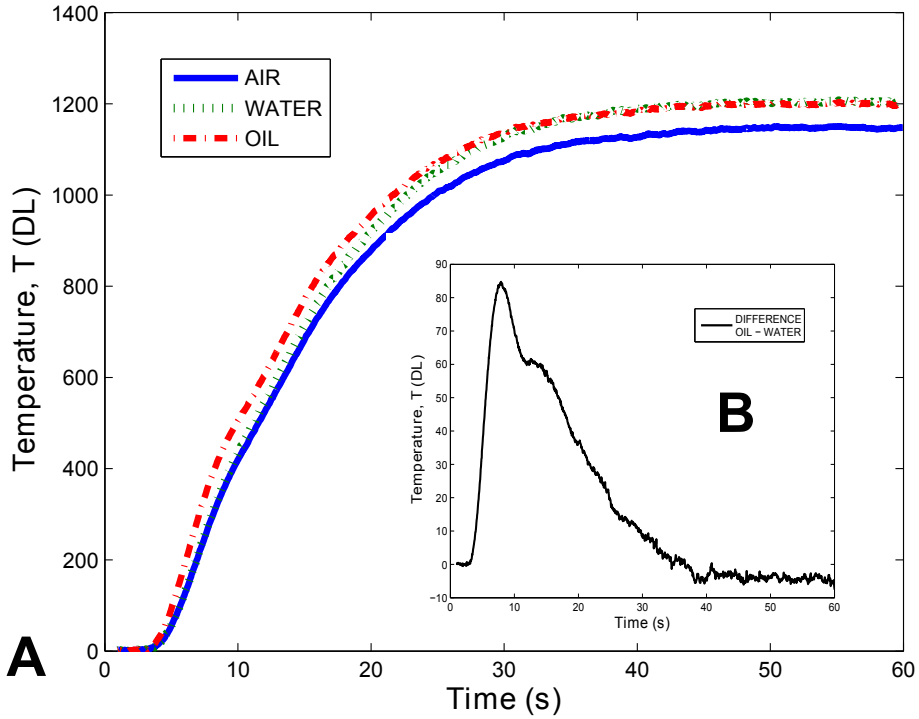

Figure 2.10: A. Temperature profiles of the three stationary media when a thermal constraint is applied from T_p=25 to 35°C. B. Temperature difference between the oil and the water phases

control the imposed temperature.

***PID controller**

To hold the temperature of the chip constant, a regulatory system is necessary. For that, basic controllers, called proportional (P), integral (I), and derivative (D) controllers, or a combination of PID controller can be used. In practice, PI and PID controllers are the most commonly used industrial and commercial control systems. In our case, a PID regulatory system (model 5R6-900) from Oven Industries Inc. is used. This device is composed of Peltier modules, which regulate the temperature of the isoperibolic chip. These modules are placed under an aluminum plate measuring 3 mm in thickness; a Pt100 sensor probe linked to the PID controller is placed on top of the aluminum plate and is used to measure the temperature variation. The temperature set points can range from -10 °C to 100 °C. This range depends on the Peltier capacities and the module arrangement, which may include stacking (i.e., a stacking arrangement is also called a cascade or multi-stage module configuration). With this configuration, a control accuracy of 0.1 °C is obtained.

*** Heat sink**

In electronic systems, a heat sink is a passive heat exchanger component that cools a device by dissipating heat into the surrounding air. Heat sinks are used with high-power semiconductor devices to maintain the semiconductor junction temperature. A heat sink is designed to increase the surface area in contact with the

air cooling medium surrounding the heat generator. The air velocity, nature of the material, geometrical design and surface treatment are some of the factors involved in the thermal performance of a heat sink. In our experimental device, the isoperibolic chip is supported by a heat sink, which was chosen according to the parameters of:

- Lowest pressure losses
- Lowest thermal resistance
- Highest heat exchange surface

According to these specifications, a hollow-fin cooling set-up with a fixed axial fan from Fisher Electronik was chosen to enable an efficient cooling system and high heat dissipation by forced convection. The heat sink is illustrated in figure 2.11, where the heat exchange surface measures 150 x 120 mm. A 24-V DC power supply was selected to enable lower thermal resistance for the same surface R_{th}=0.09$K.W^{-1}$ and for a milled flat semiconductor mounting surface.

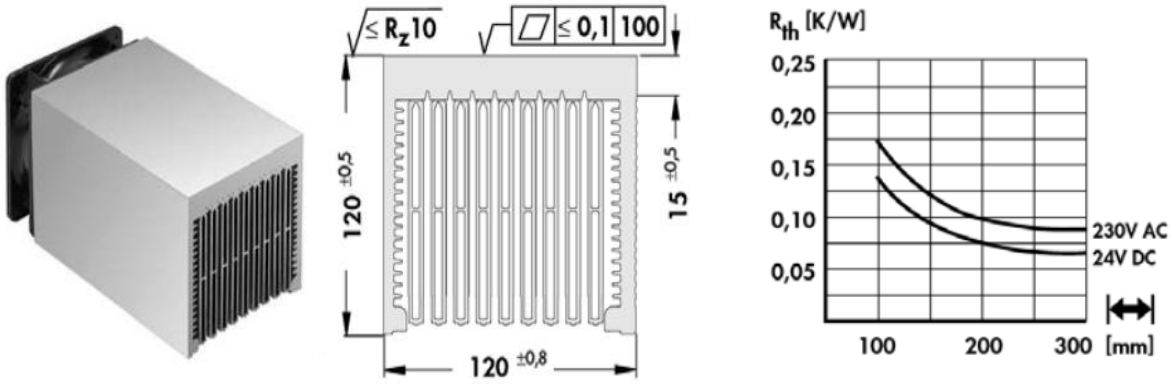

Figure 2.11: The geometry of the heat sink enables optimized airflow for heat dissipation

Figure 2.12 presents a sketch of the layers of the thermal regulation system. A framework for centering the Peltier elements is proposed (illustrated in figure 2.12.A). Then, an aluminum plate is placed on the device structure, figure 2.12.B. This dynamic distributor has a sensor groove to enable the insertion of the thermal sensor, which will further ensure the best sensing behavior of temperature regulation. The isoperibolic brass chip is then placed above the aluminum plate, as shown in figure 2.12.C. It is important to note that the last layer represented in figure 2.12.D is placed to limit convective exchange. This terminal layer is a cover made of TEFLON (FEP, 25 μm thickness), which is transparent to the IR range of the infrared camera, allowing observations of the thermal scene.

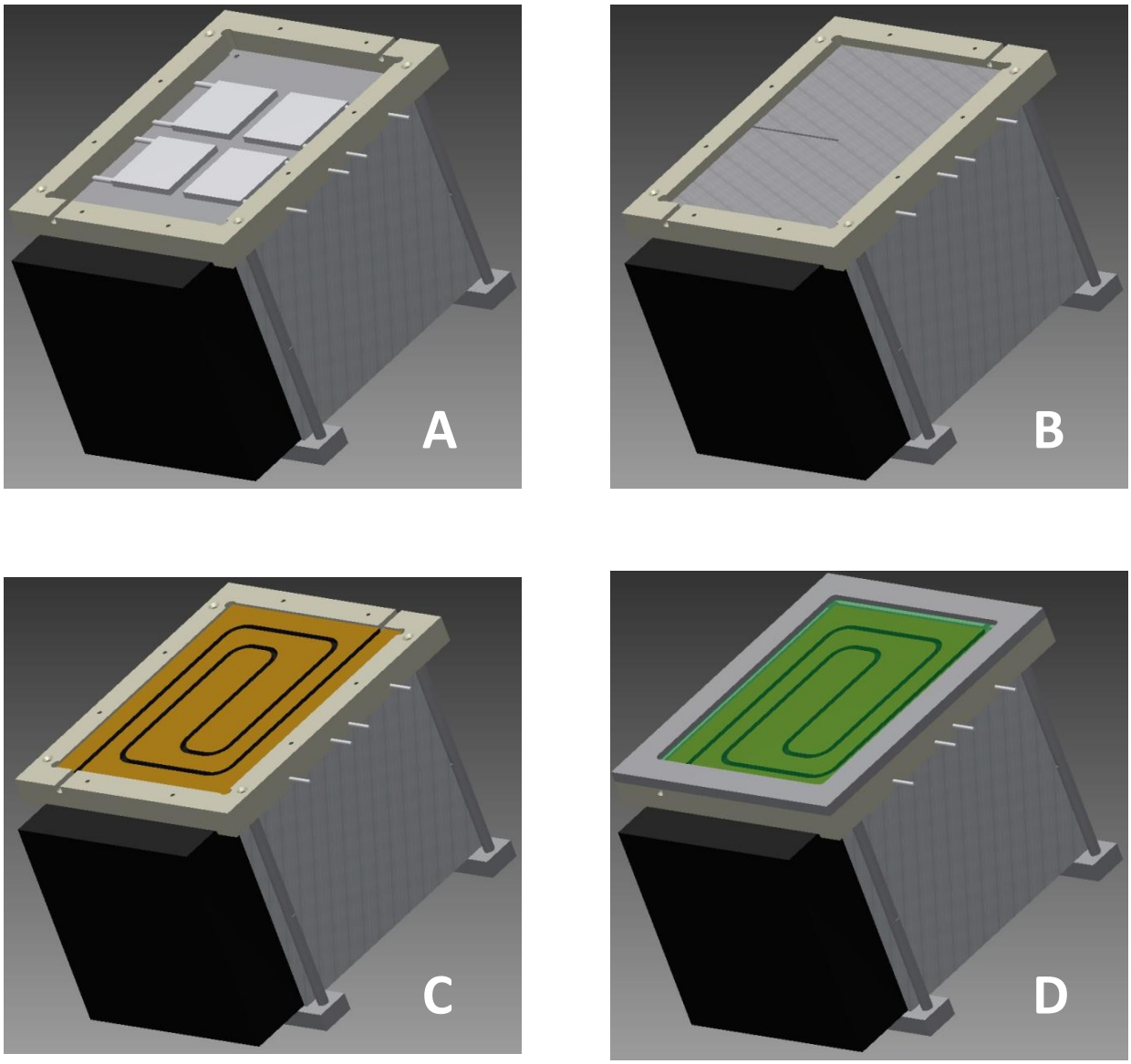

Figure 2.12: A. The layer of Peltier devices. B. Aluminum layer with the sensor groove. C. Brass millifluidic chip. D. Chip cover

*** Peltier elements**

The Peltier effect is the introduction of heating or cooling at an electrified junction of two different conductors. When current is passed through a junction between two semiconductors, A and B, heat may be generated (or removed) at the junction. The Peltier heat generated at the junction per unit time $\dot{Q}$ is equal to:

$$\dot{Q} = (\Pi_A - \Pi_B)\, I \tag{2.5}$$

where Π_A and Π_B are the Peltier coefficients of conductors A and B, respectively, and I is the electric current from A to B. Note that the total heat generated at the junction is not determined by the Peltier effect alone because it may also be influenced by Joule heating and thermal gradient effects. The Peltier coefficients represent

how much heat is carried per unit charge. Because the charge current must be continuous across a junction, the associated heat flow will develop a discontinuity if Π_A and Π_B are different. The Peltier effect can be considered as the back-action counterpart to the Seebeck effect: if a simple thermoelectric circuit is closed, then the Seebeck effect will drive a current, which in turn (via the Peltier effect) will always transfer heat from the hot to the cold junction. A typical Peltier heat pump device involves multiple junctions placed in series, through which a current is driven. Some of the junctions lose heat due to the Peltier effect, while others gain heat. Thermoelectric heat pumps exploit this phenomenon, as do the thermoelectric cooling devices found in refrigerators. These devices are illustrated in figure 2.12.A.

*** Sensor**

The miniaturized probes used for thermal regulation in this work are flexible sensors that are easily mounted on adjacent surfaces. In our set-up, this sensor is inserted into a small groove, engraved inside the aluminum plate. The sensor is made of polyimide and PTFE wires. The dimensions of this sensor are 3 x 1.5 mm. The temperature ranges from -50 to 200 °C. The temperature evolution is followed by using this type of sensor probe (type: Pt-100) and is the analyzed as a function of time. The process dynamics and the control of the set-point temperature are achieved by the feedback between this sensor and PID regulation, which send the command to the Peltier modules, as illustrated in figure 2.12.B.

*** Hood cover**

A cover was fitted to the regulatory system to carry out the experimental work in a hood. Fume hoods serve as local ventilation devices and are designed to limit exposure to hazardous or toxic fumes, vapors or dusts. Hence, it is common to establish an experimental set inside a fume hood.

Other secondary functions of this device may include explosion protection, spill containment, and other functions necessary to the work being carried out within the fume hood. Typically, the hood protects only the user; hence, fume hoods are most commonly used in laboratory environments where hazardous or noxious chemicals are released during testing, research or development.

In our case, it is important to adapt our system to the hood conditions. Consequently, and from a thermal point of view, the air flow within the hood could be a significant drawback with respect to establishing temperature stability because the flow could lead to forced convection at the surface of the reactor. The thermal regulation chamber in which the experimental device is placed is proposed with different layers and insulating boundary conditions to limit convective heat exchanges due to the hood airflow. Additionally, although the aim of the cover is to limit convective exchanges, nonetheless it is important to note that this final layer in figure 2.12.D must be transparent within the range of absorbance of the infrared camera. A sapphire window measuring 4

mm in thickness can be used, although this approach is very expensive relative to the use of a TEFLON (FEP) film measuring 25 μm in thickness. The latter is an affordable option and can be easily adapted to the size and shape of the system.

*** Double chamber**

The double chamber is illustrated in figure 2.13 and 2.14 is used to thermalize the products at the desired temperature. The main idea of the double chamber is to heat the chemical reagents and the oil to the desire operating temperature before the reagents encounter each other. During the residence time in the preheating chamber, all streams are carried in different tubes to avoid any contact among them. Once all streams have reached the imposed temperature, the streams will meet at the entry of the second chamber (i.e., droplet generation), called the reaction chamber. Inside this chamber, the imposed temperature is the same as that inside the preheating chamber to ensure that the only contribution of dissipated heat arises from the chemical reaction inside the droplets.

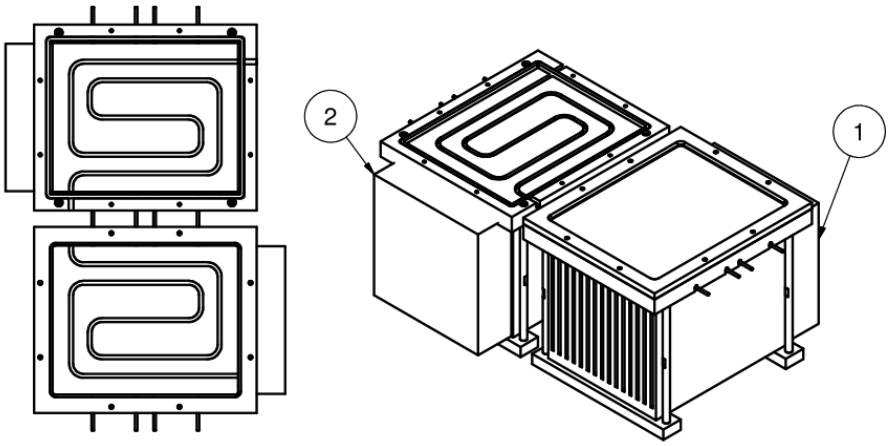

Figure 2.13: Sketch of the double chamber

2.2.8 Chip conception

The chip conception is influenced by the same parameters as the classic reactor design. These parameters are:

- Volume (V),
- Residence time (t),
- Temperature (T),
- Pressure (P),

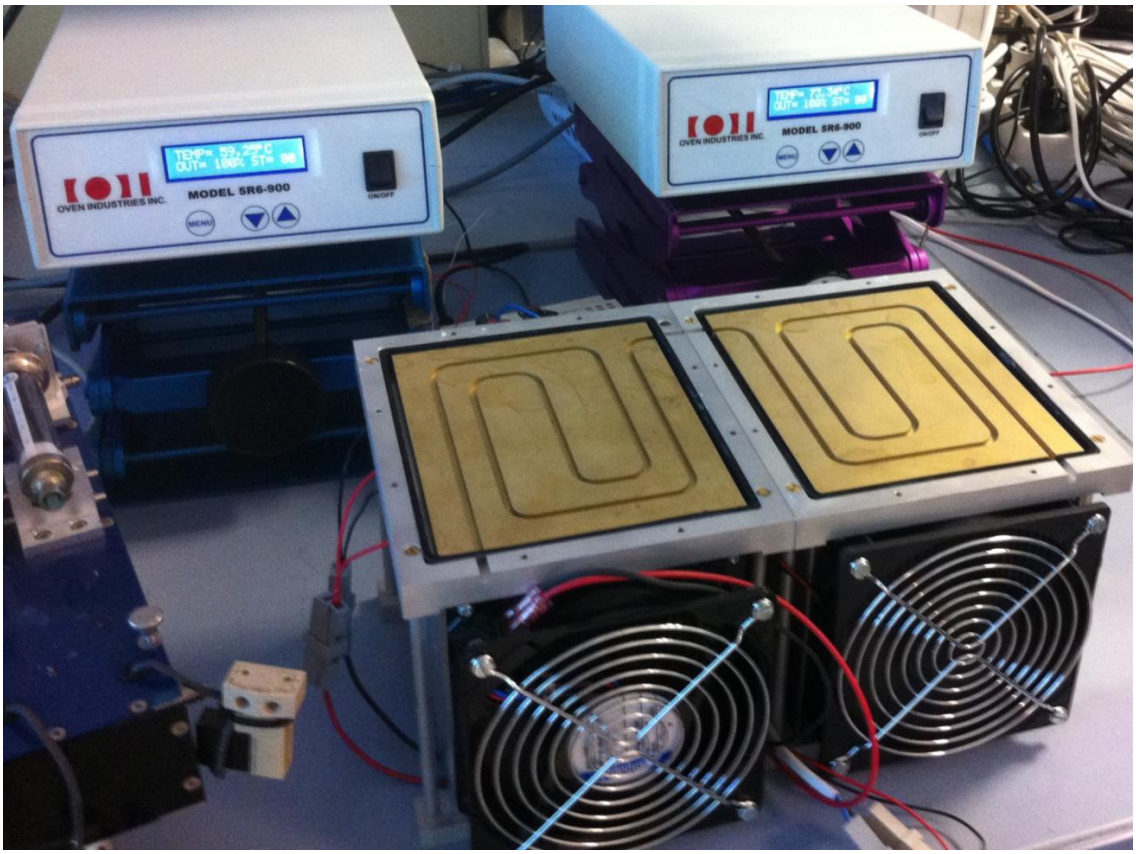

Figure 2.14: Experimental set-up of the double chamber

- Concentrations of chemical species ($C_1, C_2, C_3, ...C_n$), and
- Heat transfer coefficients (h, H)

The volume (V) is fixed by the tubing diameter and length. The residence time (t) is controlled by the imposed flow rate for a given reactor volume. The temperature (T) is overseen by the thermal regulation system previously described. The pressure (P) is approximately 1.5 -2 bars in this work, and at the proposed operating conditions, no significant pressure drop is observed. The concentrations (C_n) of the chemical species are controlled by the preparation of the solutions from standard solutions (most from Sigma Aldrich). The heat transfer coefficient (H) was determined by a calibration protocol that will be described later in detail. Further, in this work, all of the chemical reactions that will be performed in the reactor are either exothermic or endothermic. Hence, our chemical reactor is equipped with an isoperibolic boundary to control the temperature elevation in the reactor due to the heat released during the reactions. Additionally, other parameters must be taken in account to improve the reactor design to obtain suitable experimental conditions for the reactive flow, as well as for the observation window. That is, the evolution of the reaction is monitored by infrared and visible cameras, so the shape and the dimensions of the chip must be optimized to improve the number of pixels inside the channel. Because the shape of the reactor is fixed by the selected tubing, the volume of the reactor (tubing) is a function of the tube length. The conception of the millifluidic brass chip is drawn with various layouts (see

figure 2.15.A). These prototypes were machined in the CRPP's[4] workshop (see figure 2.15.B.).

Each pixel of the IR camera represents a temperature measurement point. For this reason, it is important to have good spatial resolution, i.e., a significant number of pixels inside the reactor, to obtain sufficient sensitivity. Hence, as the number of pixels along the channel is increased, better spatial resolution will be obtained. The chip is designed to be a function of the optimized parameters, listed as follows.

- Because the IR matrix is rectangular, it is better to design a rectangular chip that will benefit from the larger surface.
- Based on the principles of optics, the working distance between the objective and the camera will determine the pixel size.
- The radius of curvature (bends) of the proposed path must be designed with a length that is 6 times the external diameter. A large bend angle is necessary to avoid any modification of the droplet flow (i.e., constriction of the flow section).
- The maximum amount of linear zones should be chosen to improve image analysis, which is based on straight line detection.

2.3 Examples of application to highly exothermic reactions

- Nitroglycerin is a powerful explosive, giving rise to four different gases when detonated.
  - If $1L$ of nitroglycerin is detonated, the dissipated energy will be on the order of 1 MJ.
  - If a $2\mu L$ droplet of nitroglycerin is detonated, the dissipated energy will be on the order of 20 J.

  The temperature elevation is $\lll 3°C$

[4] Centre de Recherche Paul Pascal, Bordeaux

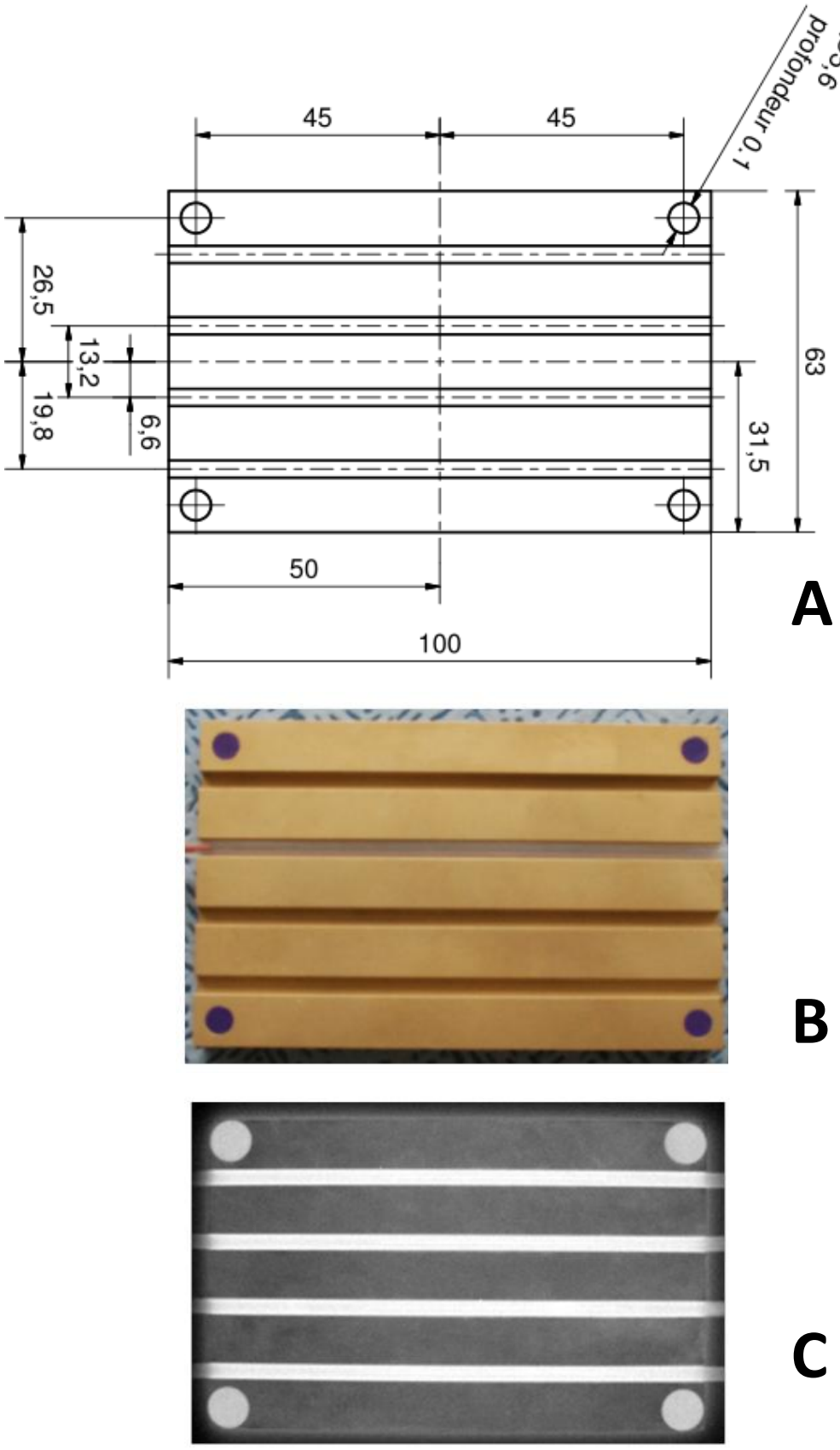

Figure 2.15: A) Computer-drawn layout of the millifluidic chip, showing the design of four straight channels. B) Features of the millifluidic isoperibolic chip, where this piece was machined from bulk brass. C) Infrared image of the millifluidic isoperibolic chip

2.4 Conclusion

A fully non-contact calorimeter was designed. Because two bulk brass chips were incorporated into the design, it was possible to obtain reactor lengths of 10 and 75 cm within the temperature range from -5 to 90 °C. The experimental set-up of the non-contact droplet flow calorimeter was reported. The use of the infrared thermography combined with isoperibolic millifluidic technology is an important asset for this device because it allows for the continuous monitoring of biphasic flows. Additionally, the combination of two imaging techniques (IRT and visible) was used to reinforce the understanding of the biphasic droplet flow. IR techniques will allow for the measurement of temperature fields, while visible imaging will be used to characterize the biphasic flow patterns. This reactive biphasic flow involves small reactive volumes, the control of the associated flow rates and perfect knowledge of the heat transfer between the reaction chamber and the wall. Based on these conditions, highly exothermic reactions can be studied safely. In the next section, an experimental study of the hydrodynamics and thermalization of the biphasic flows is presented.

Chapter 3

Experimental study of the stability and periodicity of the biphasic flow

Abstract

This chapter is devoted to the experimental study of the stability and periodicity of the biphasic flow. More specifically, the droplet flow must be characterized by using visible and infrared imaging techniques to validate (i) the estimation of the average velocity from the measurements, (ii) the periodicity of the droplet flow and (iii) the thermal periodic established state of the flow. This very important characterization section will allow for the further establishment of the hypothesis with respect to heat transfer modeling. The experimental study has shown that the hydrodynamics in such systems are perfectly controlled, which ensures the stability of droplet generation (1 to 5 Hz), as well as the reproducibility of droplet sizes (from 1.5 to 3 mm ± 10 μm) and velocities (from 2 to 6 $mm.s^{-1}$). Additionally, the thermal monitoring study has shown that the temperature profiles can be managed at two different orders: 1) the local temperature profiles allow for the study of the instantaneous flow behavior at a given time and the mean behavior of the flow over time (i.e., continuous contribution) 2) The local temperature fields allow for the study of the temperature profiles of each phase as functions of time, in addition to investigation of phenomena at the local coordinate of the droplet. Finally, it was shown that IR signals are periodic but that the intensity changes along the channel because of the influence of several thermal effects.

3.1 Infrared and visible imaging

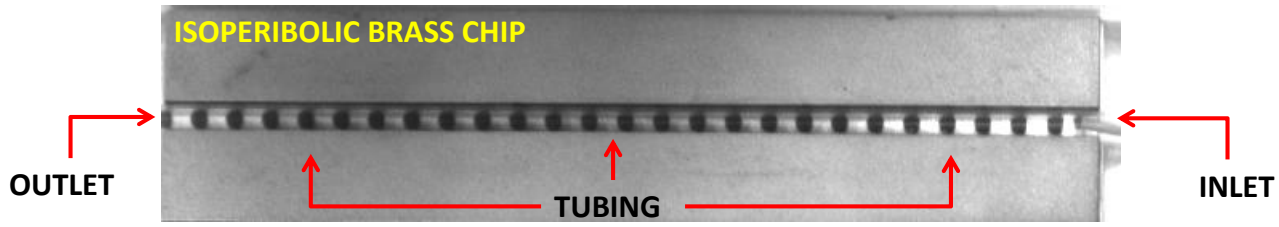

Figure 3.1: Picture of the isoperibolic millifluidic brass chip, depicting the inlet where two small tubes meet at the droplet generation zone.

Two imaging techniques are used to study the biphasic droplet flow. IR techniques allow for the measurement of temperature fields, while visible imaging is used to characterize the biphasic flow hydrodynamics. The experiments are performed in the isoperibolic set schematized in figure 3.1.

In this figure, the inlet and the outlet of the flow are indicated. The droplets are generated and spaced by oil plugs at the inlet of the tube by using a syringe pump. The droplet and the oil flow rates are given by Q_G and Q_H, respectively, which are independently controlled and adjusted to form monodisperse droplets in oil. As it can be observed in figure 3.1, a blue dye (Sensient Cosmetic Technologies) is added to the aqueous phase to increase the contrast and enable visible imaging. The concentration of the dye was approximately 0.01 mM; in this case, the surface tension between the water and the oil is unchanged.

With this technique, the droplets are generated and delivered at a constant rate. The purpose of the characterization of the biphasic flow is to (i) verify the periodicity and (ii) estimate the velocity of the flow.

To achieve this characterization set-up, the flow is monitored by both imaging techniques. Thus, a sequence of snapshots of the droplet flow along the channel is recorded at different times (t_i), where $t_i = [0 : N]$ is the time, and N is the duration of the recording. In figure 3.2, a snapshot of the droplet flow through the channel at different times is shown. The flow progresses through $z = L$ (the inlet) to the end of the channel at $z = z_0 + L$, where L is the total length of the channel groove in the isoperibolic chip. In this figure, the frames (or snapshots) are stacked one after the other, it is possible to note the droplets trajectory by the dashed red slopes.

3.2 Image processing methodology

The image sequences from the IRT and visible imaging techniques are processed by the same methodology reported in the flow diagram shown in figure 3.3. This schematic representation summarizes the processing

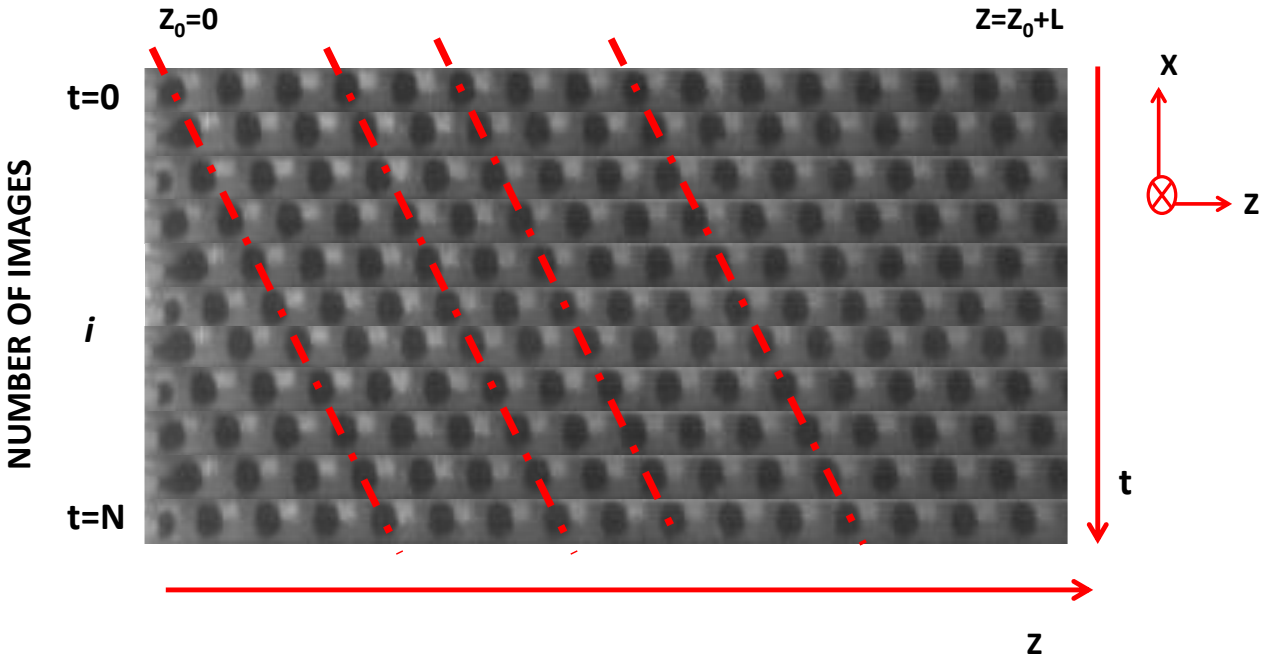

Figure 3.2: Snapshots of the droplet flow at different times are tiled one after another. It is possible to identify the droplet´ s trajectory based on the dashed red slopes.

steps for information extraction.

1. **Raw data extraction**

   Raw images are processed by MATLAB to obtain a matrix; this process can be very expensive in terms of processing power and challenging to accomplish when the image size is wide or when the image sequence contains many images. Because MATLAB uses at least 1 GB [1] of both memory types, the hard drive and RAM [2], when image analysis is performed, it is recommended to use a computer with at least 4 GB of RAM. To reduce image analysis time and processing demands, it is possible to reduce the matrix size by choosing a Region Of Interest (ROI) in the image.

2. **Region of interest (ROI)**

   It is important to detect the ROI within the image sequence, regardless of the reactor shape (i.e., whether a straight channel or serpentine) to monitor the biphasic flow during the experimental time. To do so, a rigorous methodology for data extraction has been developed. The method computed by J. Toutain was already used in the doctoral work of C. Hany [96]. The method is described below.

   - **Pretreatment:** Build a curvilinear mesh respecting topology in accordance with the dimensions of the chip (manufacturing layout) to generate all of the variables related to the geometry of the system, as shown in figure 3.4. Here, a geometry library is established.

[1] GigaBite
[2] Random-Access memory

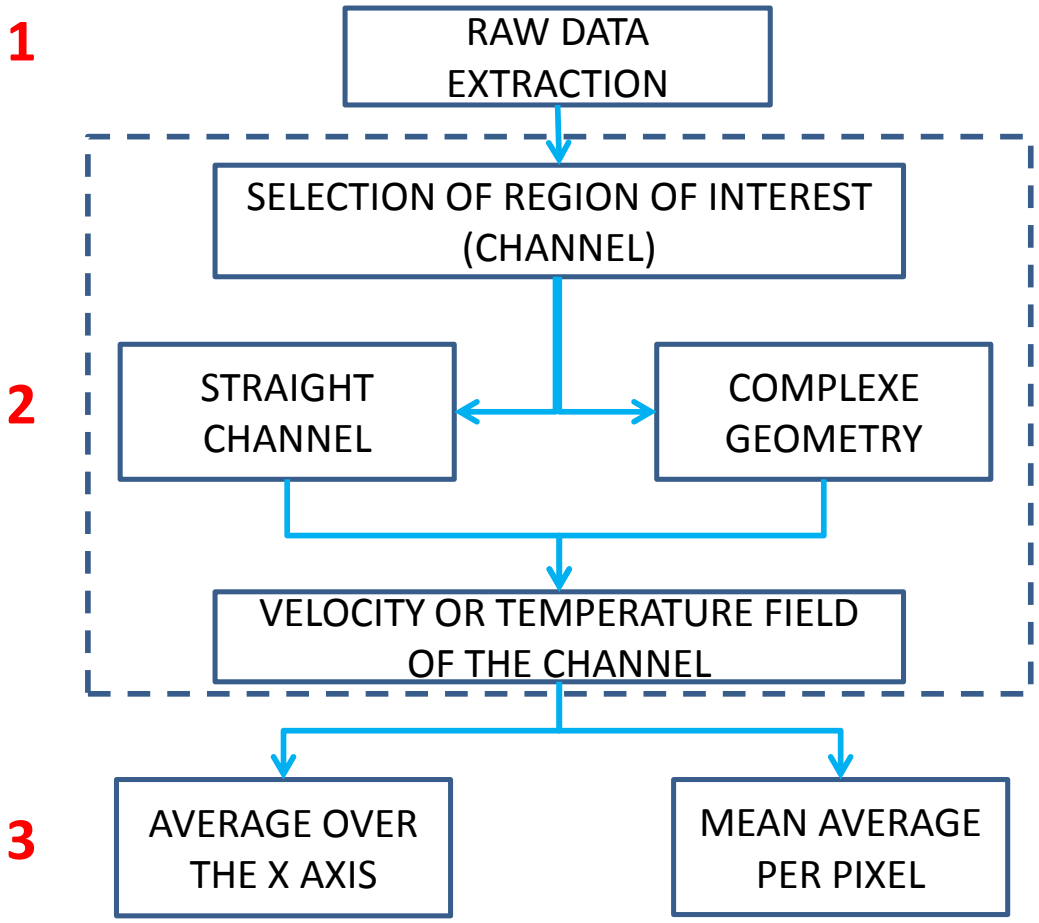

Figure 3.3: An overview of the basic algorithm for rigorous data extraction

- **Scaling:** In this step, after selecting the geometry, the user must place the layout mask directly on the infrared image. This mask corresponds to the ROI, i.e., the tubing. Due to the limitations of image resolution, this placement is approximate. Next, a specific algorithm is applied to optimize the placement of the mesh, which serves as an image interpolation grid. A numerical study of synthetic images was used to estimate the mesh accuracy and the performance of the algorithm. The associated incertitude was found to be less than 0.1 μm.

- **Extraction:** Once the curvilinear mesh is correctly positioned, the field along the axis of the tube is obtained by linear interpolation.

Regardless of reactor shape, the goal is to unfold the geometry for matrix construction. Subsequently, the matrix from the ROI is stored in a three-dimensional array; as schematically depicted in figure 3.5, the size of this array is defined as m x n x t. Here, m is the width of the channel (i.e., number of pixels), n is the length of the channel, and t is the time or the number of frames. The matrix from the visible image

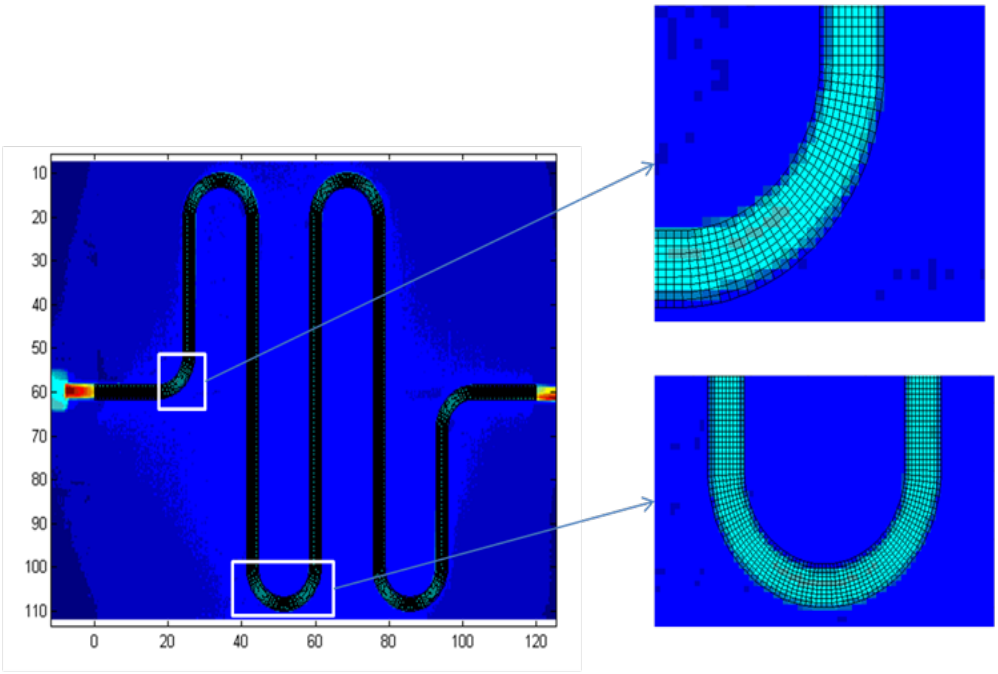

Figure 3.4: Curvilinear mesh of a millifluidic chip

will inform us of the velocity field and the composition of the biphasic flow (figure 3.5.A), while the IR image will identify the temperature field (figure 3.5.B).

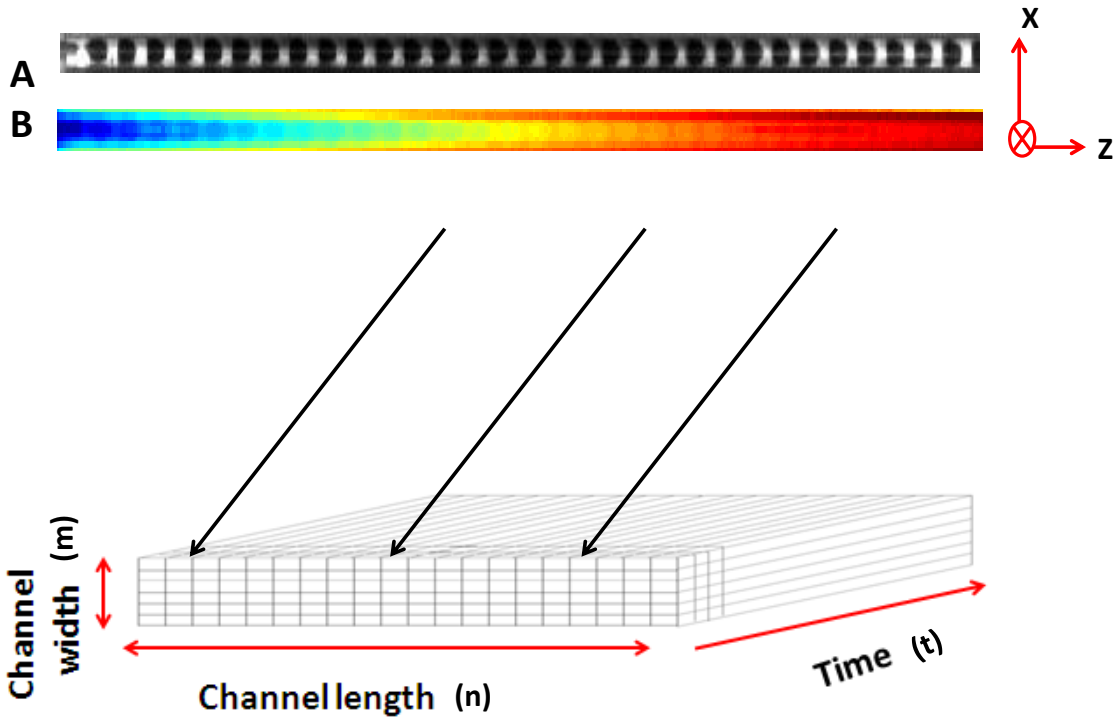

Figure 3.5: Droplet flow monitored by A) a visible camera and B) IRT. Construction of a three-dimensional array, in which the temperature fields are stored.

3. **Usual operations**

A raw visible or IR image is selected such that I (x,z,t), where a three-dimensional array contains the raw experimental data (images I) used for further heat treatment. In accordance with the methods used for either the velocity estimation or thermal processing, two main techniques are relied upon, as listed below:

1. Average over the width of the channel (x axis).

$$\overline{I(z,t)} = \int_x I(x,z,t)dx \tag{3.1}$$

2. Mean average of each pixel over time.

$$\overline{I(z)} = \int_t I(z,t)dt \tag{3.2}$$

The techniques can be easily understood and give us the possibility to simplify the observed phenomena. The previous operations may be combined for analysis of the data from different points of view. Subsequently, other combinations of these or other typical operations can be developed. It is important to note that droplet flows are periodic and add a fourth dimension to our problem, so it is necessary to develop image analysis methods that are devoted to changes in space, which may arise from the periodic measured data relative to the transient local space of the plugs.

3.2.1 Time and space imaging analysis

The observed periodic data given by the droplet flow are averaged as a function of time. To do so, the average over the width of the channel value is obtained along the z-direction for each image, and then, the averages are plotted as a function of time for the IR set (figure 3.6.B) and the visible set (figure 3.6.A). From these representations, two cartographies are built. The one from the IR image set allows us to build the temperature cartography as function of space and time. Additionally, the hydrodynamic flow cartography is built from the visible images.

It is important to note that from the visible images, it is possible to precisely detect the trajectory of each droplet. As shown in figure 3.6.B, the intensity (Digital Level, DL) of the temperature evolution of each pixel along the channel is strongly influenced by the thermal heat transfer inside the tubing. In contrast, the digital level of the same flow, as measured by the visible camera (figure 3.6.A), gives better contrast and spatial resolution. Moreover, the IRT image allows for verification of the thermal periodically established state of the droplet flow.

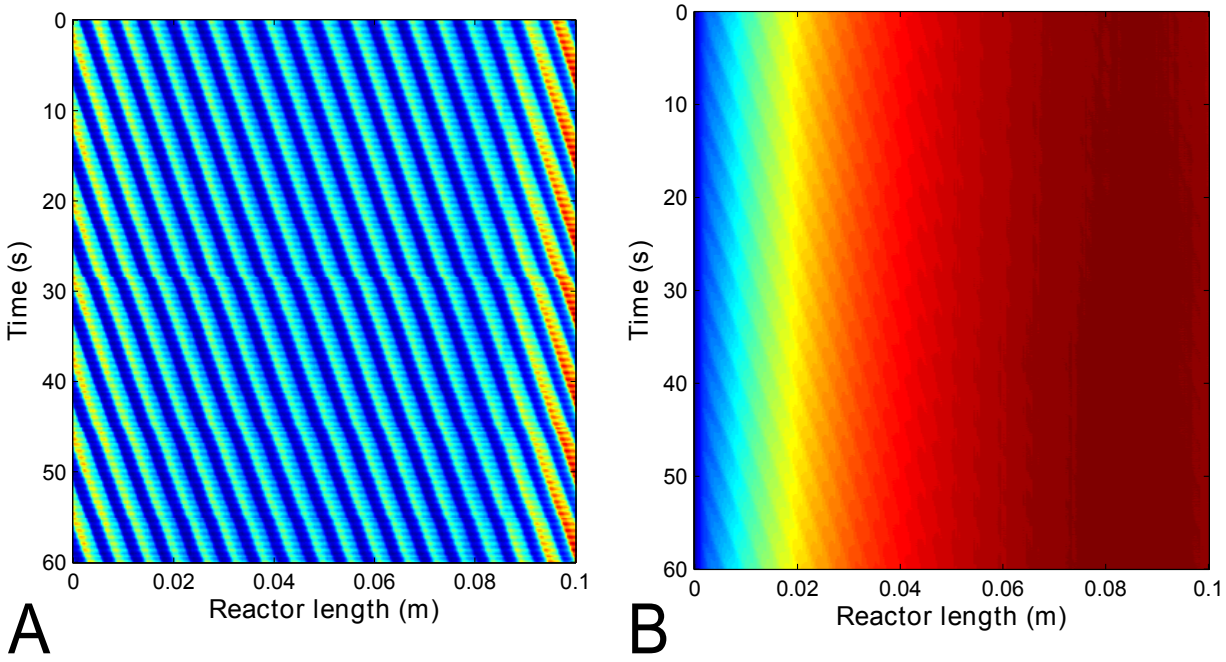

Figure 3.6: A. The flow patterns and droplet trajectories can be precisely observed by using a visible camera. B. Temperature cartography giving the temperature profiles as functions of space and time for a given set of flow conditions. Each line corresponds to a temperature profile, and the map evidences the drops trajectories.

In figure 3.6.B, it can be observed that when both phases of the biphasic flow (droplet and oil) have the same initial temperature, while the isoperibolic chip has a different temperature, a characteristic distance is necessary for the biphasic flow to reach the chip temperature. From this analysis, it can be concluded that these techniques allow us to:

1. Estimate the average velocity based the inverse of the slope of each cartography
2. Verify the periodicity of the droplet flow by using visible cartography
3. Use IR cartography to demonstrate that the thermal regime of the droplet flow is a periodically established state

3.3 Droplet flow patterns

In this section, the main idea is to use the visible images to detect perfectly the edge of the two plugs, to determine the lengths of the droplets and the oil. From a thermal point of view, and due to the diffusion and heat exchange processes, the measured temperature fields are blurred compared to the visible one. Then, by using visible data, the estimation of these hydrodynamics and geometric parameters will be enhanced. To do so, the image processing approach is presented here, as well as the results obtained for several flow rate conditions.

This characterization section is very important and will allow us to establish a further hypothesis concerning the construction of the heat transfer model.

3.3.1 Processing method: Edge detection between the phases

To measure the sizes of the droplets and oil, a threshold method based on image segmentation is used. The goal of segmentation is to simplify and/or change the representation of an image into something that is more meaningful and easier to analyze. Typically, from a gray scale image, thresholding is used to create binary images. This technique is typically used to locate objects and boundaries (lines, curves, etc.) in images. Image segmentation is the process of assigning a label to every pixel in an image such that pixels with the same label share certain particular characteristics. A sequence of images is recorded when the droplet flow has reached the periodic established state. It is important to remember that the droplets are generated at the same frequency by the imposed flow rate. In this periodic state, we assume that the droplets have the same length and spacing. By using this image analysis technique, we typically succeed in verifying this important assumption. The following operations are performed on each image, and the process is illustrated in figure 3.7. To measure the sizes of the droplets and oil, the distance between two droplets and the velocity based on the thresholding method using image segmentation was developed.

1. The mean of the image is established over the width of the channel (x-direction) to obtain an X vector over the length of the channel (z-direction), as illustrated in figure 3.7.A.

2. The derivative of the vector X (the explicit finite difference) is calculated, and a new vector X2 is returned, as illustrated in figure 3.7.B.

3. From X2, the minimum and maximum values are extracted and plotted in figure 3.7.B as red dots and green crosses, respectively, to indicate the front and back interfaces of each droplet.

4. The estimated edges are also indicated by the vector X, as observed in figure 3.7.A.

5. Finally, the same values are plotted on the visible image to validate the agreement between the estimated edges and those observed in the visible image (see figure 3.7.C).

The analysis performed on one image is then performed on all of the images in the sequence (a statistical approach) to characterize the droplet flow, as described in the following section.

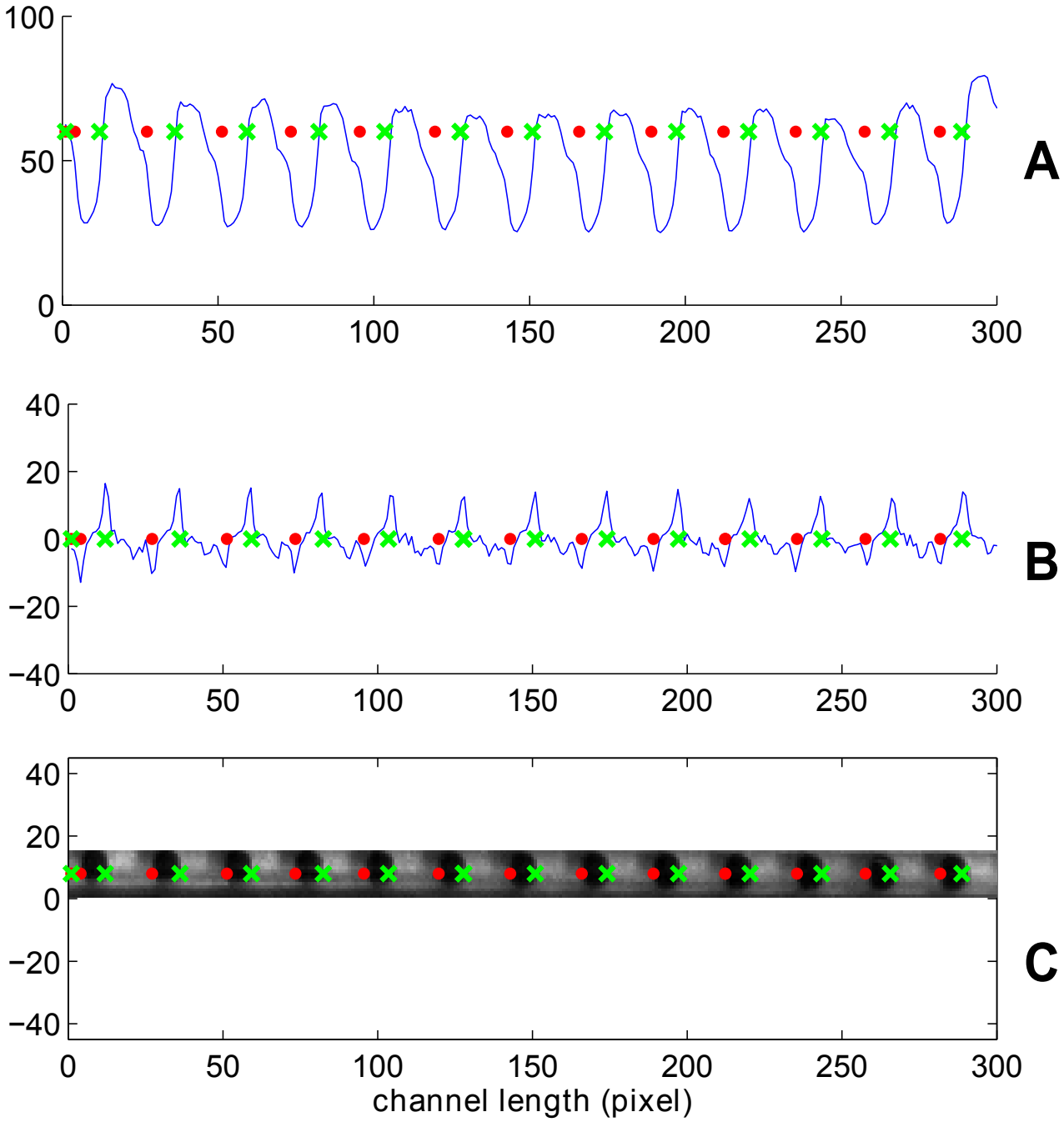

Figure 3.7: Image analysis: The locations of the edges are indicated by red dots and green crosses, placed on the droplets. This approach is based on a homemade thresholding method that is used to find the minimum and maximum values.

3.3.2 Hydrodynamic characterization

The droplet shape and size depend mainly on the flow focusing geometry design (injector) and the flow rates of the IKV 32 fluorinated oil (Q_H) and water (Q_G). As previously demonstrated in the literature [97], the ratio R = Q_G/Q_H is the most important parameter under the conditions of biphasic flow. As a result of flow rate variations, the R ratio changes, as well as the size of the droplets. Three constant total flow rates and

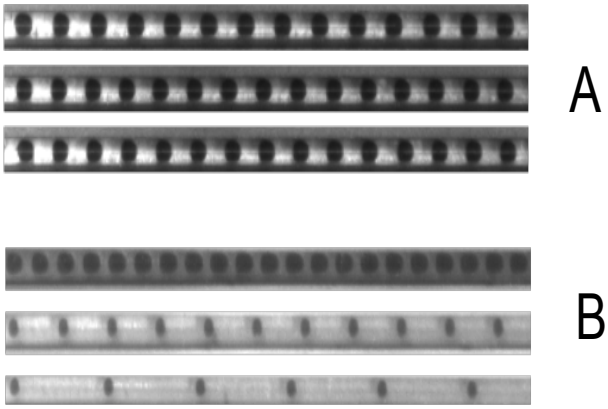

Figure 3.8: A. Visible image of droplet flows for three different total flow rates (Q_T) with constant R=2 (Q_H/Q_G=2), from top to bottom Q_T=10, 20 and 30 $mL.h^{-1}$. B. Visible image of droplet flows with constant total flow rate (Q_T=20 $mL.h^{-1}$) and various oil-water ratios of R=1, 4 and 10, from top to bottom.

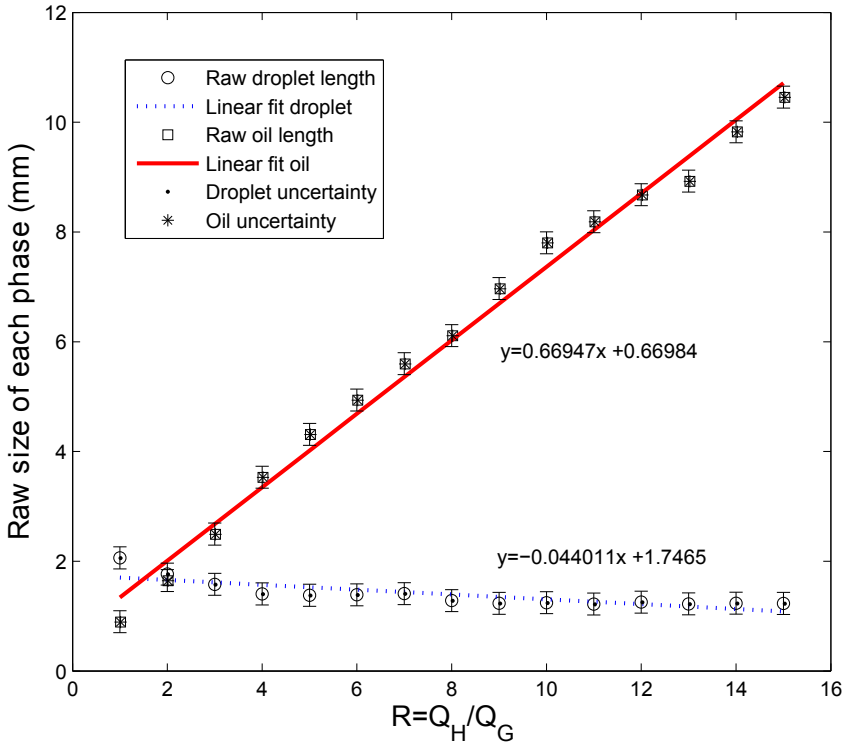

Figure 3.9: The raw length for the droplet L_G and for the oil L_H as a function of the flow rate ratio (R). R ranges from 1 to 15. For R=1, the same flow rate is imposed on the oil and aqueous phase, whereas R=15 means that the imposed oil flow rate is 15 times greater than that of the aqueous phase

flow rate ratios, R, between Q_H and Q_G, are established by using a syringe pump. For example, see figure 3.8.B. For a given total flow (Q_T), it can be shown that the length (L_G) and the shape of the droplets can be significantly modified by varying the R ratio. This significantly affects the thermal behavior (i.e., heat transfer) that arises between the droplet and the oil and, in particular, the heat exchange surface between the fluid and the tubing wall. Moreover, in figure 3.8.A, for an imposed ratio R, it can be observed that the length and shape of the droplets and oil plugs are independent of the total flow rate variation. From the thermal and chemical

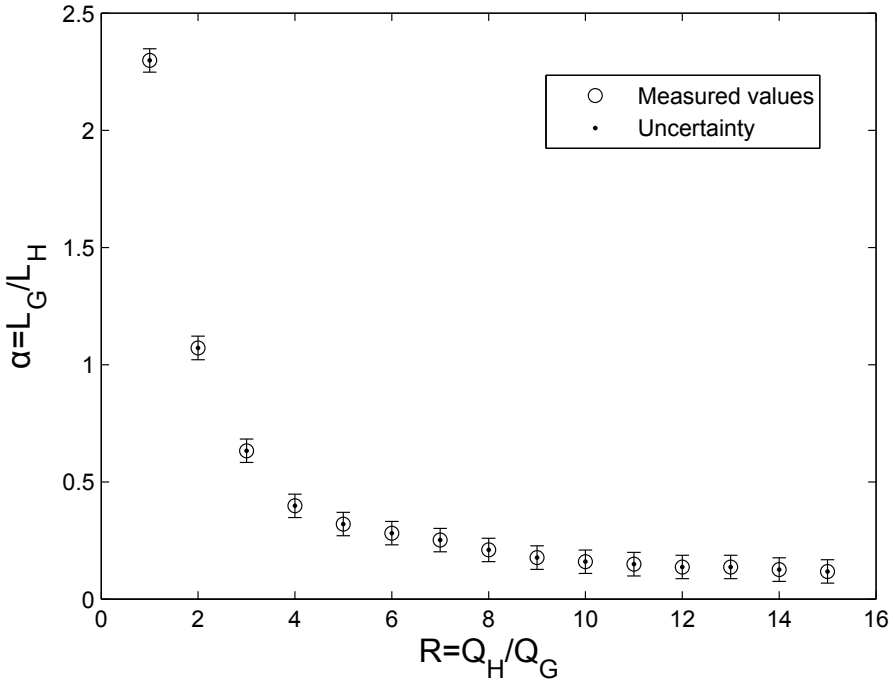

Figure 3.10: The inverse of the length ratio alpha ($1/\alpha$=L_G/L_H) as function of the flow rate ratio R, measured from the visible images at Q_T=20 $ml.h^{-1}$.

perspectives, increasing the total flow only affects the residence time and the mean velocity of the flow, allowing for the improvement of the related temporal resolution.

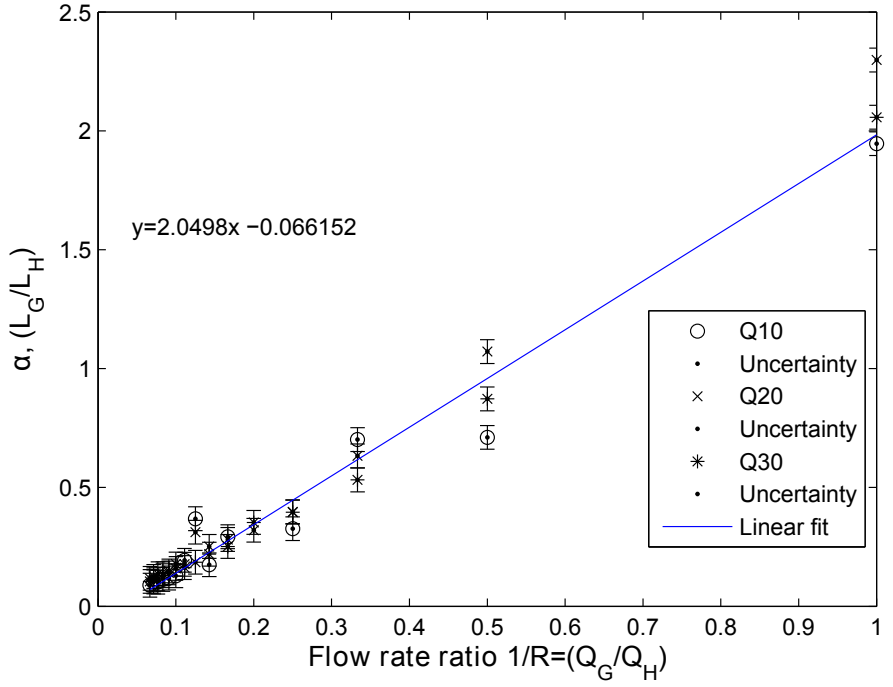

Figure 3.11: The inverse of the flow ratio $1/R$ versus the length ratio α of the segmented flow for three different total flows, 10, 20 and 30 $mL.h^{-1}$, which are represented, respectively, by empty circles, crosses and stars

From these visible images, it is possible to determine the length of each phase, using the previously described

method (see section 3.3). In figure 3.9, we observe that the oil length increases with the flow rate ratio, while the droplet length decreases to a constant value. Additionally, as shown in figure 3.10, the relation between the ratio R and the ratio α (L_G/L_H) is reported. It can be observed that as the ratio R increases, alpha tends to decrease. If the length of the period (L_T) is defined as $L_T = L_H + L_G$, the oil flow rate affects the size of the period.

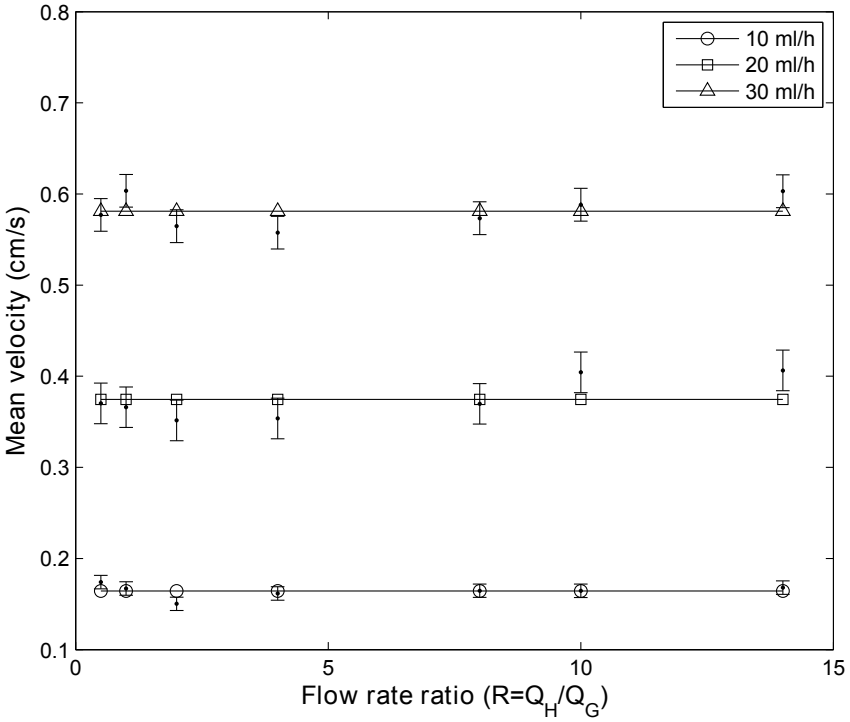

Figure 3.12: Measured mean velocity $\bar{U}$ ($cm.s^{-1}$) of the biphasic flow as function of the flow rate ratio R, for different total flow rates Q_T

Figure 3.11 illustrates the relationship between α (L_G/L_H) and the inverse of the flow rate ratio ($1.R^{-1}$) for three different total flows. It can be observed that the relationship between α and the inverse of the flow rate ratios R ($1.R^{-1}$) is independent of the total flow. Thus, for a given R, the observed α ratio between the length of the phases is the same, regardless of the total flow.

From the methodology reported in the literature [31, 97, 98] and by using the previous data processing approach, the results reported in figure 3.11 were obtained for various R values and three total flow rates. A direct linear relationship exists between the flow rate ratio R and the α. This relationship is independent of the total flow rate. Figure 3.12 shows that the mean velocity $\bar{U}$ remains approximately constant when the flow rate ratio R is varied. Additionally, figure 3.13 illustrates that the mean velocity $\bar{U}$ (calculated by the previous method presented in 3.2.1) varies linearly with the total flow.

From this hydrodynamic analysis, we can identify several important results in our experimental conditions:

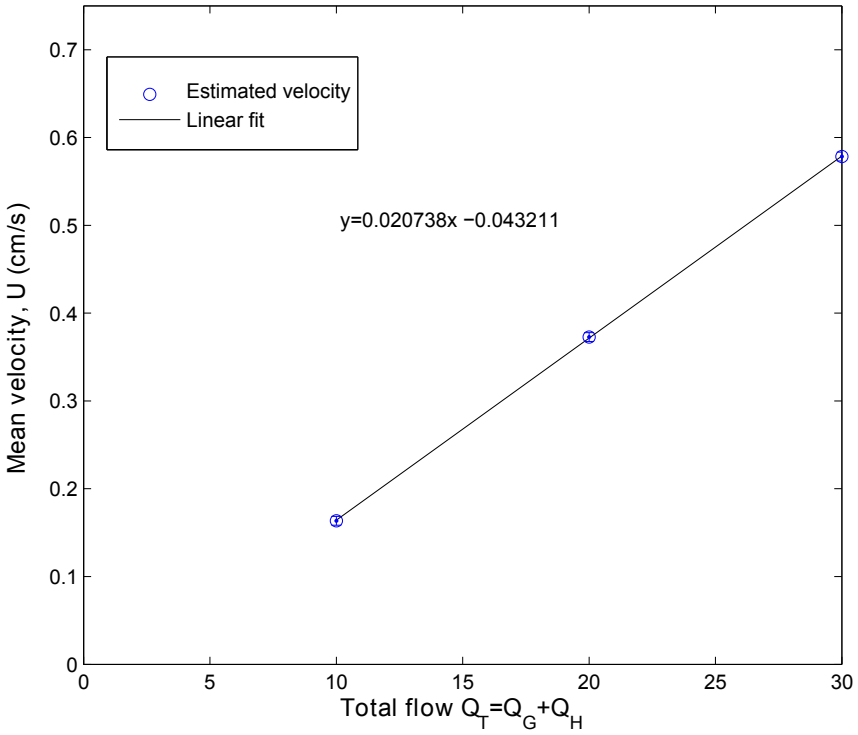

Figure 3.13: The total flow Q_T is plotted versus the mean velocity $\bar{U}$ from figure 3.12

1. **The droplet size is quasi-constant when R is greater than 4.**
2. $\alpha = L_G/L_H$ **is quasi-constant when R is greater than 7.**
3. **The mean velocity** $\bar{U}$ **is independent of the flow rate ratio R.**
4. **The** α **ratio and the inverse of the flow ratios R** $(1.R^{-1})$ **are independent of the total flow.**
5. **The mean velocity** $\bar{U}$ **varies linearly with the total flow** (Q_T)**.**

From these flow pattern measurements, it is clearly demonstrated that the hydrodynamics in such systems are perfectly controlled, which ensures good stability and the reproducibility of the droplet sizes and velocities. The standard deviation of the plug length measurements indicates less than 3% uncertainty. From this analysis, we can assume that the droplets have periodic patterns with a very well known average velocity.

3.4 Infrared monitoring

In this section, the idea is to use infrared (IR) imaging to depict the thermal behavior of the biphasic flow toward a temperature constraint. From a thermal point of view, three scenarios are possible for

the measurement of temperature inside the biphasic flow:

- The same inlet temperature of both phases ($T_{G0} = T_{H0}$) and a different temperature of the isoperibolic chip (T_p) .
- The same temperature between the oil and the isoperibolic chip ($T_{H0} = T_p$) and a different initial temperature of the droplet (T_{G0}). This case is very close to the chemical reaction inside the droplet.
- The same temperatures of the droplet and the isoperibolic chip ($T_{G0} = T_p$) and a different initial temperature of the oil phase (T_{H0}).

The strategy is to inject the water droplets and the oil phase at the same temperature (room temperature), while imposing a higher temperature on the isoperibolic chip. A summary of the selected conditions is given here:

- Both fluids, the droplet (water) and oil, have the same inlet temperature $T_{G0} = T_{H0} = 20°C$
- The wall temperature is imposed at $T_p = 30°C$

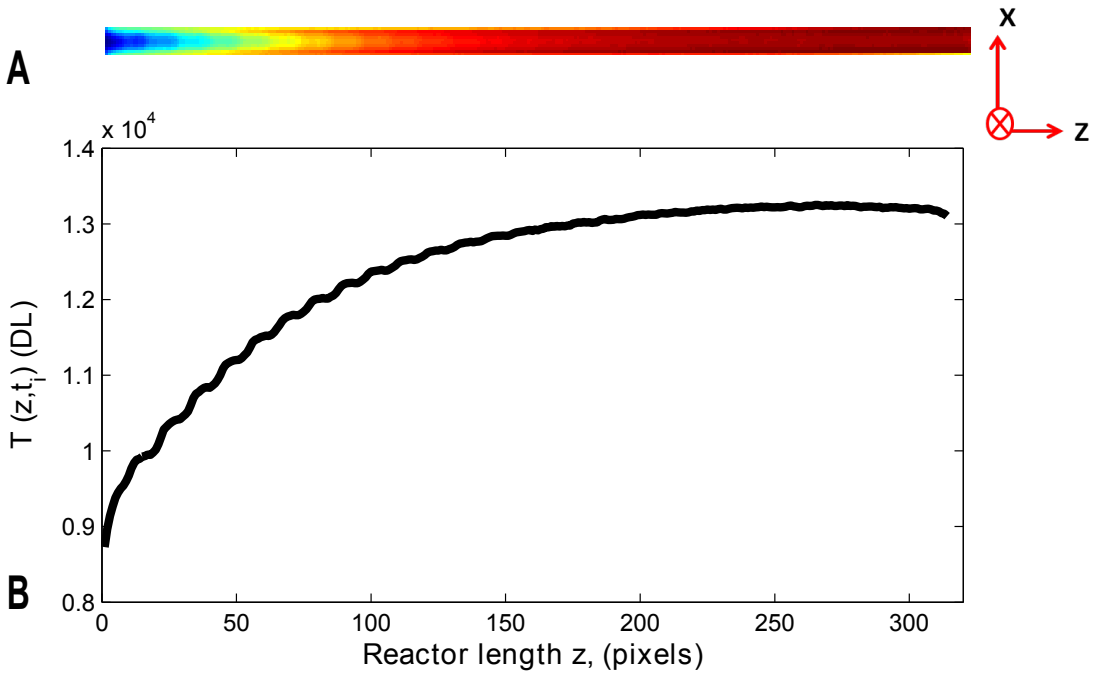

Figure 3.14: (a) IR temperature field at a given time (t_i). (b) Average temperature profile from this IR image as a function of the length of the reactor, as described in equation 3.1.

In figure 3.14.A, a raw temperature field is illustrated, while figure 3.14.B depicts the average (x-direction) temperature profile for any time, represented as a function of the z-direction. This raw temperature profile resembles a damped harmonic oscillator. This damped oscillation corresponds to

the temperature difference between the water and oil phases. Nevertheless, it can be observed that a Continuous Component (CC) is also present in the damped profile. From a thermal point of view, we can assume that a global heat exchange between the biphasic media and the tubing wall occurs (this corresponds to the continuous component). However, another heat exchange between the phases also exists (this corresponds to the damped oscillation). The level of this oscillation or fluctuation is directly proportional to the thermal parameters of each phase.

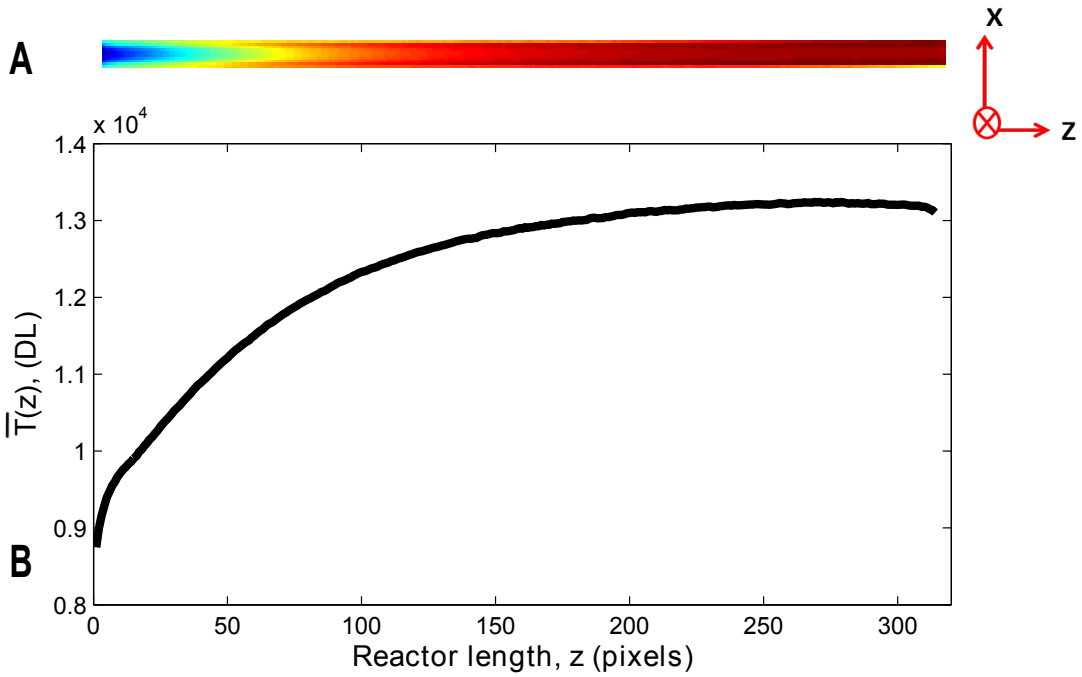

Figure 3.15: (a) Mean of the IR temperature field over the total observed time (t_N). (b) Mean temperature profile from the average IR image as a function of the length of the reactor, as described by equation 3.2.

Moreover, if the mean of all temperature profiles is calculated, the temperature profile along the channel is smoothed, as illustrated in figure 3.15.B. In this case, the generated temperature profile represents the mean behavior, or Continuous Component (CC), of the biphasic flow. When the temperature profiles are averaged, it is possible to achieve a good signal-to-noise ratio (SNR=100). Moreover, if the CC behavior is subtracted from the damped harmonic oscillator (i.e., to subtract the profile on figure3.15.B to the profile on figure 3.14.B), it is possible to enhance the fluctuations of the damped oscillator, which are shown in figure 3.16.B. In figure 3.16.A, the same operation has been applied to the fields, and both phases can now be better appreciated.

Based on the experimental temperature fields measured by IRT and illustrated in figures 3.14.A to 3.16.A., it can be observed that the total temperature function of the width (x) and the length of the channel (z) can be decomposed according to two contributions, (i) the continuous contribution

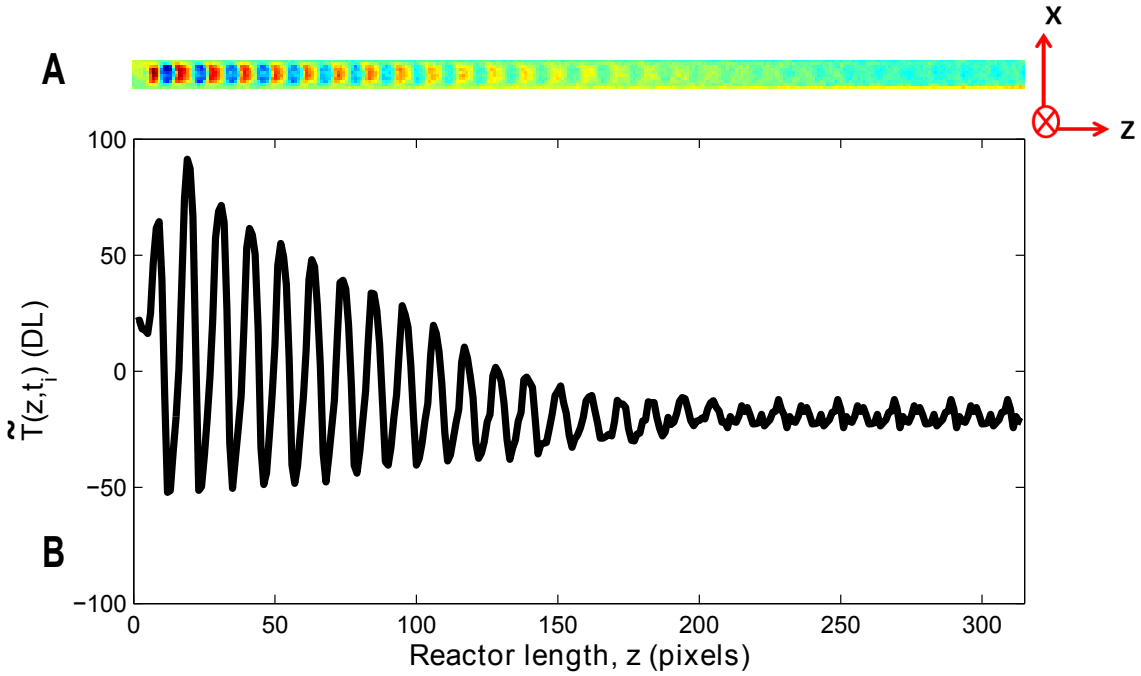

Figure 3.16: (a) Differential IR temperature field at a given time (t_i). (b) Differential temperature profile obtained from the difference between the profile at a given time minus the CC as a function of the length of the reactor.

($\overline{T}(x,z)$) and (ii) the fluctuating contribution ($\tilde{T}(x,z,t_i)$, according to the following expression:

$$T(x,z,t_i) = \overline{T}(x,z) + \tilde{T}(x,z,t_i) \tag{3.3}$$

Based on the experimental profiles (average over x) measured by IRT, figures 3.14.B to 3.16.B, it can be observed that the total temperature can be decomposed according to two contributions, the (i) continuous contribution and (ii) and the fluctuating contribution, according to the following expression:

$$T(z,t_i) = \overline{T}(z) + \tilde{T}(z,t_i) \tag{3.4}$$

Figure 3.14.B illustrates a raw temperature profile along the channel at time t_i ($T(z,t_i)$). From this raw signal, the phenomena can be distinguished at different orders:

- $\overline{T(z)}$, The temperature profile along the channel (z) is averaged over N periods. This is a first-order contribution (i.e., a continuous contribution, CC), as illustrated in figure 3.15.B.
- $\tilde{T}(z,t_i)$, Temperature fluctuation profile along the channel (z) at a given time t_i. This fluctuating

contribution is a second-order contribution and is illustrated in figure 3.16.B.

It is important to note that the fluctuating component highlights the presence of the biphasic flow, as shown in figure 3.16.B, although the component also represents less than 5% of the averaged signal of the continuous component ($T\bar{(z)}$, figure 3.15.B). The Continuous Component (CC) resulting from the mean average value over N periods of each pixel of the channel ($T\bar{(z)}$) is a function of the volume ratio of each phase. A similar process can be followed to achieve an overall space average in the local coordinates of the droplet-oil space.

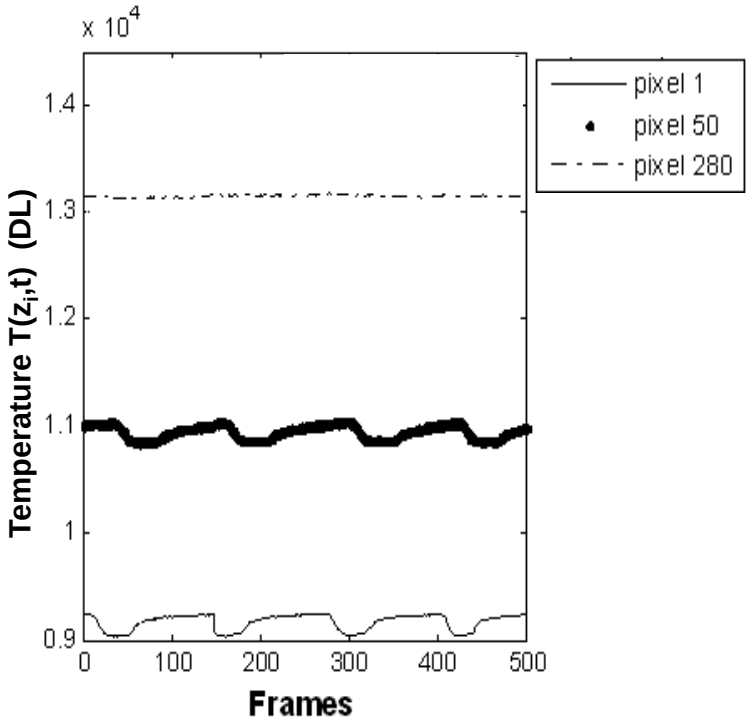

Figure 3.17: Raw temperature profiles $T(z_i, t)$ at several positions as functions of the acquisition time (frames), where pixels 1, 50 and 280 correspond, respectively, to the entry, middle and the end points of the channel.

If we analyze the raw experimental profiles for a given ratio R at different positions along the channel, as shown in figures 3.17 and 3.18, first, it can be noticed that the profiles have periodic fluctuations given by the oil and droplet train. To enhance the biphasic thermal behavior, the averaged value of the established state $\bar{T}(z)$ is subtracted (figure 3.18). In this case, the temperature evolution profiles of both phases can clearly be observed. It is interesting to note that at the end of the channel, where the imposed temperature is reached, the droplet cannot be distinguished from the oil (figures 3.17 and 3.18 pixel 280 plotted by a dashed line - - -). The periodic behavior of the biphasic flow enables working in the droplet coordinates by using a Lagrangian approach.

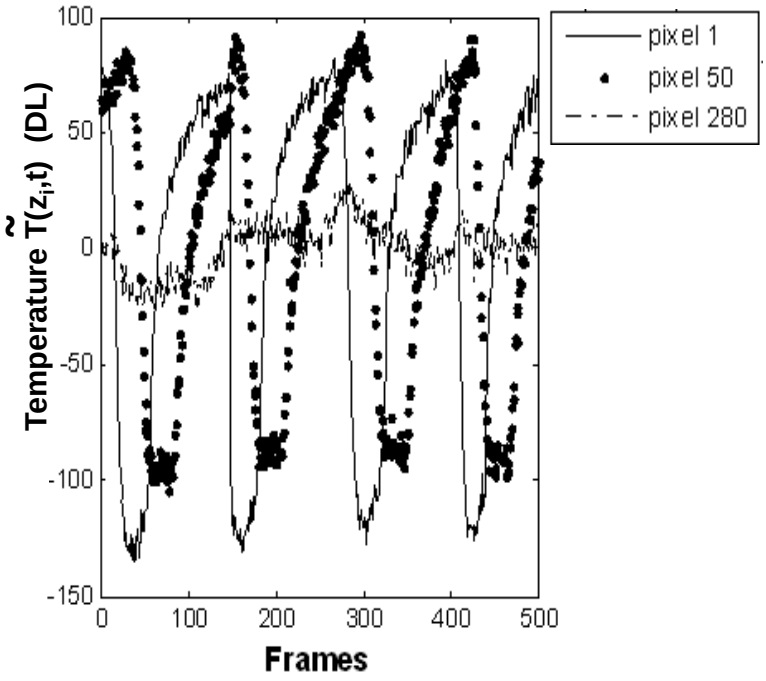

Figure 3.18: Fluctuating temperature profiles $\tilde{T}(z_i, t)$ when the mean average $\bar{T}(z_i)$ is subtracted at several positions as a function of the acquisition time (frames), where pixels 1, 50 and 280 correspond, respectively, to the entry, middle and the end points of the channel.

3.4.1 Local temperature profile

It is also possible to analyze the raw profiles from a slightly different point of view. The profiles as functions of time at different positions (pixels) are extracted and plotted $T_x(\bar{z}, t)$ in figure 3.19. In figure 3.19.A, the positions in the visible cartography are identified by black lines, while in figure 3.19.B, the positions in the infrared cartography are specified by colored lines. It is important to note that the same positions have been chosen in both images.

The profiles as functions of time are plotted in figures 3.20 and 3.21. It is important to note that the profiles at four different pixels, as determined from the visible images, are the same. Thus, to avoid overlap, the profiles have been plotted at the corresponding intensity of the IR profiles for the same position (see figure 3.20). In contrast, the IR profiles at different pixels exhibit different shapes due to heat transfer (see figure 3.21). The visible images are highly homogeneous, except at the edges because of the variations in luminosity. Thus, the profiles measured from this image at different pixels exhibit the same contrast and spatial resolution at all positions of the channel, figure 3.20. However, in the infrared image, an important gradient is observed. As shown in figure 3.21, the intensity (Digital Level, DL) of the temperature evolution of each pixel along the channel is significantly influenced

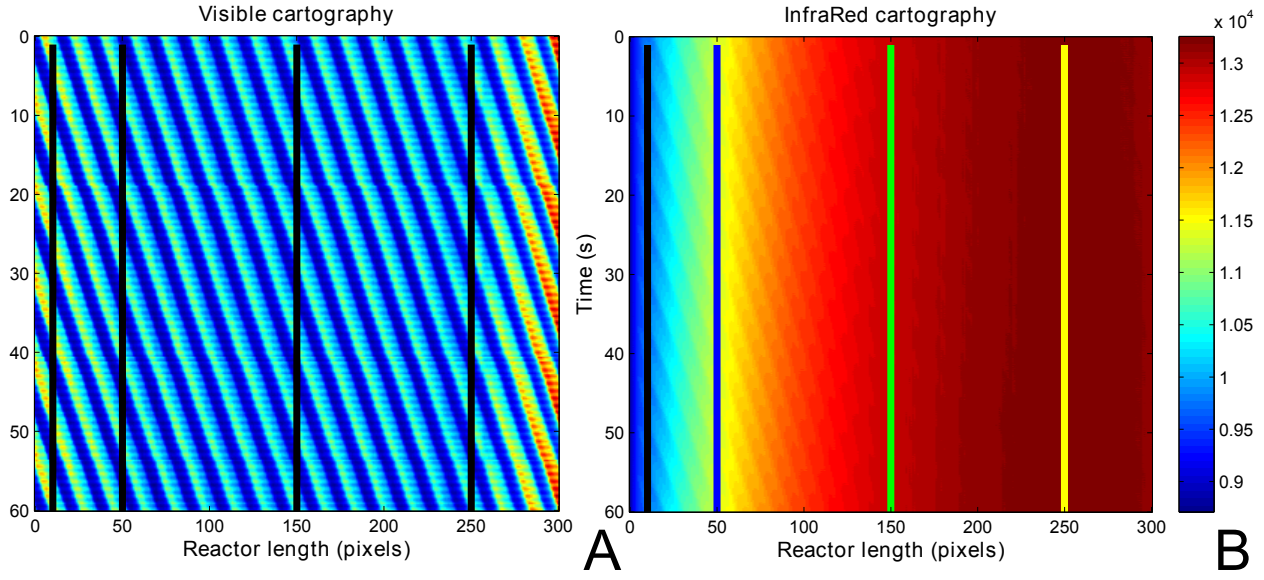

Figure 3.19: A. Visible cartography, where the black lines indicate the pixel positions of 10, 50, 150 and 250. B. Infrared cartography, where the colored lines indicate the pixel positions of 10 (black), 50 (blue), 150 (green) and 250 (yellow).

by the process of thermal homogenization throughout the tubing, i.e., diffusion between the phases and the heat losses. It is also important to note that the profiles from both imaging techniques at pixel 10 are nearly identical. This is because at the inlet of the tubing, the thermal effects are not yet established, hence due to the different thermophysical properties of both phases, it is possible to distinguish the biphasic flow with IR measurements alone.

To better understand the difference of the periodic signals, in figure 3.22, the visible and IR signals are compared with a step-like periodic signal, which represents the ideal optimum case of a synthetic biphasic flow. In this figure, it can be observed that the degradation between the step signal and the visible signal is due to shading and luminosity effects. The differences between the step signal and the IR signal are directly related to thermal diffusion between the phases, thermal homogenization throughout the tubing, and conductive heat losses with the surroundings. These factors impact the profile along the channel, as shown in figure 3.21.

From the presented profiles, it is possible to manage and analyze the raw signals from different points of view, such as

- By following the minima and the maxima of the periodic signals
- By following the mean behavior of the periodic signal

These two approaches provide different types of information. The contribution of the information gleaned from these two analyses is complementary.

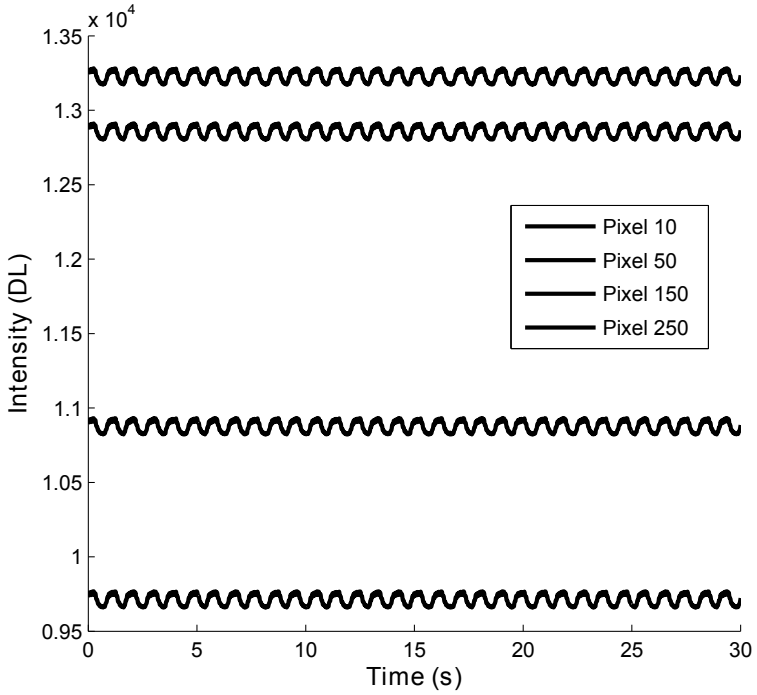

Figure 3.20: Profiles at the pixel positions of 10, 50, 150 and 250, indicated by the black lines. It is important to note that the profiles from the visible image have been plotted and placed at the intensity of the IR profiles to prevent overlap.

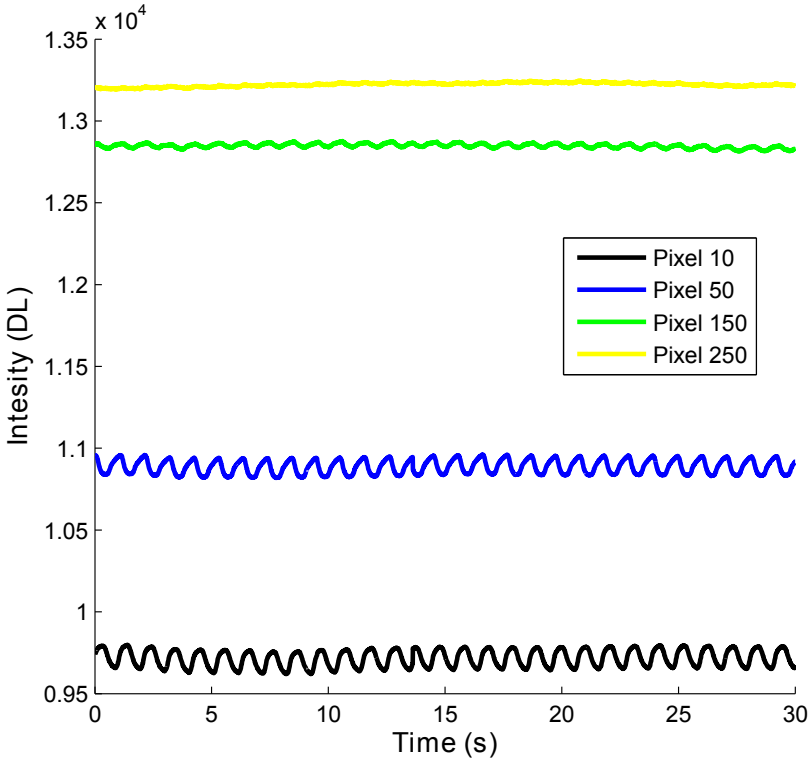

Figure 3.21: Infrared cartography, in which the colored lines indicate the pixel positions of 10 (black), 50 (blue), 150 (green) and 250 (yellow).

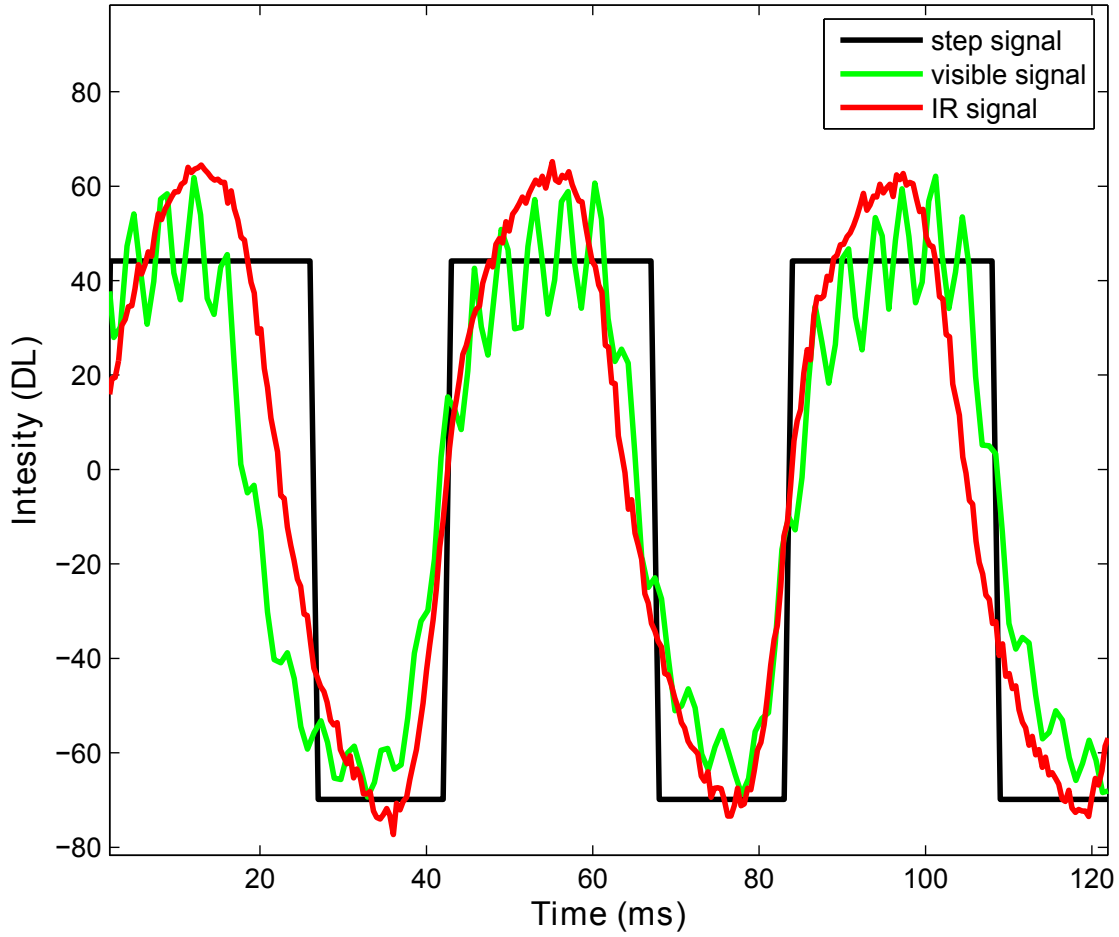

Figure 3.22: Comparison of three different profiles as functions time. The step and the visible signal were adapted at the same intensity of the corresponding IR profile. The synthetic step periodic signal (black line), the droplet visible signal at pixel 10 (green line), and the IR droplet signal at pixel 10 (red line) are shown.

3.4.2 Temperature local field

It is possible to work in the local coordinate of the droplet, i.e., to track the temperature field of a droplet and oil plug over time. Tracking the droplet is possible when the velocity is well known and significant contrast exists.

Based on the previous thermal images 3.19.B, in which the mean profiles were plotted as functions of space and time for a given set of flow conditions and ratio R, it can be observed that each line corresponds to a temperature profile, and the map evidences the drop trajectories. Taking this into account, it is possible to apply image processing techniques based on a similar principle as the Hough transform [99, 100]. This technique is applied to the temperature field to enhance the droplet flow, as well as to increase the contrast between the phases (water and oil) as evidence of the droplet trajectories, where the enhancement is illustrated in figure 3.23.A. The mean temperature profile has

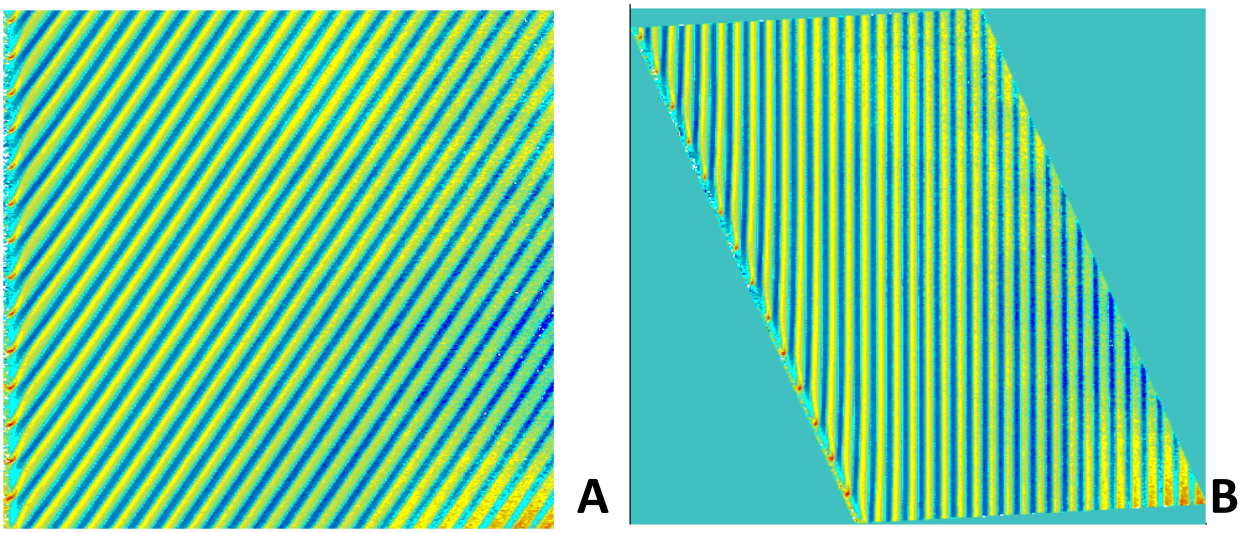

Figure 3.23: Image processing to enhance the droplet trajectories as straight lines adapted to the Hough transform

been subtracted from each temperature profile at a time t_i.

Usually, the assembly of these trajectories can be observed as an array of straight lines which is favorable for the Hough transform, which is based on straight line detection, as observed in figure 3.23.B. Using this approach, it is possible to estimate useful parameters, such as the droplet generation frequency and velocity and the distance between two successive drops. It is also possible to count the number of droplets injected. Additionally, the estimation of all the necessary parameters for tracking the droplet can be estimated. From a Lagrangian point of view, the history of a droplet (and the oil surrounding it) during its passage through the device can be reconstructed. As illustrated in figure 3.24, based on the image processing approach, three snapshots of the droplet at different times are presented.

In figures 3.24 and 3.25, several phenomena can be observed after the mean behavior of the flow has been subtracted. In this case, only the dynamic evolution of the biphasic flow toward reaching the temperature of the isoperibolic shape is observed when both phases have the same initial temperature:

- at t=5s
  - The two phases appear to have different temperatures at this time.
  - The heat capacity of the water is almost twice the heat capacity of the oil.
  - The red phase is the oil, while the blue phase is the water droplet.

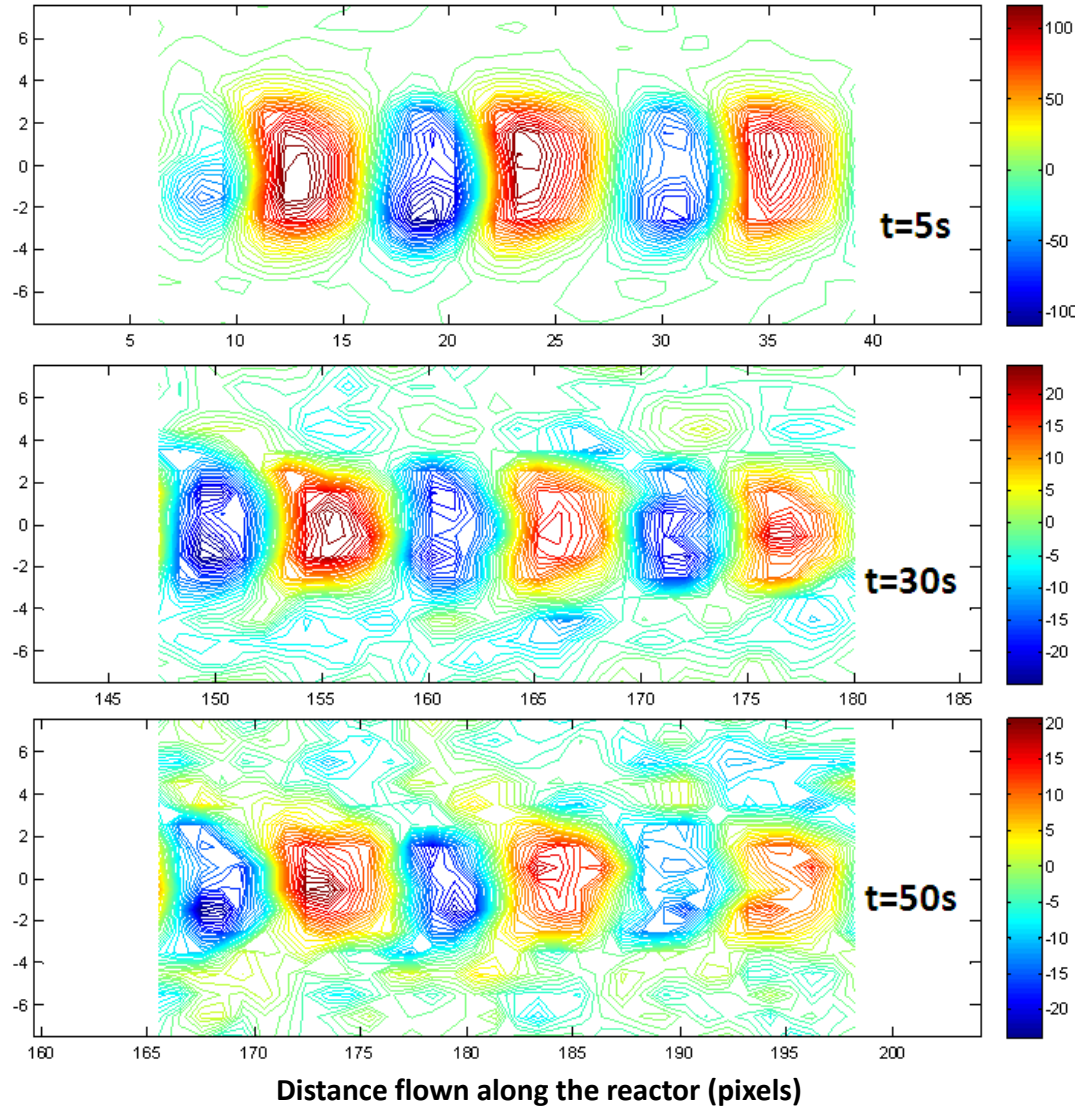

Figure 3.24: Lagrangian snapshot of a droplet at different times. These profiles illustrate the temperature variations on a digital level (DL).

  - The shape and size of each phase appear to be well defined.

- at t=30s

  - The shape and size of each phase appear to be well defined.

  - However, compared with the image at t=5s, the size and shape have changed significantly.

  - The temperature scale has decreased, and the biphasic flow approaches the temperature imposed by the isoperibolic chip.

- at t=50s

  - The phases cannot be distinguished.

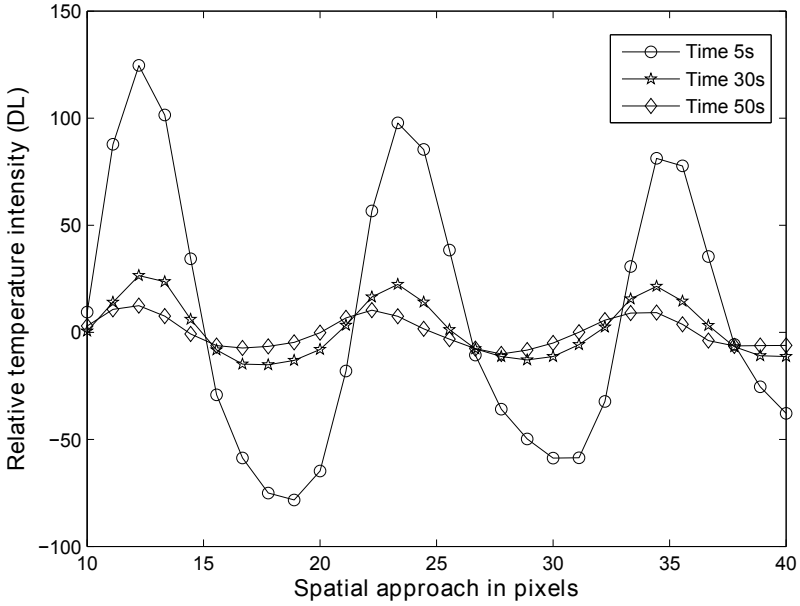

Figure 3.25: Spatial temperature profiles from figure 3.24. These profiles are extracted along a channel over the distance traveled (or flown) by the droplets. In this figure, we superimposed the profile to simplify the observation. The temperature profiles at 5, 30 and 50 seconds are plotted with empty circles, star and diamonds, respectively.

– The size and shape of the phases have changed significantly.

– The biphasic flow nearly attains the isoperibolic chip temperature.

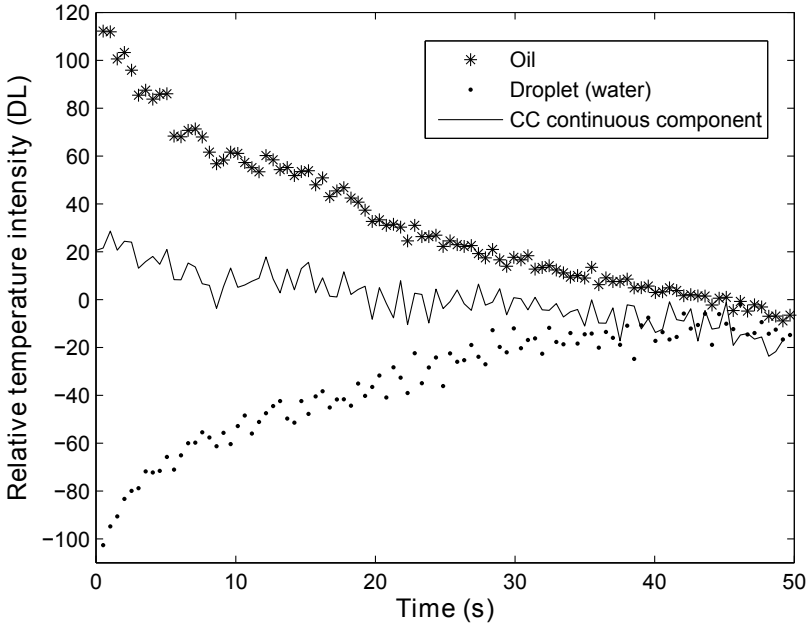

Figure 3.26: The relative intensity temperature of both phases

While the droplet is tracked along its passage inside the channel, the temperatures of the droplet and the oil are extracted. The relative intensity of the temperatures of both phases are plotted in figure

3.26. It is important to remember that the observed temperature fields were obtained by subtracting the mean temperature field from each temperature field at a time t_i. Hence, in this case, we observe the variation of the temperature around the mean behavior, which is why both profiles reach the same final temperature imposed by the isoperibolic chip and, ultimately, a null value.

From the local profile presented, is it possible to manage and analyze the raw signal from a Lagrangian point of view, which allows us to:

- Observe the local temperature profiles of each phase as functions of time and
- Study the phenomena from the local coordinates of the droplet.

3.5 Conclusions

This chapter was devoted to the experimental study of the stability and periodicity of the biphasic flow. The original approach of combining two imaging techniques to study the biphasic droplet flow was presented. The IRT technique allowed the measurement of the temperature fields, while visible imaging was used to characterize the biphasic flow hydrodynamics.

- The biphasic flow is perfectly controlled, ensuring the stability and reproducibility of the droplet sizes and velocities. We also concluded that:
  - The velocity varies linearly with the total flow (Q_T),
  - The velocity is independent of the flow rate ratios R,
  - The ratio R is independent of the total flow rate, and
  - $\alpha = L_G/L_H$ is quasi constant when R is greater to seven.
- Precisition of the characterization results:
  - The droplet is generated with a frequency from 1 to 5 Hz, where the precision is 10 μs, relative to the precision of a quartz clock at 1 ns. In this case, some effort still must be carried out to reduce the fluctuation that this level of precision induces.
  - The droplet sizes are reproducible from 1.5 to 3 mm ± 10 μm.
  - The typical velocities in this study are from 2 to 6 $mm.s^{-1}$.
- The biphasic flow was monitored by infrared (IR) imaging. The temperature profiles were carefully extracted from the IR raw data, where several ways exist to manage this extracted information:
  - The local temperature profiles allow us (i) to study the instantaneous behavior of the flow at a given time and (ii) to study the mean behavior of the flow over time (i.e., the continuous contribution).
  - The local temperature fields allow us (i) to extract the local temperature profile of each phase as a function of time and (ii) to study the phenomena at the local coordinates of the droplet.

  It was demonstrated that IR signals are periodic, exhibiting intensity changes along the channel

length because of the influence of several thermal effects, such as:

- Thermal diffusion between the phases
- Thermal homogenization throughout the tubing
- Convective heat losses with the surrounding

As a result of the different ways to manage the IR experimental information, in the next chapter, we are able to work at different orders of observation. The aim of the next chapter is to propose a thermal model that can explain the thermal behavior of the biphasic flow when several thermal effects occur in the miniaturized isoperibolic tubing-based chip.

Chapter 4

Quantitative thermal analysis of the droplet flow

Abstract

This chapter is devoted to quantitative thermal analysis. The thermal effects present in a complex system are discussed and modeled. To provide a global overview when both the hydrodynamic and thermal effects are coupled in a biphasic system, a 3D numerical model is presented. Consequently, from this study, some hypotheses were assumed to simplify the thermal model. Thus, a 1-Dt analytical model in Lagrangian space was proposed. According to the thermal analysis, two thermal scenarios were identified. Two simplified analytical thermal models based on the thin body approximation were proposed. After validating the "thin body approximation", it is demonstrated that when no source is present inside the media and a constant flux is imposed on the isoperibolic wall, the characteristic convective coefficient (H) can be predicted by the proposed mixing law. In contrast, when a heat source is present inside the droplet, it was observed that the heat exchanges varied, tending not follow the proposed mixing law, likely because the oil plug exhibits a thermal fin behavior instead of a thin body behavior. A correlation method was proposed to estimate the characteristic convective coefficient. It was shown that no obstacles exist with respect to estimating the heat source in a biphasic flow by applying the proposed methodology as a previous thermal calibration.

4.1 Presentation of multiphase flows in miniaturized devices

Recently, the development of microfluidic devices in biology [101], chemistry [102] and materials science [103] has shown tremendous progress. In particular, multiphase immiscible microflows have opened opportunities for the generation of controlled hydrodynamic structures, such as droplet, jets and plugs. Today, there exist a wide range of techniques for the generation of such segmented flows. One of the most important aspects is flow control, which is necessary for describing and understanding the transport phenomena.

The use of multiphase flows in miniaturized systems is a broad topic. In such systems, the exchange phenomena of mass, momentum and energy among different phases (disperse flows, gas − liquid and liquid − liquid flows, flows in porous media, boiling, granular flows, etc.) can be observed.

This works considers the study of the energy exchanges in multiphase flows, in particular, the liquid−liquid biphasic flow. Many studies regarding the heat exchanges of boiling flow, gas-liquid flow and liquid-liquid flow have been published [15, 104]. Most of these studies were concerned with either boilers, evaporators for use in industrial applications or the cooling systems of miniaturized electronic devices, developed to improve micro-heat exchange capabilities.

The heat exchange behaviors of monodisperse droplets are studied here for liquid−liquid laminar flows. This configuration is of high interest with respect to the chemical reactions performed in micro- and millifluidic systems. Emulsions and double emulsions can also be used for nanoparticle synthesis or drug microencapsulation. Miniaturized droplets can be envisioned as single microreactors in biodetection systems. In many application fields, it is necessary to control the flow temperature to control the overall experimental conditions (the boundary condition) of the reactions. In this chapter, an analytical study is presented to understand and model the heat exchange mechanisms involved in a two-phase flow.

4.1.1 An overview of a multiphase flow

In fluid mechanics, multiphase flows involve two or more phases of different physical or chemical properties. This type of flow occurs in a wide range of applications, such as oil recovery (petroleum extraction), chemical engineering (i.e., bubble columns, reactors, aeration systems), and energy production (i.e., oil transportation, steam generators, cooling systems, heat exchangers), among many more examples.

It is important to note that a two-phase flow is considered stable when, for any disturbance, the new operating conditions tend toward the initial conditions. The two-phase flow becomes unstable when, for any disturbance, a rapid transition from one state to another is observed. For example, if instabilities occur in power generation and heat transfer systems, boiling flows appear, and the growth of bubbles is observed. Instabilities are reportedly one of the most complex topics because several effects occur simultaneously and each plays an important role [12]. Several experimental results have been reported [53, 105, 106, 107, 108] on the analysis of the phenomena involved in such situations, for where a significant number of parameters must be taken into account. The influence of vapor quality and the Reynolds number on heat transfer coefficients has been reported. It has been observed that local heat transfer decreases sharply from the inlet to the outlet of a channel, as the gas phase increases. In the annular slug regime [1], the average heat transfer was reported to be approximately 6,000 $W.m^{-2}.K^{-1}$. Moreover, compared to normal and hypergravity conditions, the heat transfer coefficient increases in microgravity (30 %).

For reaction engineering purposes, the use of a segmented flow, such as a liquid−gas flow in a capillary (known as a Taylor flow), has increased in popularity in recent years [3]. Additionally, the study of these biphasic flows has recently exhibited several advances with respect to the cooling systems of miniaturized electronic devices, toward the improvement of micro-heat exchangers. The first studies of the segmented flow [4, 5, 6] were performed by using numerical and analytical approaches. More recent studies were carried out by applying a uniform wall temperature or heat flux thermal boundary condition under different geometries. In such cases, the multiphase flows showed two mechanisms that increase convective heat transfer, (i) the generation of bubbles (gas slugs) and (ii) circulation within the liquid slugs. Several experimental studies concerned with the thermal effects and the thermal characterization of segmented liquid gas flows have been reported [7, 8, 9, 10, 11]. These studies analyzed the influence of slug length with respect to enhancing the heat transfer in microchannel heat sinks.

A numerical study of the thermal effects of heat transport in a droplet-laden laminar flow, such as a liquid−liquid flow, was reported by [13]. In this work, the authors demonstrated that the effective rate of forced heat transfer in a droplet-laden flow is higher than in Poiseuille single−phase flow. Nevertheless, neither experimental nor analytical thermal characterizations of liquid-liquid biphasic flows in millifluidic systems have been studied. In this work, we have paid particular interest to understanding the heat transfer exchanges that occur in an isoperibolic chip. Isoperibolic means that

[1] Annular slug regime: A flow characterized by the presence of a liquid film flowing between the channel and the wall

a uniform wall temperature is imposed, allowing the biphasic flow to be studied under conditions of imposed temperatures, the total flow rate and ratio, and with or without a heat source. However, in such a configuration, it is important to understand the thermal heat transfer mechanisms sufficiently before studying any chemical reaction, phase change transitions, species mixing or wetting processes, which are generally strongly influenced by the effects of temperature.

4.1.2 Thermal effects and heat transfer

In this section, the thermal effects in a two-phase flow within a miniaturized channel in which the fluid dynamics and thermal exchanges are coupled are discussed. Here, two heat exchanges scenarios are depicted.

1. The inlet temperature of both phases is the same, while the temperature of the wall is different.
2. The inlet temperature of the droplet is different from that of the oil and the wall (i.e., a chemical reaction occurs inside the droplet).

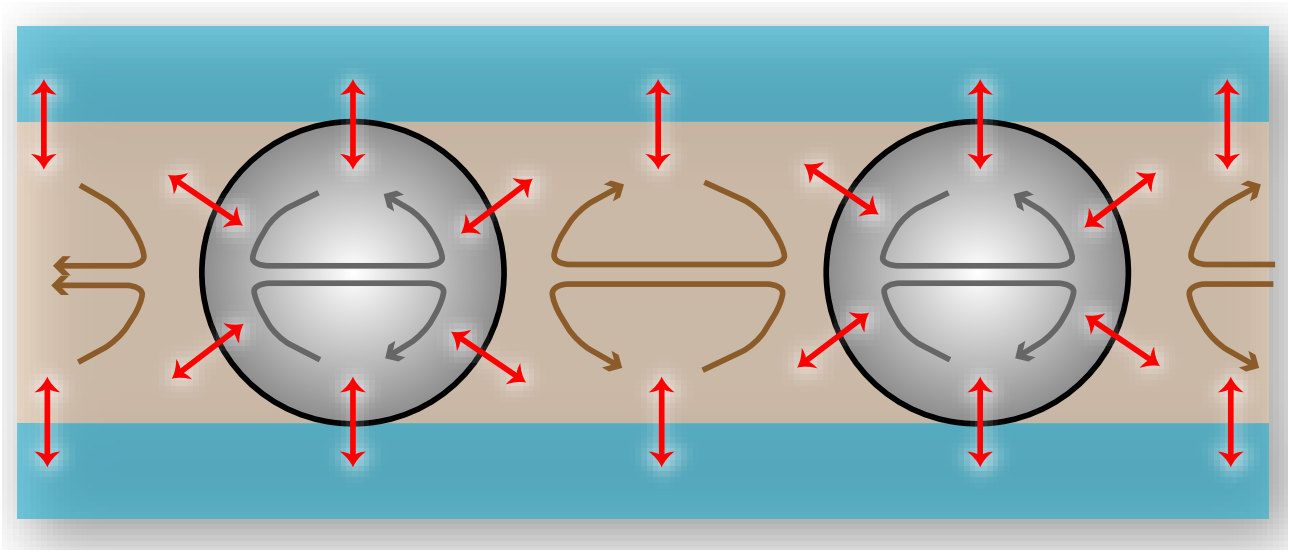

Figure 4.1: Sketch of the thermal exchanges in the case of biphasic flows. The red arrows illustrated the heat flux due to thermal diffusion, whereas the other arrows schematically depict the convective heat flux.

The listed scenario helps us to identify the energy balance (i.e., the direction in which heat flux occurs). As a first approximation, it is important to note that the exchange occurs within the droplet flow. In figure 4.1, heat exchanges are depicted according to several phenomena:

- The diffusion inside each phase
- The diffusion between the phases and the wall
- The convection between the phases

- The field of velocity of the flow
- The chemical reaction (heat source) inside the droplet
- The heat losses (convection and radiation) with the surrounding

Diffusion between the phases is a form of heat transfer that is due to microscopic diffusion and the collision of particles (phonon), which results from a temperature gradient (from the high to the low temperature of the body). Thermal diffusion exchanges can be observed among the contacting phases, i.e., the droplet−oil, oil−wall, droplet−wall contacts, as shown in n figure 4.1. The exchanges are illustrated by red arrows.

Additionally, by considering the exchanges that occur by thermal convection between the phases, transport by diffusion and advection can be considered. The droplets are advected (carried by the continuous phase), and diffusion occurs between these phases. As a result, convection may develop naturally due to the temperature difference.

Moreover, forced convection between the phases is induced by the imposed flow rate (i.e., the syringe pumps). This generates intra- and inter-drop recirculation patterns. In figure 4.1, such exchanges are illustrated by gray arrows inside the droplets and brown arrows for the oil plug.

Some dimensionless numbers are used to highlight the relevant physical parameters that act within such thermal phenomena.

The first dimensionless parameter characterizing the ratio between convective and conductive heat transfer is the Nusselt number (Nu), defined as:

$$Nu = \frac{hL}{\lambda_f} \tag{4.1}$$

where h ($W.m^{-2}.K^{-1}$) is the convective heat transfer coefficient of the boundary (i.e., the wall), L (m) is the characteristic size (e.g., diameter for pipes), and λ_f ($W.m^{-1}.K^{-1}$) is the thermal conductivity of the fluid. Some convective heat transfer relationships are usually expressed in terms of the Nusselt number as a function of the Reynolds and Prandtl numbers.

The second number is the Biot (Bi) number, which represents the interaction between conduction within a solid and convection at its surface. The numerical value of Bi gives a direct indication of the relative importance of the conduction and convection processes during heat transfer. Usually, if Bi <1, the system can be modeled as a thin body model.

$$Bi = \frac{hL_b}{\lambda_b} \tag{4.2}$$

Then, the Grashof (Gr) number is a dimensionless number in fluid dynamics and is determined as the heat transfer relative to the ratio of the buoyancy to the viscous force acting on a fluid. The Gr frequently arises in the study of natural convection cases. In pipes, the number is defined as:

$$Gr = \frac{g\beta\left(T_s - T_{bulk}\right)D^3}{\nu^2} \tag{4.3}$$

where D (m) is the characteristic size, g ($m^2.s$) is the acceleration due to Earth's gravity, and β (K^{-1}) is the volumetric thermal expansion coefficient (i.e., equal to approximately $1/T$, for ideal fluids, where T (K) is absolute temperature). T_s and T_{bulk} are the surface and bulk temperatures, respectively, and ν is the kinematic viscosity.

The Prandtl number (Pr) is defined as the ratio between the kinematic viscosity (ν) and the thermal diffusivity (α) and is expressed as follows:

$$Pr = \frac{\nu}{\alpha} = \frac{C_p\mu}{\lambda} \tag{4.4}$$

In heat transfer problems, the Prandtl number expresses the relative thickness of the momentum and thermal boundary layers. When Pr is small, the heat diffuses very quickly compared to the transport of velocity (momentum). This number is introduced to obtain access to the correlation between the Reynolds and Nusselt numbers, for example, equation 4.5 shows a correlation [109] for laminar flows when Re< 1.

$$Nu = 1.64 * (Re * Pr)^{1/3} \tag{4.5}$$

Finally, the Peclet number (Pe) is the ratio of the thermal energy convected to the fluid to the thermal energy diffused within the fluid and is expressed as follows:

$$Pe = \frac{UL}{\alpha} = (Re \cdot Pr) \tag{4.6}$$

where L (m) is the characteristic length, U ($m.s^{-1}$) is the velocity and α ($m^2.s^{-1}$) is the thermal diffusivity. The heat transported by the fluid per unit area is proportional to ρC_p, while the heat conducted

per unit area is proportional to λ/L. This criterion is useful for quantifying convective phenomena by comparing the advection versus diffusion processes.

			$L \to \infty$	$L \to 0$
Nu	Convective heat transfer / Conductive heat transfer	$Nu = \frac{hL}{\lambda_f}$	Nu >1 Convective	Nu <1 Conductive
Bi	Convection at the surface / Conduction in a body	$Bi = \frac{hL_b}{\lambda_b}$	Bi >1 Temperature gradient Inside the droplet is important	Bi <1 Temperature inside the droplet is homogeneous

Figure 4.2: Asymptotic Nusselt and Biot analysis as a function of the droplet length (for 0 and $+\infty$)

In figure 4.2, it is important to observe the difference between the Nusselt and Biot numbers. Nu (equation 4.1) quantifies the convective heat transfer as function of the conductive heat transfer. In contrast, Bi (equation 4.2) provides a way to compare the conductive resistance to the convective resistance. This simple dimensionless analysis applies to small droplets (Bi<1) and establishes that the temperature inside the droplets is homogeneous, while the heat transfer is emitted by conductive exchanges (Nu<1). For larger droplets (Bi>1), temperature gradients occur inside the droplets, and diffusion takes place.

It is important to determine whether the convection is forced or natural. To do so, the ratio between the Gr and the Re numbers is used:

$$\frac{Gr}{Re^2} = \frac{g\beta\,(T_s - T_{bulk})\,D}{U^2} \tag{4.7}$$

- $Gr/Re^2 >> 1$ forced convection may be neglected
- $Gr/Re^2 << 1$ natural convection may be neglected

If the ratio is approximately one, then both forced and natural convection must be taken into account. The analysis expressed by equation 4.7 reveals that for a fixed inner diameter, as the speed of the flow

is increased, the natural convection contribution may be neglected; in contrast, as the temperature difference between the fluid and the bulk is increased, forced convection may be neglected. In our case, we are working under an isoperibolic boundary condition, so $T_s - T_{bulk}$ (the temperature difference between the surface (s) and the bulk) is very weak because the volume of the droplet is small (i.e., T_s). For a fixed inner diameter, the Gr/Re^2 relationship decreases as the mean velocity is increased. As a result, natural convection predominates with increasing mean velocity.

4.1.3 Dimensionless analysis of the isoperibolic millifluidic system

Conductive transport is driven by a parameter gradient, while convective transport is always accompanied by a volume flow rate with a certain mean velocity. Transfer flow is introduced for complex geometries and flow situations in which a boundary layer with thickness e determines the transport process and the transport coefficient includes all conductive elements. The Peclet number represents the ratio between the convective heat transfer, which is governed by the fluid velocity (U), and the thermal diffusivity (α). Additionally, when the thermal diffusivity α is considered, the thermal inertia of the material is observed, for example, a substance with a high thermal diffusivity becomes isothermal very quickly. A description of this thermal effect also defines the most useful dimensionless numbers, i.e., those that delineate the relative importance of the forces under static and dynamic conditions. Additionally, when working with multiphase flows, it has been demonstrated [8, 9] that the most important characteristic dimensions are the length of the plugs (L_s) and the channel diameter (D). Usually reported as the ratio L_s/D, this parameter (L_s/D) has been shown to significantly influence the heat exchange coefficient.

Some studies investigated the influence of slug length on the heat and mass transfer characteristics of the system. Table 4.1 summarizes the experimental variables of these studies. The focus of the two-phase experimental studies listed in table 4.1 is on the heat transfer of a bulk tube with an isothermal wall boundary condition, although the numerical studies show the local heat transfer rates. To date, few experimental studies have been undertaken to examine heat transfer in liquid−liquid systems. For this reason, the characteristic values of this work are summarized in table 4.2.

Even if our millifluidic configuration has a Biot number that is very low (Bi<1), assuming that the thin body approximation can be used, then a complete thermal model of the system can be performed.

	Horvath et al.[110]	Lakehal et al.[111]	Walsh et al.[7]
Parameter	Min - Max	Min - Max	Min - Max
L_G/D	1.6-20	1.92-6.1	0.45-0.8
L/D	260	40	1000
D	2.32 mm	1 mm	2 mm
Re	3-220	1396-2135	56.4-1127
Pr	1700	5.5	-
Pe	51,000-374,000	7678-11,472	-
Type	Gas-Liq	Gas-Liq	Gas-Liq

Table 4.1: Order of magnitude of the parameters in this work, as well as those available in the literature

	This work
Parameter	Min - Max
L_G/D	1-2
L_H/D	3-10
L/D	62.5 - 470
D	1.6 mm
Re	0.09-0.4
Pr	6.98-244
Pe	0.63-97.6
Bi	0.34-1
Gr	1-1000
Type	Liq-Liq

Table 4.2: Order of magnitude of the parameters in this work, as well as those available in the literature

4.2 From 3D numerical modelization to 1Dt analytical solution

4.2.1 3D numerical modelization of biphasic flow

The idea of this section is to numerically model the complete coupled problem of both the hydrodynamic and thermal effects. To do so, by using THETIS [2], we can generate the temperature fields resulting from the coupled phenomena based on a 3D numerical analysis, which must include the following:

- The local equilibrium of the fluid (the equation of state)
- The conservation of mass (continuity equation)
- The fundamental law of dynamics (the momentum balance equation)
- The conservation of energy (the energy balance equation)

[2] A collaboration with R. Guillaument on numerical modeling by using THETIS, a multi-fluid Navier Stokes solver developed by the I2 M-TREFLE CNRS laboratory at the University of Bordeaux 1

From a numerical point of view, the equation of state is strongly dependent on the nature of the fluid (i.e., the fluids viscosity, surface tension).

Then, after writing the Navier Stokes equations for each phase [112], where the connection of the velocity field at the interface is ensured (jump conditions are imposed on the velocity and the stress tensor [113]), the complete equation system can be solved. In this case, a numerical solution is needed to resolve the model and simulate the two-phase flows (involving separated phases), i.e., the characteristic interfacial length scale is larger than the smaller space step of the computational grid. From another point of view, it is assumed in this work that a unified flow model that is valid in all phases and at the interface can be defined. This single fluid, which is also called 1-fluid, based on the model of Kataoka [114], is widely used in problems involving three-dimensions and significant interfacial deformation. In this modeling framework, the two-phase flow representation is restricted to non-miscible, incompressible and isothermal fluids. Moreover, a constant surface tension is assumed. The required, valid jump equations at the interface [113] are directly integrated in the 1-fluid model by convolving the single-phase conservation equations using a phase function that describes the interfacial evolution over time through a material advection equation.

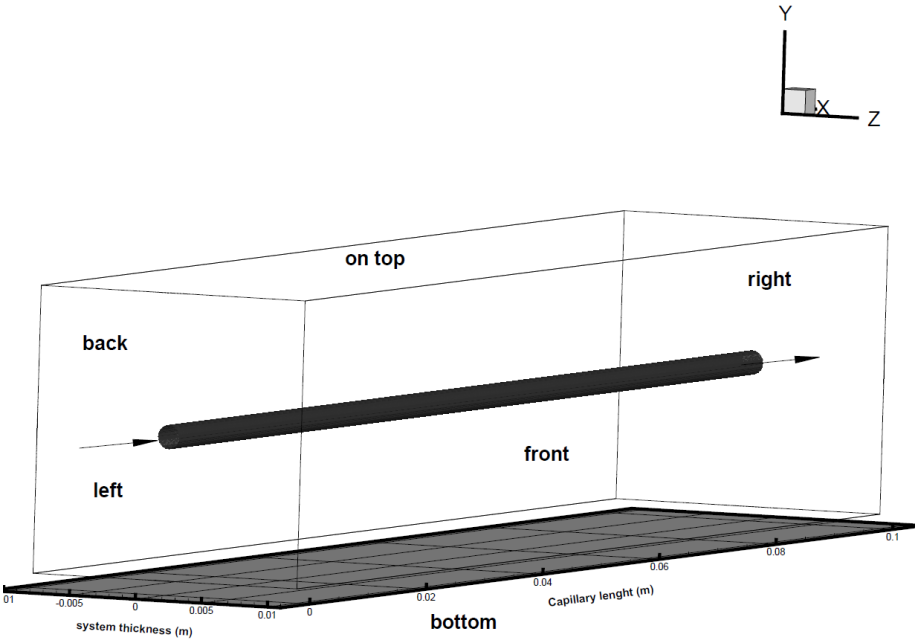

Figure 4.3: Scheme of the boundary conditions

The boundary conditions schematized in figure 4.3 are summarized in table 4.3.

To develop such a model, the use of 32 processors on a Xeon cluster SGI with MPI procedures is required, and the calculations are carried out over 1,000 hours. In figure 4.4, an example of the temperature field obtained at a given time is shown.

Equations	Boundaries conditions
hydrodynamics	Neumann conditions velocity of oil $6.02X10^{-3} m.s^{-1}$ velocity of water drop $18.8X10^{-3} m.s^{-1}$
energy	temperature limit on top is Fourier condition temperature limit right is adiabatic condition other limits are at a constant condition at $20°C$ temperature of oil $20°C$ temperature of water drop $30°C$ temperature domain initial is $20°C$

Table 4.3: Boundary conditions used for the 3-D numerical model

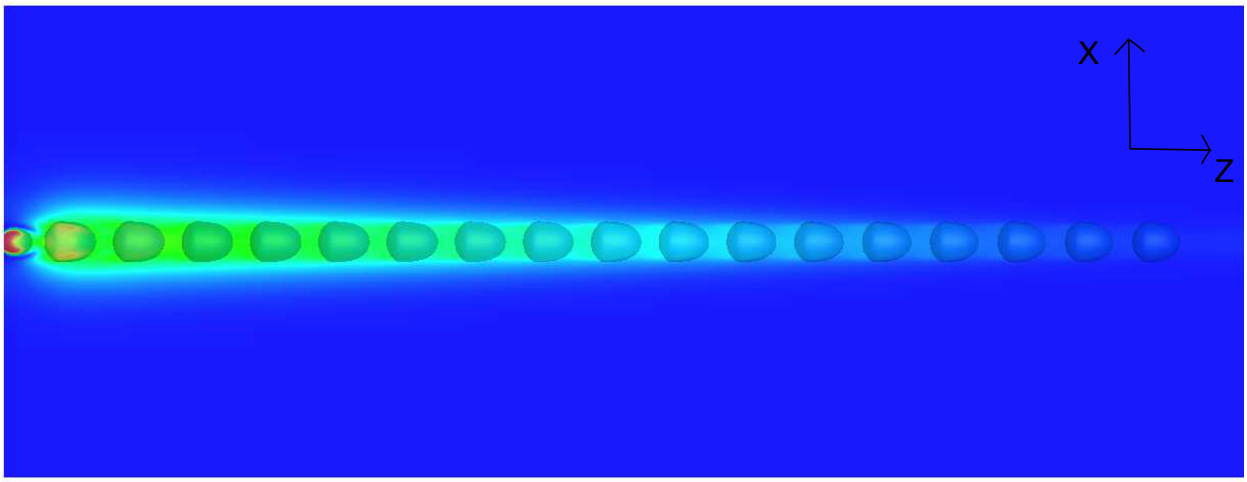

Figure 4.4: Droplet train obtained by performing 3-D numerical modeling along the z-axis at time t^k

4.2.2 The resulting hypothesis used to simplify the heat transfer model

The 3-D numerical model study offers the possibility to obtain a good overview of the global behavior of a biphasic system. When the fluid dynamics and heat transfer are coupled, the observed fields are functions of several parameters, such as the pressure, temperature and velocity. Thus, it becomes possible to assume a hypothesis to simplify the thermal model:

- From the 3-D analysis, it is possible to demonstrate that the temperature is homogeneous over the radius (r) direction, as illustrated in figure 4.5.
- The velocity stability already investigated in section 3.3.2 is confirmed by the 3-D numerical model. As illustrated in figure 4.6, it is important to note that the velocity field within the droplet suggests the presence of recirculation activity, while the velocity field within the oil phase reveals velocity fields that are closed to a plug flow (or piston flow).
- The isoperibolic boundary condition allows us to:

– Master the parietal heat losses around the channel.

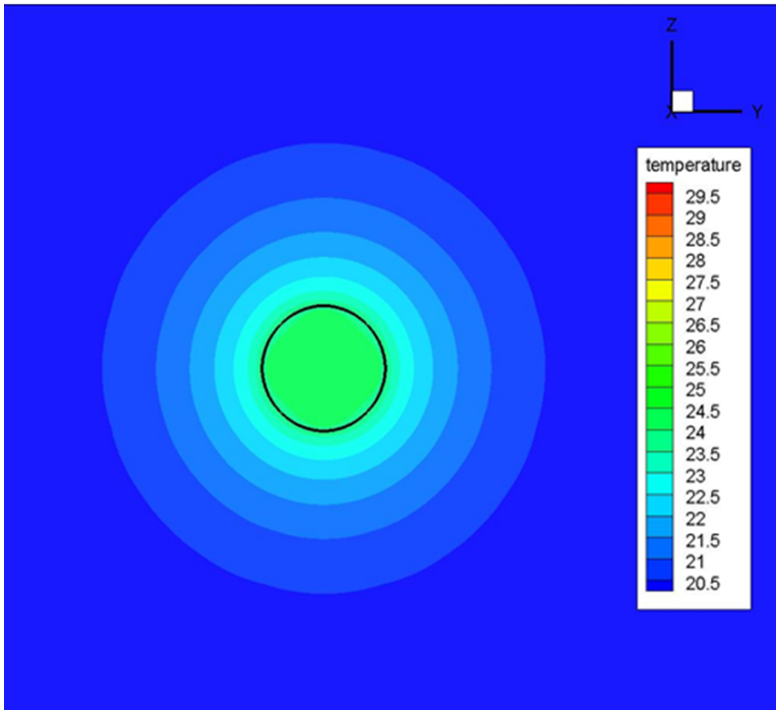

Figure 4.5: From the transverse temperature slice at z=1.6 cm relative to the reactor length, one can observe that the temperature is homogeneous along the radius.

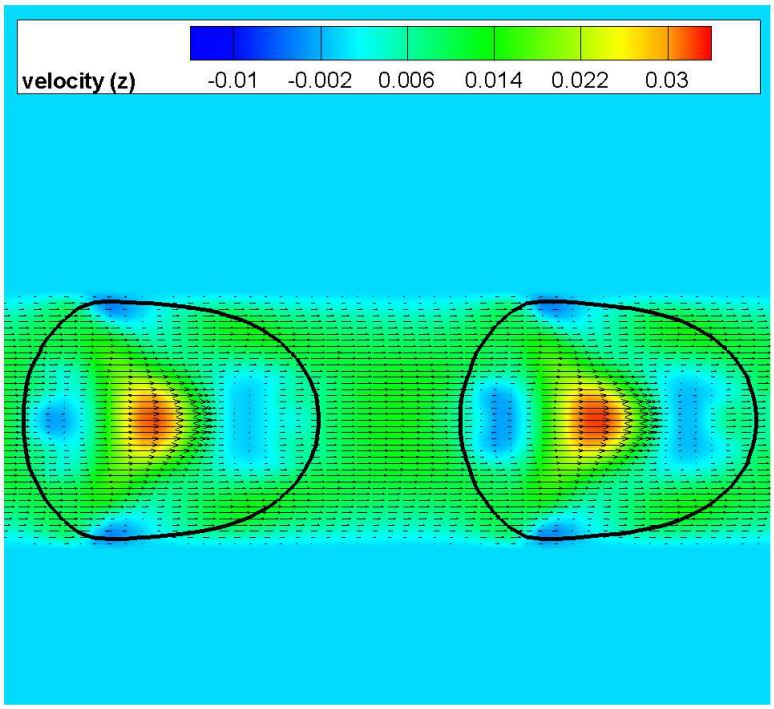

Figure 4.6: Droplet velocity field given by the 3-D simulation and the following boundary conditions in table 4.3

The complete model proposed here and schematized in figure 4.7 consists of a two-media system, composed of a half-plug of water and a half-plug of oil, assumed to be in perfect contact (here, the

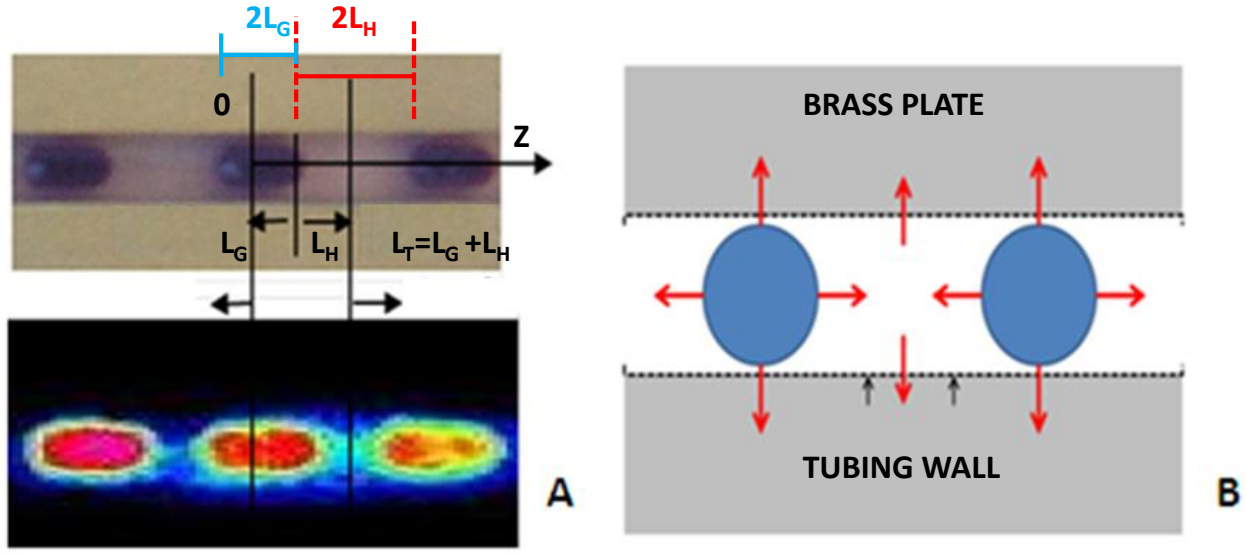

Figure 4.7: A. Visible and thermal images in the local coordinate system (Lagrangian) of one droplet-oil period. B. Schematic of the heat exchange between the droplet (water), the continuous phase (oil) and the wall (brass plate) trough the tubing.

total length of the oil and water is assumed to be $2L_G$ and $2L_H$). We assume that convective exchange occurs between each phase and the bulk (i.e., the isoperibolic condition) and that thermal diffusion takes place inside and between each media.

From a thermal point of view, we can assume that a 1-Dt analytical model of two diffusive media in contact in Lagrangian space is sufficient to represent the thermal behavior of this system. The temperature homogeneity in the r direction allows us to neglect the heat transfer along this direction. Moreover, the plug velocity profile of the continuous phase (i.e., the oil) is another important consideration that allows us to assume the problem in Lagrangian space. Then, recirculation inside the droplet also enhances the homogeneity of the temperature. This allows us to consider the droplet as a thin body. Moreover, due to the width of its length (i.e., depending on the flow rate ratio R), the oil can be taken as a thin fin. Finally, from all of these assumptions, a thin-fin two-media model can be used to approximate the global heat transfer in such a millifluidic and isoperibolic tubing-based system.

4.2.3 1-Dt analytical two-phase model in Lagrangian space

Taking into account the previous listed hypothesis, a biphasic flow performed in a millimetric isoperibolic device (schematized in figure 4.7) can be considered a 2-Dt axisymmetric two-layered periodic system (r,z,t). Because the goal of our study is to perform data processing to quantify the thermal behavior of the system of interest, the idea is to develop a simplified thermal model that sufficiently

represents the complete model. First, due to the very large ratio between the lengths of the biphasic plug versus the length of the tubing diameter, we assume that the temperature along the radial direction (r) is quasi-constant so that the thermal problem can be approximated in the z-direction alone. Consequently, the temperature measured over the entire channel is averaged in the r-direction to obtain T(z,t), as a function of space, z, and time, t.

With the representation shown in figure 4.7, we suppose that each medium has adiabatic flux boundary conditions due to problem symmetry (or periodicity). From this, the general heat transfer equation (transient thin fin approximation) of each medium can be expressed as follows:

$$\frac{\partial^2 T_i(z,t)}{\partial z^2} + \Phi(z,t) - H_i(T_i(z,t) - T_p) = \frac{1}{a_i}\frac{\partial T_i(z,t)}{\partial t} \tag{4.8}$$

Where:

$$\Phi(z = 0 \;\; to \;\; L_G, t) = \frac{\Phi_G(z,t)}{\lambda_G S\, dz}$$

and

$$\Phi(z = L_G \;\; to \;\; L_H, t) = 0$$

where T (K) is the temperature along the z-direction, H (m^{-2}) is the effective heat transfer coefficient between each medium and the bulk, and a ($m^2.s^{-1}$) is the thermal diffusivity of both fluids, where the index i can denote either the droplet (G) or the oil (H), and $\Phi(z,t)$ represents the heat source (in this study, the heat source is limited to the droplet, where the chemical reaction occurs).

$$\Phi_i(z,t) = \frac{\phi(z,t)}{\lambda_i S\, dz} \;\; and \;\; H_i = \frac{4h_p}{\lambda_i d} \tag{4.9}$$

The characteristic coefficient H ($W.m^{-2}.K^{-1}$) is defined by the convective heat exchange coefficient, the thermal conductivity λ ($W.m^{-1}.K^{-1}$) and the inner diameter d (m). The overall heat source $\Phi(z,t)$ is the heat source $\phi(z,t)$ divided by the thermal conductivity (λ) and the heat exchange surface S (m^2) over the selected section dz (m). The calculations are presented directly in Laplace space by using the following transformation:

$$\Theta_i(z,p) = \int_{t=0}^{t=+\infty} T_i(z,t) e^{-pt} dt \tag{4.10}$$

In equation 4.10, the integrated temperature in Laplace space for either the droplet (Θ_G) or the oil (Θ_H) is represented. Due to the isoperibolic condition, the temperature of the wall (T_P) is held constant. Equation 4.8 is rewritten in the Laplace domain by using the equation 4.10, as follows:

$$\frac{d^2\Theta_i(z,p)}{dz^2} - \frac{4h_p}{\lambda_i d}\left(\Theta_i + \frac{p}{a_i}\right) = -\frac{T_i(0)}{a_i} - \frac{4h_p}{\lambda_i d}\frac{T_p}{p} - \Phi(p) \tag{4.11}$$

Equation 4.11 is rewritten for each phase in the Laplace domain. First, the equation for the droplet is presented as follows:

$$\frac{d^2\Theta_G(z,p)}{dz^2} - \frac{4h_p}{\lambda_G d}\left(\Theta_G(z,p) + \frac{p}{a_G}\right) = -\frac{T_G(0)}{a_G} - \frac{4h_p}{\lambda_G d}\frac{T_p}{p} - \Phi(p) \tag{4.12}$$

Then, the equation for the oil plug is expressed as:

$$\frac{d^2\Theta_H(z,t)}{dz^2} - \frac{4h_p}{\lambda_H d}\left(\Theta_H(z,p) + \frac{p}{a_H}\right) = -\frac{T_H(0)}{a_H} - \frac{4h_p}{\lambda_H d}\frac{T_p}{p} \tag{4.13}$$

If we suppose:

$$\beta_i^2 = \left(\frac{4h_p}{\lambda_i d} + \frac{p}{a_i}\right) \;\; ; \;\; S_G(p) = -\frac{T_G(0)}{a_G} - \frac{4h_p}{\lambda_G d}\frac{T_p}{p} - \Phi(p) \;\; ; \;\; S_H(p) = -\frac{T_H(0)}{a_H} - \frac{4h_p}{\lambda_H d}\frac{T_p}{p} \tag{4.14}$$

The solution for the non-homogeneous ordinary differential equations 4.12 and 4.13 is given by:

$$\Theta_G(z,p) = Ae^{-\beta_G z} + Be^{\beta_G z} - \frac{S_G(p)}{\beta_G^2} \;\; ; \;\; \Theta_H(z,p) = Ae^{-\beta_H z} + Be^{\beta_H z} - \frac{S_H(p)}{\beta_H^2} \tag{4.15}$$

Thus, the boundary conditions, schematized in figure 4.7.A., are expressed in equations 4.16 to 4.19:

$$\frac{d\Theta_G(z,p)}{dz} = 0 \;\; at \;\; z = 0 \;\; and \;\; \frac{d\Theta_H(z,p)}{dz} = 0 \;\; at \;\; z = L_T \tag{4.16}$$

Rewriting the general solution for the droplet and applying the boundary conditions, the equation can be expressed as follows:

$$\Theta_G(z,p) = \Theta_{GO}(p) + A\left(e^{-\beta_G z} + e^{\beta_G z}\right) \tag{4.17}$$

The equation for the oil:

$$\Theta_H(z,p) = \Theta_{HO}(p) + B\left(e^{-\beta_i} + e^{\beta_i(z-2L_T)}\right) \tag{4.18}$$

The continuity of the temperature and the heat flux at L_G for the drop-oil interface is taken as:

$$-\lambda_G \frac{d\Theta_G(z,p)}{dz} = -\lambda_H \frac{d\Theta_H(z,p)}{dz} \text{ and } \Theta_G(L_G,p) = \Theta_H(L_G,p) \text{ at } z = L_G \tag{4.19}$$

With:

$$\beta_G = \sqrt{\frac{p}{a_G} + \frac{4\pi h_p}{\lambda_G d}} \text{ and } \beta_H = \sqrt{\frac{p}{a_H} + \frac{4\pi h_p}{\lambda_H d}} \tag{4.20}$$

Applying the boundary conditions to solve the temperature profile for each phase, we find the general solution for the droplet temperature profile from $z = 0$ to L_G:

$$\Theta_G(z,p) = \Theta_{G0}(p)(+\frac{\Theta_0 e^{-\beta_G(L_G-z)}}{(1-FE)(1+e^{-2\beta_G L_G})}(1+e^{-2\beta_G z}) \tag{4.21}$$

Applying the boundary conditions from $z = L_G$ to L_T (where $L_T = L_G + L_H$), the general solution for the oil temperature profile is:

$$\Theta_H(z,p) = \Theta_{H0}(p) + \frac{\Theta_0 FE e^{-\beta_H(z-L_G)}}{(1-FE)(1+e^{-2\beta_H L_H})}(1+e^{-2\beta_H(z-L_T)}) \tag{4.22}$$

Where:

$$F = \frac{\lambda_G \beta_G}{\lambda_H \beta_H} \text{ and } E = \frac{(1-e^{-2\beta_G L_G})(1+e^{2\beta_H L_H})}{(1+e^{-2\beta_G L_G})(1-e^{2\beta_H L_H})} \tag{4.23}$$

The initial temperatures are calculated according to the following expressions:

$$\Theta_{G0}(p) = \frac{T_{G0} + H_G \frac{T_p}{p} + \frac{\phi(p)}{\rho_G C_{pG} V_G}}{p + H_G} \quad ; \quad \Theta_{H0}(p) = \frac{T_{H0} + H_H \frac{T_p}{p}}{p + H_H} \tag{4.24}$$

$$\Theta^0 = \Theta_{H0} - \Theta_{G0} \tag{4.25}$$

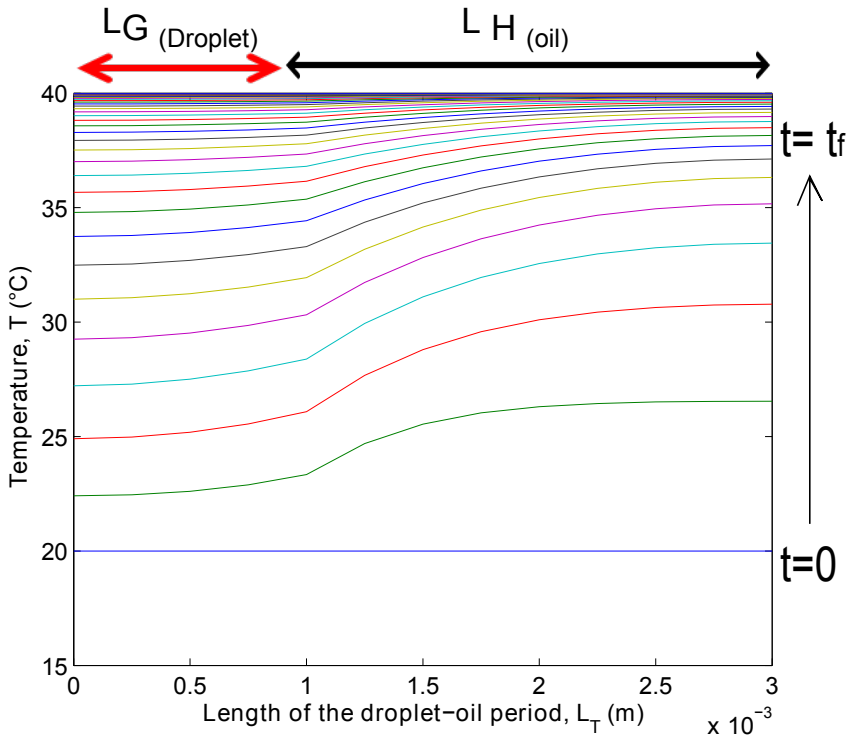

Figure 4.8: Calculated temperature profiles along the z-axis as functions of time for $T_G = 20°C$ and $T_H = 20°C$ when the imposed wall temperature is $T_P = 40°C$, for a given ratio of R=2 corresponding to the droplet oil length of L_G =1 mm L_H= 2 mm.

From the solutions expressed in equations 4.21 and 4.22, a numerical inverse Laplace transform in the time domain (t) is performed by using the Den Iseger algorithm [115].

Figure 4.8 shows the analytical solution of the temperature profile of the droplet-oil period ($L_T = L_G + L_H$), represented as function of space, corresponding to the period length. Then, due to heat transfer by convective-diffusion, each of the phases evolves differently according to its respective thermophysical properties. Figure 4.9 represents the temperature of each phase shown in figure 4.8 as a function of time. It can be observed that at the initial time of $t = 0s$, both phases have the same initial temperature; in contrast, at long times of $t = 50s$, both fluids tend toward the temperature of the plate $T_p = 40°C$.

Hence, this complete model takes in account the diffusive heat exchanges inside each medium, the interfacial diffusion between the droplet and the oil, and finally the convective heat exchanges between

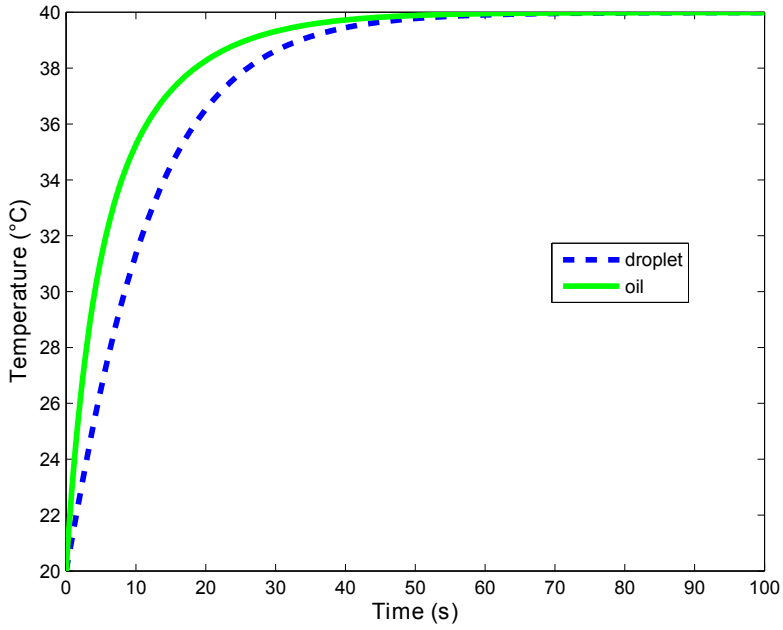

Figure 4.9: From figure 4.8, the average temperature profiles of each phase are represented over the z-direction as functions of time.

the liquid and the isoperibolic bulk.

The hypothesis assumed to simplify the thermal model is verified to be well-selected. It is demonstrated that a 1-Dt biphasic analytical model is sufficient to represent the heat transfer in such a complex system.

4.3 From the 1-Dt analytical model to the thin body approximation

4.3.1 Statement of the problem

This new vision of the problem is based on a thin body approximation. We propose a thermal approximation, based on a low Biot number (see table 4.2), which implies that the temperatures of both phases are spatially homogenous and that it is possible to work with the average temperature of each phase. As shown in section 3.4, the temperature measured by IRT can be decomposed into two components. To perform a parameter estimation, a sensitivity analysis is first performed, with the results reported in appendix B. From this study, two cases will be studied:

1. **The same inlet temperature for both phases ($T_{G0} = T_{H0}$) and a different temperature of the isoperibolic chip (T_p), as illustrated in figure 4.10**. This corresponds to a case that lacks a heat source.

2. **The same temperature between the oil and the isoperibolic chip ($T_{H0} = T_p$) and a different initial temperature of the droplet (T_{G0}). This case is very close to the chemical reaction inside the droplet, as illustrated in figure 4.11**

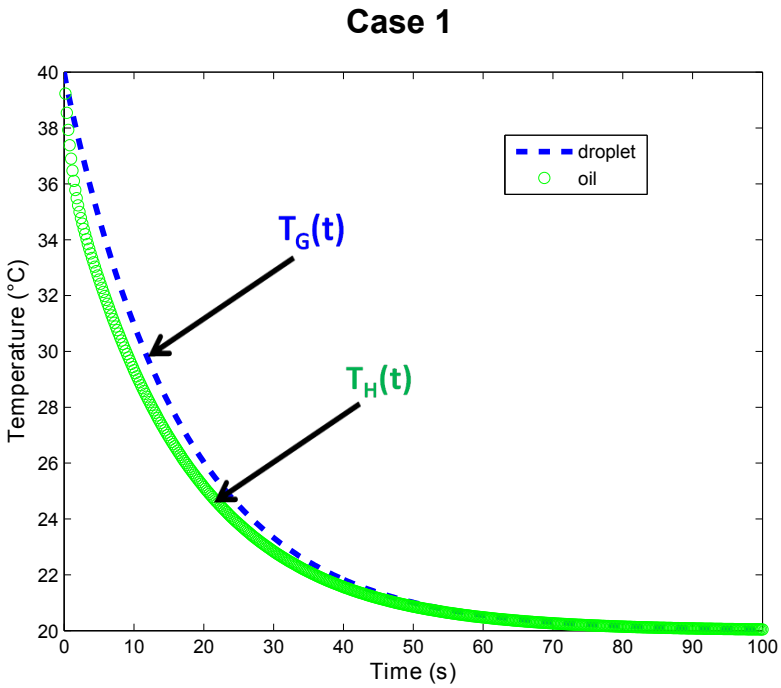

Figure 4.10: The initial temperatures of both media are the same, given by $T_{G0} = T_{H0}$=40°C, and the plate temperature is T_{G0} 20°C, for a given ratio of R=2 corresponding to the droplet oil length of L_G =1 mm L_H= 2 mm

The approach is to work within the local coordinates of the droplet-oil plug. Thus, two thermal models are proposed to analyze these cases:

- 2T thin body model and
- 1T homogeneous equivalent medium

4.3.2 2T thin body modelization

The main idea is to propose a simplified model by using an average temperature profile for each phase to model the diffusion at the interface of each phase by using a simple convective exchange. By applying this thin body hypothesis, the convective-diffusion equations 4.12 and 4.13 can be rewritten as a simple 2T thin body model:

$$\frac{dT_G(t)}{dt} = -H_{GP}(T_G(t) - T_P) - H_{GH}(T_G(t) - T_H(t)) + \Phi(t) \tag{4.26}$$

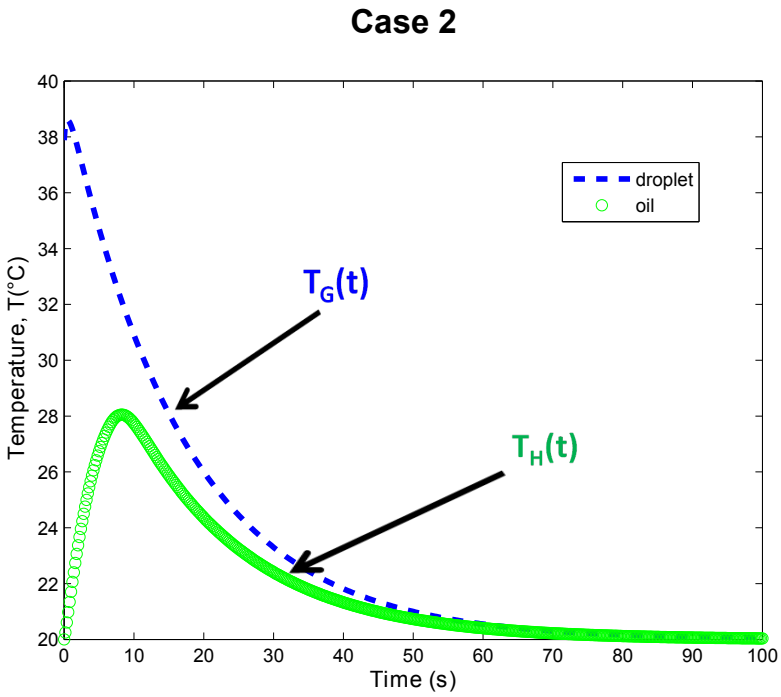

Figure 4.11: The initial temperatures of both media are the same, given by $T_p = T_{H0}$= 20°C, and the plate temperature is T_{G0}=40°C, for a given ratio of R=2 corresponding to the droplet oil length of L_G =1 mm L_H= 2 mm

$$\frac{dT_H(t)}{dt} = -H_{HP}(T_H(t) - T_P) - H_{HG}(T_H(t) - T_G(t)) \tag{4.27}$$

The temperature profiles of the droplet (T_G) and the oil (T_H) are averaged over the space, according to equation 4.28.

$$T_G(t) = \int_0^{L_G} = T_G(z,t)dz \;\; ; \;\; T_H(t) = \int_{L_G}^{L_T} = T_H(z,t)dz \tag{4.28}$$

Both equations are composed of two characteristic coefficients, noted as H. These coefficients are expanded into the equation 4.29, where the H coefficients are defined as the inverse of the characteristic time (s^{-1}) and are expressed as follows:

$$H_{GP} = \frac{h_P S_{GP}}{\rho_G C_{PG} V_G} \quad H_{GH} = \frac{h_i S_{GH}}{\rho_G C_{PG} V_G} \quad H_{HP} = \frac{h_P S_{HP}}{\rho_H C_{PH} V_H} \quad H_{HG} = \frac{h_i S_{HG}}{\rho_H C_{PH} V_H} \quad \Phi(t) = \frac{\phi(t)}{\rho_G C_{PG} V_G} \tag{4.29}$$

The equations are functions of the thermophysical properties of each medium, specified by the index G for the droplet, H for the oil, i for the interface and P for the wall. The H coefficients describe

the convective heat transfer interaction between the phases and/or the wall in accordance with the properties of each medium. This last assumption is based on the isoperibolic condition established by the bulk brass. The temperature inside the chemical reactor is a function of the heat transfer coefficient between the imposed temperature of the bulk brass and the inner diameter of the tube. The thermal characteristics are summarized in chapter 2 section 2.2. In appendix C, an investigation of the influence of the boundaries conditions on the thermal behavior is presented. An important aspect of our approach is the estimation of this coefficient because classical convective correlations are insufficient to represent this type of heat exchange. $\Phi(t)$ represents the heat source that is present only within the droplet (i.e., where the chemical reaction occurs).

By assuming that the geometric configuration of the flow can be taken as a cylinder, the H coefficients between the phases and the wall are reduced to functions of the inner diameter of the tubing, given as:

$$H_{i-P} = \frac{4h_p \pi d L_i}{\rho_i C_{Pi} \pi d^2 L_i} = \frac{4h_P}{\rho_i C_{Pi} d}$$

where i can be either the properties for the droplet or the oil. However, the H coefficients that describe the exchanges between the phases are influenced by the length of each phase:

$$H_{GH} = \frac{4h_i \pi d^2}{4\rho_G C_{PG} \pi d^2 L_G} = \frac{h_i}{\rho_G C_{PG} L_G}$$

and

$$H_{HG} = \frac{4h_i \pi d^2}{4\rho_H C_{PH} \pi d^2 L_H} = \frac{h_i}{\rho_H C_{PH} L_H}$$

Finally, equations 4.26 and 4.27 are solved in the Laplace domain according to the same Laplace transform as in equation 4.10, and the profiles of each phase (the oil and the droplet) are obtained:

$$\Theta_G(p) = \frac{(H_{GP}\Theta_P + T_G(0) + \Phi(p))(p + H_{HP} + H_{HG}) + (H_{HP}\Theta_P + T_H(o))H_{GH}}{(p + H_{GP} + H_{GH})(p + H_{HP} + H_{HG}) - H_{GH}H_{HG}} \tag{4.30}$$

$$\Theta_H(p) = \frac{(H_{HP}\Theta_P + T_H(0))(p + H_{GP} + H_{GH}) + (\Phi(p) + H_{GP}\Theta_P + T_G(o))H_{HG}}{(p + H_{GP} + H_{GH})(p + H_{HP} + H_{HG}) - H_{GH}H_{HG}} \tag{4.31}$$

With:

$$\Theta_P(p) = \frac{T_p}{p}$$

4.3.3 1T homogeneous equivalent media model

The first-order thermal behavior, which is also called the continuous component (CC), is modeled here (see section 3.4). From an analytical point of view, and due to the periodicity of the flow, this continuous component can be expressed as a spatially weighted average, calculated as a function of time between the two plugs (the oil and the water):

$$\overline{T_{CC}(t)} = \frac{L_G \int_0^{L_G} T_G(z,t)dz + L_H \int_{L_G}^{L_T=L_H+L_G} T_H(z,t)dz}{L_T} \tag{4.32}$$

In equation 4.32, it should be noted that the weighted average profiles derived from the second-order thermal behavior (equations 4.21 and 4.22) can be represented by a continuous component. Here, the idea is to show that this continuous component, which results from the weighted average equation 4.32, can be simply represented by an equivalent homogeneous medium expressed by a mixing law function of the volume fraction and the thermal property ratios of each phase. More precisely, in this approximation, only the parietal exchanges between this equivalent homogenous medium and the bulk would be taken into account. From this last assumption, a one-temperature thin body equivalent homogenous medium model can be expressed as follows:

$$(\rho C_P V)^* \frac{d\overline{T(t)}}{dt} = \phi(t) - h_p S \left(\overline{T(t)} - T_P\right) \tag{4.33}$$

where $\phi(t)$ represents the heat source, h_p ($W.m^{-2}.K^{-1}$) is the parietal heat exchange coefficient between the tubing and the isoperibolic boundary, and S is the heat exchange surface ($S = \pi d L_T, m^2$). $\rho C_P V^*$ defines the mixing law between the droplet and the oil phase, denoted by the suffixes G and H, respectively, and detailed as follows:

$$(\rho C_P V)^* = \rho_G C_{PG} V_G + \rho_H C_{PH} V_H = (\rho_G C_{PG} L_G + \rho_H C_{PH} L_H) S \tag{4.34}$$

where ρ ($kg.m^{-3}$) is the density, C_P ($J.kg^{-1}.K^{-1}$) is the specific heat and V (m^3) is the volume of each phase. The volume is defined by $S.L_i$, where S is the heat exchange surface between the phases

(i.e., the inner diameter), and L_i is the length of each plug (i=G for the droplet and i=H for the oil). Assuming that $W = h_p S$, equation 4.33 can be rewritten as:

$$\frac{d\overline{T(t)}}{dt} = \frac{\phi(t)}{(\rho C_P V)^*} - \frac{W}{(\rho C_P V)^*}\left(\overline{T(t)} - T_P\right) \tag{4.35}$$

Assuming that $H = \frac{W}{(\rho C_P V)^*}$, equation 4.35 can be rewritten as:

$$\frac{d\overline{T(t)}}{dt} = \frac{H\phi(t)}{W} - H\left(\overline{T(t)} - T_P\right) \tag{4.36}$$

The variable are summarized as:

$$W = h_P \pi d L_T \quad and \quad H = \frac{W}{(\rho C_P V)^*} \quad \Phi = \frac{H\phi(t)}{W} \tag{4.37}$$

If we assumed that:

$$\alpha = \frac{L_G}{L_H} \quad and \quad K = \frac{\left(\rho C_p\right)_G}{\left(\rho C_p\right)_H} \tag{4.38}$$

The characteristic coefficient H can also be expressed as:

$$H = \frac{h_P \pi d L_H (1-\alpha)}{\rho_H C_{pH} L_H (1 + K\alpha)} = \frac{h_P \pi d (1-\alpha)}{\rho_H C_{pH} (1 + K\alpha)} \tag{4.39}$$

From equation 4.36, the temperature profile for a single flow can also be represented as:

$$\frac{d\overline{T(t)}}{dt} = \frac{H\phi(t)}{W} - H\left(\overline{T(t)} - T_P\right) \quad \texttt{in this case} \quad H = \frac{W}{\rho_i C_{Pi} V_i} \tag{4.40}$$

Here, the suffix i represents the properties of the fluid (i.e., either the water or the oil).

- **Reflexion concerning the parietal heat exchange coefficient h_P**

The parietal heat exchange coefficient h_P is assumed to be known, or the coefficient can be estimated by applying a constant source (the calibration part discussion presented in section 5.1.1) into equation 4.36 in the Laplace domain:

$$(p + H)\overline{\Theta(p)} = \frac{H}{W}\phi(p) \tag{4.41}$$

Expression of the temperature profile over the time in the Laplace domain

$$\overline{\Theta(p)} = \frac{\frac{H}{W}\phi(p)}{p + H} \tag{4.42}$$

The Laplace transformation of the temperature profile:

$$T(t) = \frac{\phi(p)}{W}(1 - e^{-Ht}) \tag{4.43}$$

If equation 4.43 is evaluated at $t = 0$ and $T = 0$ (or at steady state), the relation ϕ/W is obtained, which demonstrates that the parietal heat exchange h_p coefficient can be experimentally measured when the injected power is known. This is demonstrated further in section 5.1.1.

- **Time to space correspondence**

Due to the absence of dispersion, the droplets move at a constant velocity (see chapter 3.3); from this point of view, it is possible to establish the time to space correspondence by using the relation $z = t.\bar{U}$. Here, z is the space, t is the time and $\bar{U}$ is the mean velocity. It is possible to change the variables in equation 4.36 to describe the temperature profiles as functions of space.

$$\frac{d\overline{T(z)}}{dz} = \frac{H\phi(z)}{W} - H\left(\overline{T(z)} - T_P\right) \tag{4.44}$$

In this case, the effective heat exchange coefficient H (m^{-1}) is defined as:

$$H = \frac{W}{(\rho C_P V)^* U} \; where: \; U = \frac{Q_T}{S} \tag{4.45}$$

where $\bar{U}$ is the mean velocity ($m.s^{-1}$), which can also be expressed as the ratio between the total flow Q_T ($m^3.s^{-1}$) and the inner section of the tube S (m^2). The following analytical solution is obtained in the Laplace domain:

$$\overline{\Theta_z(p)} = \frac{p\Theta_z - HT_P + \Phi(p)}{p(p + H)} \tag{4.46}$$

To develop the parameter estimation, two inverse methods are used:

- The first is based on the 2T thin body model.
- The second is based on the 1T homogeneous equivalent media model.

4.4 Inverse processing methods

For example, inverse problem methods are devoted to the estimation of thermal parameters, unknown initial or boundary conditions or unknown heat source terms. The latter problems are called inverse heat conduction problems (IHCPs). To resolve an IHCP, certain measurements are necessary to estimate the unknown parameters or functions. Such a procedure is based on an inverse formulation of the classical scheme of cause→effect. The latter is an ill-posed problem, where the obtained solution is highly sensitive to measurement error; in some cases, the obtained solution also might be non-unique. This means that the experimental design and the associated measurement procedure are the main factors contributing to the quality of the results. Further, a good model is also important for estimating the correlated parameters without introducing any bias due to model approximations.

4.4.1 2T thin body model inverse processing

We assume that the measured average temperatures of both media (the droplet and the oil) as functions of time at the observable (inlet data) of our problem. The principle is presented for the droplet (water) temperature profile, described by the equation 4.30, and then, the same methodology is applied for the oil profile. The main idea is to integrate equation 4.26 as a function of time and then to rewrite it as a matrix, to estimate the four parameters:

$$\begin{bmatrix} T_{G(1)} \\ \vdots \\ T_{G(N)} \end{bmatrix} = \begin{bmatrix} 1 & \int_0^{t_k} T_G dt & \int_0^{t_k} T_H dt & t_1 \\ \vdots & \vdots & \vdots & \vdots \\ 1 & \int_0^{t_N} T_G dt & \int_0^{t_N} T_H dt & t_N \end{bmatrix} \begin{bmatrix} T_{G(0)} \\ (H_{GP} + H_{GH}) \\ -H_{GH} \\ H_{GP} T_P \end{bmatrix} \tag{4.47}$$

where t_k is the experimental time, $k = [1 : N]$. N is the time base of the measurement. The equation 4.47 is written under the general linear form $Y = X.P$, where P is the parameter vector to be estimated, X represents the sensitivity matrix of the experimental measurements and Y is the observable of the system, that is, the noisiest data. The oil equation 4.27 can also be expressed with the same general

form. The Gauss Markov least squares method [116] is used to perform the parameter estimation by solving the least square problem:

$$P = ([X]^T [X]^{-1}) \cdot [X]^T Y \tag{4.48}$$

From the estimated parameters P, each characteristic coefficient (H) can be calculated, as well as the initial temperature of each medium ($T_H(0)$ and $T_G(0)$) and the imposed temperature of the wall (T_P). Additionally, the influence of the signal-to-noise ratio (SNR) is analyzed and reported in appendix D. When comparing an important SNR of 6.25 to that given by our experimental device, the IR camera (SNR=100), small estimation errors of the H coefficients ($< 3\%$) and the initial temperatures ($< 10^{-2}$) are obtained.

4.4.2 1T homogeneous equivalent media inverse processing

Here, equation 4.36 (with $\phi(t) = 0$ is integrated (equation 4.49) and written in matrix form (equation 4.50) for application to the proposed inverse method, used to estimate the H coefficient.

$$\overline{T(t)} - T_0 = -H \int_0^{t_k} (\overline{T(t)} - T_P) dt \tag{4.49}$$

$$\begin{bmatrix} T(t)_{(1)} \\ \vdots \\ T(t)_{(N)} \end{bmatrix} = \begin{bmatrix} 1 & \int_0^{t_k} T(t)dt & t_1 \\ \vdots & \vdots & \vdots \\ 1 & \int_0^{t_N} T(t)dt & t_N \end{bmatrix} \begin{bmatrix} T(t)_{(0)} \\ H \\ HT_P \end{bmatrix} \tag{4.50}$$

Equation 4.50 is written under the general linear form $Y = X.P$, where P is the parameter vector to be estimated, X represents the sensitivity matrix of the experimental measures and Y is the observable of the system, that is, the noisiest data.

4.5 Analytical Validation: Thermal behavior without heat source

The goal of this part is to validate the use of a “thin body approximation″ used to represent the complete analytical problem proposed in the previous modeling sections. In this first validation, the heat source is not taken into account, and both phases are taken to have the same inlet temperature

(the first case study mentioned in section 4.3.1; see figure 4.10). This case can also be explained using a schematic analogy from electronics, presented in figure 4.12.

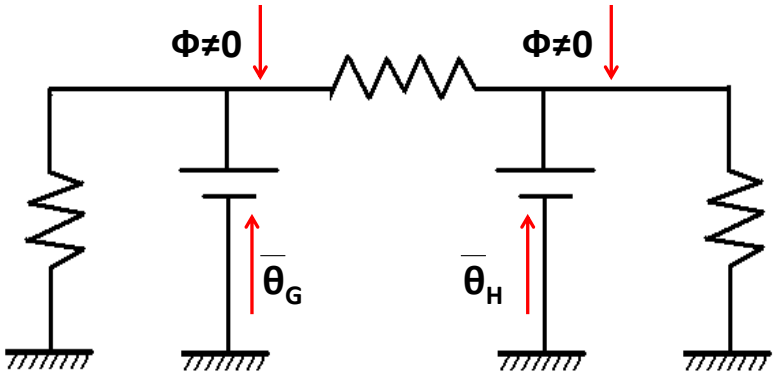

Figure 4.12: Electronics analogy of the heat exchanges that occur between both media when a constant heat flux is applied to the wall

In this electrical schematic, it can be noted that heat exchanges take place between both phases and the wall, specifically, when a constant heat flux is applied, represented by a resistance. Additionally, the media interexchange heat by thermal resistance. The thermal resistance between the media is a function the length and thermal diffusivity values of the media.

In summary:

- By applying a hypothesis, a simplified 1Dt complete model was expressed in Lagrangian space. This model takes into account both diffusive and convective heat transfers (equations 4.21 and 4.22) .
- A 2T thin body approximation with only convective heat exchange between each phase and the bulk, as well as between the phases, was proposed.
- A 1T homogeneous equivalent medium model (or continuous component, CC), in which only exchanges between the homogeneous media and the bulk are taken in account, was developed to represent the thermal behavior of the system. Here, the heat exchanges were estimated by applying a mixing law to the phases.

From these proposed analytical models, temperature profiles can be generated for validation. The proposed inverse methods are applied to the estimation of the H coefficients, and the resulting temperature profiles are illustrated in figure 4.13. These profiles can be compared to those generated using the 1-Dt Analytical model (see section 4.2.3).

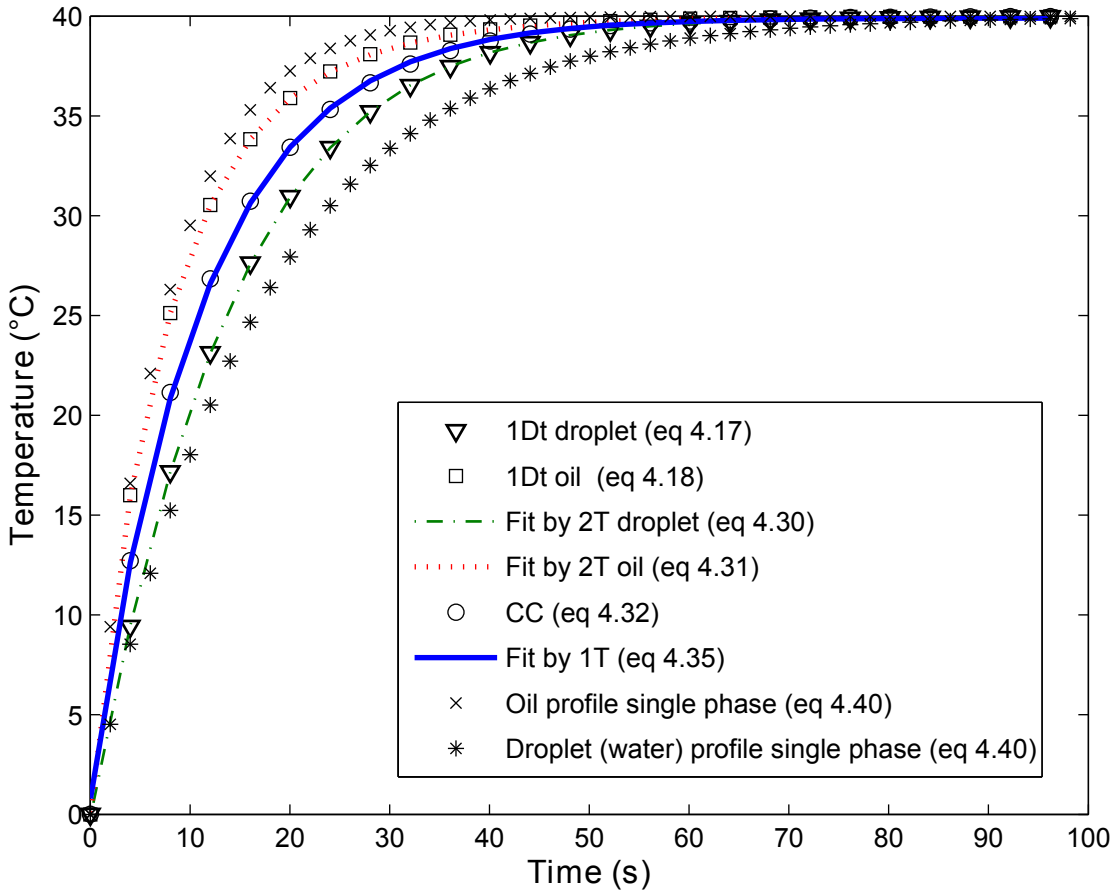

Figure 4.13: Temperature profiles generated by the equation depicted in the legend. Sufficient agreement between the complete model and the simplified model is obtained. The two edges of the curve arrays are the single-phase fluids (oil (x) and water (∗)). By applying the complete analytical solution, the oil and water profiles can be estimated, taking their lengths at R=4. Accordingly, the continuous component can be estimated.

From the generated temperature profiles in the validation illustrated in figure 4.13, the estimation of the respective heat exchange coefficients h depicted in equation 4.29 is found to have the following order of magnitudes h_p=150 $W.m^2.K$, and h_i=223.60 $W.m^2.K$

From figure 4.13, the validity of all of the simplified models is demonstrated. First, the thermal behavior of the oil and water phases (i.e., coflow) is represented. These two temperature profiles represent the upper and lower boundaries of the problem.

Figure 4.14 shows the residuals values, expressed as:

$$Res = \frac{T_{\texttt{complete}} - T_{\texttt{simplified}}}{T_{\texttt{max}} - T_{\texttt{min}}} * 100 \tag{4.51}$$

This equation can be calculated from the profiles generated by the equation 4.21 and 4.22 of the

complete models and can be estimated with the simplified models depicted in equations 4.30 and 4.31. For both the water and the oil, the representation errors are less than 0.5%. In contrast, the residual error expressed in equation 4.52 can be calculated from the average complete model in equation 4.32 and the equivalent model described by equation 4.36, which is either on the order of magnitude of 2%, or less.

$$Res = \frac{T_{\texttt{complete second order}} - T_{\texttt{first order}}}{T_{\texttt{max}} - T_{\texttt{min}}} * 100 \tag{4.52}$$

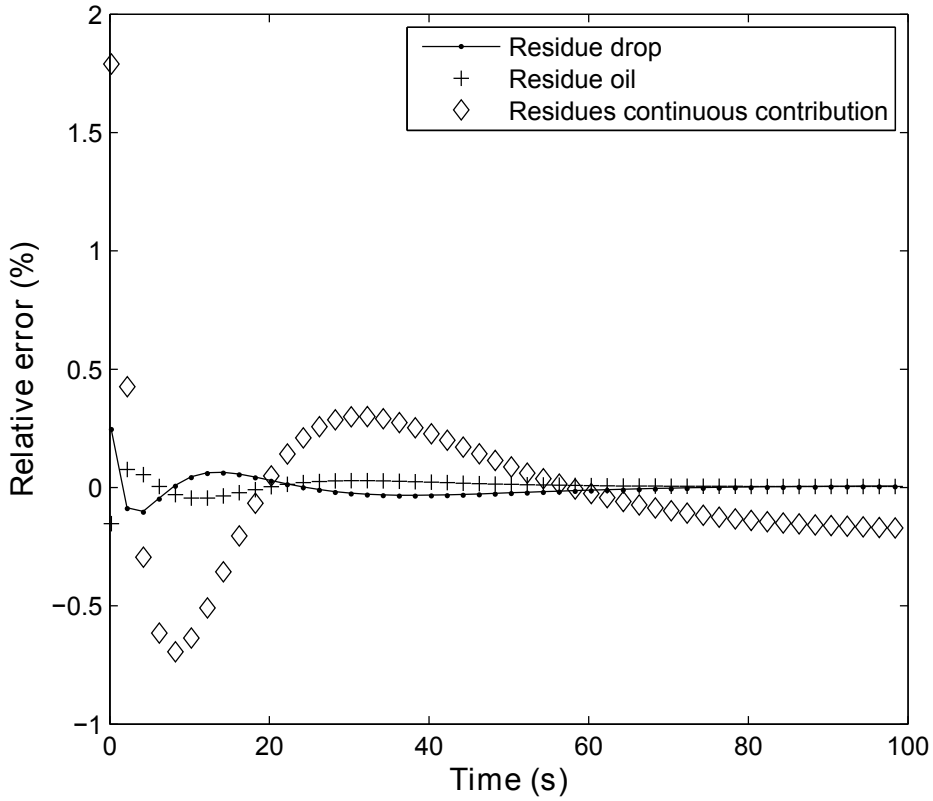

Figure 4.14: Residuals between the temperature profiles of each phase, calculated from the complete analytical model and simplified analytical models.

From these results, we demonstrate that the use of the 1-D homogenized thin body model induces a representation error that is less than 1% of the heat transfer behavior. Moreover, when using the 2-D thin body model, the induced error is negligible.

4.5.1 Mixing law

The previous validation was performed at a fixed α=L_G/L_H, when both phases have the same inlet temperature $T_{G0} = T_{H0}$, while the temperature of the plate T_p is different. Here, the strategy consists

of changing α to generate temperature profiles from the weighted average by applying equation 4.32. To change the lengths of the phases, the length of the droplet was fixed at L_G=1 mm, then the length of the oil plug was varied from R= 1 to 12. For better visibility in the graph, some of the generated flow rate ratios (R) are presented. The characteristic lengths of these profiles are summarized in table 4.4.

Ratio − >	1	3	5	7	10
$L_G(mm)$	1	1	1	1	1
$L_H(mm)$	1	3	5	7	10
$L_T(mm)$	2	4	6	8	11
Oil fraction	0.50	0.75	0.83	0.875	0.90

Table 4.4: The length of each phase for the given ratio (R), where L_T is the total length of the period, which is described by the sum of the length of each phase (L_H + L_G)

In figure 4.15, the synthetic profiles are shown. In this figure, the edges of the curves are bounded by the oil and water single-phase profiles. It should be noted that when the homogenous media is composed of 50% water and 50% oil, the thermal behavior (Ratio 1 plotted by o in figure 4.15) is placed in the middle of the two edges of the singles phase flows, which is a signature of the mixing law. When the flow is composed of 10% water droplets and the remainder, oil (R=10), the thermal behavior of the homogenous media is similar to that of oil alone.

Using the previously mentioned inverse process methodology, the characteristic coefficients are estimated for the biphasic flow ratios ranging from R=0.5 to 12 and are plotted in figure 4.16. On the abscissa at 1 and 0, the inverse of the H coefficients of water and oil in a single phase have been identified, respectively. The inverse of the characteristic coefficient (H^{-1}) from the mixing law decreases when the length of the oil plug is increased (i.e., the volume fraction of oil). This is the primary means by which the mixing law influences the heat exchange coefficient.

The characteristic coefficients (H) of the droplet flow were previously estimated, and it was demonstrated that the H coefficients can be predicted by the following relation:

Using the previously mentioned inverse process methodology, the characteristic coefficients are estimated for the biphasic flow ratios ranging from R=0.5 to 12 and are plotted in figure 4.16. On the abscissa at 1 and 0, the inverse of the H coefficients of water and oil in a single phase have been identified, respectively. The inverse of the characteristic coefficient (H^{-1}) from the mixing law decreases when the length of the oil plug is increased (i.e., the volume fraction of oil). This is the primary means by which the mixing law influences the heat exchange coefficient.

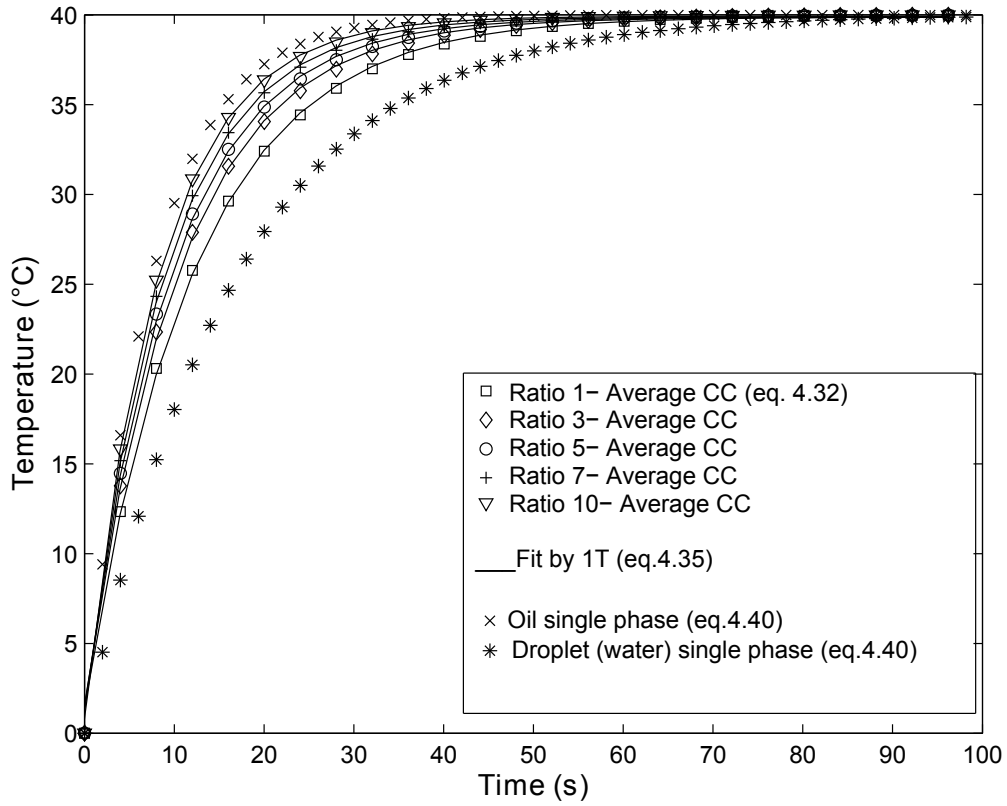

Figure 4.15: Continuous component profiles for a given total flow (Q_T) at different water-oil flow rate ratio, R.

The characteristic coefficients (H) of the droplet flow were previously estimated, and it was demonstrated that the H coefficients can be predicted by the following relation:

$$H = \frac{W}{(\rho C_P V)^* U} \tag{4.53}$$

With:

$$(\rho C_P V)^* = \rho_G C_{PG} V_G + \rho_H C_{PH} V_H = (\rho_G C_{PG} L_G + \rho_H C_{PH} L_H) S$$

The characteristic coefficient H reveals a strong dependence on the mixing law, defined by the thermophysical properties of both phases and the length of the plugs (L_G and L_H). Because the droplet length is greater than the oil length ($L_G \gg L_H$), the temperature profile exhibits a dynamic thermal behavior almost that resembles that of water alone; in contrast, when $L_G \ll L_H$, temperature profile exhibits a dynamic thermal behavior that resembles that of oil alone.

4.5.2 Estimation of the thermal physical properties: ρC_p

It is possible to measure the thermal properties of one phase when the other phase is assumed to be well known. To perform the thermal property estimation, the inverse of the characteristic coefficient derived from equation 4.44 can be represented according to the following formulation:

$$\frac{1}{H} = S \cdot u + O \; with: \; S = \frac{1-K}{K_0} \; ; \; O = \frac{K}{K_0} \tag{4.54}$$

With:

$$K_0 = \frac{\pi d h_p}{Q_T \left(\rho C_p\right)_H} \; ; \; K = \frac{\left(\rho C_p\right)_G}{\left(\rho C_p\right)_H} \; ; \; \alpha = \frac{L_G}{L_H} \; ; \; u = \frac{1}{1+\alpha} \tag{4.55}$$

Where:

$$u = \frac{1}{1+\alpha} = \frac{L_H}{L_T} = \texttt{volume fraction of oil} \tag{4.56}$$

where L_H and L_G (assumed to be well-known) are extracted from the visible image measurements (see section 3.3).

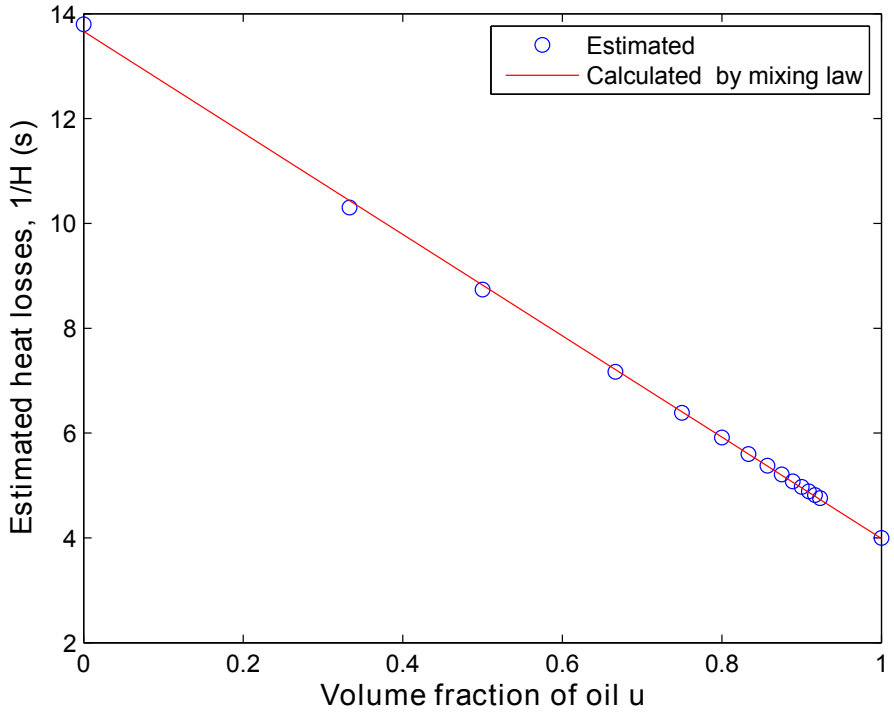

Figure 4.16: The estimated characteristic coefficients from the thermal profiles shown in figure 4.15 versus the oil volume fraction, indicated at the abscissa values of 0 and 1, respectively, for the H values of the water and oil single phase flows. The solid line represents the mixing law given by equation 4.53.

In conclusion, from a thermal point of view, diffusion can be totally neglected in this type of case. Then, due to the highly weak contribution of the fluctuating component, it becomes possible in a first approximation to only consider either the CC or homogenous equivalent model, in which the global thermal behavior of the system can be identified by only one characteristic coefficient H. In turn, this coefficient H can be represented by a mixing law function of the specific heat, density, volume fraction of each biphasic phase and the inner diameter of the tube. From the proposed mixing law, it is possible to estimate the thermophysical properties of one phase when the other is assumed to be known. This is further demonstrated by the experimental results presented in section 5.1.2.3

4.6 Analytical validation: The thermal behavior with a heat source

The goal of this section is to validate the source estimation. This case study is carried out under conditions of the oil and the isoperibolic chip possessing the same temperature ($T_{H0} = T_p$), while the droplet has a different initial temperature (T_{G0}). This case is illustrated in figure 4.17 and is very close to the case of a chemical reaction taking place inside a droplet. The chemical reaction can be viewed as a Dirac source, where only the relaxation is observed.

In figure 4.18, the temperature profiles are illustrated as functions of the space. These profiles reveal that when a heat source is added to the droplet, the heat exchanges between the oil plug and the droplet take place in a distinct manner relative to those previously shown. This case can also be explained using a schematic analogy from electronics, as shown in in figure 4.19.

In this electronic schematic, when the heat source is placed inside the droplet, the heat exchanges that occur between both phases can be simplified. This is true if we carry out a comparison with the previous analogy shown in figure 4.12. When initial temperature of the oil is precisely the same as that imposed on the wall ($T_{H0} = T_p$), the heat source is dissipated, and the heat transfers to the oil, as represented by the $\beta_H = \sqrt{(p/\alpha_H) + \left(4\pi h_p/\lambda_H d\right)}$ (which is derived from the analytical parameters 4.14).

An asymptotic analysis of these parameters can be proposed:

- If $p \to 0$ (i.e., $t \to +\infty$):

$$\beta = \sqrt{\left(4h_p/\lambda_H d\right)}$$

The oil behaves as a fin under steady state with a heat exchange characteristic length

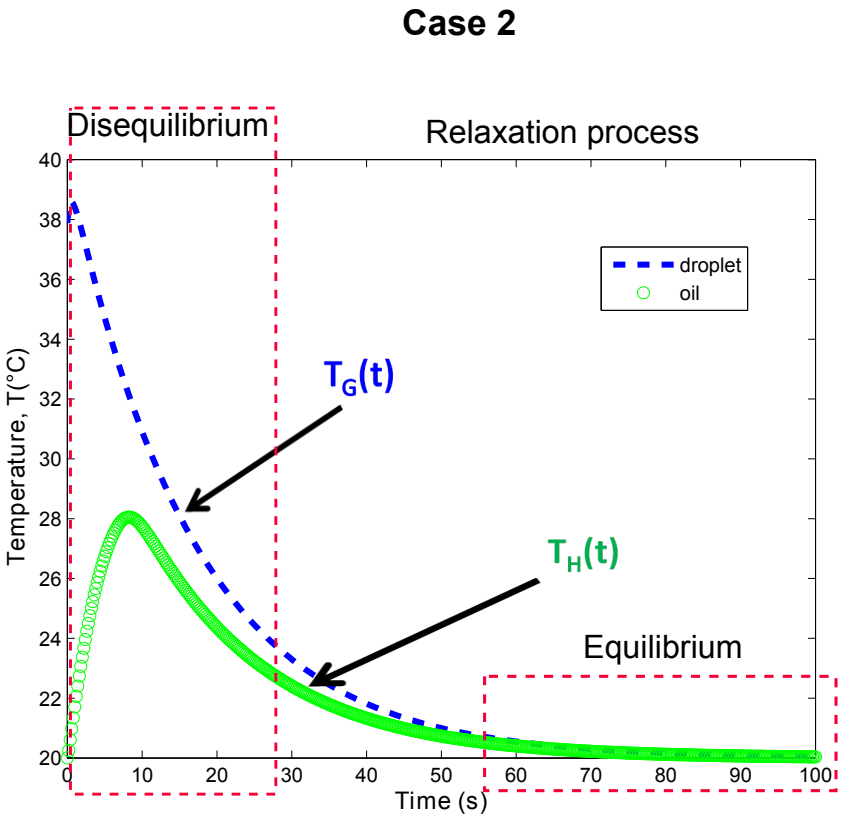

Figure 4.17: Temperature profiles of both phases as functions of time when $T_p = T_H = 20°C$. The initial temperature of the droplet T_G is different because a heat source exists inside, for a given ratio of R=2 corresponding to the droplet oil lengths of L_G =1 mm and L_H= 2 mm.

- If $L_H \to 0$ a characteristic thermal resistance (R_{ther}) can be expressed as:

$$R_{ther} = 3L_H/\lambda_H$$

- If $L_H \to +\infty$ a characteristic thermal resistance (R_{ther}) can be expressed as:

$$R_{ther} = \frac{\sqrt{d\lambda_H/4h_p}}{\lambda_H}$$

It should be noted that the characteristic length can be expressed as a limited length (L_{lim}), where the temperature of the oil is held constant and is equal to that of the wall (T_p). Figure 4.18 illustrates the case in which the length of the oil is important (at higher ratios of R), where the limited length (L_{lim}) can clearly be observed in figure 4.18. In section 3.3.2, the ratio lengths α are presented in figures 3.9 and 3.10.

From these considerations, and by assuming that the chemical reaction will be performed for the R

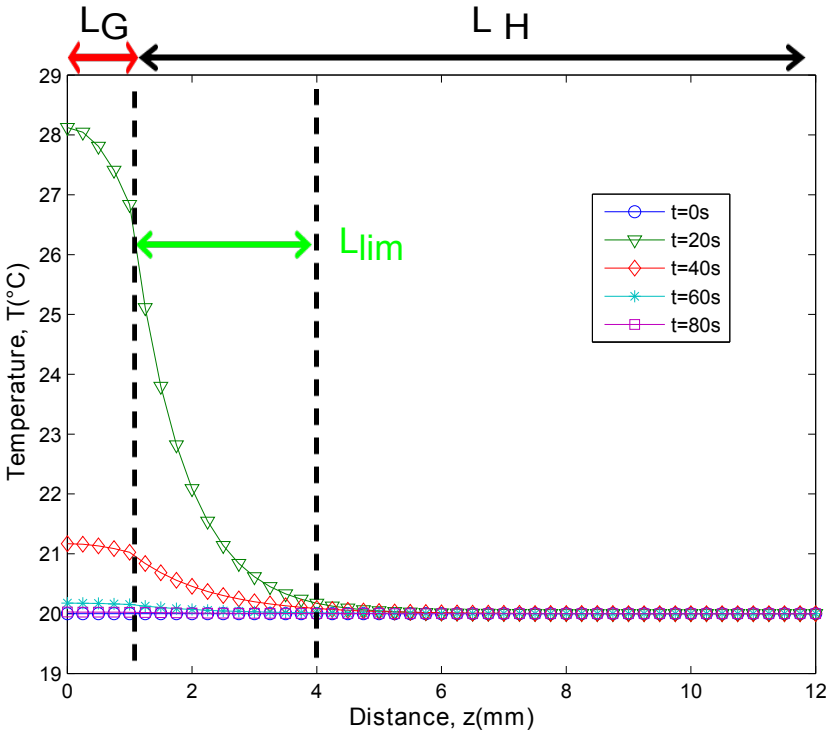

Figure 4.18: Calculated temperature profiles along the z-axis as functions of time when the oil and the wall have the same initial temperature $T_p = T_H = 20°C$. Here, a source is placed inside the droplet, so the initial temperature T_G is different. These droplet-oil profiles are derived for a flow rate ratio of R=12, where the droplet-oil lengths are L_G =1 mm and L_H= 12 mm.

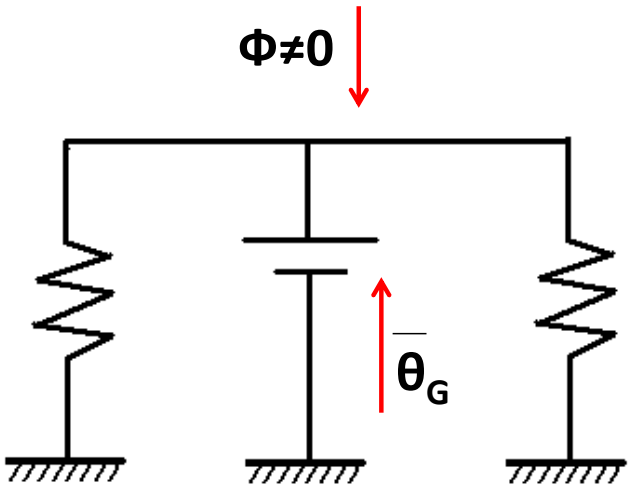

Figure 4.19: Schematic analogy from electronics of the heat exchanges that occur between both media and the wall, when heat flux exists inside the droplet.

ratio at which $L_H \ggg L_{lim}$, a new thermal model can be written:

$$(\rho_G C_{pG} V_G)\frac{d\overline{T_G(t)}}{dt} = \phi(t) - h_p S(\overline{T_G(t)} - T_p) - h_a S(\overline{T_G(t)} - T_H) \tag{4.57}$$

If we assume that $T_p = T_H$, the equation 4.57 can be rewritten as:

$$(\rho_G C_{pG} V_G)\frac{d\overline{T_G(t)}}{dt} = \phi(t) - h_{Gfin} S(\overline{T_G(t)} - T_p)) \tag{4.58}$$

Where:

$$h_{Gfin} = h_p + h_a \tag{4.59}$$

The h_{Gfin} coefficient is the effective heat exchange coefficient between the phases and the media. This heat exchange surface is defined as a function of the inner diameter and the droplet length L_G. Thus, the droplet temperature profile can be expressed as:

$$(\rho_G C_{pG} V_G)\frac{d\overline{T_G(t)}}{dt} = \phi(t) - h_{Gfin}(\overline{T_G(t)} - T_p) \tag{4.60}$$

$$\frac{d\overline{T_G(t)}}{dt} = \frac{\phi(t)}{(\rho_G C_{pG} V_G)} - \frac{h_{Gfin}}{(\rho_G C_{pG} V_G)}(\overline{T_G(t)} - T_p) \tag{4.61}$$

where:

$$H_{Gfin} = \frac{h_{Gfin}}{(\rho_G C_{pG} V_G)} \tag{4.62}$$

In this case, the previously proposed inverse processing methodology cannot be used for the estimation when a heat source exists inside the droplet medium. One way to estimate the characteristic coefficient H_{Gfin} is by the correlation methodology, which is presented in the next section as an estimation process.

4.6.1 Inverse method: development of the correlation method for simultaneous estimations

The correlation method is applied for the simultaneous estimation of the heat source and the heat losses. The inverse process depicted here is an alternative method to the Gauss Markov estimation presented in section 4.4. When a heat source is present in equation 4.61, the difficulty that develops

in the estimation resides in the evolution of the source term, which is correlated with the heat losses. To remove the heat loss information, it is important to detect the times during which only the heat source or the heat losses can be estimated. Our approach to solving this problem is to find a statistical estimator that can clearly detect the period at which the heat source is on and/or the heat losses are occurring. To detect this zone, the coefficient of correlation must be considered:

$$\rho^{F_t} = \frac{\sum_{F_t} \bar{T}^k \frac{d\bar{T}^k}{dt}}{\sqrt{\sum_{F_t} \bar{T}^{k^2}} \sqrt{\sum_{F_t} \frac{d\bar{T}^{k^2}}{dt}}} \tag{4.63}$$

where T is the mean temperature of the thin layer, $d\bar{T}/dt$ is the temporal derivative of the average temperature of the thin layer, and F_t is a temporal window of length $F_t = [k : k + lt]$, with k as the time step and lt as the length of temporal window. The correlation coefficient represents the normalized measure of the strength of the linear relationship between two variables [117]. In our case, and according to equation 4.61, the mean surface temperature of the thin layer and its time derivative are the two variables of this linear relationship, expressed as follows:

$$Y = aX + b \tag{4.64}$$

With:

$$Y = \frac{d\overline{T(t)}}{dt} \;\; ; \;\; X = \overline{T(t)} - Tp \;\; ; \;\; a = -H \;\; ; \;\; b = \phi(t) \tag{4.65}$$

The development of coefficient values close to 1 suggests that a positive linear relationship exists between the data columns. Coefficient values close to -1 suggest that one column of data has a negative linear relationship relative to another column of data (anti correlation). Coefficient values close to or equal to 0 suggest that no linear relationship exists between the data columns. In the case of our thermal model, if the correlation coefficient is close to -1, it is proof that the thermal model behaves linearly with an ordinate at the origin. That is, the heat source is ON. In contrast, if the correlation coefficient has a value close to 1, then the heat source is OFF. In the latter case, the heat losses related to the slope of figure 4.21 can be calculated with the formula:

$$H(t) = \rho^{F_t} . \frac{\sum_{F_t} \bar{T}^k \frac{d\bar{T}^k}{dt}}{\sqrt{\sum_{F_t} \bar{T}^{k^2}}} \tag{4.66}$$

To illustrated this method, an example generated from equation 4.64 with the parameters H and Φ is

proposed here. First, in figure 4.20, the resulting temperature profile from the imposed heat source is represented:

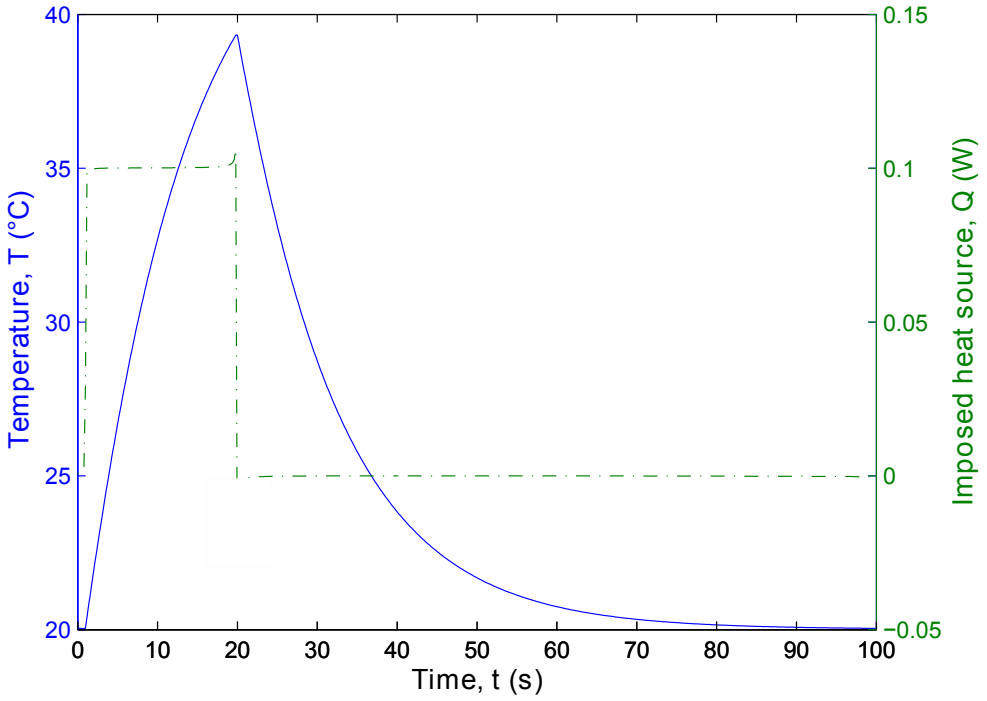

Figure 4.20: Temperature profile resulting from the imposed heat source, and the heat source profile.

By using equation 4.64, the time derivative can be plotted as a function of the temperature, as shown in figure 4.21.

In this case, when a square heat source is imposed, two linear behaviors can be clearly be observed, one passing through the zero origin ordinate, and the other with an origin ordinate. From this representation, we can distinguish the case in which the heat source is ON from the case in which the source is OFF. Nevertheless, to identify precisely the time-step at which the heat source develops, the correlation representation coming from equation 4.66 is better. As observed in figure 4.22 (where both the correlation coefficient and heat source are represented), by plotting the correlation coefficient as a function of time, the two zones corresponding to the time evolution of the heat source are clearly separated with values of the correlation coefficient equal to -1 when the heat source is ON, and 1, when it is OFF:

From prior knowledge of the exact zone in which the heat source is OFF, i.e., where only the heat losses are present, it is possible to use the relationship in equation 4.66 to estimate the H coefficient as a function of time. From a practical point of view, the resulting H coefficient is averaged over all time-steps, according to the following expression:

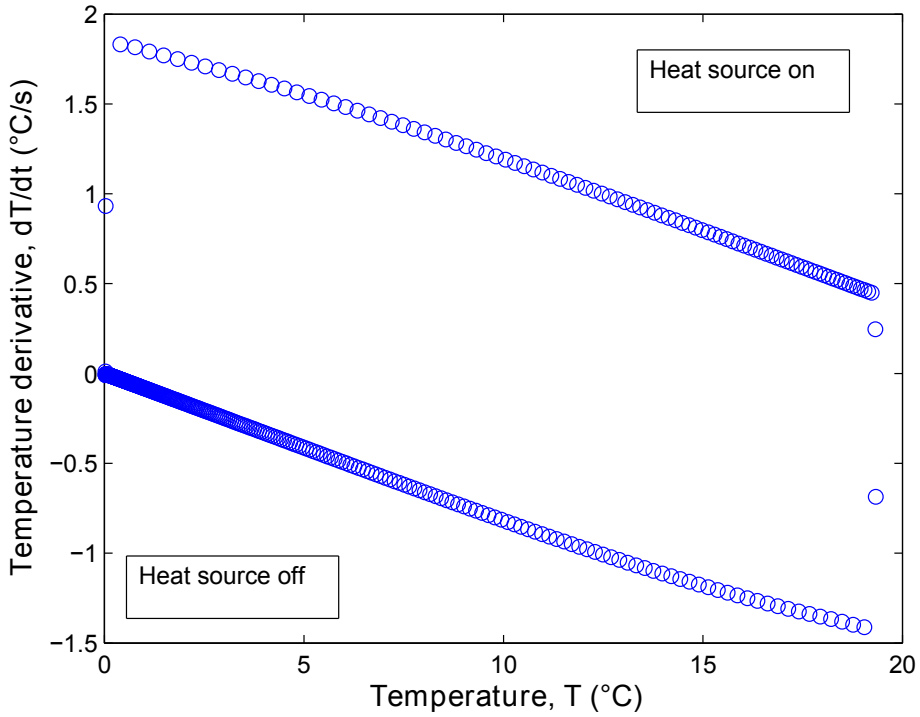

Figure 4.21: The time derivative plotted as function of the temperature (T-T_p)

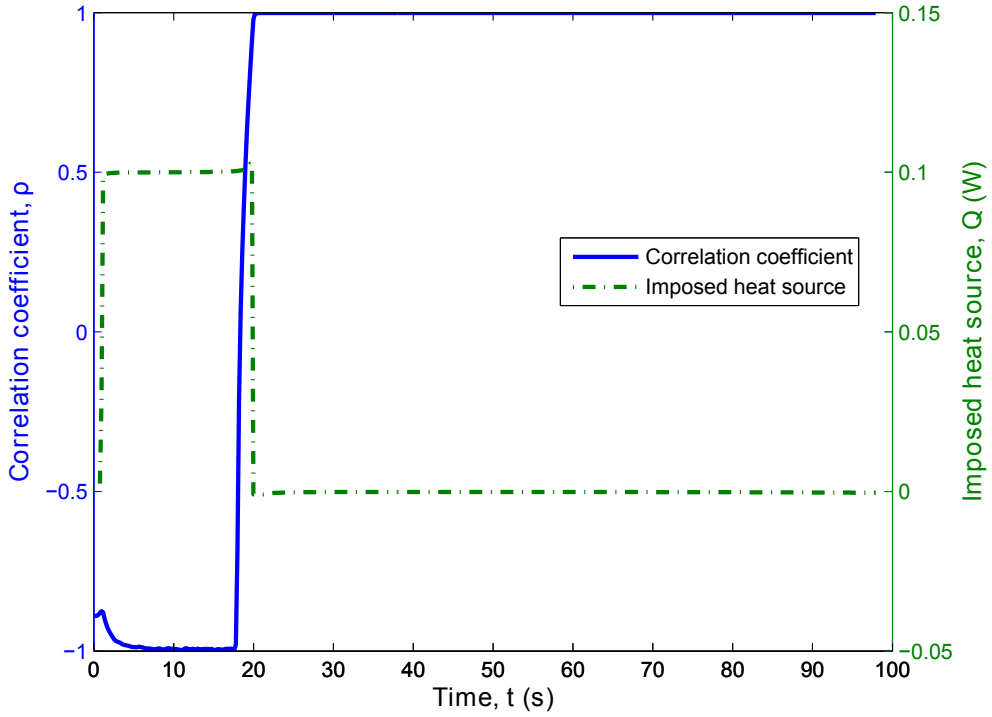

Figure 4.22: The correlation coefficient over time and the heat source profile over time are represented

$$\bar{H} = \int_{t_i}^{t_i+t_{cor}} H(t)dt \tag{4.67}$$

From prior knowledge of the heat losses, and by using equation 4.66, the imposed heat source can be determined. The result obtained in this case is represented in figure 4.23. The results show good agreement between the imposed and estimated heat sources:

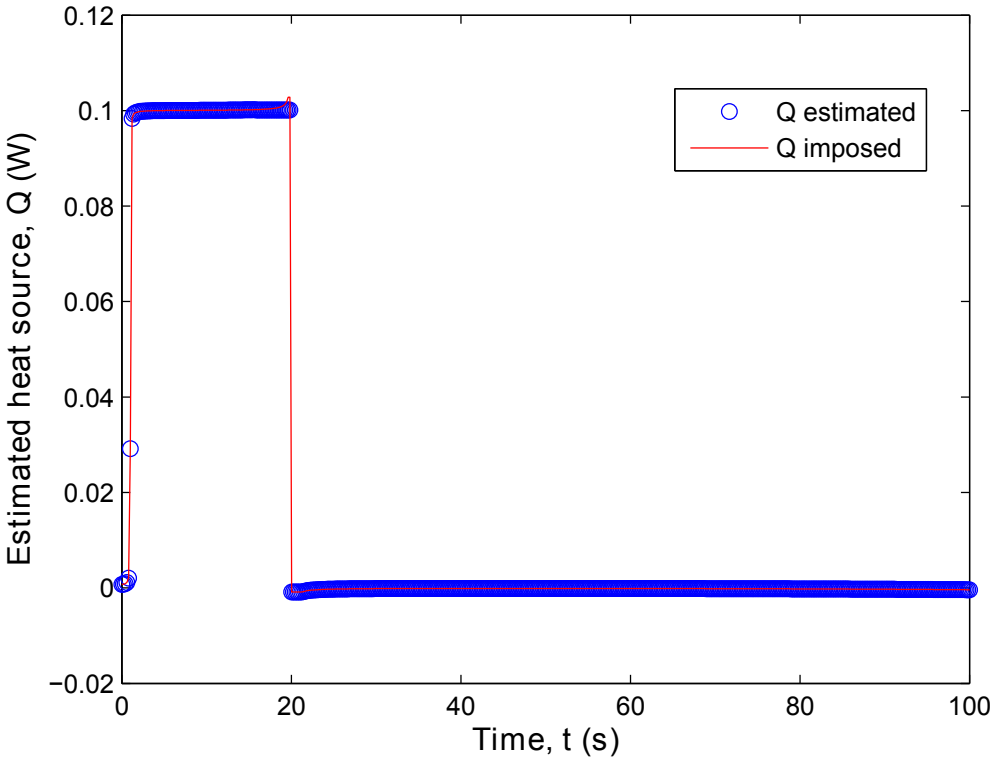

Figure 4.23: Estimate and injected heat source as function of time

Finally, the use of this correlation method for the inverse processing of temperature profiles in which both the heat source and heat losses are combined is a practical tool for the automatic detection of the presence of a heat source, which allows for the proper estimation of heat losses and the retrieval of the imposed heat source. The only drawback of this method is its sensitivity to the SNR. This problem is discussed in chapter D, in which the experimental results are treated.

4.6.2 Source estimation: Kinetics and enthalpy

In this validation section, a heat source is placed inside the droplet; in this case, the heat losses are estimated using the previously described method, after the heat source has been turned OFF. A step function heat source is added to the complete model, $\Phi(t) \neq 0$, as observed in equation 4.21. The heat source is applied to the droplet (i.e., a chemical reaction), and then the heat source is turned ON from 1 to 20 seconds. Due to the continuity of the temperature and the heat flux conditions (equation 4.19), this source also affects the oil plug profile. As previously shown, an average temperature profile is

created by the application of equation 4.32, here recalled as:

$$\overline{T_{CC}(t)} = \frac{L_G \int_0^{L_G} T_G(z,t)dz + L_H \int_{L_G}^{L_T=L_H+L_G} T_H(z,t)dz}{L_T}$$

For a given ratio (R), this behavior can be described by equation 4.68. The aim here is to estimate the heat source by applying equation 4.69. Then, by applying equation 4.70, the integral of the estimated heat source over time can be estimated and then compared to the integral of the injected heat source. From equation 4.61, and according to appendix E, the new system for the CC is given as:

$$(\rho C_p V)^* \frac{d\overline{T_{CC}(t)}}{dt} = \frac{\phi(t)}{(1+R} - h_p S(\overline{T_{CC}(t)} - T_p) \tag{4.68}$$

$$\phi(t) = \left[(\rho C_p V)^* \frac{d\overline{T_{CC}(t)}}{dt} + h_p S(\overline{T_{CC}(t)} - T_p)\right](1+R) \tag{4.69}$$

$$\Phi = \int_{t=0}^{t=end} \phi(t)dt \tag{4.70}$$

NOTE: The reported estimations of the source in figure 4.24 must be adjusted by multiplying the source by $(\rho_G C_{pG} V_G)(1+R)$. This procedure is detailed in appendix E. However, in figure 4.24, the observed differences in the rise and the descent may be induced primarily by the fact that the estimated heat source is overrun by the weighted average profile as the result of using a simplified model with only one convective exchange between the homogenous flow and the bulk. However, it is also important to note that the amplitude of the estimated source decreases as the ratio is increased.

A step source is applied to the droplet flow at different flow rate ratios of R ranging from 0.5 to 12. More precisely, the length of the droplet is fixed to 1 *mm*, and the length of the oil plug is increased.

- The heat source estimated from the equivalent homogeneous profiles (i.e., the CC, or continuous component, described by equation 4.71) is illustrated in figure 4.24.
- The heat source estimated from the droplet profile, as described by equation 4.61, is illustrated in figure 4.25.

In contrast, when the heat source is estimated from the droplet profile (described by equation 4.61)

at different ratios of R, the estimated source is in very good agreement with the injected source, as illustrated in figure 4.25. Here, the injected source is plotted with dashed lines, and solid lines represent the estimated source. Thus, the shapes of the injected and the estimated step sources are the same.

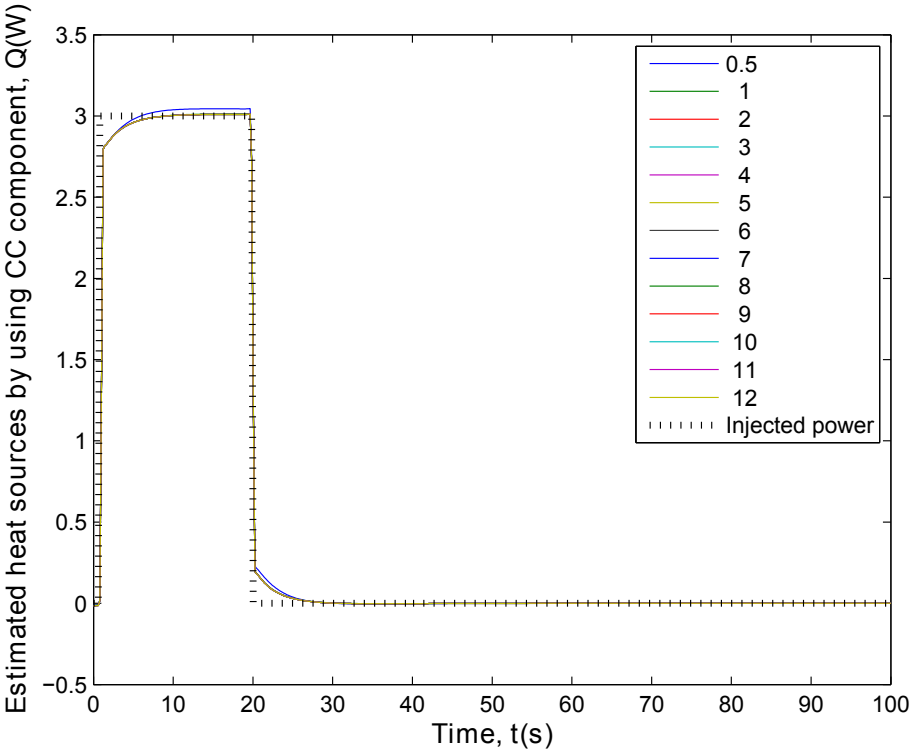

Figure 4.24: Injected power over time (black dashed lines) and estimated power from the equivalent homogenous profiles (CC) at different flow rate ratios (R) over time (solid lines)

From the adjustment presented in appendix E, the following equation is introduced 4.71:

$$\Phi(t) = \frac{\phi(t)}{(\rho_G C_{pG} V_G)(1+R)} \tag{4.71}$$

Additionally, it is possible to apply the previous correlation methodology to the estimation of the characteristic coefficient. According to the methodology, the resulting H coefficient is averaged over all time-steps according to equation 4.67. The estimation of the heat losses H (s^{-1}) for all flow rate ratios (R) is illustrated in figure 4.26. It is important to note that the estimated values from both profiles are almost the same, regardless of which heat source is estimated (either the CC or the droplet). The trends of both estimations are the same, e.g., the H coefficients remain constant beyond the given ratio of R=2.

Finally, the relative errors between the source profiles (injected and estimated) are calculated (see

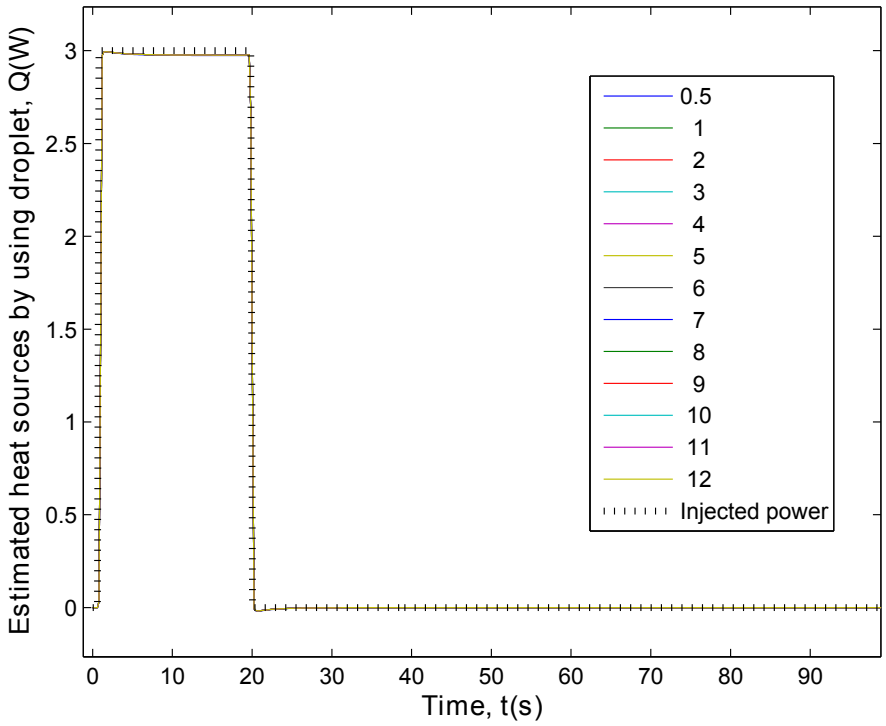

Figure 4.25: The injected power over time (the black dashed lines), estimated power from the droplet profiles at different flow rate ratios (R) over time (the solid lines)

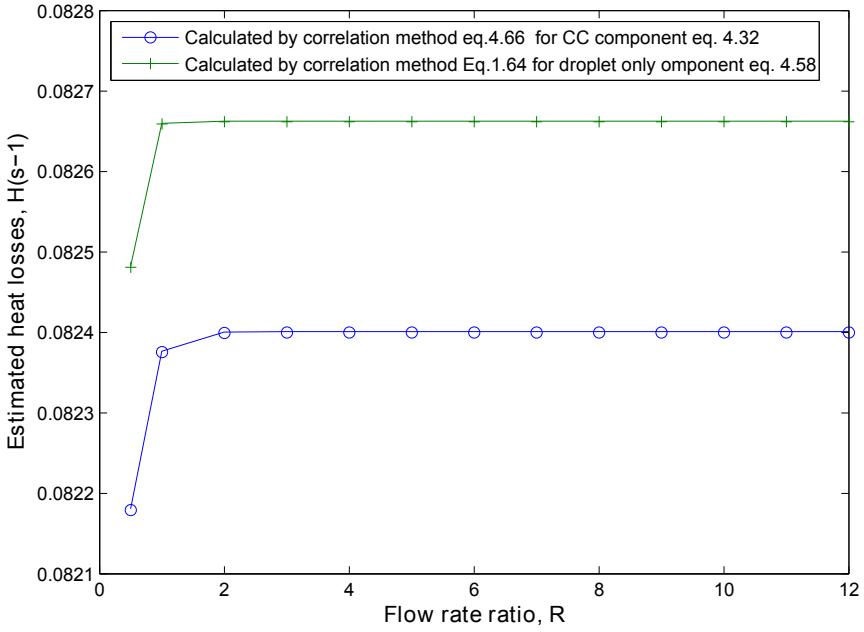

Figure 4.26: Estimation of the heat losses H (s^{-1}) for all flow rate ratios (R) for both cases. Estimation of the heat losses from the CC heat source estimation (equation 4.53) and from the droplet heat source estimation (equation 4.62)

E). The residuals demonstrate that when the heat sources are estimated from the droplet profiles, the estimation error is less than 1%. In contrast, when the heat sources are estimated from the equivalent

homogenous profiles (CC), the error is approximately 6%.

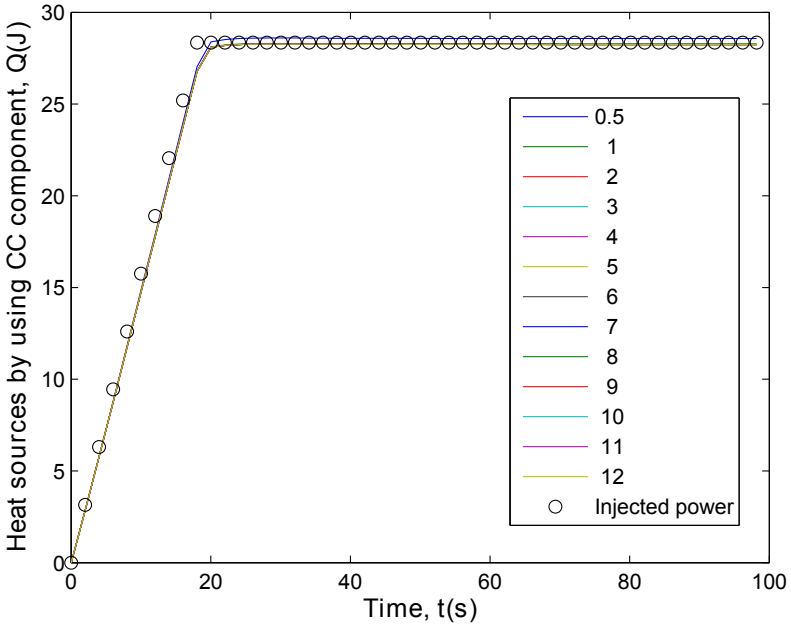

Figure 4.27: The integrated source over time is shown in black dots, and the integrated source over time from the CC component for each droplet flow at a given R.

From a practical point of view, it is easier to work with the CC profiles. Working with the equivalent homogeneous medium (CC) is faster in terms of data processing and in terms of the overall simplicity of image processing. In contrast, processing only the droplet profiles leads to a very accurate estimation but requires complex image processing techniques to obtain accurate droplet profiles. The heat source estimation enables the estimation of the chemical reaction enthalpies.

To estimate the kinetics of the chemical reaction, the source profiles in figure 4.24 are integrated over time. As a result, very good agreement between the input power and the estimated source can be observed, as shown in figure E.5. When the source profiles in figure 4.25 are integrated over time, good agreement between the input power and the estimated source can be observed, as shown in figure E.6. In this case, the integral shapes over time of the input and the estimated source are almost the same, while the integral value is exactly the same.

The integrated sources over time demonstrate that the estimations of the enthalpy (heat source) and kinetics (integrated source) can be made by using this methodology. It is now important to analyze the influence of noise on the previous estimations.

In appendix F, a study is performed to test the influence of noise on the estimation of the heat source profiles. The integrated noisy heat source profiles from the CC as functions of time show very good agreement between the input power and the estimated source at short time scales. However, at long

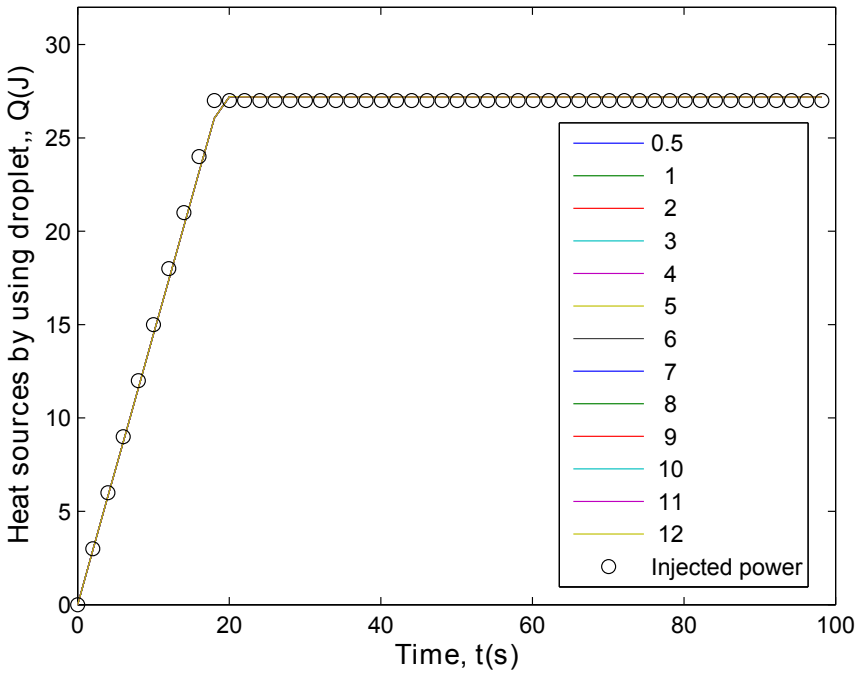

Figure 4.28: The integrated source over time is shown in black dots and the integrated source over time from the droplet profiles for each droplet flow at a given R.

time scales, the estimated profiles deviate. In contrast, the integrated noisy heat source profiles from the droplet heat source profiles are shown to be in good agreement with the integrated injected source profiles.

Integrating the sources over the time at which the noise is added demonstrates that the kinetics estimation can be performed by using this methodology.

4.7 Conclusion

In this chapter, the thermal effects present in a two-phase flow in an isoperibolic chip were modeled. A 3-D numerical model study was proposed to provide a global overview of the system when both the hydrodynamic and thermal effects are coupled in a biphasic systems. Consequently, from the 3-D study, several hypotheses were assumed to simplify the thermal model. A 1-Dt analytical model in Lagrangian space was proposed, in which convective exchange occurs between each phase and the bulk (i.e., the isoperibolic condition), and thermal diffusion takes place inside and between each medium, to represent the heat transfer in this complex system. From the thermal analysis, two thermal scenarios were explicitly identified:

1. **The same inlet temperature of both phases and a different temperature of the isoperibolic chip, i.e., the case without a heat source.**

2. **The same temperature between the oil and the isoperibolic chip and a different initial temperature of the droplet, i.e., similar to the case of a chemical reaction inside the droplet.**

These approaches were modeled by using two simplified analytical models based on the thin body approximation.

The "thin body approximation" was validated. The aim was to demonstrate that the proposed models were good representations of the first scenario. To do so, the complete analytical problem was developed without a heat source ($\Phi = 0$).

By validating the results, it was shown that the 1T homogenized thin body model induced a representation error less than 1% of the heat transfer behavior. Moreover, with the 2T thin body model, the induced error was negligible. Both models delivered good agreement with the behavior predicted by the 1-Dt thermal model.

From the first-order continuous component, the characteristic coefficients (H) were estimated. From this analysis, a mixing law was proposed for the prediction of H. The estimated values were compared to those calculated by the mixing law. It was shown that depending on the ratio of oil to water, H increases with increasing oil fraction and is always bounded by the values for pure water and oil. Additionally, it was shown that it is possible to measure the thermal properties ρC_p of one phase when the other is assumed to be well known.

To validate the second scenario, i.e., the case similar to a chemical reaction inside the droplet, a complete analytical problem was developed with a heat source ($\Phi \neq 0$).

Additionally, from the analysis of the thermal behavior with the heat source, it was noted that the heat exchanges are different and do not follow the proposed mixing law. This observation is due in part to the fact that the oil plug exhibits thermal fin behavior instead of thin body behavior. In this case, the correlation method was applied to estimate the characteristic coefficient (H). Then, it was demonstrated that the heat source can be estimated from the CC and the droplet profiles. This approach implies errors less than 6% and 1%, respectively. Additionally, when these sources were integrated over time with or without the addition of noise, the enthalpy and the kinetics could be estimated using this methodology. When the heat sources were estimated from the droplet profiles, the estimation errors were less than 2%; in contrast, when the heat sources were estimated from the equivalent homogenous profiles (CC), the errors were approximately 6%.

In reality, working with the equivalent homogenous medium (CC) is faster in terms of data processing and in terms of the simplicity of image processing. However, processing only the droplet profiles leads to very accurate estimations but requires complex image processing techniques to obtain precise droplet profiles.

The conclusions of this work demonstrate that no obstacles exist with respect to estimating heat sources in biphasic flows by applying the proposed methodology as a prior thermal calibration.

Chapter 5

Experimental validations and chemical applications

Abstract

The purpose of this chapter is to present the experimental validation and some chemical applications of the proposed novel non-contact calorimeter for the characterization of the kinetics and enthalpy of exothermic chemical reactions. The originality of this work lies in the application of a very simple model based on a homogenized thin body approximation model to the performance of calorimetry estimations. This novel calorimeter requires two calibration steps to estimate the heat losses of the system. Additionally this simplified model allows for an estimation of the thermophysical properties of one phase with an error less than 5%. The estimation of the heat source was validated using a well-known reaction (acid-base), for which the characteristic coefficients H (m^{-1}) for each flow rate ratio (R) were estimated by using the correlation method; as a result, the enthalpy was estimated with an error less than 2%. Additionally, the methodology used to estimate the mixing kinetics of the reaction was verified by a comparison between the thermal analysis (the heat source along the channel) and spectroscopy analysis (the evolution of the reaction intensity). Finally, we have shown through two chemical applications that this novel non-intrusive calorimetry technique based on millifluidics and IR thermography is a convenient and powerful tool for the characterization of chemical reactions performed in droplet flows.

5.1 Calibration of the isoperibolic chip

Device calibration is the most important step toward achieving the source estimation. During an ideal process of chemical reaction, the reagents are pre-heated to a given temperature. In this configuration, the oil phase, the reagents (T_{rx}) and the isoperibolic chip (T_p) have the same initial temperature at the inlet of the chip (z=0). In this case, the temperature profile is described only by the contribution of the heat released by the chemical reaction and the heat losses. That is, the temperature is described by the following equation:

$$\frac{d\overline{T_{rx}(z)}}{dz} = \Phi(z) - H\left(\overline{T_{rx}(z)} - T_P\right) \tag{5.1}$$

If we assume $T^*_{rx}(z) = \overline{T_{rx}(z)} - T_P$, then the difference between the time average measured temperature profile of the chemical reaction over the length of the reactor ($\overline{T_{rx}(z)}$) and the temperature of the wall T_p (note T_p is constant and equal to the initial value of $T_{rx}(z = 0)$). The temperature profiles are experimentally monitored by IRT and are measured in terms of the digital level (DL) in arbitrary intensity units. Equation 5.2 can be rewritten as:

$$\frac{d\overline{T_{rx}(z)}}{dz} = \Phi(z) - H\left(T^*_{rx}(z)\right) \tag{5.2}$$

If we assume the following relations:

$$W = h_P \pi d L_T \quad and \quad H = \frac{W}{(\rho C_P V)^* \bar{U}} \quad \Phi(z) = \frac{H\phi(z)}{W} \tag{5.3}$$

Then, equation 5.2 can be rearranged, and the thermal model of the system to determine the spatial heat source $\phi(z)$ is described as:

$$\phi(z) = \frac{W}{H}\left(\frac{dT_{rx}}{dz} + H(T^*_{rx}(z))\right) \tag{5.4}$$

where W ($W.DL^{-1}$) and H (m^{-1}) are the calibration coefficients and the heat loss characteristic length, and L is the total length of the chemical reactor (m).

5.1.1 Parietal heat transfer coefficient W

The parietal heat transfer is defined as $W = h_p S$ (previously presented in section 4.3.3). The heat transfer coefficient W is experimentally measured as the thermal resistance at the tubing interface and the isoperibolic chip.

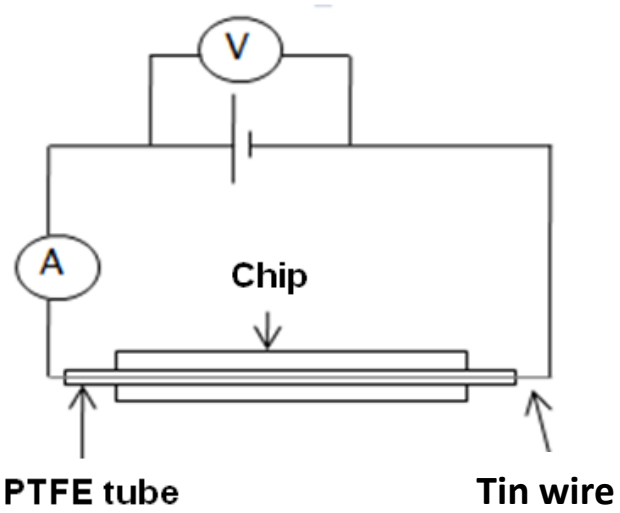

Figure 5.1: Schematic of the experimental set-up used to determine the thermal resistance at the tubing interface

This calibration allowed the heat source dissipated inside the tubing to be linked with the temperature measured at the surface of the tubing, for which the experimental set-up is schematized in figure 5.1. Accordingly, an electrically conductive tin wire is introduced inside the tubing channel. Then, the channel is filled with oil, and various electrical powers, ranging from 0 to 1 W, are applied to the tin wire. When steady state is reached as ($\frac{dT_{tube}(z)}{dz} = 0$), the temperature variation between the channel (T_{tube}) and the brass plate (T_P), which is fixed here at room temperature, is measured by the IR camera. Figure 5.2 shows a typical image when an electrical power is applied to the tin wire inside the tube. From these images, temperature profiles can be extracted by using image analysis techniques (see section 3.2); the extracted profiles are plotted in figure 5.3. In this configuration, equation 5.4 is simplified by assuming the relationship between the temperature measured at the surface of the tube and the injected power according to the following energy balance:

$$\phi = W\left(T^*_{tube}(z)\right) \tag{5.5}$$

where ϕ is the power dissipated by the Joule effect and W is the calibration coefficient ($W.DL^{-1}$). The value of $\overline{T^*_{tube}}(z) = \overline{T_{tube}} - T_P$, which is the difference between the average temperature profile of the tube at steady state and the temperature of the wall T_p, is assumed to be constant, where the

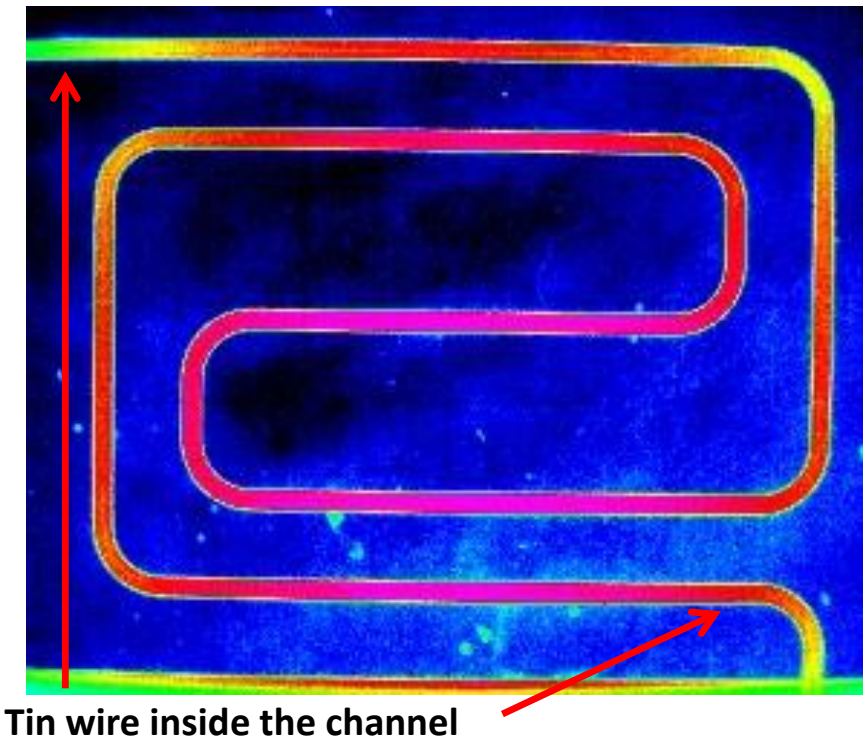

Figure 5.2: Infrared image of the serpentine chip during the calibration of the electric Joule effect. It is important to note that the wire twists when it is introduced inside the channel; additionally, it is very difficult to place the wire at the center of the TEFLON tube.

temperature profiles are measured in values of a digital level (DL), which is an arbitrary unit.

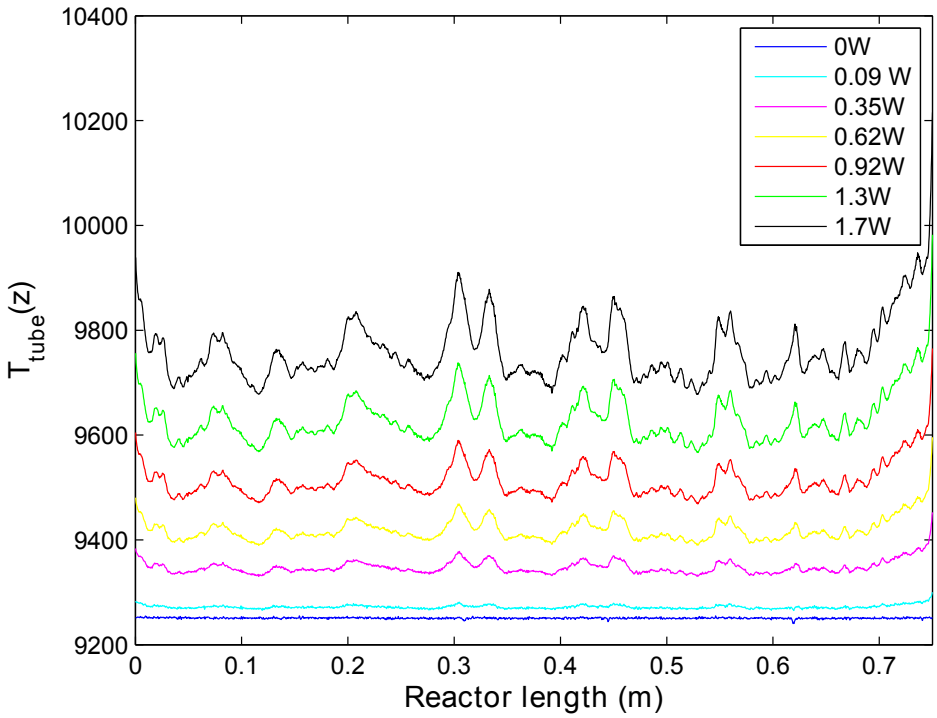

Figure 5.3: The temperature profiles (DL) along the channel when various electrical powers are applied to the tin wire inside a serpentine chip. It is important to note that the defaults along the channel are due to the bending of the serpentine chip and the twisted parts of the wire.

Figure 5.4 shows the linear relationship between the injected power and the temperature variation between the tubing and the plate, which is represented by equation 5.5. The relationship is linear, and the calibration coefficient $W = h_P \pi dL$ is given by the slope, W ($W.DL^{-1}$). This key parameter with respect to the heat losses due to the global thermal resistance of the tubing is calibrated by using this experimental approach.

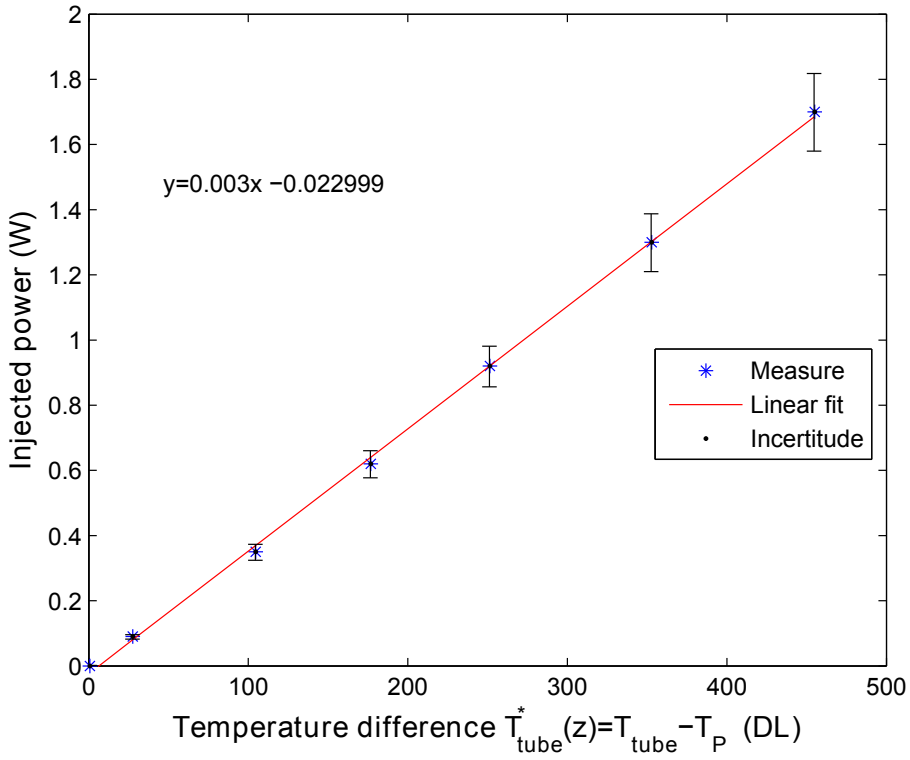

Figure 5.4: Relationship between the injected power versus the average temperature difference ($\overline{T^*_{tube}}$(z)) between the tubing ($\overline{T_{tube}}$) and the brass chip (T_p)

To determine the uncertainty of the calibration coefficient, W, a repeatability study was carried out for the two chips. Twelve measurements were performed for each chip. To highlight the dispersion of the results, the distribution function for the two series is represented by normalized values, calculated as:

$$Normalization = \frac{W - \bar{W}}{\sigma_W}$$

where W ($W.DL^{-1}$) is the estimated calibration coefficient, $\bar{W}$ ($W.DL^{-1}$) is the mean value of the experimental estimation and σ_W ($W.DL^{-1}$) is the standard deviation. In figure 5.5, the distribution of the results is represented by a normalized histogram.

Because the distribution is narrow, it is appropriate to calculate a mean value of these two series. The

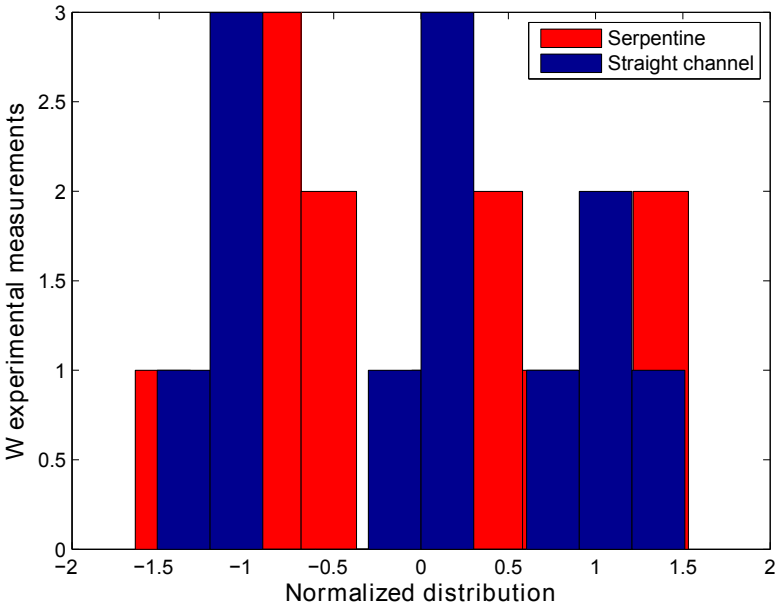

Figure 5.5: Distribution of the normalized results

experimental standard deviation σ is used to estimate the uncertainty of the measurements repeatability:

$$UR_{repeatability} = \frac{\sigma}{\sqrt{n}} \tag{5.6}$$

where n is the number of experimental estimations. Thus the relative uncertainty (the coefficient of variation) of the experimental value W is given by the following equation:

$$UR(\%) = \frac{UR_{repeatability}}{\bar{W}} * 100 \tag{5.7}$$

The results are summarized in table 5.1. The uncertainties of the repeatability are acceptable, that is, the experimental repeatability for the estimation of the calibration coefficient W is approximately 95%, so it is accurately estimated.

	Straight channel	Serpentine
Mean W ($W.DL^{-1}$)	1.2x10^{-3}	3.3x10^{-3}
Standard deviation ($W.DL^{-1}$)	2.316x10^{-4}	4.7314x10^{-4}
Uncertainty repeatability ($W.DL^{-1}$)	6.6856x10^{-5}	1.3658x10^{-4}
Relative incertitude UR(%)	5.8	4.17

Table 5.1: Uncertainty in the measurement of the W calibration coefficient for the isoperibolic chips used

5.1.2 Characteristic coefficients H

5.1.2.1 The continuous component (CC) without a source

To calibrate the effective heat transfer coefficients (H), it is necessary to assume $\Phi(z) = 0$ in equation **??** to be able to estimate the values of H by the following equation:

$$\frac{d\overline{T_{tube}(z)}}{dz} = -H\left(\overline{T_{tube}(z)} - T_P\right) \tag{5.8}$$

In this validation section, an experimental data set is fitted with the analytical solution 4.46 by the inverse methodology already proposed in equations 4.49 and 4.50. Thus, the characteristic coefficient (H) is estimated by applying the inverse method from the experimental temperature profiles (see section 4.6), and then, an analytical temperature profile is generated with the H coefficient by applying equation 4.46.

⋙ Experimental procedure

A droplet train is generated by using a syringe pump, thus it is possible to easily master the flow rate ratio (R) between the continuous phase (oil) and the droplet (water) phase (see section 3). Thus, for a given total flow (Q_T), several flow rate ratios (R) were applied, the details of which are listed as:

- Water with blue dye (from Sensient Cosmetic Technologies, at the concentration of 0.01 mM)
- Continuous phase IKV 32 fluorinated oil
- A total flow rate of Q_T= 20 mL.h^{-1}
- Flow rate ratios ranging from R = 0.5 to 9
- Use of a 20-mL syringe for the oil and a 5-mL syringe for each reagent
- Use of a straight channel with the bulk brass chip temperature imposed at T_p=30°C
- An inlet temperature of the oil and water that was specified as room temperature

In figure 5.6, the temperature profiles of the droplet flow under the listed conditions are shown. Additionally, the temperature profiles for both the water and the oil alone in the coflow at the same total flow are plotted. The temperature gap between the brass plate and room temperature is taken to be approximately 10°C; this temperature difference is important to obtaining a good signal-to-noise ratio. When steady state is reached, a sequence of IR images is taken. Image processing is applied to extract

the temperature profiles of the channel (see section 3.2). In figure 5.6, the tubing temperature (T_{tube}) is plotted versus the time (i.e., the residence time inside the tubing). The profiles are normalized as follows:

$$\texttt{Normalized temperature} = \frac{T_{tube} - T_{min}}{T_{max} - T_{min}}$$

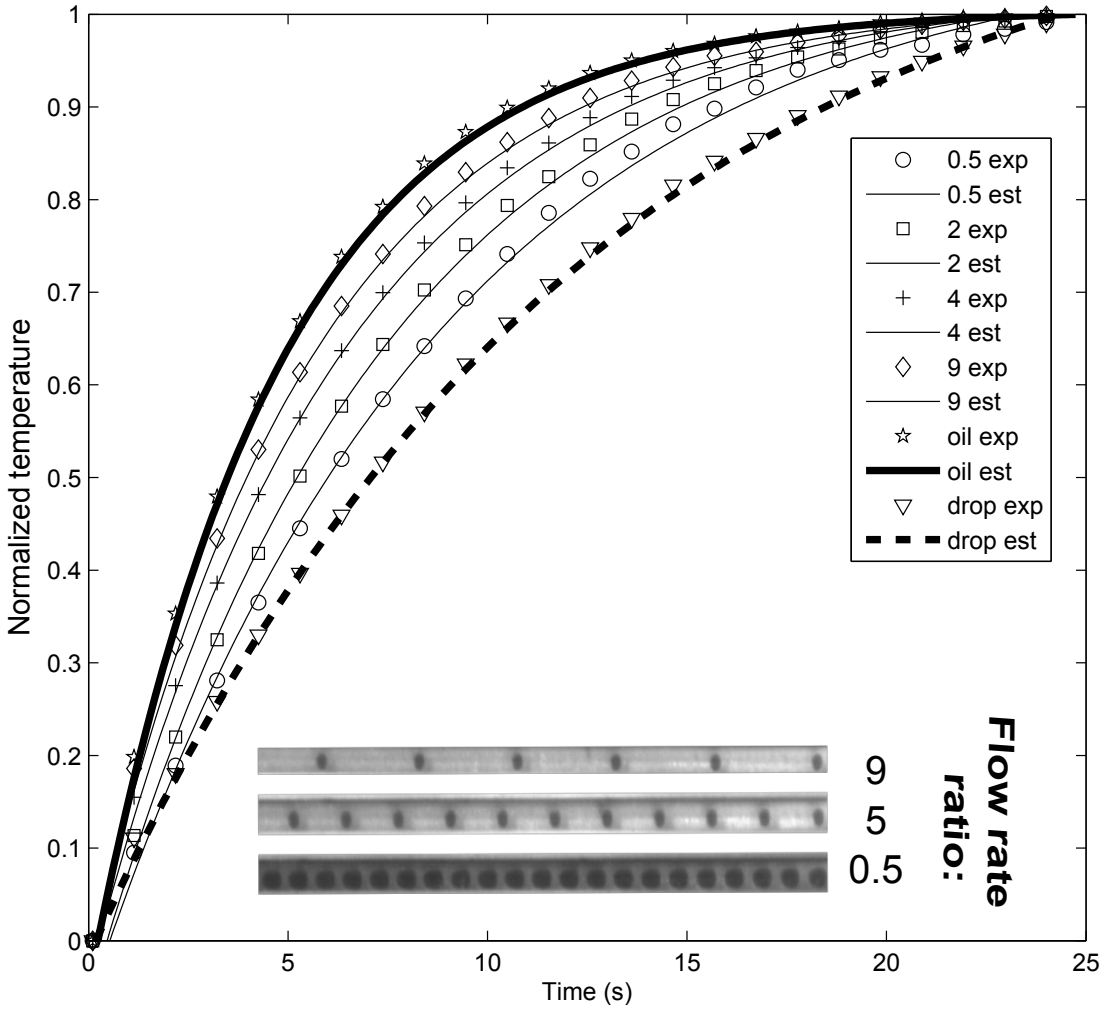

Figure 5.6: Continuous component (CC) profile for a given total flow (Q_T) at different water-oil flow rate ratios. In the legend, the label *exp* denotes the experimental data, while the label *est* identifies the estimations

Figure 5.6 shows that the measured CC temperature profiles are functions of the flow rate ratio between the water and oil phases. When the volume fraction of the water droplets is higher (at R=0.5), the average behavior of the system is similar to that of water alone.

In contrast, when the volume fraction of the oil increases (at R = 9), the behavior of the CC is similar to that of oil alone. Moreover, in figure 5.6, the profiles estimated by the equation 5.8 are also

represented. All of these analytical profiles are represented by solid lines, which fit the experimental measurements with good agreement. It should be noted that in figure 5.6, both the space and the droplet shape are modified as R is varied. From a thermal point of view, this affects the heat transfer, and in particular the heat exchange surface, between the fluids and the bulk. Nevertheless, the global thermal behavior in terms of heat released is bounded by the behavior of the water and oil. Moreover, the estimated coefficients follow the behavior predicted by the equation 5.8. By investigating the characteristic coefficient through the continuous component, it is possible to deliver two analyses:

1. **Estimation of the characteristic coefficient, H**: this process is carried out to calibrate the system as functions of the total flow (Q_T) and the droplet vs. oil flow rate ratio R (i.e., the ratio α, ratio between the length of L_H and L_G)

2. **Estimation of the thermophysical properties**: this approach delivers a measurement of the thermal properties of one of the phases when the other is assumed to be well known.

5.1.2.2 Experimental characteristic coefficient

This calibration allows us to identify the convective heat losses due to the effects of convection between the biphasic fluid under flow inside the channel and the surrounding (brass plate and ambient air). The previous experiment at a given total flow and five ratios (R) was reproduced using the experimental conditions of:

- Total flow rate Q_T= 10, 20 and 30 mL.h^{-1}

- Flow rate ratio from R = 0.5 to 9.

From the experimental temperature profiles at the three total flows (Q_T), the H coefficients were estimated according to the equation 5.8 by using the methodology described in section 4.5. Here, the H estimation was also performed for three different oils, as summarized in table 5.2.

Oil type	Commercial name	Kinematic viscosity	Supplier
		cSt at 25°C	
Silicone oil	PDMS oil	250	Sigma Aldrich
Fluorinated oi	IKV 32	32	IKV tribologique
Fluorinated oil	Fomblin YU700	700	Solexis

Table 5.2: Selected oils

In figure 5.7, the inverse H estimation approach is illustrated as a function of the oil volume fraction, which is calculated by the ratio of the length of the oil (L_H) and the total length of a droplet oil period (L_T).

Figure 5.7 shows clearly that the inverse of the characteristic coefficients decreases as the oil volume fraction increases (R=9). So, when the droplet flow is performed at R=9, the continuous component exchanges almost as if pure oil were flowing at the same total flow (represented at the abscissa of 1). When the droplet train has an important volume fraction of drops, this flow behaves almost as pure water flowing at the same total flow (represented at the abscissa of zero). Figure 5.7 also shows, for all of the experimental set-ups, that the inverse of the characteristic coefficient tends to decrease with decreasing total flow.

5.1.2.3 Estimation of the thermophysical properties

The characteristic coefficients (H) of the droplet flow were previously estimated, where it was demonstrated that the H coefficients can be predicted by the following relation:

$$H = \frac{W}{(\rho C_P V)^* U} \tag{5.9}$$

With:

$$(\rho C_P V)^* = \rho_G C_{PG} V_G + \rho_H C_{PH} V_H = (\rho_G C_{PG} L_G + \rho_H C_{PH} L_H) S$$

The effective heat exchange coefficient H reveals a strong dependence of the mixing law. The continuous component describes the behavior of the biphasic flow as an equivalent homogenous medium, defined by the thermophysical properties of both phases and the length of the plugs (L_G and L_H). Because the droplet length is greater than the oil length ($L_G \gg L_H$), the temperature profile will exhibit the same dynamic thermal behavior as if it were water alone; in contrast, when $L_G \ll L_H$, the temperature profile will exhibit the same dynamic thermal behavior as if it were oil alone. It is possible to measure the thermal properties of one of the phases when the other is assumed to be well known. To estimate the thermal properties, the inverse of the characteristic coefficient derived from equation 5.8 can also be represented according to the equations 4.54 and 4.56. The model development approach is detailed in appendix G.

L_H and L_G (which are assumed to be well-known, see section 3) are extracted from the visible image measurements (see section 3.3). From the estimated characteristic coefficients and by using the for-

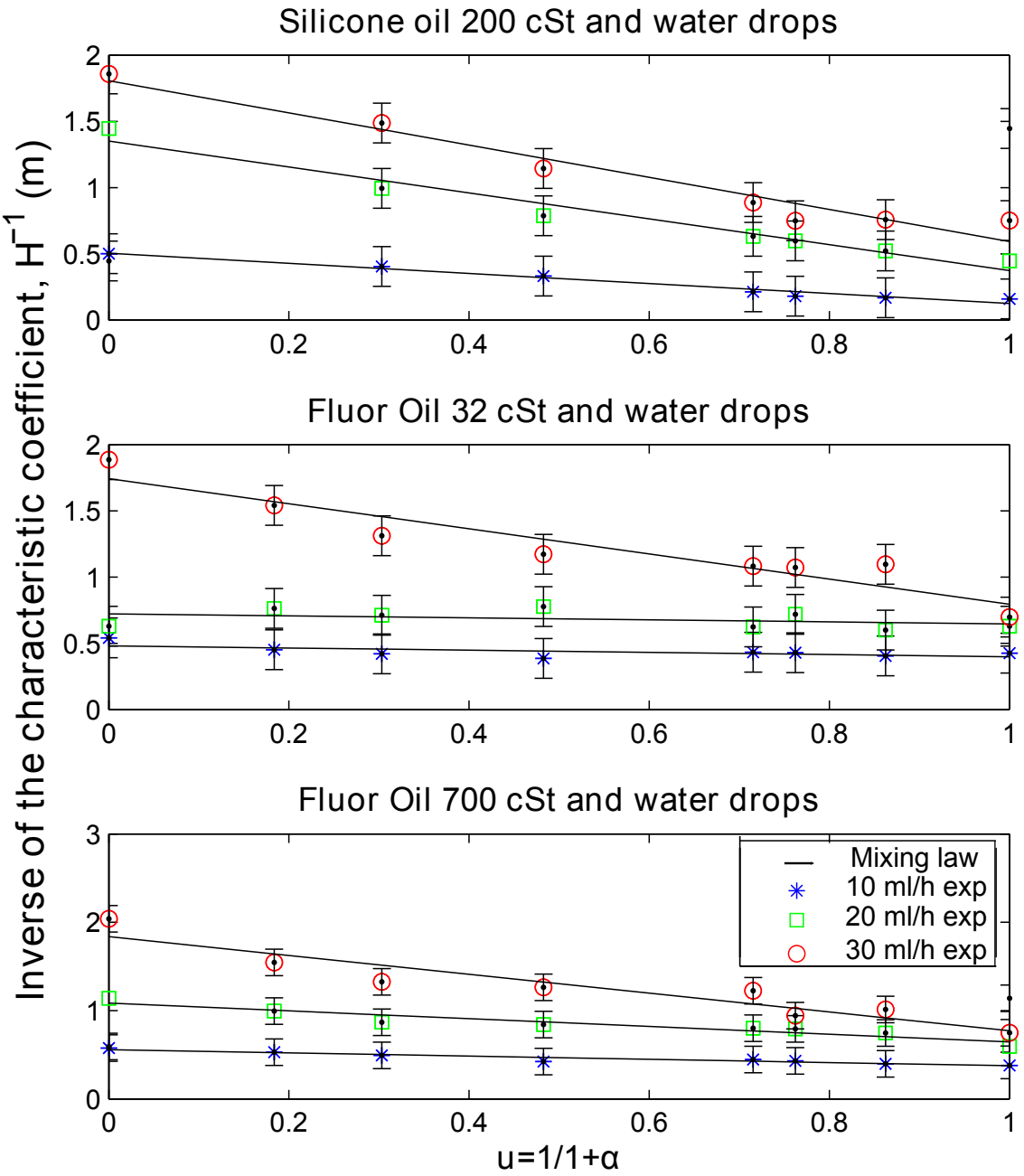

Figure 5.7: Inverse of the experimental H coefficient for several total flow rates and ratios of R. From top to bottom, the first graph concerns the calibration set when using silicone oil (250 cSt 25°C) as the continuous phase. The second graph is specified to the calibration set when using fluorinated oil (32 cSt 25°C) as the continuous phase. The third graph depicts the calibration set when using fluorinated oil (700 cSt 25°C) as the continuous phase. Pure water (abscissa 0) and oil (abscissa 1) are plotted at the edges.

mulated equation **??**, a linear regression is performed to estimate the slope S (m^{-1}) and the ordinate at origin O (m^{-1}).

The water is set as a known fluid to deduce the thermophysical properties of the three different oils, which were selected according to their nature and viscosity, as summarized in table 5.2.

From equation 4.54, and by assuming that $\alpha = L_G/L_H$ is well known, the ratio K of equation 4.55 can be estimated according to the following relation:

$$K = \frac{1}{1 + S/O} \tag{5.10}$$

where K, defined as $(\rho C_p)_G/(\rho C_p)_H$, is the ratio between the product of the mass density and the heat capacity of the two fluids (water (G) and oil (H)). From equation 5.10, and by assuming that the thermal properties of the pure water are known and taken equal to $4.18x10^6$ $(J.m^{-3}.K^{-1})$, the properties of various oils can be estimated and then compared with the values given by the suppliers and reported in figure 5.8:

Oil	Data from supplier		Estimation		Absolute error
	K	Oil ρC_p $(J.m^{-3}.K^{-1})$	K	Oil ρC_p $(J.m^{-3}.K^{-1})$	
Silicone oil 200 cSt	3.31	1.2628×10^6	3.20	1.3062×10^6	3%
Fluorinated oil 32 cSt	2.23	1.8744×10^6	2.14	1.9533×10^6	4%
Fluorinated oil 700 cSt	2.11	1.9810×10^6	2.13	1.9624×10^6	1%

Figure 5.8: Results of the thermophysical property estimation. Here, K is the ratio between the properties of both media and is both estimated and then compared with the information given by the supplier. Because the droplet phase was fixed using water, it is possible to estimate the properties of the oil phase.

The absolute error is also given in figure 5.8, where it should be noted that the absolute error is calculated as

$$E = K(\texttt{supplier data}) - K(\texttt{estimated})/K(\texttt{supplier data})) * 100$$

and is found to be less than 5%. Therefore, we are able to deduce the properties of the oil phase (ρC_p

oil) from the estimated K when the properties of the water are fixed as known.

5.2 Heat source estimation

To perform the heat source estimation, the calibration is estimated based on the previously mentioned methodologies:

- The characteristic coefficient H was estimated by the correlation method described in section 4.6.1; and
- The parietal heat transfer W was estimated by the experimental work described in section 5.1.1.

Thus, it is possible to experimentally validate the heat source estimation when a chemical reaction is performed. In this case, the heat released by a chemical reaction is the enthalpy of the reaction. Using equation 4.44, the temperature profiles are processed by taking into account the calibration coefficients to estimate the heat source.

5.2.1 Technique validation

To validate our method, a chemical reaction with a well-known enthalpy is performed. A chemical reaction between hydrochloric acid (HCl) and sodium hydroxide (NaOH) was chosen. In the case of the strong acid-base chemical reaction, the estimated spatial or temporal distributions of the heat source do not correspond to the reaction kinetics. In such a case, what is referred to as kinetics here is more of a gradual mixing of the chemical products due to mass diffusion.

In this case, the mixing evolution of the reaction is followed with a pH indicator. This reaction is a proton transfer reaction, which is considered 'a nearly instantaneous' process with a reaction constant K^0 on the order of $10^9 mol.s^{-1}$. Additionally, the characteristic neutralization time on the order of magnitude of $10^{-8} s$ is insignificant compared with the mixing time inside the droplets (more than a few seconds). Among the many acid−base color indicators available, bromothymol blue (BBT, bromothymol sulfone phthalein) is selected because it changes in the region of neutral pH and the high color contrast offered between its basic color (blue) and acid form (yellow). It also offers the advantage of being soluble in water in high concentrations ($10\ mg.L^{-1}$). The dark basic form is easily detectable by the image analysis algorithm used here; thus, it is possible to track the process of fading over time.

- **Experimental conditions**

The reaction was performed at a total flow of 10 $mL.h^{-1}$. The following two reagents were added to the droplets at the same initial concentration (C_0 = 0.5 M) and flow rates ($Q_{acid} = Q_{base}$):

- The BBT is dissolved at a concentration of 5 $X10^{-2}$M in a solution of sodium hydroxide (NaOH) as a dark blue solution, as well as
- A colorless solution of hydrochloric acid (HCl)
- A continuous phase of IKV 32 fluorinated oil
- A straight channel brass chip at room temperature
- The use of a 10-mL syringe for the oil and 2.5-mL syringe for each reagent

The total flow of the droplet is equal to the sum of both reagent flows $Q_G = Q_{acid} + Q_{base}$. When the acid is mixed with the base, the color indicator turns yellow. Because the reaction is limited by the mixing (mass transport), once the reagents are in contact, the reaction can be followed by the "fading" color of the droplet. Thus, when the reactants are completely mixed, the droplet will have turned completely yellow. Several R ratios are analyzed, and the results are summarized in table 5.3.

R Q_H/Q_G	Oil flow $Q_H, (mL.h^{-1})$	Droplet flow $Q_G, (mL.h^{-1})$
0.5	3.33	6.66
2	6.67	3.33
4	8	2
8	8.89	1.11
10	9.09	0.91

Table 5.3: Experimental droplet-oil flow rate ratios

It is important to remember that the droplet is now seen as an isolated chemical reactor in which the reagents are injected. It is important to note that at this concentration, the thermal properties of the drops can be assimilated to those of the water (the reagents are sufficiently diluted). Finally, the reagents are injected at the same temperature to which the isoperibolic chip is set (room temperature).

This set of experiments will allow us to achieve the validation of:

- The heat source estimation
- The methodology demonstration for the kinetics estimation.

- The apparent diffusion coefficient.

5.2.1.1 Heat source estimation

The temperature profiles of the chemical reaction are described according to equation **??**. In figure 5.9, the continuous contribution for different flow rate ratios (R) is illustrated. It can be observed that the temperature profile intensity of the acid-base reaction tends to decrease with increasing R. When the droplet-oil ratio is weak (e.g., R=0.5), the relaxation time is higher and is proportional to a higher molar flow; as the ratio increases (until R=10), the molar flow decreases and the biphasic flow reaches the temperature of the isoperibolic chip sooner. It is important to note that the temperature profiles for the ratios of R=8 and 10 are almost the same because the volume of the droplet is also almost the same.

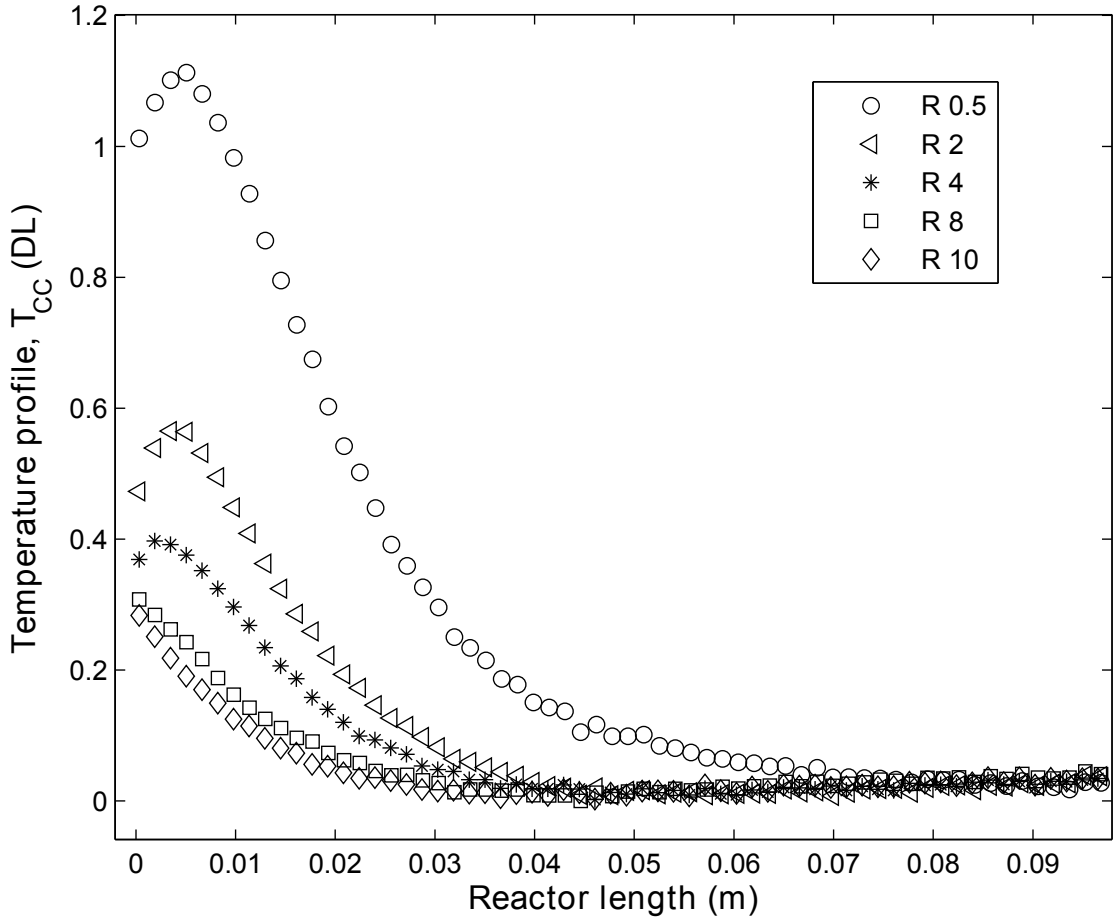

Figure 5.9: Measured continuous contribution for a given total flow rate $10mL.h^{-1}$ of an acid-base chemical reaction at the different flow rate ratios summarized in table 5.3, carried out at room temperature

Additionally, in figure 5.9, it should be noted that the reactive biphasic flows reach the set-point

temperature before the end of the channel and that the initial blue color will turn yellow by this point, which indicates that the reaction is complete inside the channel.

To perform an accurate estimation of the heat source (reaction enthalpy, ΔH), the heat losses are estimated when the chemical reaction is finished (the heat source is off), based on the correlation methodology (see section 4.6.1). In figure 5.10.A, the correlation as a function of time is shown, hence it can be observed that when the heat source is on (i.e., the chemical reaction is taking place), the correlation is equal to -1. Then, when the chemical reaction is finished, the correlation values are equal $+1$. From the moment at which the correlation values become positive, the heat losses are estimated. Figure 5.10 shows the H (m^{-1}) characteristic coefficient for each flow rate ratio R. As expected by the analytical validation (see section 4.6.2), it becomes possible to experimentally verify that the H characteristic coefficient tends to stabilize after R=2, tending to a constant value.

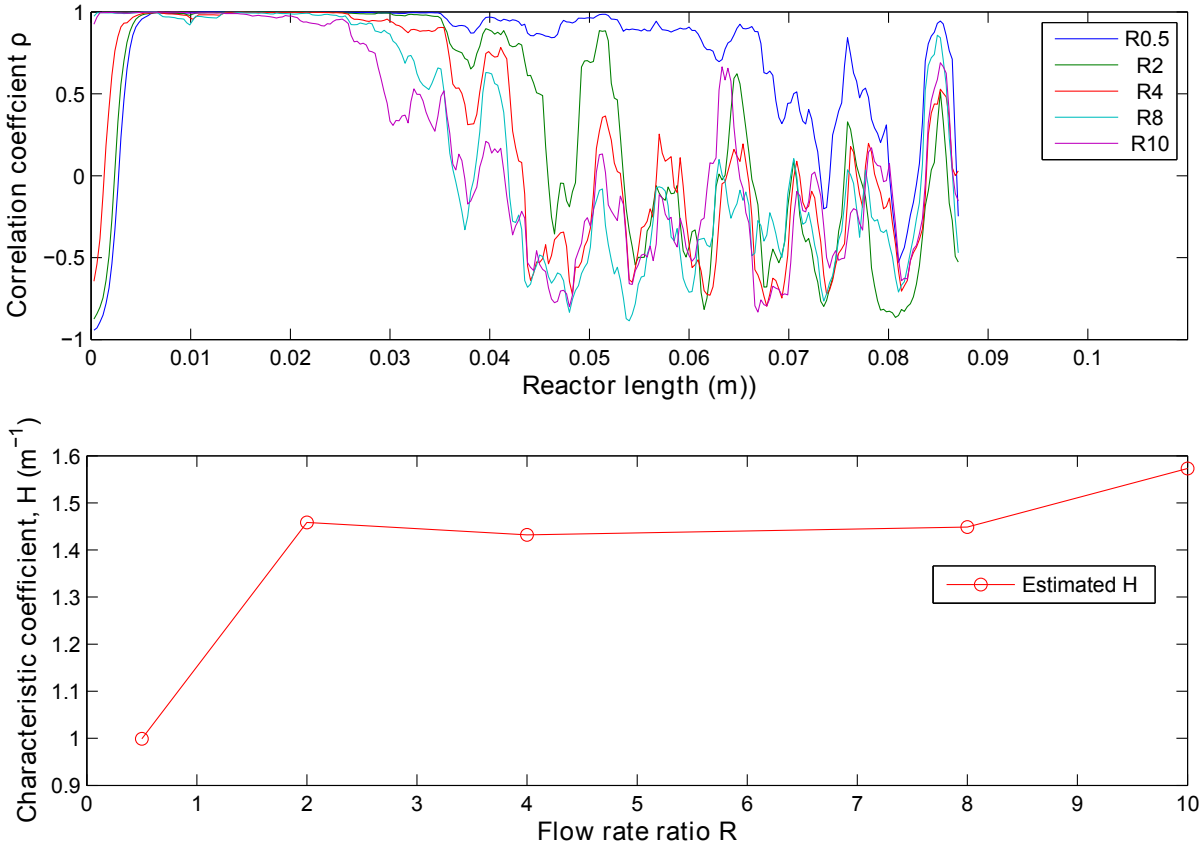

Figure 5.10: A. The correlation coefficient over time. B. The estimation of the characteristic H coefficient (m^{-1}) from the experimental flow rate ratios of R. The estimations are made by applying the correlation methodology to the CC profiles shown in figure 5.9

Here, the chemical reaction is characterized by the reaction enthalpy (ΔH). To estimate the dissipated heat source from the reaction enthalpy, the temperature profiles shown in figure 5.9 are processed according to equation 4.44, by taking into account the estimated H (see figure 5.10). Thus, the dis-

sipated source along the channel is estimated, as shown in figure 5.11. In this figure, we observe that the intensity of the dissipated heat sources tends to decrease as the ratio is increased; this occurs because the molar flow of the reagents also decreases. It can also be observed that once the maximum heat source has dissipated, the source remains constant over the channel. Additionally, this plateau is not reached at the same time for all R ratios, which may be a signature of the mixing time. To make an accurate estimation of the enthalpy, the reaction must be carried to completion (fully mixed). This is because the integration of the heat source, when the conversion is complete inside the channel, provides direct access to the reaction enthalpy.

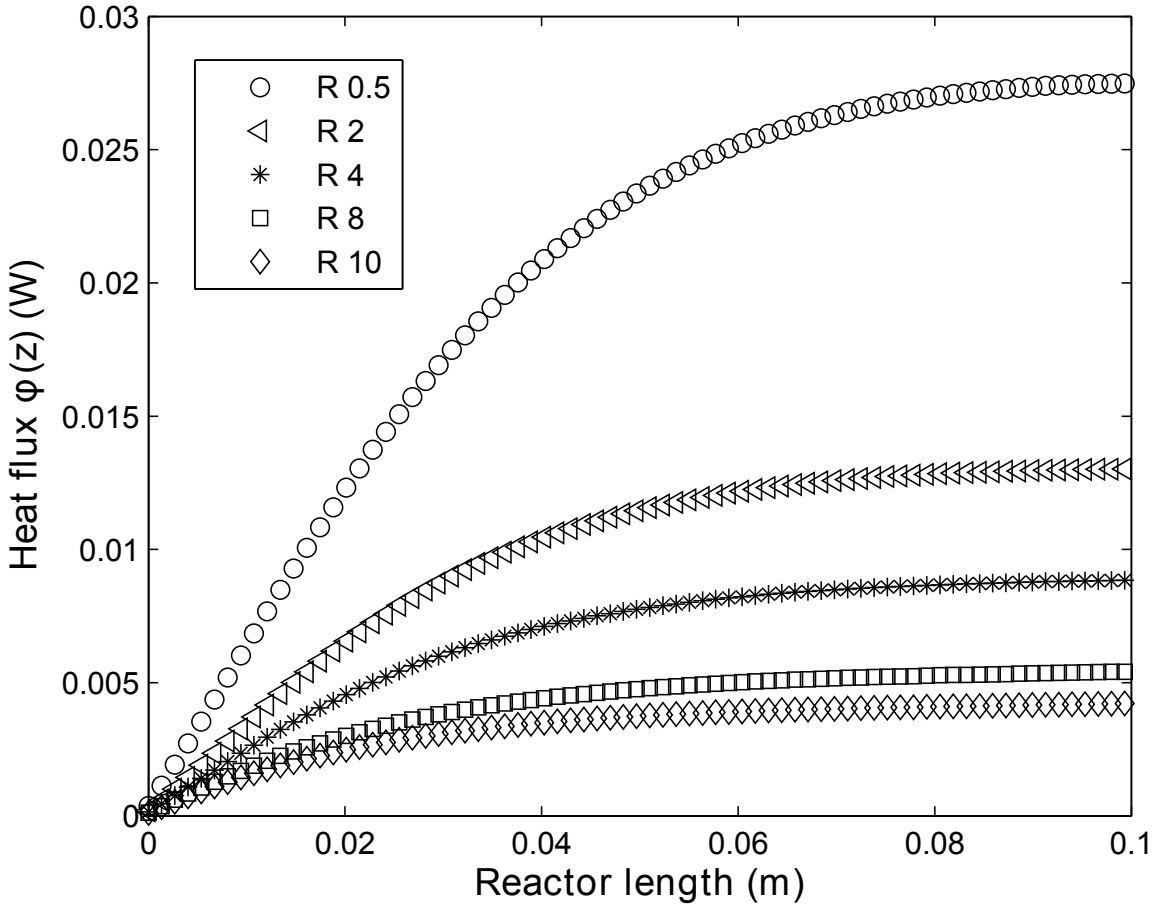

Figure 5.11: Dissipated heat source of the acid-base chemical reaction along the channel

Thus, from the estimation of the heat source along the tube, as shown in figure 5.11, and by applying equation 5.11, the total heat source dissipated by the chemical reaction is characterized by integrating the heat source Φ (W) along the tube length.

$$\Phi = \int_{z=0}^{z=L_T} \phi(z)dz = M\Delta H \tag{5.11}$$

In this case:

$$M = \frac{Q_{lim} C_0}{2}$$

where M represents the molar flow ($mol.s^{-1}$), C_0 is the initial concentration of the limiting reactant ($mol.l^{-1}$), and Q_{lim} is the limiting reactant flow ($l.s^{-1}$). In this equation, M is divided by 2 because the reactive flows and the initial concentrations are the same.

The enthalpy estimation ΔH is carried out by plotting the integrated heat source Φ with the molar flow M ($Q.C = mol.s^{-1}$). Figure 5.12 shows the integrated heat source as a function of the molar flow rate of the injected reagent. From this data, the enthalpy of the reaction (mixing, in this case) can be estimated through a linear regression analysis. The slope represents the estimated enthalpy, where the obtained value is 57.22 $kJ.mol^{-1}$, which is in good agreement with the value given in the literature, i.e., 56 $kJ.mol^{-1}$ [118]. Finally, the estimation exhibits an error of less than 2%.

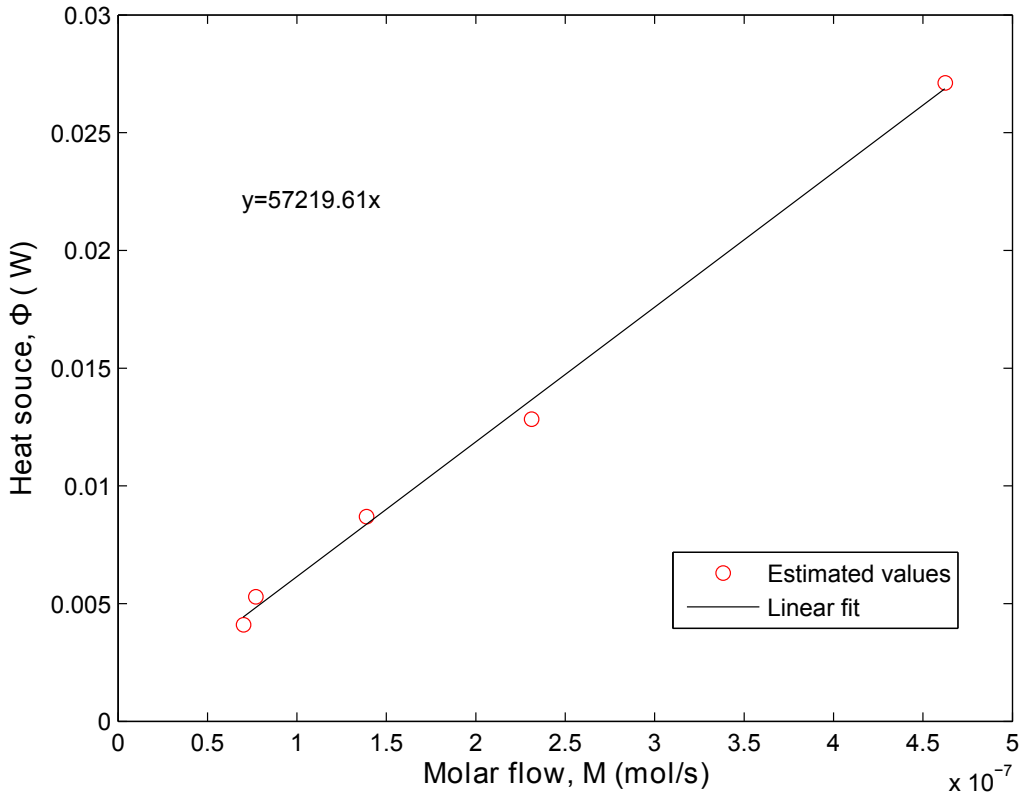

Figure 5.12: Estimated heat source for the acid-base reaction at a total flow of 10 $mL.h^{-1}$ for different droplet-oil flow ratios (as summarized in table 5.3) as a function of the molar flow.

To estimate the uncertainty of the repeatability of the enthalpy estimation ΔH, a repeatability study was carried out. Twenty-one measurements were performed. To highlight the dispersion of the results, the distribution function of the two series is represented by the normalized values, calculated as:

$$Normalization = \frac{\Delta H - \bar{\Delta H}}{\sigma_{\Delta H}}$$

where ΔH ($J.mol^{-1}$) is the estimated calibration coefficient, $\overline{\Delta H}$ ($J.mol^{-1}$) is the mean value of the experimental estimation and $\sigma_{\Delta H}$ is the standard deviation. In figure 5.13, the distribution of the results is represented by a normalized histogram.

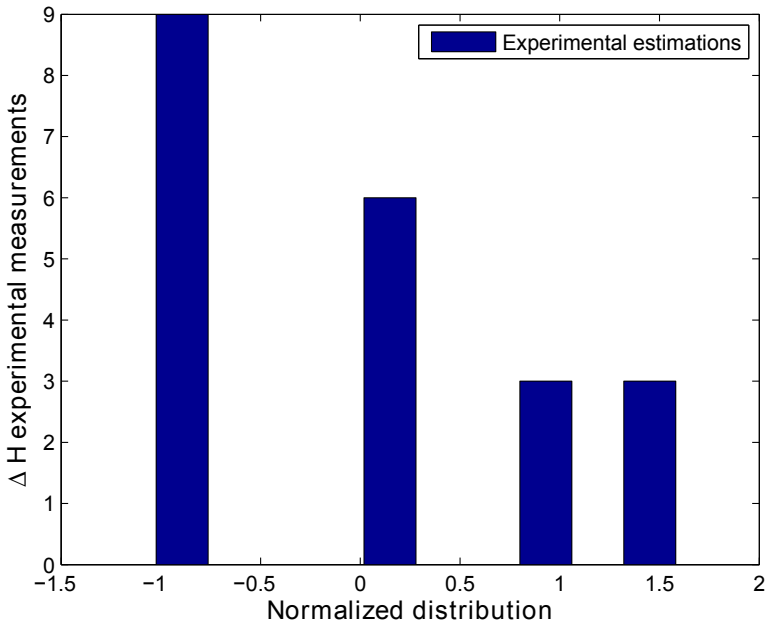

Figure 5.13: Distribution of the normalized results

Because the distribution is narrow, it is appropriate to calculate a mean value of these two series. The experimental standard deviation σ is used to estimate the uncertainty of repeatability:

$$UR_{repeatability} = \frac{\sigma}{\sqrt{n}} \tag{5.12}$$

where n is the number of experimental estimations. Thus, the relative uncertainty (the coefficient of variation) of the experimental value ΔH is given by following the equation:

$$UR(\%) = \frac{UR_{repeatability}}{\bar{\Delta H}} * 100 \tag{5.13}$$

The results are summarized in table 5.4. The uncertainties of the repeatability are acceptable, and the experimental repeatability for the enthalpy ΔH estimation is approximately 94%, implying that the repeatability is accurately estimated.

	Acid Base reaction
Mean ΔH ($J.mol^{-1}$)	$5.6571x10^4$
Standard deviation ($J.mol^{-1}$)	$1.5353x10^3$
Uncertainty repeatability ($J.mol^{-1}$)	335.0297
Relative incertitude UR(%)	5.9

Table 5.4: Uncertainty of the repeatability of the ΔH estimation for the isoperibolic chips used

5.2.1.2 Demonstration of the methodology for the kinetics estimation

This is a neutralization reaction. When the acid and base properties of $H+$ and OH are neutralized, the species combine to form H_2O, which gives a water molecule and a salt molecule $NaCl$. The acid-base neutralization reaction is described as:

$$HCl(aq) + NaOH(aq) \longrightarrow Na^+ + Cl^- + H_2O$$

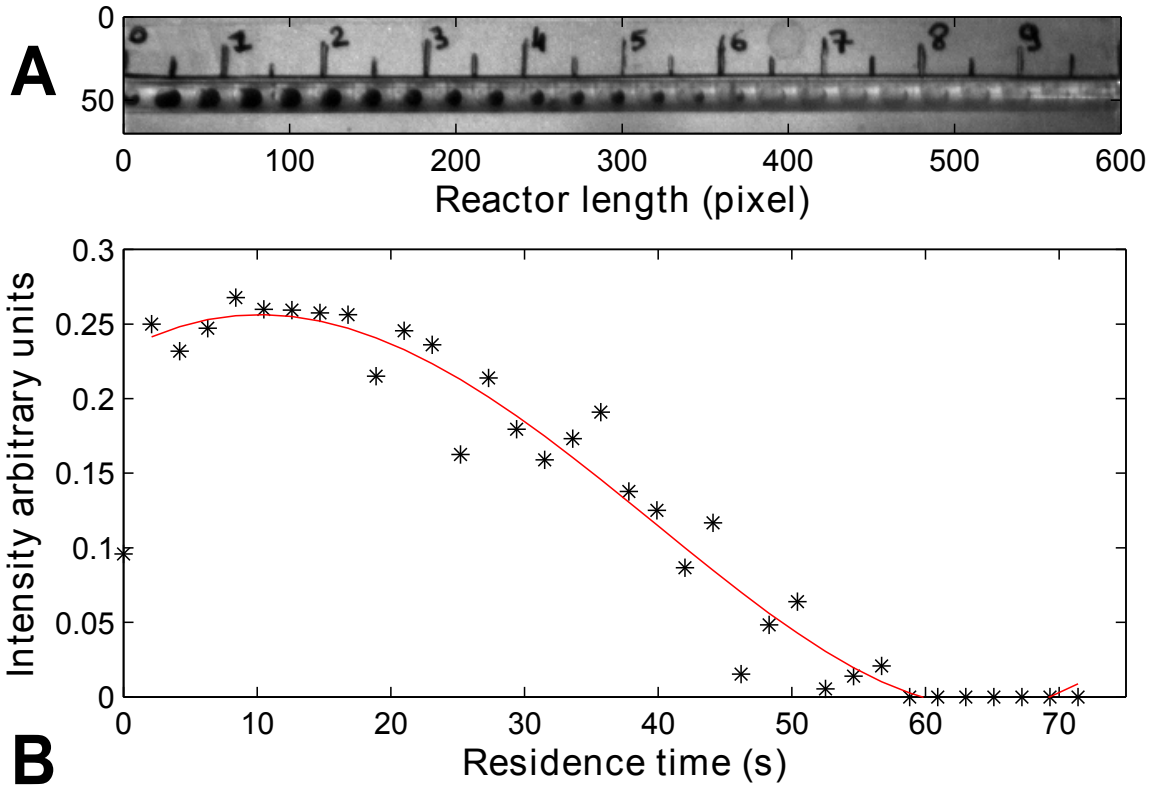

Figure 5.14: (a). Snapshot of the acid-base reaction along the isoperibolic chip. (b). Evolution of the reaction intensity, monitored by detecting the fading color of the droplets along the channel, as a signature of the reaction evolution based on the changing of pH (from blue to yellow).

It should be noted that the cations and the anions simply switch places in this process: the Na+ from the NaOH combines with the Cl- from the HCl to form NaCl, while the OH from the NaOH combines with the H+ from the HCl to form H_2O. Hence, using color detection, it is possible to detect the pH change. In this case, the kinetics of the reaction are demonstrated by the shift from blue to yellow.

From the visible images, it is possible to detect the fading color of the droplets along the channel. The reaction evolution along the channel is plotted in 5.14. Through image analysis, it is possible to detect the evolution of the intensity of the droplets (gray scale, presented here in arbitrary units) as a function of the residence time. Due to the steady state of the fluidic configuration, a direct relationship between space (z-axis) and time is given by $z = Q_T/S$, where Q_T is the total flow and S is the inner tubing section. It is possible to deduce the advancement of the reaction by applying the relationship expressed in equation 5.14, where χ represents the conversion, I_0 represent the initial intensity and I the intensity evolution as a function of time.

$$\chi = 1 - \frac{I(t)}{I_0} \tag{5.14}$$

The intensity of the reaction is tracked over the channel length by applying the visible technique. Then, by using equation 5.14, it is possible to estimate the evolution of the reaction in terms of the conversion rate ($d\chi/dt$). Then, the conversion rate ($d\chi/dt$) at the same R and total flow is compared with the estimated heat source ($\phi(t)$).

These profiles were shown previously and described as functions of the space; here, the space to time correspondence is applied to rescale both profiles as functions of time. This comparison is shown in figure 5.15, from which it can be noted that the curve trends are similar. Both behaviors are plotted against each other to quantify this similarity, as illustrated in figure 5.16.

From the linear relationship shown in figure 5.16, the dissipated heat source $\phi(t)$ ($W.s^{-1}$) corresponding to the chemical reaction is related to the conversion rate χ of the reaction by the following relation:

$$\phi(t) = M\Delta H\chi \tag{5.15}$$

where M ($mol.s^{-1}$) represents the molar flow, and ΔH ($J.mol^{-1}$) is the reaction enthalpy.

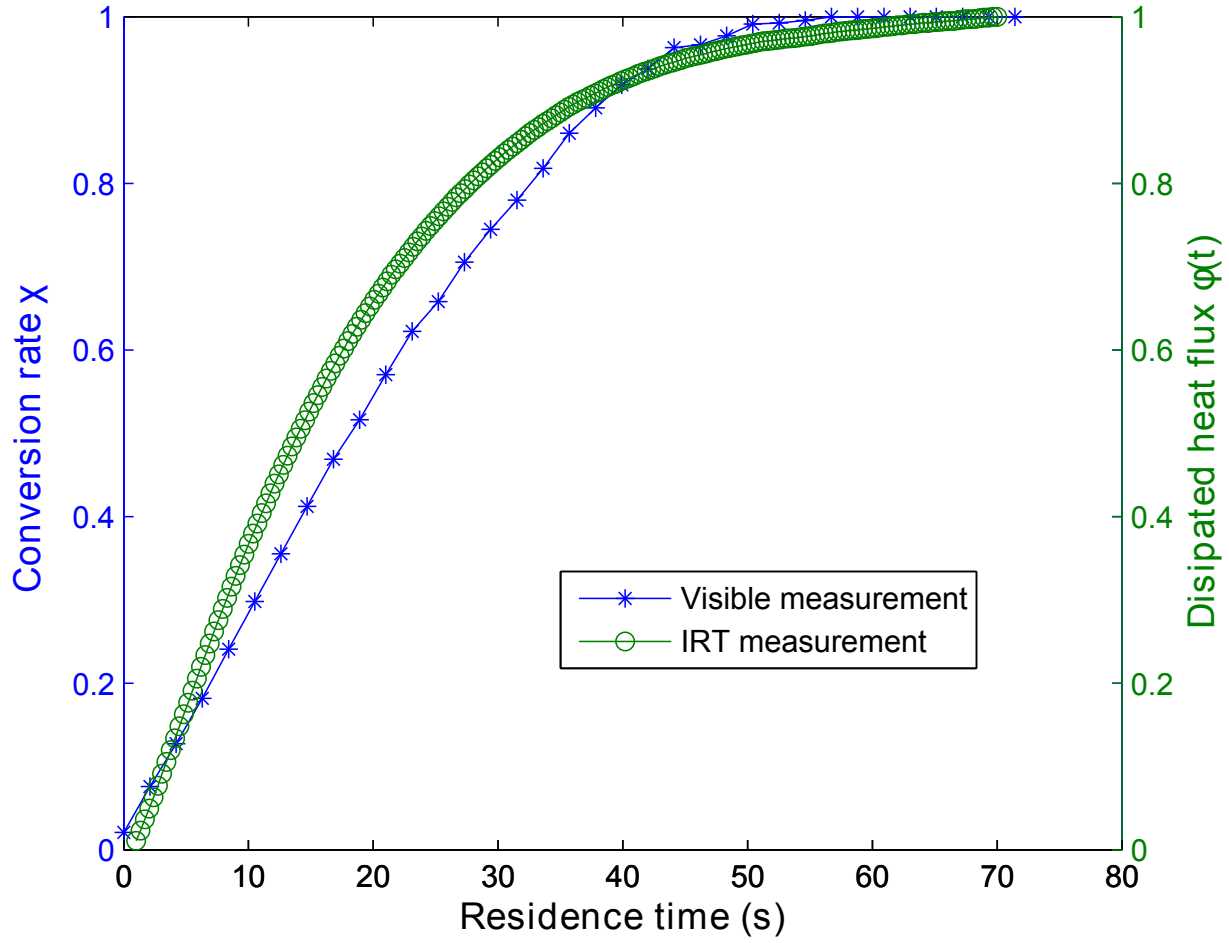

Figure 5.15: Conversion rate ($d\chi/dt$) of the acid-base reaction can be expressed as a function of time; in the graph it is represented by blue stars. Additionally, the dissipated heat source as a function of time ($W.s^{-1}$) is represented by the green dots in the graph. These profiles were developed at R=2 and 10 $mL.h^{-1}$ and room temperature

$$log(\phi(t)) = log(\chi) + log(M\Delta H) \tag{5.16}$$

In figure 5.16, the relationship expressed by equation 5.16 is plotted. The order of magnitude of the slope is ≈ 0.9, implying that the mixing kinetics based on visible imaging can be predicted at 85% by the IRT heat source estimations. The visible imaging technique applied to track the evolution of the mixing kinetics is not sufficiently precise to provide an accurate profile of the reaction evolution, although it is good enough to demonstrate the methodology. The neutralization reactions have equilibrium kinetics that can be extremely difficult to reach (a thermodynamic equilibrium that is slowly achieved). The kinetics prediction based on the IRT methodology is a more universal technique than the color indicator-based approach (BBT).

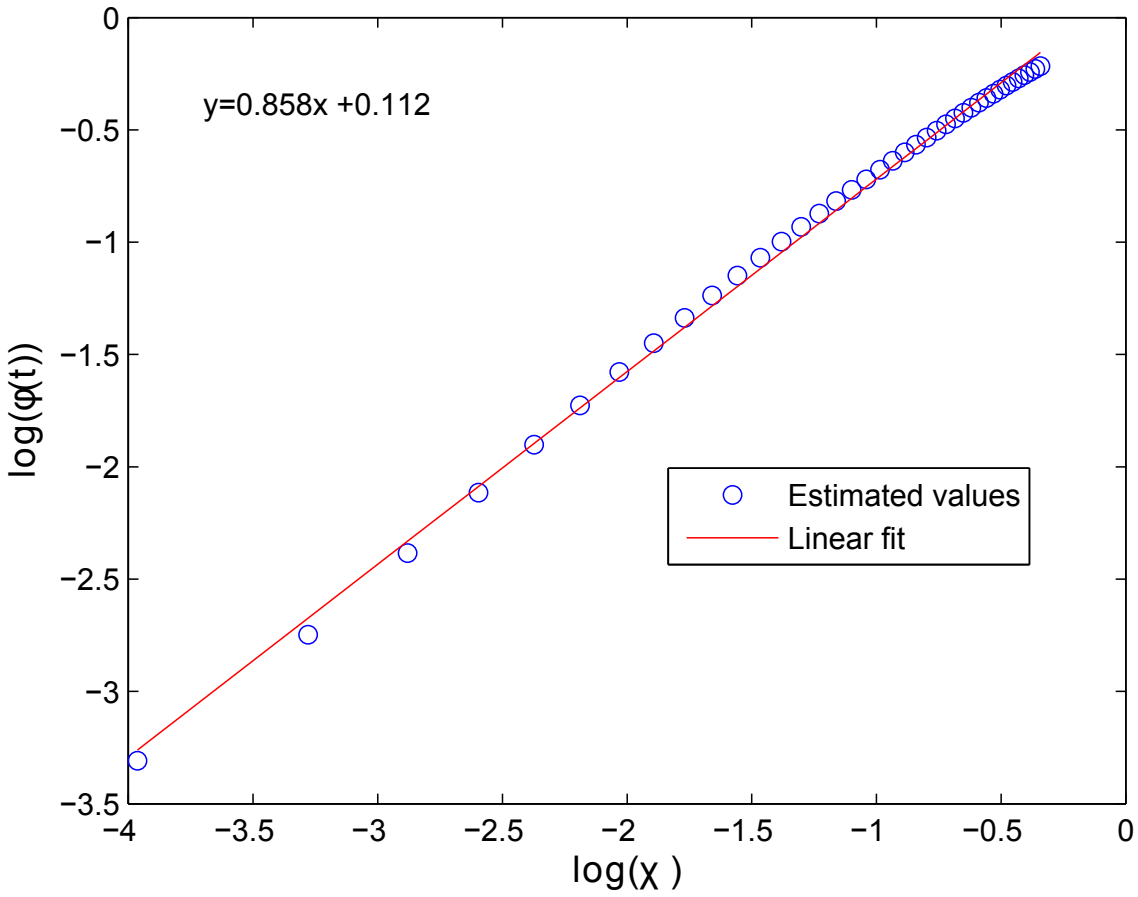

Figure 5.16: The logarithm of the conversion rate (i.e., mixing) is plotted versus the logarithm of the dissipated heat source, through the relationship expressed by equation 5.16. It is important to note that this behavior corresponds to the same experiment at R=2 and 10 $mL.h^{-1}$ and room temperature

5.2.1.3 Apparent diffusion coefficient

In the case of the strong acid-base chemical reaction, the spatial distributions of the chemical reaction correspond to a gradual mixing of the chemical products due to mass diffusion. Because BBT was used, it is possible to follow the mixing dynamics inside the droplets by analyzing the visible images. Then, by applying image analysis techniques, it is possible to determine the mixing distance. Additionally, the droplets behave as isolated batch reactors in which the reagents mix and then react (mixing time $\ggg$ reaction time). Because the reagents move at a constant velocity U along the channel, the distance d between the initial point and a given position in the channel corresponds to a mixing time of $t = d/U$. Thus, this particular reaction is very convenient for studying the apparent diffusion coefficient, that is, to determine the moment at which the reagents are perfectly mixed within the droplet.

To estimate the apparent diffusion coefficient of the isolated reactors, the methodology reported by

Sarrazin et al. is applied [17].

- Influence of droplet length on the mixing time

Sarrazin et al. demonstrated that the mixing time is sensitive to droplet width. This is directly related to the width of the channel, w_g (m), and the scale significantly influences the magnitude of the mixing time, T_{mix} (s). In our case, we are studying the influence of the droplet length for a given inner diameter. Thus, the mixing time within droplets is related to their size based on a diffusion law:

$$T_{mix} = \frac{(0.5w_g)^2}{D_{ap}} \tag{5.17}$$

where D_{ap} is a constant ($m^{-2}.s$). The investigated scale of influence in this study is the length of a droplet, so it is possible to rewrite the previous relation as function of the studied characteristic scale (L_G). Accordingly, it is possible to deduce an apparent diffusion coefficient D_{ap} based on the following relation.

$$T_{mix} = \frac{(L_G)^2}{D_{ap}} \tag{5.18}$$

In figure 5.17, the mixing time is plotted versus the square of the droplet length for three complete flows (Q_T) and several ratios of R=0.5 to 10. It is possible to observe two regimes: 1) in the first regime, R=0.5 and 1, and the droplet lengths (approximately 3.5 and 2 mm, respectively) exhibit the maximum mixing time. 2) For R≥ 2, the droplet lengths (approximately 1.8 to 1.5 mm) present a linear relationship with the mixing time. Hence, we turn our focus to the linear regime to investigate the apparent diffusion coefficient given by the inverse of the slope, as described in equation 5.18.

In figure 5.18, it can be clearly observed that for a given complete flow, the slope varies. These estimations are summarized in table 5.5. It is important to mention that the order of magnitude of the molecular diffusion coefficient of the basic BBT in the acid phase in a coflowing system is $3\text{x}10^{-9}m^2.s^{-1}$. Macroscopically, the mixture within the droplet can be represented as a diffusive phenomenon, where the species are carried inside the droplet by an apparent diffusion coefficient that is more than 10 times the molecular coefficient. The relationship between the estimated apparent coefficient D_{ap} and the total flow (Q_T) is shown in figure 5.19.

- The mixing time decreases:
  - As the velocity increases, i.e., the total flow appears to influence the mixing process within

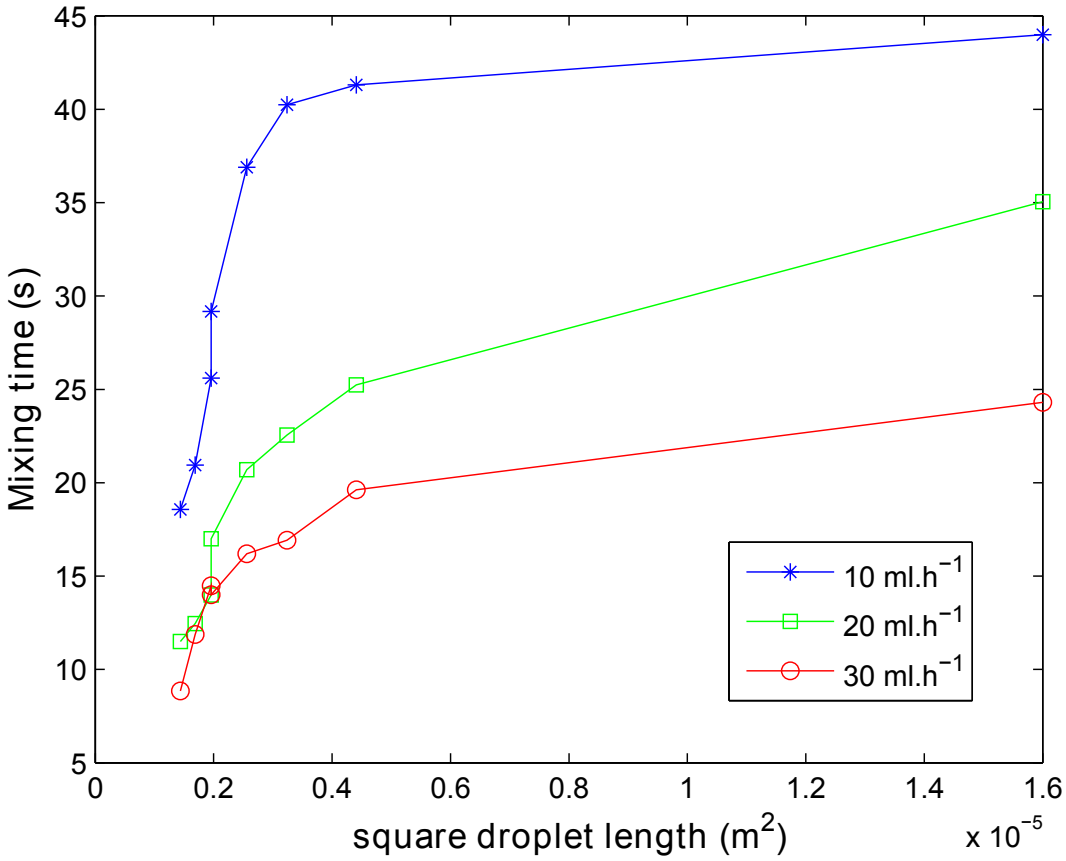

Figure 5.17: The mixing time versus the square of the droplet length for three complete flow paths (Q_T) is plotted for investigated rate ratios. At R=0.5, the droplet length is approximately 4 mm; at R=10, the droplet length is approximately 1.4 mm.

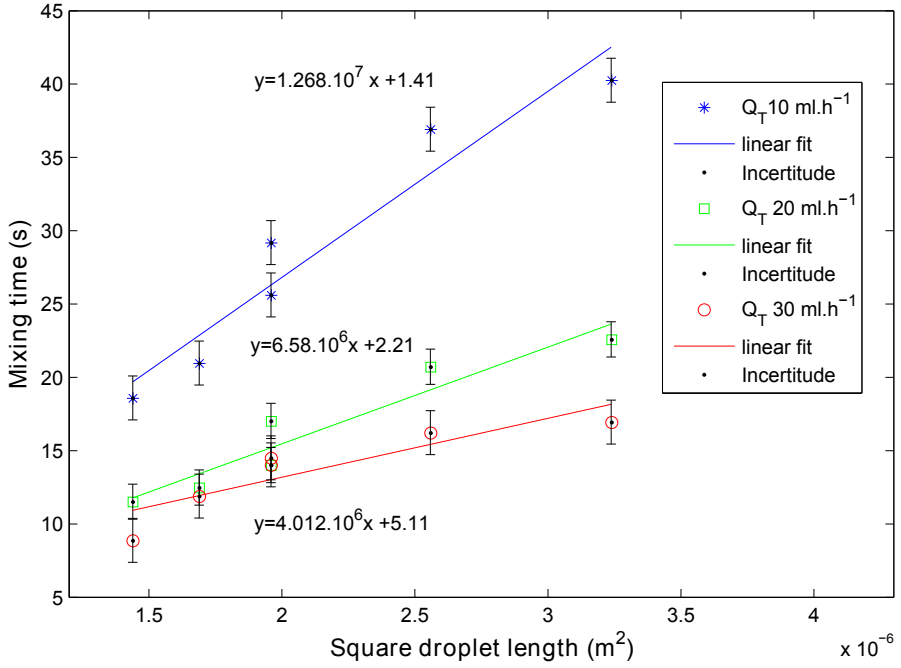

Figure 5.18: Mixing time versus the square of the droplet length (R=2 to 10) for three complete flows.

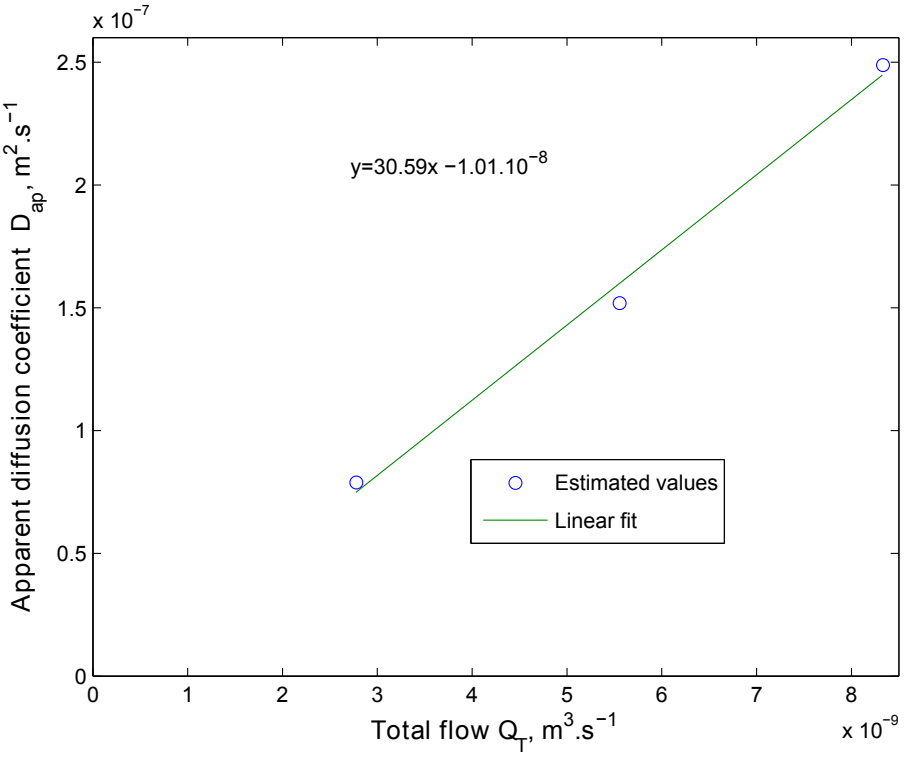

Figure 5.19: Linear relationship between the total flow and the measured mixing time.

Total flow, Q_T $(mL.hr^{-1})$	Total flow $(m^3.s^{-1})$	K $(s.m^{-2})$	D_{ap}, $(m^2.s^{-1})$
10	2.77 x10^{-9}	1.268 x10^{7}	7.883 x10^{-8}
20	5.55 x10^{-9}	6.586 x10^{6}	1.52 x10^{-7}
30	8.33 x10^{-9}	4.012 x10^{6}	2.49 x10^{-7}

Table 5.5: Summary of the experimental values of the apparent diffusion coefficient D_{ap}, from figure 5.19

the droplet, as observed in figure 5.17; alternatively,

– As the length of the droplet decreases, the mixing time decreases proportionally, as observed in figure 5.18.

In conclusion, the mixing time of millifluidic droplets depends on the inner diameter of the channel; additionally, for a given diameter, both the droplet length and velocity significantly influence the mixing time. These experimental findings suggest that the diffusive and convective contributions may be coupled. The analysis of the dimensionless numbers comparing these two effects requires additional experimental data to express the observed trends that drive the phenomena considered. Understanding these phenomena is of great importance toward analyzing the evolution of the concentration inside the droplets and obtaining the correct kinetics of the system. Moreover, it is very important to determine the moment at which the reagents are perfectly mixed within the droplet; after this point, any variation in the internal composition of the droplet is only due to the chemical reaction, which is particularly interesting when the mixing time is negligible in comparison with the reaction time. After the point

at which total mixing has occurred, the evolution of the reaction will continue to be influenced by the mixing performance (i.e., competitive consecutive reactions).

5.3 Application and characterization

The objective of this part is to present some applications of the non-contact millifluidic calorimeter developed in this work. This device will be used as previously described to estimate:

- The reaction enthalpy and
- The reaction kinetics.

First, a redox reaction is characterized by determining the enthalpy and reaction kinetics. Then, a click reaction is performed.

5.3.1 Di-iodine generation

Iodine is widely used in pharmaceuticals, antiseptics, medicine, food supplements, dyes, and catalysts. One approach to the production of diiodine, which is the normal diatomic form of iodine (I_2), is the reaction between potassium iodide (KI) and sodium persulfate ($Na_2S_2O_8$).

$$2KI + Na_2S_2O_8 \longrightarrow I_2 + 2SO_4^{2-} + 2K^+ + 2Na^+$$

In this reaction, both reagent are colorless. To estimate the enthalpy value of this reaction, it is important to study the two redox couples, which are characterized by a redox potential $E_{ox/red}$ [118].

$$S_2O_8 + 2e \dot{\rightleftharpoons} 2SO_4^{2-} \quad E^0 = 2.12V$$

$$2I^- \dot{\rightleftharpoons} I_2 + +2e \quad E^0 = 0.54V$$

The Nernst equation is applied as follows:

$$\Delta G = -nF\Delta E^0 \quad where \quad \Delta E^0 = 2.12 - 0.54 = 1.58V \tag{5.19}$$

where n is the number of electrons transferred, specifically, 2 electrons are exchanged, and F is the

Faraday constant (F=9.648534 X10^4 J.V^{-1}.mol^{-1}), the redox difference potential ΔE^0 (V), where the negative sign is because a spontaneous reaction has a negative free energy ($J.mol^{-1}$). The estimated enthalpy is 305 kJ.mol^{-1}.

- **Experimental conditions**

The reaction is performed at a total flow of 10 $mL.h^{-1}$. The following two reagents are added into the droplets at the same flow rates $Q_{Na_2S_2O_8} = Q_{KI}$, and the initial concentrations of $C_{Na_2S_2O_8}$ and C_{KI} are introduced in stoichiometric proportions, taking into account the effects of dilution. The limiting reactant is the sodium persulfate ($Na_2S_2O_8$).

- $C_{Na_2S_2O_8}$ = 0.5 M
- C_{KI} = 1 M
- The continuous phase is IKV 32 fluorinated oil
- A serpentine brass chip at room temperature
- 10 mL syringe for the oil and 2.5 mL syringe for each reagent

The flow rates are summarized in table 5.6, where the droplet flow is defined as $Q_G = Q_{Na_2S_2O_8} + Q_{KI}$. Additionally, this experiment is carried out using the serpentine chip at room temperature.

R Q_H/Q_G	Oil flow $Q_H, (mL.h^{-1})$	Droplet flow $Q_G, (mL.h^{-1})$
1	5	5
2	6.67	3.33
4	8	2
8	8.89	1.11

Table 5.6: Experimental droplet-oil flow rate ratios

The temperature profiles of the chemical reaction are described according to equation **??**. In figure 5.20, the continuous contribution for different flow rate ratios (R) is illustrated. It can be observed that the temperatures profile intensity of the redox reaction tends to decrease with increasing R. When the droplet-oil ratio is low (e.g., R=1), the relaxation time is higher because it is proportional to a higher molar flow; as the ratio increases (to R=8), the molar flow decreases.

Additionally, it should be noted that the reactive biphasic flow reaches the set-point temperature (room temperature) before the end of the channel, as observed in figure 5.20. Hence, the reaction is completed within the channel.

To perform an accurate estimation of the heat source (reaction enthalpy (ΔH)), the heat losses are

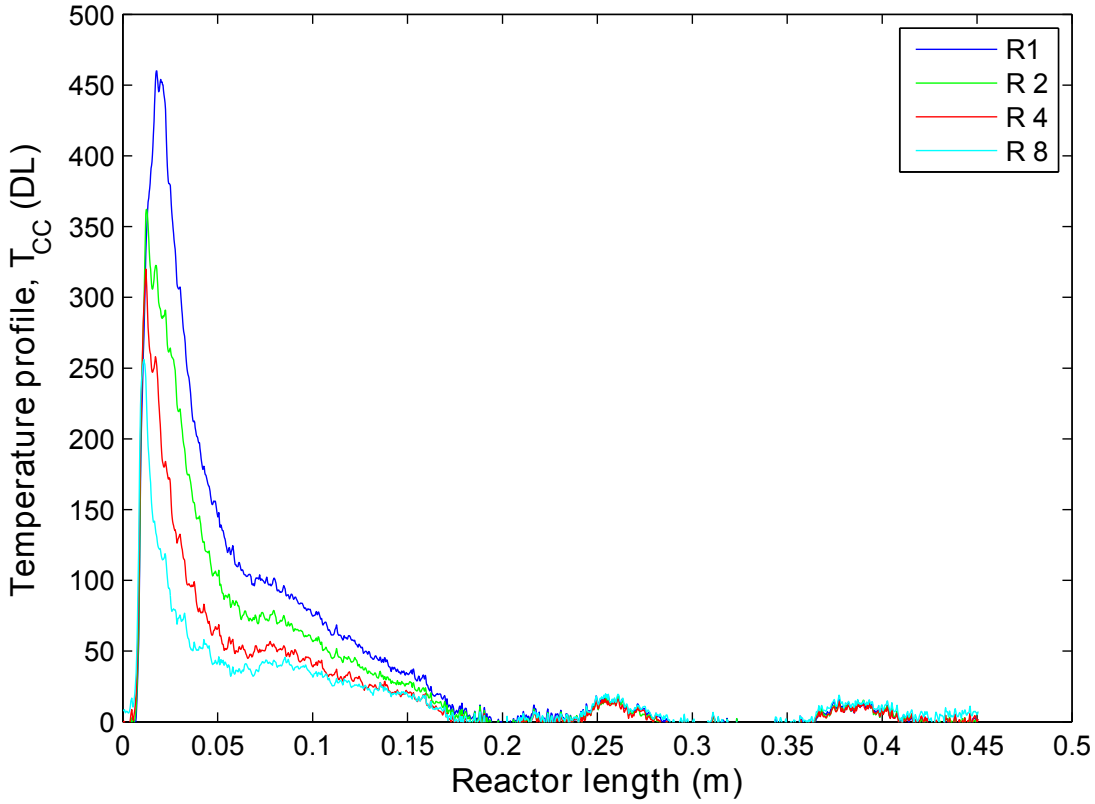

Figure 5.20: Measured continuous contribution for a given total flow rate $10mL.h^{-1}$ of the redox chemical reaction at different flow rate ratios, as summarized in table 5.6, and performed at room temperature

estimated when the chemical reaction is complete by using the correlation methodology (see section 4.6.1). Figure 5.21 shows the H (m^{-1}) characteristic coefficient for each experimental flow performed at a given rate ratio R. As expected based on the analytical validation (see section 4.6.2), it is possible to experimentally verify that the H characteristic coefficient tends to stabilize at a constant value after R=4.

The chemical reaction is characterized by the reaction enthalpy (ΔH). To estimate the dissipated heat source, the temperature profiles shown in figure 5.20 are processed according to equation 4.44, taking in account the estimated H (see figure 5.10). Thus, the dissipated source along the channel is estimated, as shown in figure 5.22. In this figure, it can be observed that the intensity of the dissipated heat sources tends to decrease with increasing reaction ratio. This is because the molar flow of the reagents also decreases. It can also be observed that once the maximum heat source has been dissipated, the source remains constant along the channel. Additionally, this plateau is reached at the same time for all R ratio, where we only observe the contribution of the chemical reaction (and not the mixing effect) because $T_{reaction} \ggg T_{mixing}$.

Thus, from the estimation of the heat source along the tube $\phi(z)$ ($W.m^{-1}$), as shown in figure 5.22, then

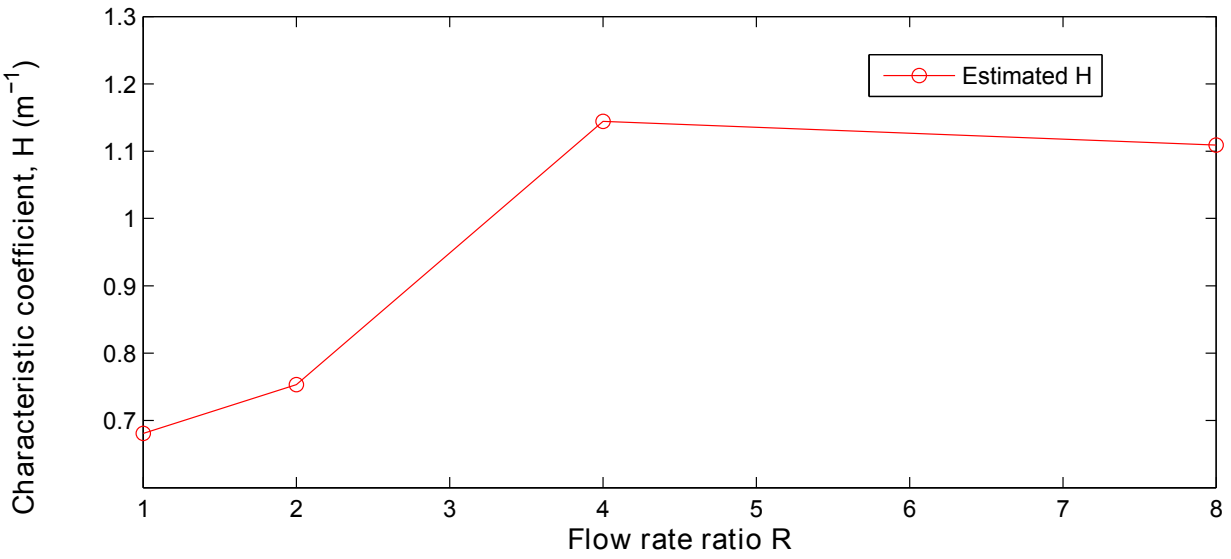

Figure 5.21: Estimation of the characteristic H coefficient (m^{-1}) from the experimental flow rate ratios, R. The estimations are made by applying the correlation methodology to the CC profiles shown in figure 5.20.

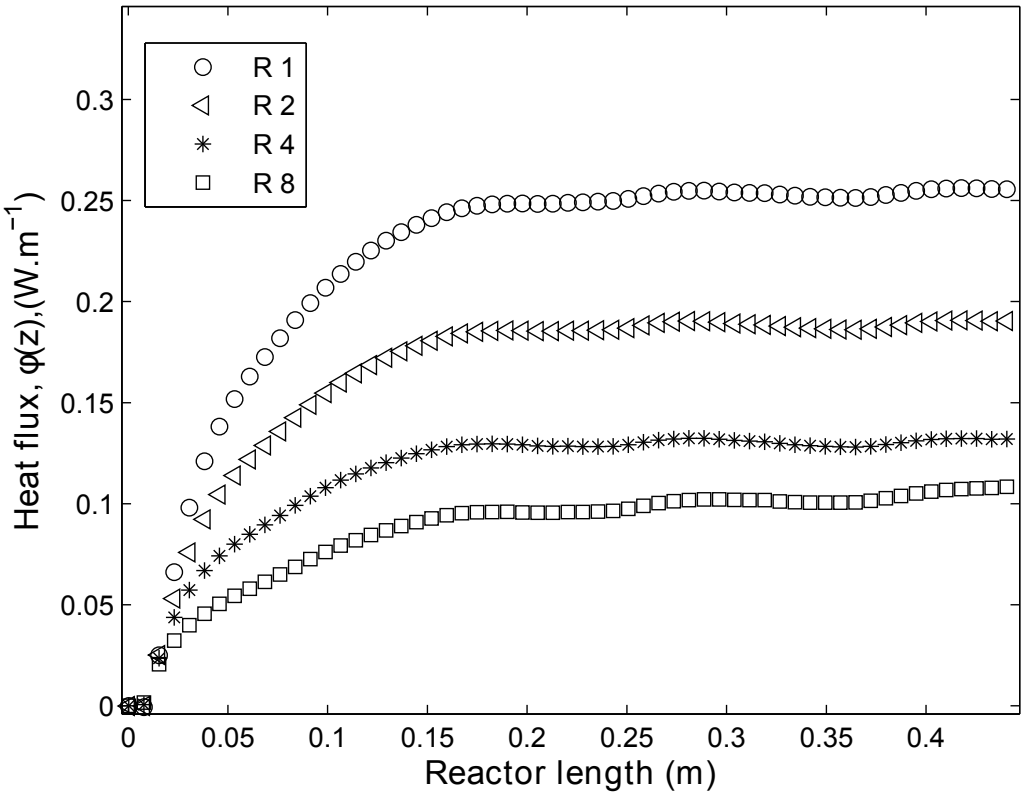

Figure 5.22: Dissipated heat source of the redox chemical reaction along the channel

by applying the equation 5.11, the total dissipated heat source Φ by the chemical reaction is integrated at the limits of the tubing. Figure 5.23 shows the integrated source Φ as a function of the molar flow rate M of the injected reagents. Here, M is calculated using the initial concentration of sodium persulfate $C_{Na_2S_2O_8} = 0.5$ and its corresponding flow $Q_G/2$. From these data and through a linear

regression analysis, the enthalpy of the reaction can be estimated. The calculated slope represents the estimated enthalpy, which gives an obtained value of 297 $kJ.mol^{-1}$ that is in good agreement with the previously calculated value developed from the redox potentials in the literature 305 $kJ.mol^{-1}$ [118]. The estimation exhibits an error that is less than 3%.

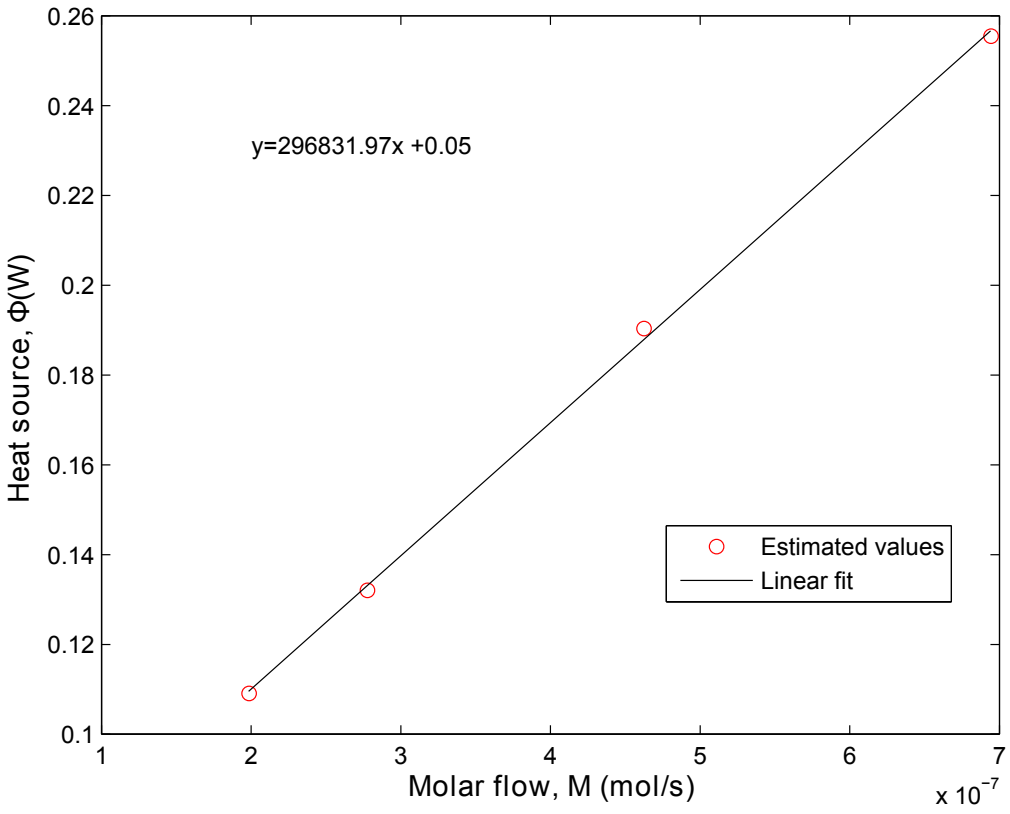

Figure 5.23: Estimated heat source for the redox reaction at a total flow of 10 $mL.h^{-1}$ for different droplet-oil flow ratios (summarized in table 5.6) as a function of the molar flow (M) of the sodium persulfate, i.e., the limiting reactant.

As previously mentioned, the reagents are colorless. When the reagents are introduced in stoichiometric proportions, the precipitation of iodine (I_2) occurs. This is because the iodine (I_2) concentration in the solution exceeds its solubility. Elemental iodine is only slightly soluble in water, with one gram dissolving in 3,450 mL at 20°C and 1280 mL at 50°C. The presence of iodine crystals inside the droplets inhibits our ability to monitor the evolution of the concentration with online spectroscopy techniques.

For this reason, potassium iodide was added in excess to solubilize the iodine (I_2) via the formation of triiodide ions (I_3^-). When I^- is in excess, a second reaction takes place:

$$I^- + I_2 \rightleftharpoons I_3^-$$

The triiodide ion (I_3^-) is a colored species, more specifically, it is yellow; therefore, triiodide is absorbed in the purple region (the complementary color on the color wheel). The kinetics of the redox reaction are studied by UV-vis spectroscopy, where the details of the calibration and experimental measurements performed in batch and online are detailed in appendix H. The technique consists of monitoring the evolution of the color along the channel, where the color is proportionally to the I_2 concentration, as observed in figure 5.24.

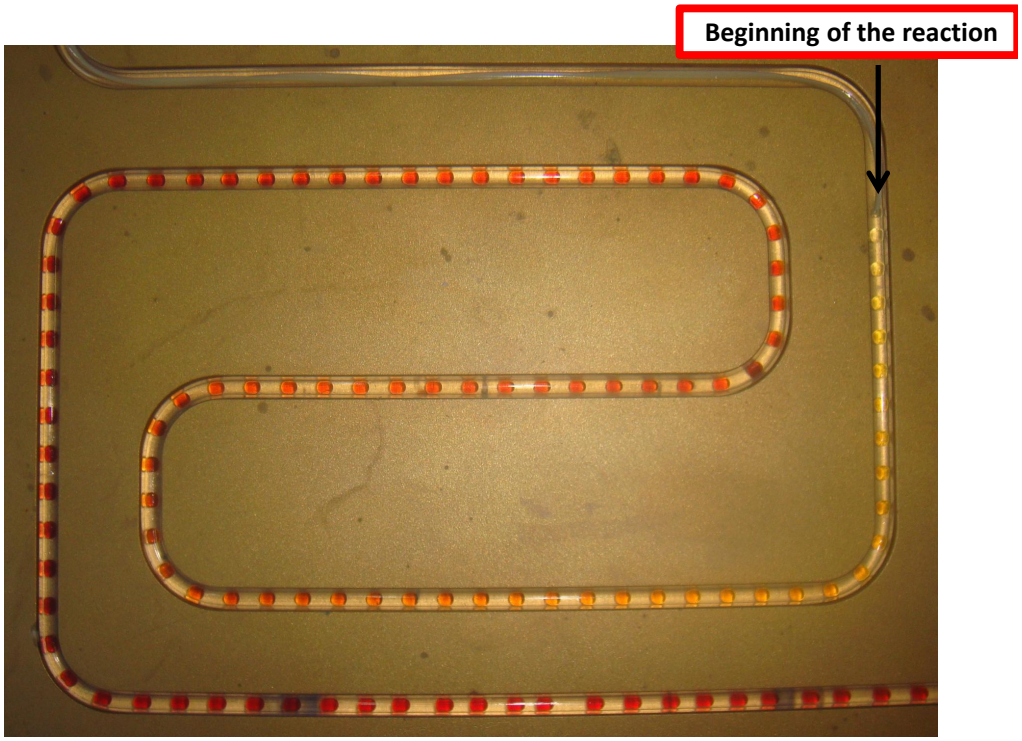

Figure 5.24: An image of the redox reaction occurring along the isoperibolic serpentine chip at Q_T=10 $mL.h^{-1}$. The reagents are initially colorless, then they meet at the inlet (the initial concentration is $C_{Na_2S_2O_8}$=0.2 X10^{-4} M and C_{KI} = 0.06 M). Next, as the reaction proceeds, the droplet turns orange at room temperature. This experiment corresponds to a flow rate ratio of R=2 and a total flow of 10 $mL.h^{-1}$, carried out at room temperature.

It is important to mention that the detection limit of the UV-vis spectrometer, according to the I_2 concentration analysis, was found to be very low at approximately 10^{-4} M. However, this concentration is too low for measurement by the IRT, so the kinetic analysis performed based on IRT had to be carried out at a higher concentration of 10^{-1} M.

⋙ The operating conditions for the spectroscopy analysis were:

- Room temperature,
- A total flow of Q_T=10 $mL.h^{-1}$
- A flow rate ratio of R=2, as described in table 5.6

- An initial concentration of $C_{Na_2S_2O_8}$=0.2 X10^{-4} M
- An initial concentration of C_{KI} = 0.06
- A dilution ratio of 3,000 between the concentration of the reagents ($C_{KI}/C_{Na_2S_2O_8}$)

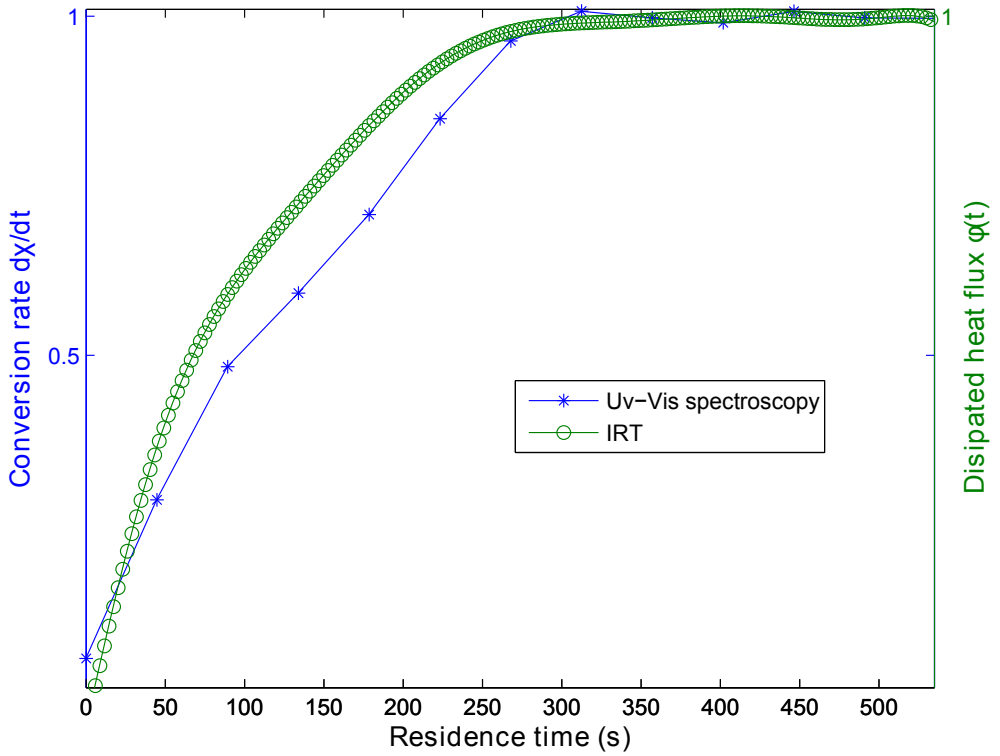

Figure 5.25: Conversion rate ($d\chi/dt$) of the redox reaction can be expressed as a function of time; in the graph, it is represented by blue stars. Additionally, the dissipated heat source as a function of time ($W.s^{-1}$) is represented by green dots on the graph. Both profiles correspond to the same experimental conditions for R=2 and 10 $mL.h^{-1}$, performed at room temperature

The UV-vis kinetics were measured at several positions of the serpentine chip (see figure 5.24), so the conversion rate of the reaction can be compared to the IRT experiment at the same total flow ratio and reaction ratio. This comparison is shown in figure 5.25, where good agreement can be identified, and the profile trends can be observed.

The relationship expressed by equation 5.16 cannot be applied. This is because the concentrations used to study the kinetics by UV-vis spectroscopy and IRT are not the same, so the specifics of the reactions are not identical. However, it is also important to note that the experimental time for measuring the kinetics by UV-vis spectroscopy is approximately 50 hours, while the IRT experiment takes no more than 1 hour.

5.3.2 Click chemistry

″Click chemistry” is a concept that was recently introduced by K. B. Sharpless in 2001 [119]. This novel chemistry approach has proven to be powerful, highly reliable, and useful for performing selective reactions for the rapid synthesis of new compounds and combinatorial libraries by establishing heteroatom links (C-X-C). Click chemistry exhibits high thermodynamic driving forces, usually greater than 40 $kJ.mol^{-1}$. Such chemical processes proceed rapidly to completion and also tend to be highly selective for a single product (single trajectory reactions). The most widely used click reaction is the Huisgen cycloaddition catalyzed by copper(I); this catalysis allows for the selective production of triazole.

We chose to perform the click reaction proposed by Gold et al. [120]. This is a copper-free azide-alkyne cycloaddition used to produce a triazole, so the reaction is performed without a catalyst. Usually, the cycloaddition of a fluorinated ester proceeds within hours at room temperature when using reagent concentrations of 0.5 M (k is the reaction constant, $\approx 10^{-5}\ mol.l^{-1}.s^{-1}$). This work has demonstrated that when the reaction is performed at a higher temperature ($80°C$), 100-fold acceleration of the cycloaddition can be observed. This click reaction utilizing the 4-fluorobenzyl azide (Azide) and ethyl 4,4,4-trifluoro-2-butynoate (Alkyne) to produce 1-(4-fluorobenzyl)-5-(trifluoromethyl)-1H-1,2,3,-triazole-4- carboxylate (oil) is described by the equation schematized in figure 5.26.

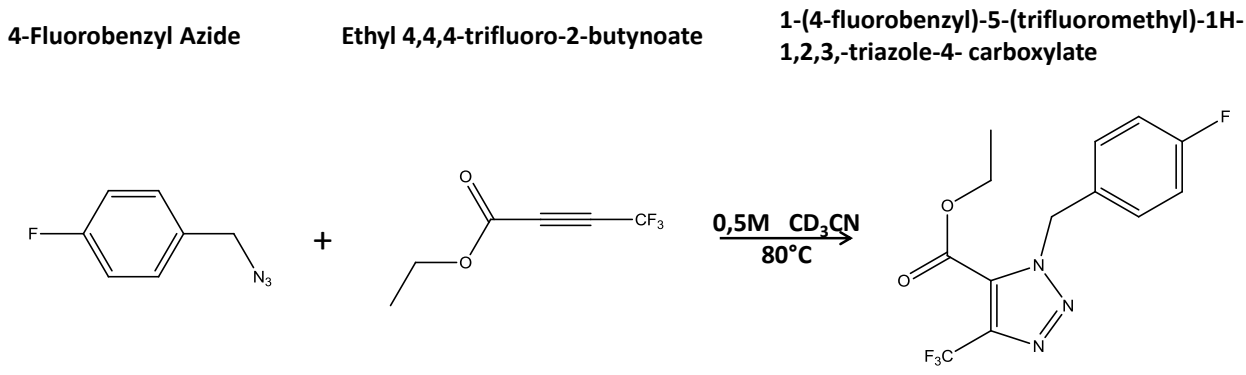

Figure 5.26: Schematic of the click reaction

Deuterated acetonitrile (CD_3CN) solvent was used to perform this reaction. It is important to note two relevant facts: (i) the boiling point of acetonitrile is approximately $82°C$, so the temperature must be strictly controlled at $80°C$ to prevent kinetic modification and bubble formation (due to boiling).

(ii) Deuterated acetonitrile is commonly used to perform RMN mass spectroscopy [1]

- **Experimental conditions**

The reaction is performed at a total flow of 5 $mL.h^{-1}$. The following two reagents are added to the droplets at the same flow rates, $Q_{Azide} = Q_{Alkyne}$, with identical initial concentrations of $C_{Azide} = C_{Alkyne}$=0.25 M. The reagents were introduced in stoichiometric proportions, taking into account the effects of dilution.

- C_{Azide}=0.25 M
- C_{Alkyne}=0.25 M
- Continuous phase of IKV 32 fluorinated oil
- Double-chamber serpentine brass chip heated to 80°C
- 20 mL syringe for the oil and 2.5 mL syringe for each reagent

This experiment is carried out using the double-chamber serpentine chip presented in section 2.2.7. The reagents and the continuous phases are preheated in the first chamber to a temperature of 80°C. Then, inside the second chamber, the reagents meet, and the droplets are generated. The temperature of this chamber is held constant at 80°C. The flow rates are summarized in table 5.7, where the droplet flow is defined as: $Q_G = Q_{Azide} + Q_{Alkyne}$.

R Q_H/Q_G	Oil flow $Q_H, (mL.h^{-1})$	Droplet flow $Q_G, (mL.h^{-1})$
1	2.5	2.5
2	3.33	1.67
3	3.75	1.25
4	4	1

Table 5.7: Experimental droplet-oil flow rate ratios

The temperature profiles of the chemical reaction are described according to equation **??**. In figure 5.27, the continuous contributions for different flow rate ratios (R) are illustrated. It can be observed that the temperatures profile intensity of the reaction tends to decrease with increasing R. When the droplet-oil ratio is low (ex. R=1), the relaxation time is higher, which is proportional to a higher molar flow. Hence, as the ratio increases (to R=4), the molar flow decreases, and the biphasic flow attains the temperature of the isoperibolic chip sooner.

Additionally, we note that the reactive biphasic flow reaches the set-point temperature (room temperature) before the end of the channel, as observed in figure 5.27. Hence, the reaction is completed

[1] Nuclear magnetic resonance spectroscopy, most commonly known as NMR or RMN spectroscopy.

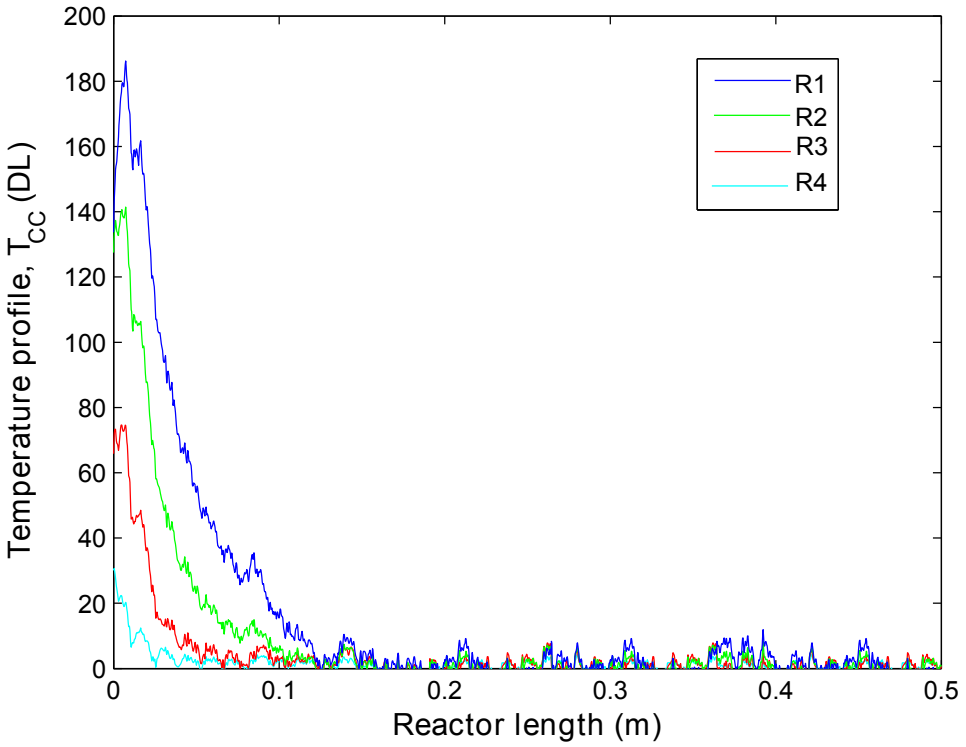

Figure 5.27: Measured continuous contribution for a given total flow rate $5mL.h^{-1}$ of the click chemical reaction carried out at different flow rate ratios, as summarized in table 5.7, and at the initial temperature of $80°C$.

within the channel.

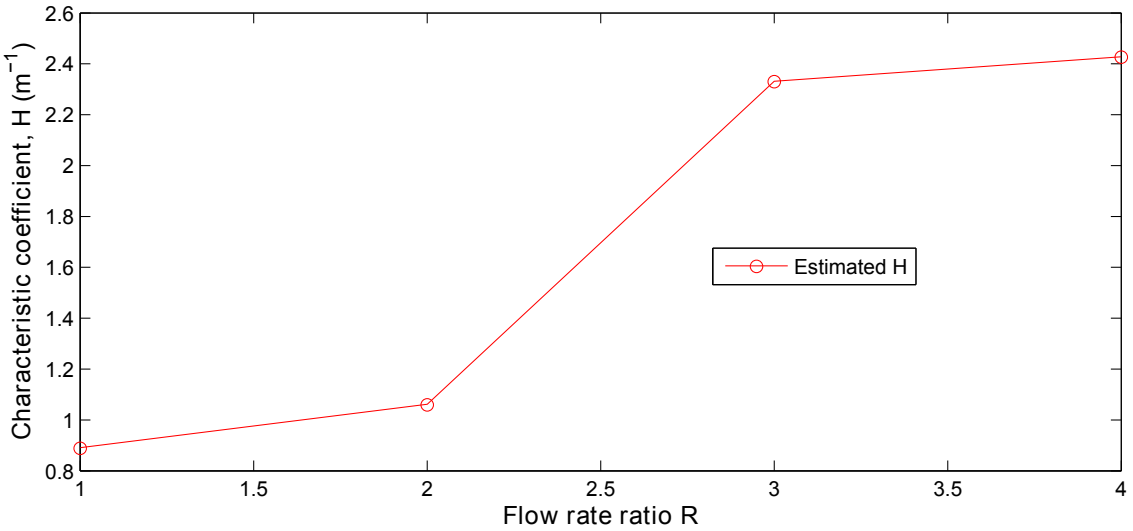

Figure 5.28: Estimation of the characteristic coefficients H (m^{-1}) for various experimental flow rate ratios (R). These characteristic coefficients are estimated from the CC profiles (equation 5.9)

To perform an accurate estimation of the heat source (reaction enthalpy (ΔH)), the characteristic coefficients (H) are estimated when the chemical reaction is complete by using the correlation methodology (see section 4.6.1). Figure **??** shows the H (m^{-1}) characteristic coefficient for each experimental flow performed at rate ratio R. As expected based on the analytical validation (see section 4.6.2), it is

possible to experimentally verify that the H characteristic coefficient tends to stabilize at a constant value after R=3.

Here, the chemical reaction is characterized by the reaction enthalpy (ΔH). To estimate the dissipated heat source, the temperature profiles shown in figure 5.27 are processed according to equation 4.44, taking in account the characteristic coefficient (see figure 5.10). Thus, the dissipated source along the channel is estimated, as shown in figure 5.29. In this figure, it can be observed that the intensity of the dissipated heat source tends to decrease as the ratio increases. This is because the molar flow of the reagents also decreases. It can also be observed that once the maximum heat source has been dissipated, the source remains constant through the channel. Thus, from the estimation of the heat source along the tube $\phi(z)$ ($W.m^{-1}$), as shown in figure 5.29 and by applying equation 5.11, the total dissipated heat source Φ based on the chemical reaction is integrated from the limits of the tubing. Figure 5.30 shows the integrated source Φ as a function of the molar flow rate M of the injected reagents. The molar flow, M ($mol.s^{-1}$), is calculated according to Q_{lim}, which is the limiting reactive flow. Here, M is divided by 2 because the reactive flows ($Q_{Azide} = Q_{Alkyne}$) and the initial concentration are the same ($C_{0Azide} = C_{0Alkyne}$).

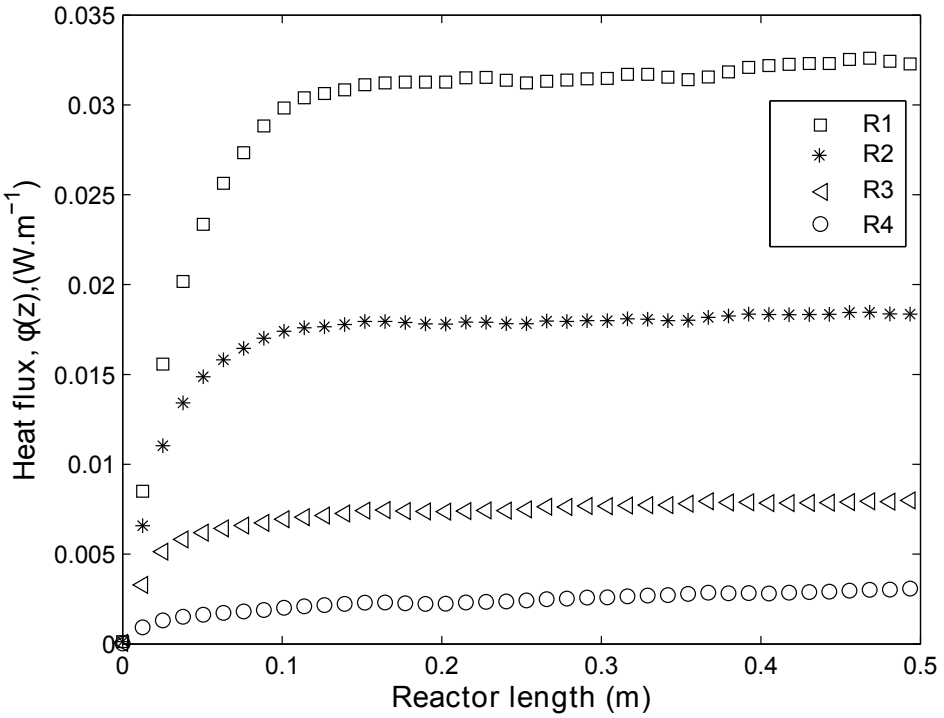

Figure 5.29: Dissipated heat source of the click reaction along the channel

From these data and through a linear regression analysis, the enthalpy of the reaction can be estimated. The estimated slope represents the estimated enthalpy, where the obtained value of 50.5

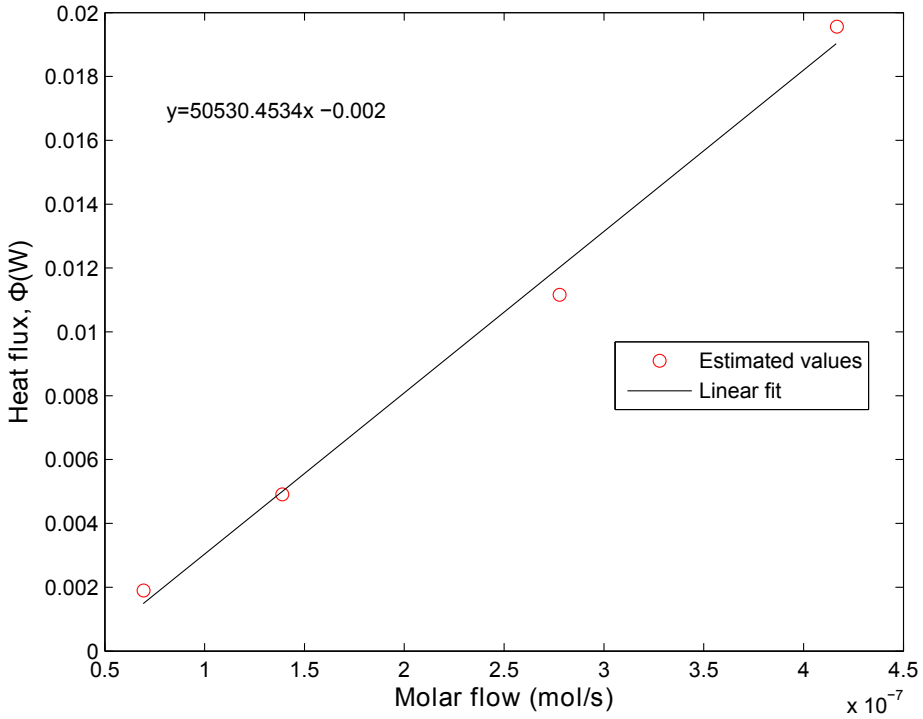

Figure 5.30: Estimated heat source for the click reaction at a total flow of 5 $mL.h^{-1}$ for different droplet-oil flow ratios (summarized in table 5.7) as a function of the molar flow.

$kJ.mol^{-1}$ is in good agreement with that provided from the literature 51.5 $kJ.mol^{-1}$ [120]. The estimation error is less than 2%.

5.4 Conclusion

A non-contact calorimeter, composed of an IR camera and an isoperibolic brass chip, was developed and validated for reactive two-phase flow characterization.

The procedure for obtaining a quantitative estimation of the heat source by using IR thermography was presented. The calibration procedure used to determine the coefficients of conduction (W) and the characteristic coefficient (H) is required. It was also demonstrated that the experimental repeatability of the calibration coefficient estimation is approximately 95%; hence, the estimation is accurately estimated.

From the continuous contribution model, the following results were demonstrated.

- When the chemical reaction occurs inside the droplet, it is possible to estimate the characteristic coefficients (H) to predict the thermal behavior of the flow (i.e., the time or length required to reach the imposed temperature).
- The thermophysical properties of one phase can be estimated when the properties of the other are known with an error less than 5%.

Using the correlation methodology, the thermal heat losses were estimated. Further, the characteristic coefficient H (m^{-1}) at each flow rate ratio (R) was estimated. This procedure was performed for each chemical reaction.

From the heat source validation performed using the acid (HCl)-base (NaOH) reaction, the following results were obtained.

- The enthalpy estimation was carried out with less than 2% error.
- The uncertainties of the repeatability were found to be acceptable. The experimental repeatability for the enthalpy ΔH estimation was approximately 94%, hence the enthalpy was accurately estimated.
- The methodology used to estimate the mixing kinetics of the reaction was verified by comparing the heat source along the channel with the evolution of reaction intensity.
- The determination of an apparent diffusion coefficient was performed, giving the following results.
  - This determination proves that macroscopically, the mixture inside the droplets can be rep-

resented as a diffusion phenomenon, where the species are carried inside with an apparent diffusion coefficient that is more than 10 times the molecular coefficient ($3x10^{-9}$m.s^{-1}).

- As the velocity increases, i.e., the total flow, the mixing process within the droplets is influenced.
- As the length of the droplet decreases, the mixing time decreases proportionally.

Finally, we have shown through two chemical applications that this novel non-intrusive calorimetry technique based on millifluidics and IR thermography is a convenient and powerful tool for the characterization of chemical reactions performed in droplet flows.

The generation of diiode through the reaction between potassium iodide (KI) and sodium persulfate ($Na_2S_2O_8$) was characterized in terms of the reaction enthalpy and kinetics.

- The enthalpy was estimated with less than 3% error.
- The kinetics obtained by UV-vis spectroscopy were compared with the dissipated heat source. Both behaviors show very good agreement.
- Otherwise, this exothermic reaction is very difficult to measure accurately when classic calorimetry techniques are applied (i.e., the reaction is too fast and dangerous).
- IRT techniques were shown to be potential tools for the acquisition of kinetics data. The experimental time required to measure the kinetics by UV-vis spectroscopy is approximately 50 hours, during which several spatial measurements are performed, while an IRT experiment takes no longer than 1 hour and delivers high-resolution measurements (up to 1,200 temperature measurements per image).

The click chemistry reaction between an azide and alkyne for the production of oil was characterized in terms of the reaction enthalpy.

- The enthalpy was estimated with less then 2% error.
- IRT techniques were shown to be potential tools for the acquisition of kinetics data. The experimental time required to measure the kinetics by RMN is costly, and it is very difficult to control the temperature conditions. Further, online spectrum acquisition cannot be used to determine the kinetics (i.e., under the same experimental conditions).
- This exothermic reaction is very difficult to measure accurately when classic calorimetry techniques are applied (i.e., the temperature conditions and the fact that the reaction is dangerous).

Another important and original point developed in this work is the simplicity of the device: this non-contact calorimeter can be used anywhere without special lighting or particular insulation. The isoperibolic chip design based on a millifluidic tubing system can be adapted and rearranged piecewise to fit specific chemical reactions (e.g., a double-chamber application). It is straightforward to change the reactor volume or residence time by changing the inner diameter of the tube, the dimensions of the plate or the path of the tube.

In conclusion, this work has shown that no obstacles are present with respect to estimating the heat source and kinetics of biphasic flows, as a result of applying the proposed methodology, which included a thermal calibration step.

Conclusion and perspectives

This PhD work was dedicated to the development of a non-contact calorimeter for biphasic flows performed in millifluidic tubing based isoperibolic chips. This original under flow and non-contact calorimeter was developed using InfraRed Thermography. This versatile technology was applied to the characterization of chemical reactions taking place inside of droplets of 1 to 3 μl. IRT and millifluidic systems represent a very promising combination for:

- Online thermal analysis
- Quantitative characterization of exo- or endothermic chemical reactions
- High level of security for the study of reactions
- High-throughput platforms

There are very few studies of the thermal analysis of liquid−liquid flows, especially concerning the development of methods for parameter estimation. This work is a pragmatic attempt to implement thermal estimation methods for liquid−liquid two phase flows in miniaturized systems.

The main objective of this exploratory work in the field of thermal microfluidics was to develop new methods to determine the enthalpy and kinetics of chemical reactions in difficult experimental conditions. Indeed, the non-contact calorimeter for biphasic flows was design to be used without any special lighting or particular insulation (i.e., the device is not confined in an isolated chamber).

This work provides the first measurements of the temperature fields of liquid-liquid two phase flows and the estimation of the heat flux and enthalpy of the reaction. To achieve these estimations, our research strategy consisted of:

1. Verifying the stability, reproducibility and velocity of the two phase flow
2. Proposing thermal models in the local space (Lagrangian approach)
3. Simplifying the thermal model to two study cases.

4. Analytical validation of both cases;

5. Experimental validation

A 3D numerical modelling study was presented in order to propose a global overview of the behavior of such biphasic systems. From this study and the experimental study related to the stability and periodicity of the biphasic flow, it was possible to establish hypotheses to simplify the thermal modelling and thus the parameter estimations.

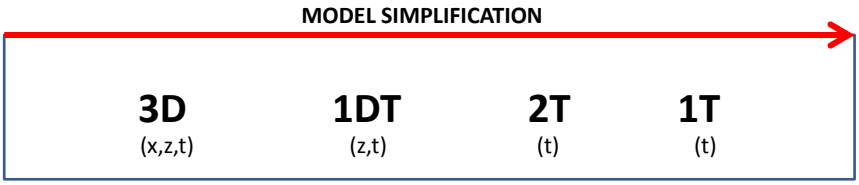

Finally, the 1T homogeneous equivalent media model (CC) is used for the validation of both cases. From the first case, in which no heat source is taken into account ($\Phi = 0$), it can be summarized that:

- The characteristic coefficient (H) can be predicted by the mixing law, which is a function of the thermophysical properties and the lengths of the phases.
- It is possible to estimate the thermophysical properties ρC_p of one of the phases when the other one is assumed to be well known.

From the second case, in which a heat source is taken into account ($\Phi \neq 0$), it can be summarized that:

- The analytical estimation of the heat fluxes showed that there is no obstacle to estimating heat sources in such biphasic flows by applying the proposed methodology.

To achieve the quantitative interpretation of the thermal measurements by IRT, a calibration protocol was developed. This novel calorimeter requires two calibration steps to estimate heat losses; the repeatability of the calibration coefficient estimation was found to be approximately 95%.

- It was experimentally demonstrated that the estimation of the ρC_p of one of the phases is possible with an error lower than 5%.

The device methodology was validated by a well known reaction (acid-base). From the characterization applications of this novel, non-intrusive calorimetry method, it was shown:

- The enthalpy is estimated with an error lower than 3%.

- The kinetics obtained by spectroscopy for slow reactions (reaction time greater than a few minutes) can be predicted at 100% by the IRT technique.
- The IRT technique has proven to be a fast tool for kinetics acquisition. In fact, the experimental time for kinetics acquisition by IRT is 25 times faster than classic online spectroscopy.

⋙ Perspectives

Although the first objective of this novel, non-contact droplet flow calorimeter was to determine the enthalpy and the kinetics of chemical reactions, this device can be applied to solve or understand other types of systems. In fact, this calorimeter was applied to the millifluidic production of metallic microparticles; here, IRT was used to evidence the cooling kinetics of a flow composed of a fusible alloy and a silicone oil. Here, the flow was generated at a high temperature (in order to obtain a liquid metal) and then cooled to promote solidification. The typical averaged temperature profiles (CC) obtained are shown in figure 5.31. Some preliminary thermal analysis was performed to estimate the dissipated heat due to the phase transition (solidification), and the enthalpy of solidification was found to be 26 $kJ.kg^{-1}$, which is in reasonable agreement with measurements performed on the same metal with conventional calorimetry 20 ±0.5 $kJ.kg^{-1}$.

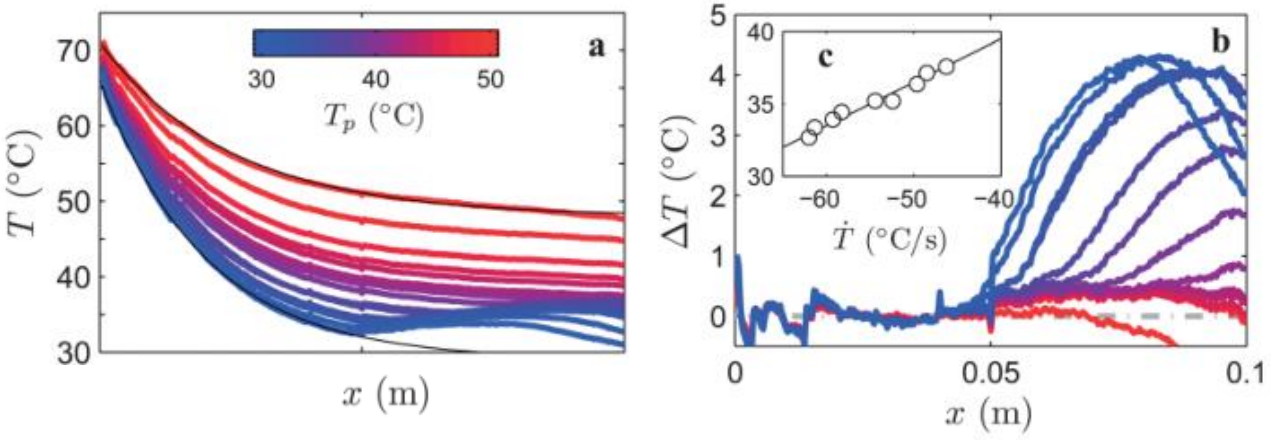

Figure 5.31: Time-averaged temperature profiles (CC) measured with IRT when the temperature T_p of the flow stage is diminished progressively (color-coded) below the solidification point of the alloy, while keeping the flow conditions constant. b) Difference between temperature profiles and exponential relaxation. c) Temperature at which heat starts to be released and the cooling rate of the drops.

Other types of materials with phase transitions can be easily studied with this method. Furthermore, the experimental protocol is very fast compared to that of conventional calorimetry (DSC).

In addition, it would be interesting to apply this technique to biological droplet based systems in order to determine heat capacities as a function of the bacteria concentration inside the droplets. Indeed, fermentation reactions will also be interesting to study under this original configuration.

From a chemical point of view, this novel tool may provide the opportunity to access kinetic reactions that are difficult to measure or that are dangerous. In addition, it might be interesting to estimate kinetic reaction constants, rates and activation energies from the IRT kinetics measurements and to compare them to spectroscopy measurements, in the case of:

- Polymerization
- Synthesis of organic molecules
- Synthesis of new materials

that might require specific temperatures and other conditions.

In fact, the developed analytical solutions can be applied to other two phase flow systems beyond liquid-liquid systems, such as liquid-gas, solid-liquid or solid-gas systems. Therefore, the method can be used to design miniaturized super heat exchangers, among many other applications.

Appendices

Appendix A

Appendix

The thermal regulation system: Power dissipation estimation

The power to be dissipated must be calculated to design the size of the equipment needed to control the temperature. The calculations are performed for working conditions of:

- from 20 to -10 ° C with a $\Delta T = 30$ and
- from 20 to 100 ° C with a $\Delta T = 80$.

Here, we have decided to use four Peltier modules, each of which has a cooling power of 80 watt; this power is more than that needed to control the imposed temperature. From a practical point of view, it is better to use four Peltier modules instead of two, because Peltier modules can have different performances, which can induce a temperature gradient. When four modules work at a lower level than the maximum, the cooling performances of the respective modules exhibit rather similar behaviors; as a result, it is possible to reduce significantly the gradient effect. Peltier modules protected by TEFLON were selected for this work.

Dimension of the Aluminium plate					
		L (m)	l (m)	h (m)	V (m3)
Parameters		0,15	0,12	0,003	0,000054
µ (kg/m3)	2700				
V (m3)	0,000054				
m(kg)	0,1458				
Cp (J/kg/K)	900				
Dimensions of the brass plate					
		L (m)	l (m)	h (m)	V (m3)
Parameters		0,15	0,12	0,004	0,000072
µ (kg/m3)	8600				
V (m3)	0,000072				
m(kg)	0,6192				
Cp (J/kg/K)	380				
System characteristics					
Tamb (°C)	20				
Tf (°C)	-10				
Tc (°C)	100				
M tot (kg)	0,765				
Cp eq (J/kg/K)	438,79647				
Power to be dissipated to switch from 20°C à -10°C Δt=30 (Tamb-Tf) :					
Cooling					
ΔT (K)	30				
P (J)	10070,379				
Cooling time (min)	10	15	20		
Cooling time (s)	600	900	1200		
P (W)	16,783965	11,18931	8,3919825		
17 W to be dissipated to switch from 20°C à -10°C in 10 minutes					
Power to be dissipated to switch from 20°C à 100°C Δt=80 (Tamb-Tf) :					
Cooling					
ΔT (K)	80				
P (J)	26854,344				
Cooling time (min)	10	15	20		
Cooling time (s)	600	900	1200		
P (W)	44,75724	29,83816	22,37862		
45 W to be dissipated to switch from 20°C à 100°C in 10 minutes					

Appendix B

Appendix

Sensitivity analysis of the 2T thin body model

Through the analysis presented here, it is possible to study the sensitivity of the model with respect to various parameters. The simplified analytical model previously described in section 4.3.2 is used here. This study is focused on the estimation of effective heat exchange coefficients according to different experimental configurations, determined by the chemical reactions used. The aim is to represent a wide range of configurations of chemical reactions (i.e., droplet lengths). Because the chemical reactions are mostly performed using dilute solutions, we can assume that the thermal properties of the chemical reactants are the same as pure water. The thermal properties of the fluids, namely, the various representative cases of chemical reactions, are reported in tables B.1, B.2 and B.3. In these tables, the investigated conditions are the inlet temperature of the fluids or plate, the surface area-to-volume ratio related to the droplet size (and thus to the flow rate ratio) and the values of the convective heat exchange coefficients (h), calculated from the Nusselt number. The values in tables B.1 and B.2 were applied to the effective heat transfer equations 4.29. The H values used are summarized in table B.3. These H values (the effective heat transfer coefficients) are used to provide an adapted order of magnitude to the heat exchanges in the sensitivity analysis.

C_{pH}	C_{pE}	$?_H$	$?_E$	$d_H = d_G$	$h_{GH} = h_{HG}$	μ_G	μ_H
$J.kg^{-1}.K^{-1}$	$J.kg^{-1}.K^{-1}$	$kg.m^{-3}$	$kg.m^{-3}$	m	$W.m^{-2}.K$	Pa.s	Pa.s
1370	4180	920	1000	$1.6x10^{-3}$	211.5	3.8	$1x10^{-3}$

Table B.1: Physical properties of the fluids

In figures B.1 to B.4, the four sensitivity cases are shown. Each case has three graphs: (A) the temperature profile of the two media, (B) as estimated from equation B.1, where β represents the parameters for which the partial derivatives are calculated and then normalized by the derivative

.	T_{G0}	T_{H0}	T_P	L_G	L_H	h_{GP}	h_{HP}
.	K	K	K	m	m	$W.m^{-2}.K$	$W.m^{-2}.K$
CASE 1	303	303	298	$1x10^{-3}$	$1x10^{-3}$	840	1560
CASE 2	*	*	*	*	$3x10^{-3}$	*	520
CASE 3	323	298	298	$1x10^{-3}$	$1x10^{-3}$	840	1560
CASE 4	*	*	*	*	$3x10^{-3}$	*	520

Table B.2: Parameters of the sensitivity analysis cases. * represents the same value as above

.	H_{GP}	H_{GH}	H_{HG}	H_{HP}
.	s^{-1}	s^{-1}	s^{-1}	s^{-1}
CASE 1	0.5	0.74	2	2.55
CASE 2	0.5	0.74	2	0.85
CASE 3	0.5	0.74	2	2.55
CASE 4	0.5	0.74	2	0.85

Table B.3: Calculated effective heat exchange coefficient for the sensitivity analysis

parameter, and (C) only the sensitivity curves of the parameters that can be estimated, each normalized by its maximum, to improve the graphical observation with respect to time.

$$S_\beta = \frac{\partial T}{\partial \beta} \times \frac{1}{\beta} \tag{B.1}$$

- Sensitivity analysis: Case 1

As illustrated in figure B.1, where the inlet temperatures of both phases are equal, as well as their characteristics dimensions, only the heat exchange coefficients are different, as summarized in tables B.2 and B.3. We note in figure B.1.A that even if the inlet temperature of each medium is the same, the continuous phase (oil) quickly reaches the temperature imposed by the wall. This can be explained by the fact that the overall heat transfer coefficient H_{HP} (exchange oil-wall) is larger than H_{GP} (the coefficient drop of the wall); therefore, the sensitivity is more important for the oil-wall coefficient. The coefficient of the oil-wall exchange shows a strong correlation with the fluid-fluid coefficients (H_{GH}, H_{HG}) (see figure B.1.B). However, the normalized sensitivity confirms that the effective exchange H_{HP} parameter can be estimated with the best accuracy (see figure B.1.C).

- Sensitivity analysis: Case 2

As illustrated in figure B.2, this example is similar to case 1, except that the characteristic length of the oil phase has been increased (3 times). Increasing the distance between two successive drops leads to a decrease in the coefficient H_{HP} (exchange oil-wall) (B.3). In figure B.2.A, the temperature profile of the oil phase exhibits a weak exchange with the wall, compared to the previous case, and reaches the imposed wall temperature at the same time as the droplet (water). Similarly, in figure B.2.B, a

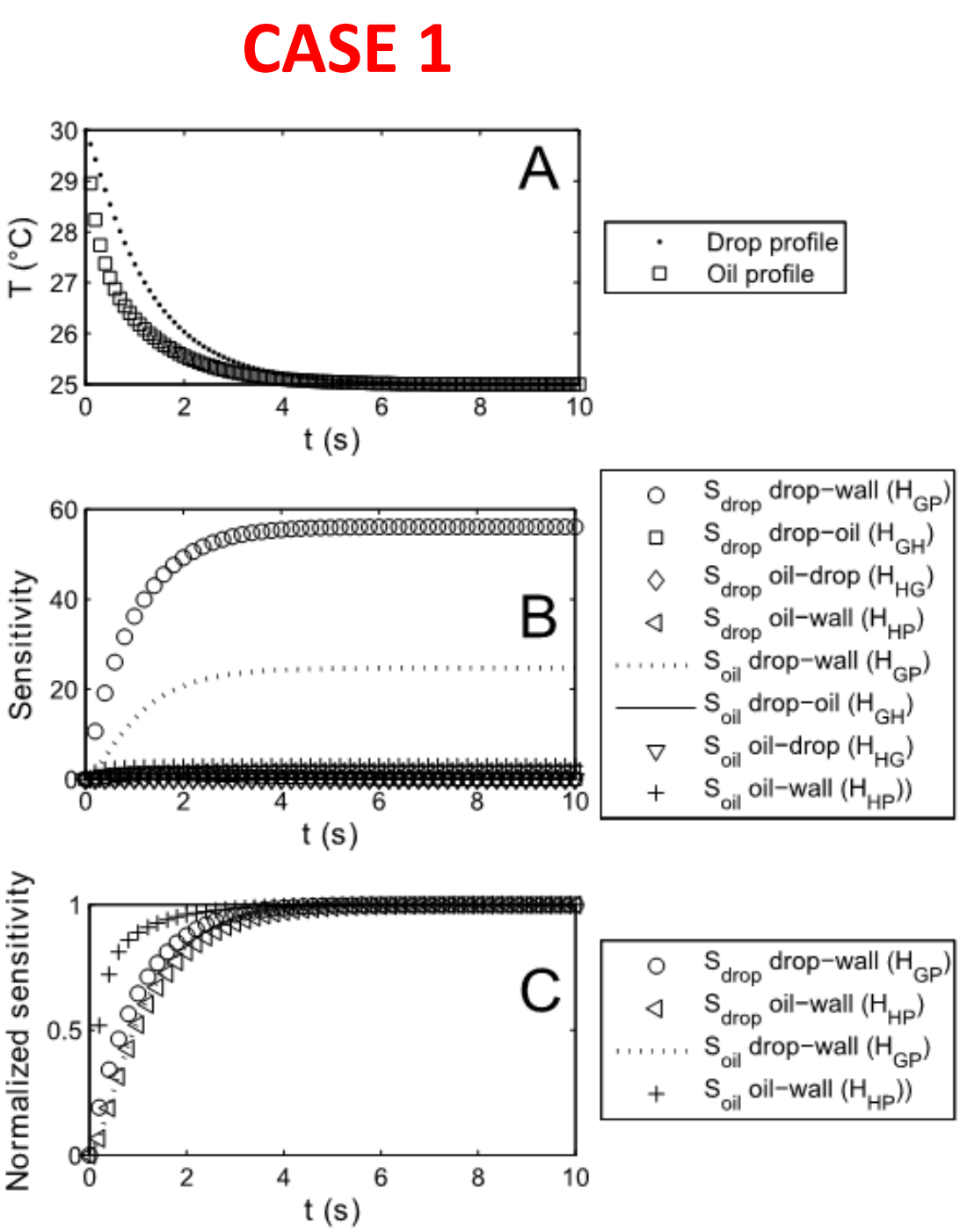

Figure B.1: A) Temperature profiles of a droplet and the oil. B) Sensitivity of the temperature profiles according to the derivative of each H coefficient. C) Normalized sensitivity.

high degree of sensitivity for the H_{HP} coefficient estimation can be seen at long times. In contrast, in figure B.2.C, a high degree of sensitivity at short times can be observed for the estimation of H_{HP} and H_{GP}.

- Sensitivity analysis: Case 3

As illustrated in figure B.3, case 3 is similar to the case 1, with the same characteristic dimensions

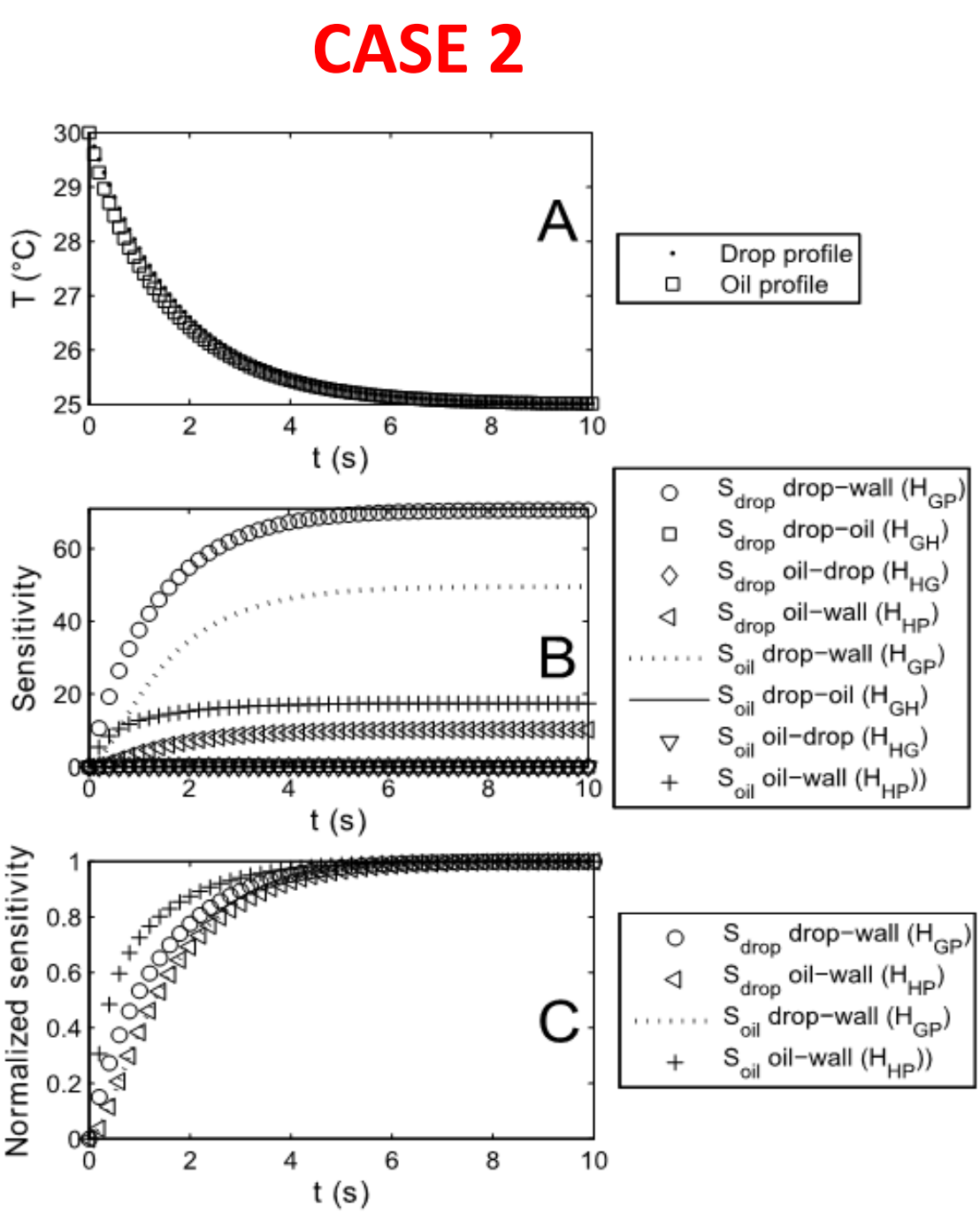

Figure B.2: A) Temperature profiles of a droplet and the oil. B) Sensitivity of the temperature profiles according to the derivative of each H coefficient. C) Normalized sensitivity.

of the fluids but different inlet temperatures (see table B.3). The inlet temperature of the droplet is higher, whereas the temperatures of the oil and plate are equal. In figure B.3.A, the oil temperature profile highlights the exchanges with the droplet and between the oil and wall. As shown in figure B.3.B, strong sensitivity for the H_{GP} coefficient (droplet-wall) is apparent. Finally, according to figure B.3.C, the dominant exchange at short times is between the droplet and the oil, which promotes the estimation of the H_{HG} coefficient. Additionally, a strong correlation can be observed, which will cause

estimation problems.

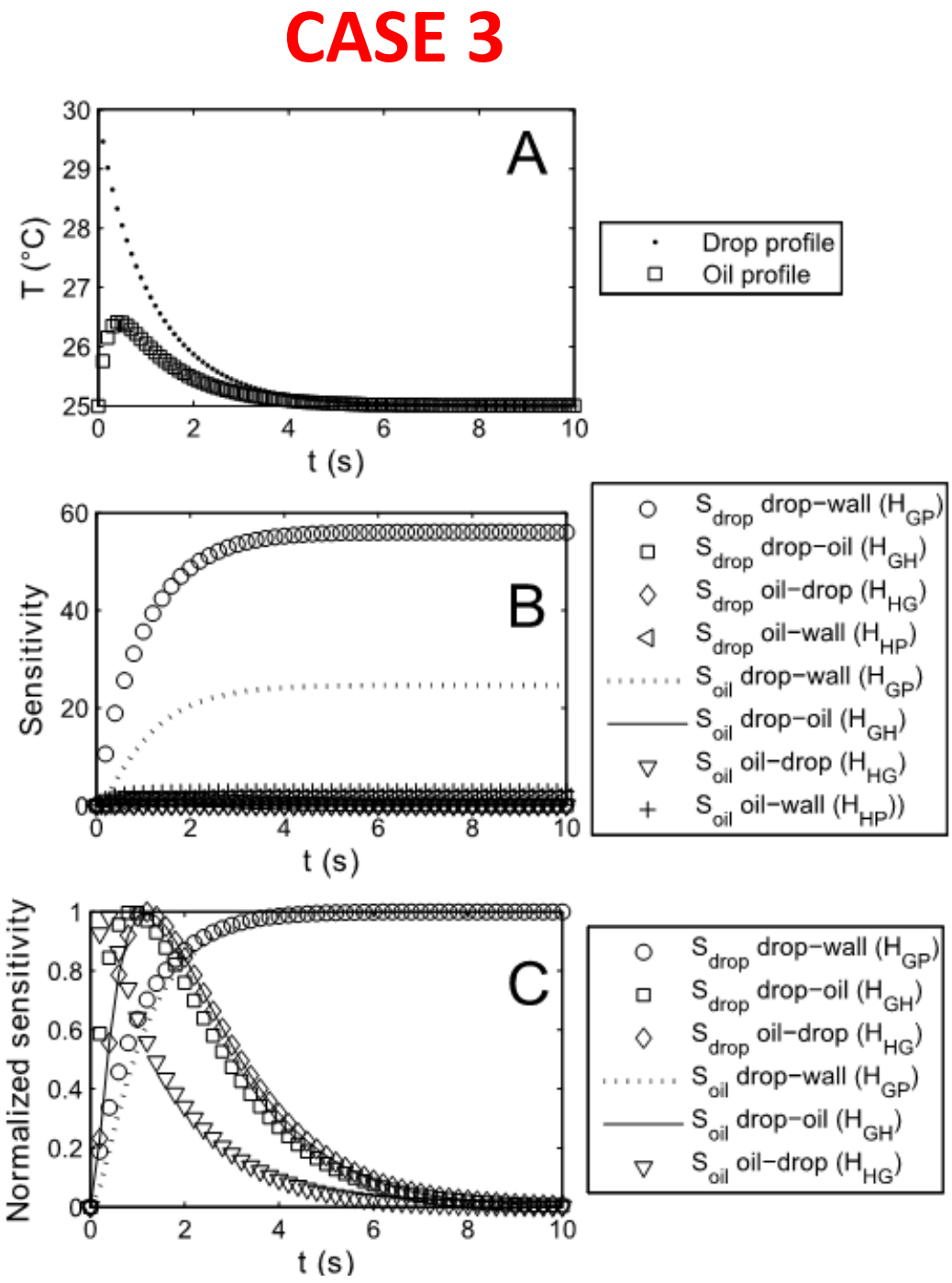

Figure B.3: A) Temperature profiles of a droplet and the oil. B) Sensitivity of the temperature profiles according to the derivative of each H coefficient. C) Normalized sensitivity.

- Sensitivity analysis: Case 4

As illustrated in figure B.4, case 4 is similar to case 3, excepted that the characteristic length of the oil phase has been increased. Increasing the distance between two successive drops leads to a decrease of the coefficient H_{HP} (the oil-wall exchange) (table B.3). In figure B.4.A, the temperature profile of the oil phase exhibits a weak exchange with the wall but a stronger exchange with the droplet. However,

figure B.4.B demonstrates the strong sensitivities of the H_{GP} coefficient (droplet-wall) as well as the H_{HP} coefficient (oil-wall). In contrast, as shown in figure B.4.C, it is possible to estimate successively the coefficients H_{GH} and H_{HG} (drop-oil exchanges) at short times. Additionally, a strong correlation is observed, which will cause estimation problems.

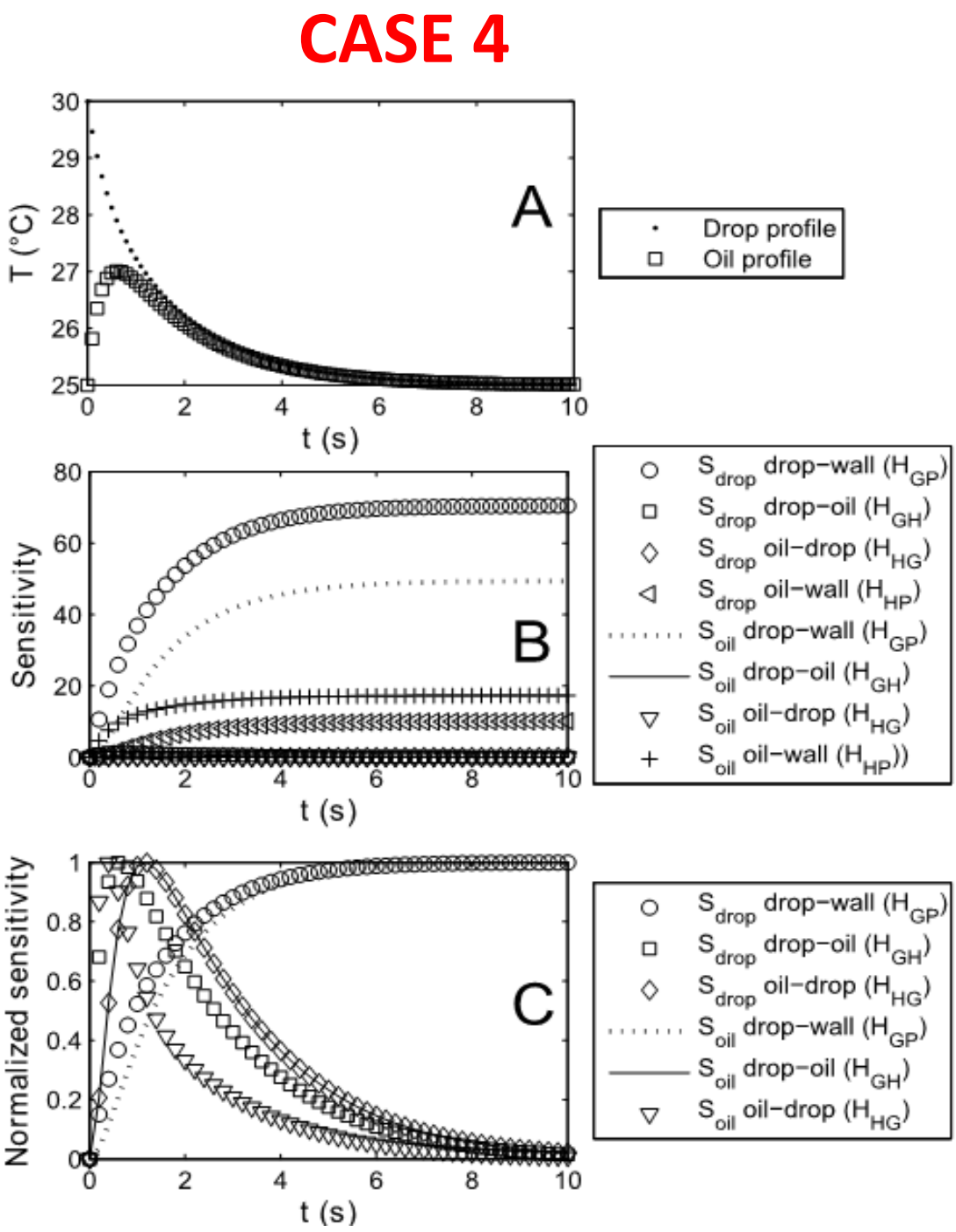

Figure B.4: A) Temperature profiles of a droplet and the oil. B) Sensitivity of the temperature profiles according to the derivative of each H coefficient. C) Normalized sensitivity.

The solutions obtained from the inverse method are highly sensitive to correlations and to measurement errors, and in some cases, the obtained solution might be non-unique. This sensitivity analysis

will define the experimental design and the associated measurement procedure, which are primary contributors to the quality of the results. In conclusion, this sensitivity analysis aids our study of the best experimental conditions in terms of estimation, further allowing us to estimate accurate parameter values through inverse processing.

Finally, to perform the best estimation of the H coefficient, the sensitivity analysis shows that a temperature difference between the phases and different lengths of the plugs may increase significantly the accuracy of the estimation of the effective heat transfer coefficient for the droplet oil exchanges. Regarding the estimation of either the oil−wall or droplet−wall exchange, the initial temperatures of both phases must be the same, and the wall temperature must be different, to carry out an accurate estimation of this coefficient.

In summary, two thermal scenarios are identified:

1. The inlet temperature of both phases is the same, while the temperature of the wall is different.
2. The inlet temperature of the droplet is different from those of the oil and the wall (i.e., a chemical reaction occurs inside the droplet).

Appendix C

Appendix

To study the influence of the boundary conditions, the 2T thin body model is applied (see section 4.3.2), without the contribution of any heat source. Thus, the temperature profiles are generated for different flow rate ratios ranging from R=0.5 to 12 by using the following strategy.

- The interfacial heat exchange coefficient between the phases is fixed at h_i=223 $W.m^{-2}.K^{-1}$, and three different boundary condition values for the heat coefficient h_p are applied, such as:
  - Adiabatic, where the tubing is inserted into thermal insulator
  - Isoperibolic, where the tubing is inserted into bulk brass (the case in this work)
  - Isothermal, where metallic tubing is inserted into bulk brass

  To observe the parietal exchanges and the dynamic thermal response of the biphasic flow under such conditions, the resulting behaviors are illustrated in figures C.1 to C.3.
- The parietal heat exchange coefficient is fixed at h_p=150 $W.m^{-1}.K^{-1}$, which is on the order of the magnitude of an isoperibolic condition, and three different values of the heat exchange coefficient h_i at the interface are applied, such as:
  - Adiabatic, where no heat exchange occurs between the two phases
  - Isoperibolic, where diffusion and convection occur at the interface (the case in this work)
  - Isothermal, where infinite heat exchange coefficients exist between the phases

  The interfacial exchanges and the dynamic thermal response of the biphasic flow under such conditions were investigated. The results are illustrated in figures C.4 to C.6.

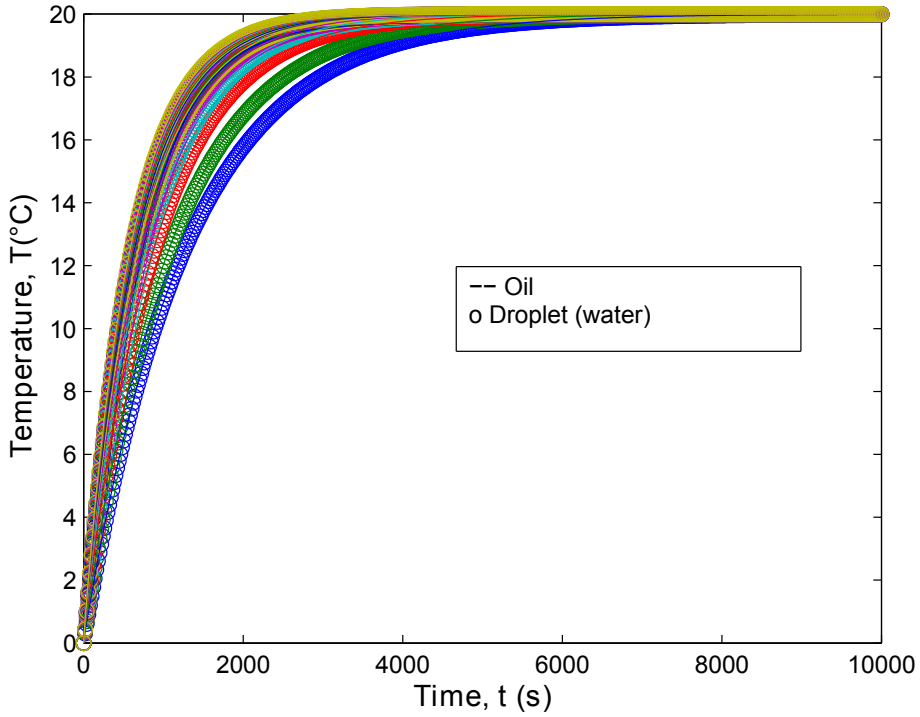

Figure C.1: Thermal behavior of the temperature profiles when the interfacial coefficient between the phases h_i is fixed and the imposed boundary condition is adiabatic h_p=1 $W.m^{-2}.K^{-1}$.

In the first study, the interfacial heat exchange coefficient between the phases is fixed (h_i), and the heat coefficient h_p of the boundary conditions are varied. The first case is illustrated in figure C.1, where an adiabatic condition h_p is imposed. This example reveals that the predominant exchange occurs between both phases ($h_i \lll h_p$). It can be observed that both phases have the same temperature evolution profiles and that the characteristic time to reach steady state is very long $t_{final} = 8,000$ s due to the adiabatic boundary condition.

The second case is illustrated in figure C.2, where an isoperibolic condition h_p is imposed. This example reveals a competition between the exchanges among the phases and toward the wall because the h coefficients are almost of the same order of magnitude ($h_p \approx h_i$). In this case, due to the isoperibolic boundary condition, the time to reach steady state (i.e., the imposed T_p temperature) is significantly decreased compared to the adiabatic case ($t_{final} = 50$s instead of 8,000 s). This demonstrates the interest in working under isoperibolic conditions. Moreover, depending on the ratio R between each phase, the thermal varies. For example, at R=0.5 (see the blue curves in figure C.2), the temperature evolution of the droplet is close to that of the water, whereas the temperature evolution of the oil plug is also close to that of the water. Moreover, when R increases, the behavior of each phase tends to the limit of each respective phase alone

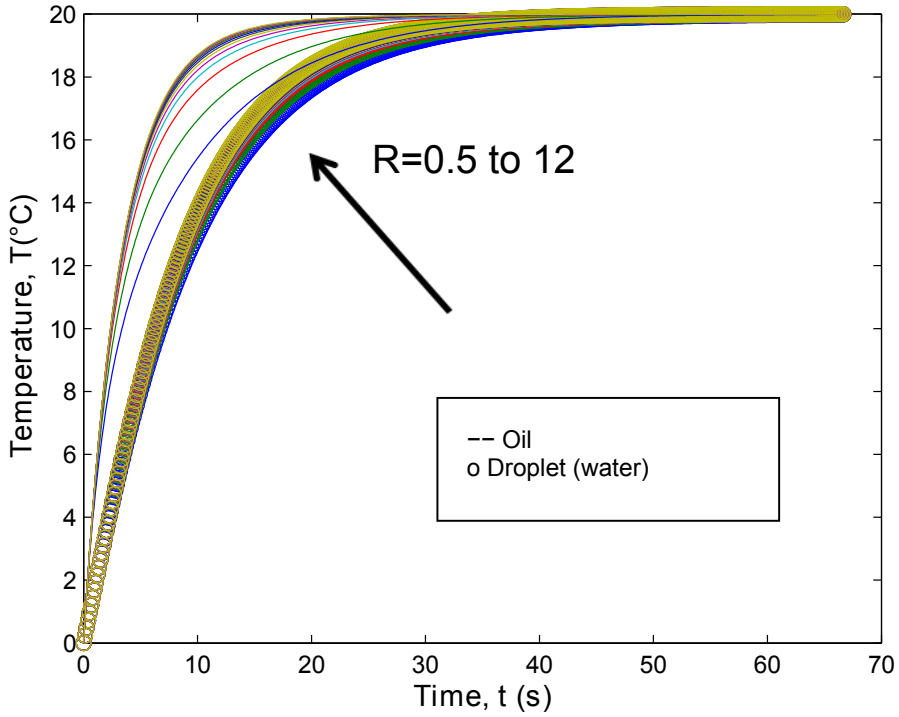

Figure C.2: Thermal behavior of the temperature profiles when the interfacial coefficient between the phases h_i is fixed and the imposed boundary condition is isoperibolic h_p=150 $W.m^{-2}.K^{-1}$.

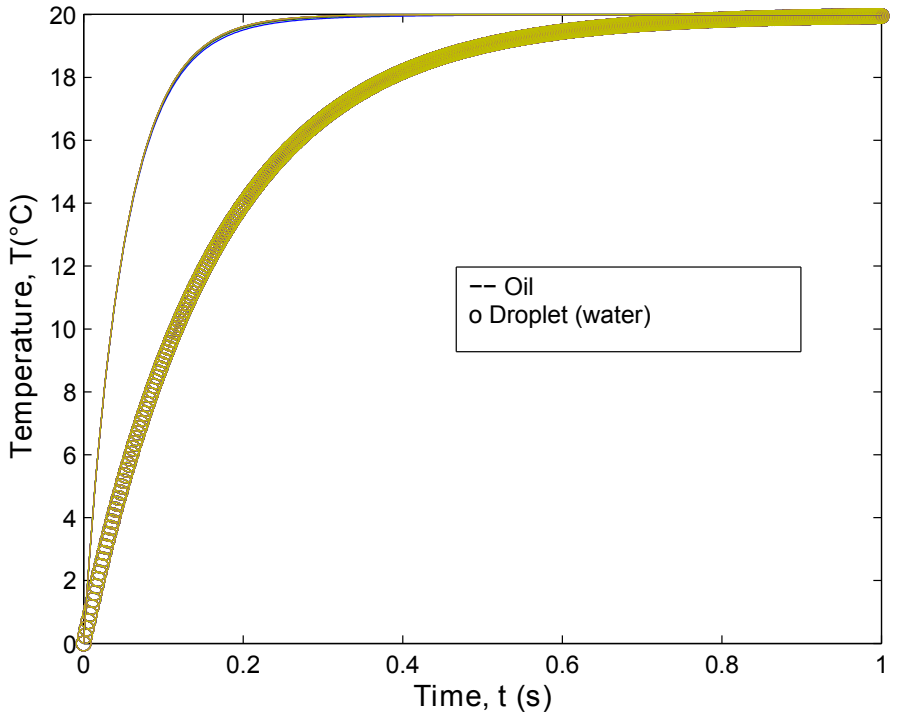

Figure C.3: Thermal behavior of the temperature profiles when the interfacial coefficient between the phases h_i is fixed and the imposed boundary condition is isothermal h_p=1,000 $W.m^{-2}.K^{-1}$.

The third case is illustrated in figure C.3, where an isothermal condition h_p is imposed. This example reveals that the predominant heat exchange occurs through the wall ($h_p \ggg h_i$), so the dynamic re-

sponse of each phase to attain the wall temperature is in agreement with the thermophysical properties (c.f. ρC_p) of the system. No exchange between the phases is exhibited. The oil phase reaches the temperature imposed by the wall within 0.2 s, while the droplet takes almost 1 s. Additionally, no dependence on the ratio R is observed.

The first case illustrated in figure C.4, where an adiabatic condition h_i is imposed at the interface of both phases, is explored in comparison to the second study, where the heat coefficient h_p of the boundary conditions is fixed (isoperibolic) and the interfacial heat exchange coefficient between the phases is changed (h_i). The comparison reveals that the predominant exchange occurs toward the wall, and no exchanges are observed between the phases because of the adiabatic condition. The dynamic response of each phase with respect to attaining the wall temperature is in agreement with the thermophysical properties (c.f. ρC_p) of the system. The oil phase reaches the temperature imposed by the wall within 20 s, while the droplet takes nearly 60 s. Additionally, no dependence on the ratio R is observed.

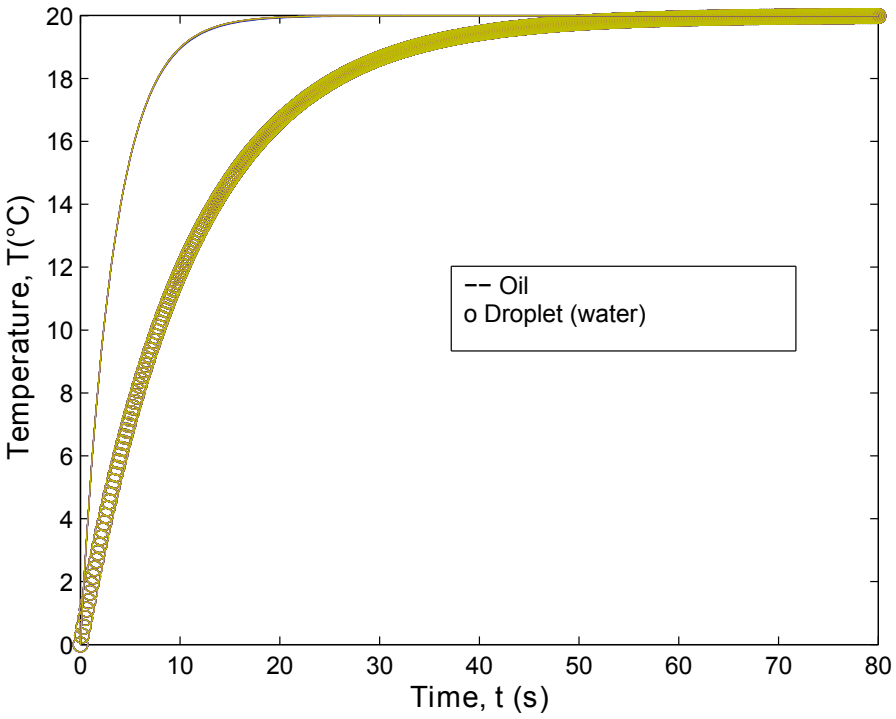

Figure C.4: Thermal behavior of the temperature profiles when the parietal coefficient h_p is fixed and the imposed boundary condition between the phases is adiabatic h_i=1 $W.m^{-2}.K^{-1}$.

The second case illustrated in figure C.5, where an isoperibolic condition h_i is imposed at the interface of both phases, reveals a competition between the exchanges among the phases and toward the wall because the h coefficients are almost on the same order of magnitude ($h_p \approx h_i$). This affects the dynamic response to attaining the wall temperature. Similarly, a weak dependence on the ratio R is

observed.

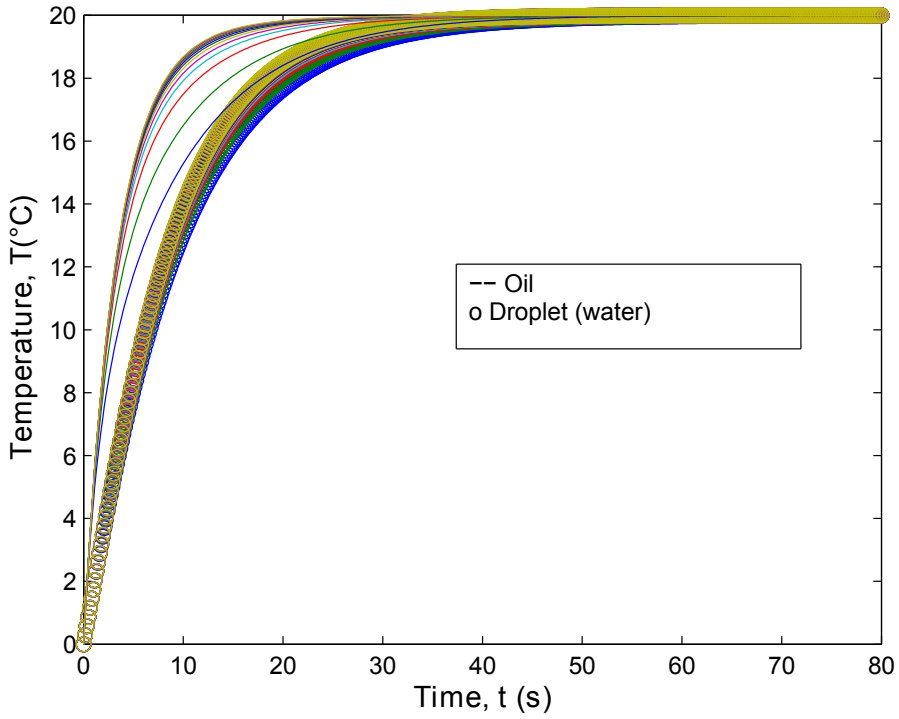

Figure C.5: Thermal behavior of the temperature profiles when the parietal coefficient h_p is fixed and the imposed boundary condition between the phases is *quasi* isoperibolic h_i=150 $W.m^{-2}.K^{-1}$.

The third case is illustrated in figure C.6, where an isothermal condition h_i is imposed at the interface of both phases, revealing that the predominant exchange occurs between the phases ($h_i \ggg h_p$). As a result, the exchange between the phases is enhanced, and both phases behave with the same dynamic response with respect to attaining the wall temperature. The influence of the ratio R can be outlined: when the ratio R is low (the lower oil volume fraction, plotted in blue), more time is required to reach the wall temperature (40 s). In contrast, when the ratio R is higher (the higher oil volume fraction, plotted in yellow), the wall temperature is reached within 20 s.

In summary, when the boundary condition for the wall h_p is adiabatic, the dynamic response time is very slow (8,000 s), and exchanges between the phases predominate. In contrast, when the h_p is isothermal, the dynamic response time is very fast (1 s). From the theoretical and experimental points of view, working with an isoperibolic condition is an excellent compromise when studying chemical reactions and thermal analysis.

However, from an experimental point of view, the boundary condition at the interface of both fluids, given by h_i, is controlled by the thermophysical properties of the phases. For example, an adiabatic boundary condition can be imposed when the biphasic flow is performed by using a gas as the con-

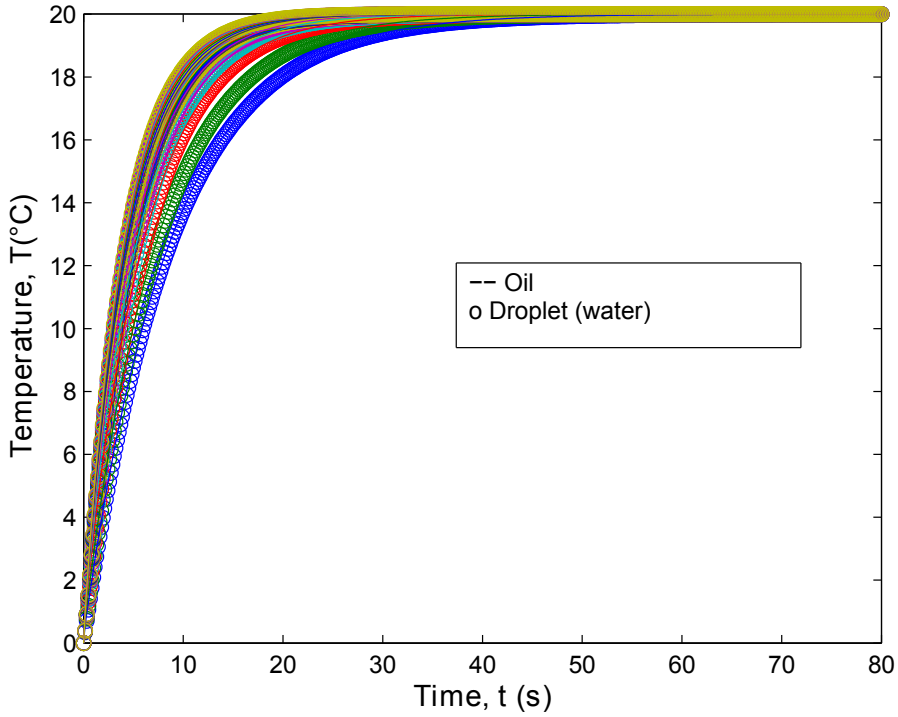

Figure C.6: Thermal behavior of the temperature profiles when the parietal coefficient h_p is fixed and the imposed boundary condition between the phases is isothermal h_i=1000 $W.m^{-2}.K^{-1}$.

tinuous phase. In contrast, an isothermal boundary can be imposed when the biphasic flow is carried out with the use of a medium with high thermal conductivity, such as a liquid metal, or more specifically, mercury. Oil appears to give an isoperibolic boundary because the thermal conductivity (0.25 $W.m^{-1}.K^{-1}$ is almost on the same order of magnitude as that of water (0.6 $W.m^{-1}.K^{-1}$).

Appendix D

Appendix

A study of the signal-to-noise ratio (SNR)

To test the influence of the noise induced by the temperature measurement uncertainties on the inverse method, synthetic case 3 (as described previously in sectionB) is illustrated in figures D.1 to D.3 with several signal-to-noise ratios (SNRs). These profiles are generated with the developed analytical solutions described by equations 4.30 and 4.31. The temperature profiles for oil and water are shown in figure D.1, representing the synthetic case in which a level of noise equal to $\sigma = 0.05$ is added to each profile. In the same graph, the temperature profile estimations are performed by the model, which then plots the estimations as stars and crossings (*,x). The same profiles are plotted with different noise levels of $\sigma = 0.3$ in figure D.2 and $\sigma = 1$ in figure D.3.

The results obtained for different SNRs and the related parameter estimation errors are summarized in figure D.4. The three levels of noise are analyzed (Gaussian variance σ), revealing that the precision of the estimation decreases with increasing noise. Nevertheless, even for an important SNR of 6.25, when compared to the error given by our experimental device (the IR camera (SNR=100)), small estimation errors of the H coefficients ($< 3\%$) and the initial temperatures ($< 10^{-2}$) are obtained. Thus, the relative residuals were calculated to the noisiest case (σ=1), as represented in figure D.4.C, based on the following:

$$\epsilon = \frac{T_{model} - T_{exp}}{T_{model}} * 100 \tag{D.1}$$

The residuals are plotted in figure D.5. These values are in good agreement with the SNR introduced into the analytical solution. The value of the error is equal to 3%, which corresponds to 3σ.

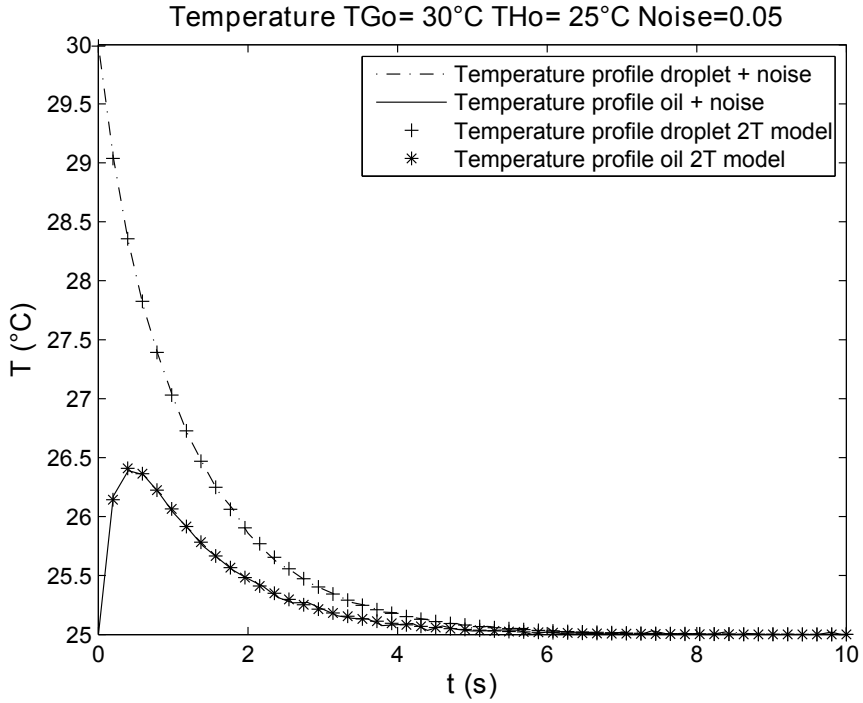

Figure D.1: Temperature profiles for oil and water with a noise level of $\sigma = 0.05$ and the estimated profiles by the model

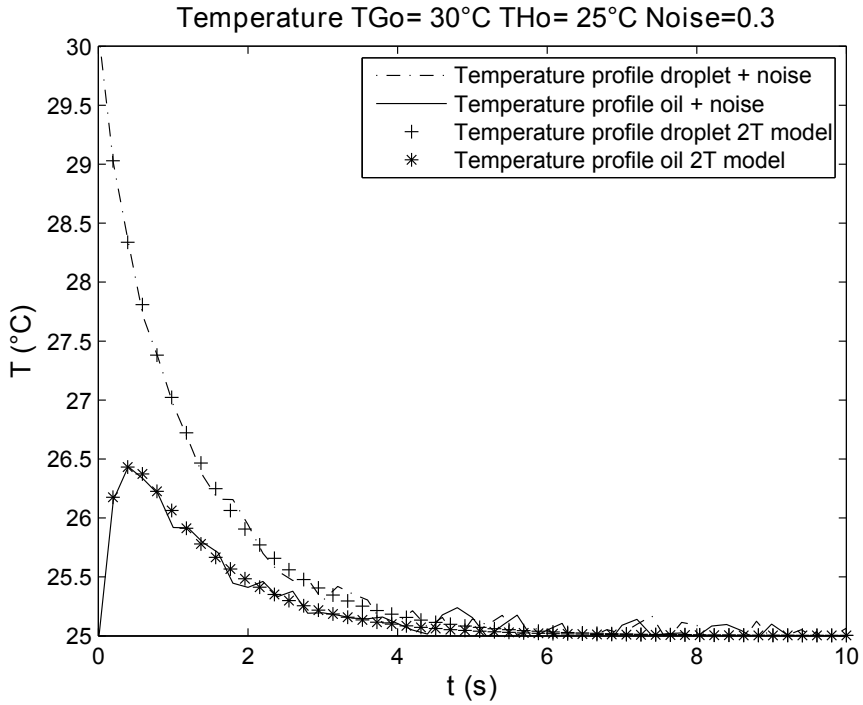

Figure D.2: Temperature profiles for oil and water with a noise level of $\sigma = 0.3$ and the estimated profiles by the model

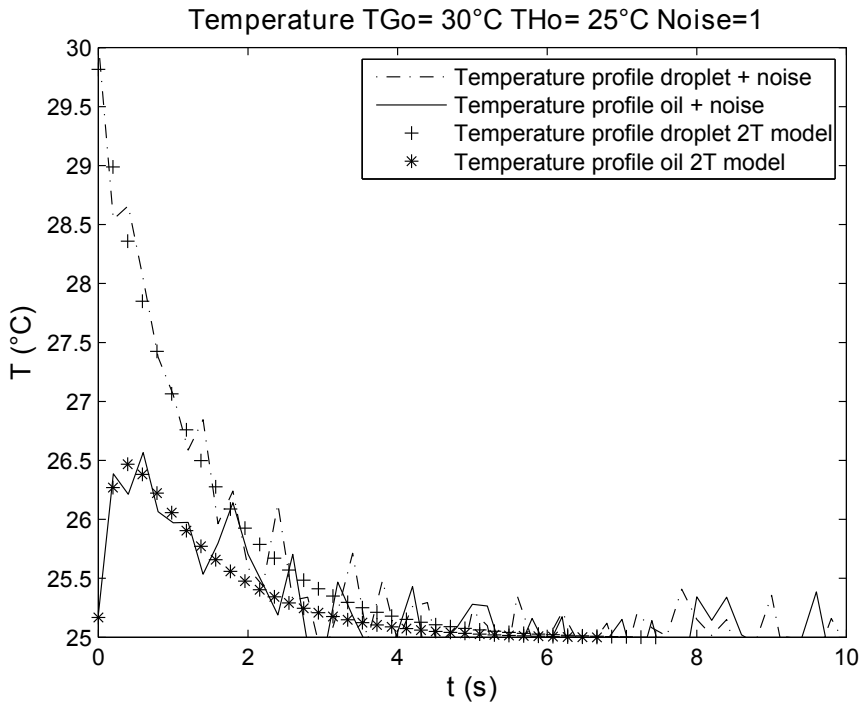

Figure D.3: Temperature profiles for oil and water with a noise level of $\sigma = 1$ and the estimated profiles by the model

Case	σ	H_{GP}	H_{GH}	H_{HG}	H_{HP}	T_G	T_H	T_P	S/B
		%	%	%	%	K	K	K	
A	0.05	0.1102	0.422	0.0355	0.0229	0.0022	0.0017	3.717×10^{-5}	125
B	0.3	0.7626	2.7384	0.2745	0.2757	0.0119	0.0121	5.447×10^{-4}	20.83
C	1	1.1074	2.8836	0.5459	1.1981	0.0020	0.0045	0.0035	6.25

Figure D.4: Relative error of the estimated H coefficients and the absolute error of the temperature

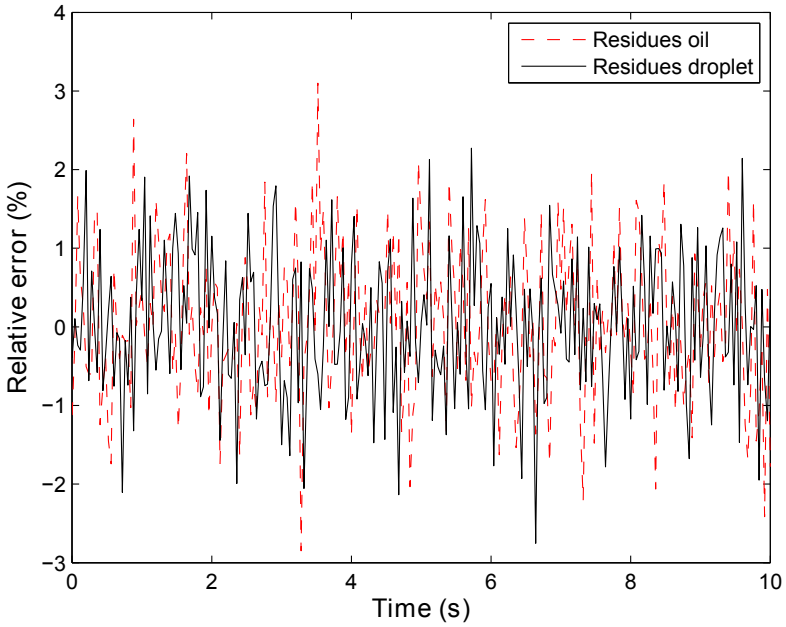

Figure D.5: Calculated relative error between the generated and estimated temperatures for a SNR of 6.25

Appendix E

Appendix

A step source was applied to the droplet flow at different flow rate ratios R ranging from 0.5 to 12, or more precisely, the length of the droplet was fixed to 1 *mm*, while the length of the oil plug was increased. In figure E.1, the estimated heat source from the equivalent homogeneous profiles (i.e., the continuous component (CC), equation 4.69) at different ratios of R is illustrated. The injected source is plotted by dashed lines, the while solid lines represent the estimated source. The shape of the estimated heat source differs from that of the injected step. The observed differences in the rise and descent of the curve may be induced by the fact that the estimated heat source is overtaken by the weighted average profile developed by the simplified model, in which only one convective exchange exists between the homogenous flow and the bulk. However, it is important to note that the amplitude of the estimated source decreases as the ratio is increased.

The error observed in the estimation illustrated in figure E.1 can be explained as follows: because the equivalent homogeneous profiles (T_{CC}) are functions of the length of both phases, when the L_{lim} boundary layer is attained, $L_H \int_0^{L_{min}} \overline{T_H}(t)dt$ becomes small. As a result, its contribution also decreases, as illustrated in figure E.2.

The equivalent homogeneous profiles (T_{CC}) are described as follows:

$$\overline{T_{CC}(t)} = \frac{L_G \int_0^{L_G} \overline{T_G}(t)dt}{L_T} \tag{E.1}$$

$$\overline{T_G}(t) = \frac{L_T \overline{T_{CC}(t)}}{L_G} = \overline{T_{CC}(t)}(1 + R) \tag{E.2}$$

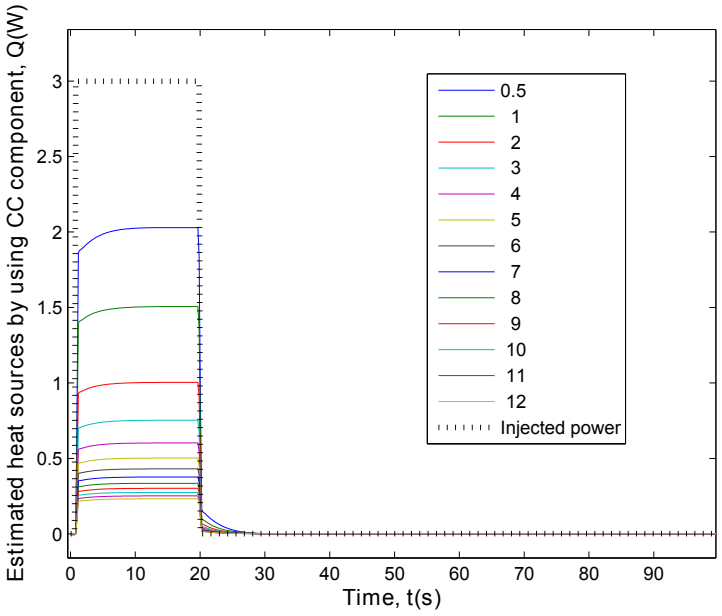

Figure E.1: Injected power over time (the black dashed lines) and the estimated power from the equivalent homogeneous profiles (CC) at different flow rate ratios (R) over time (the solid lines)

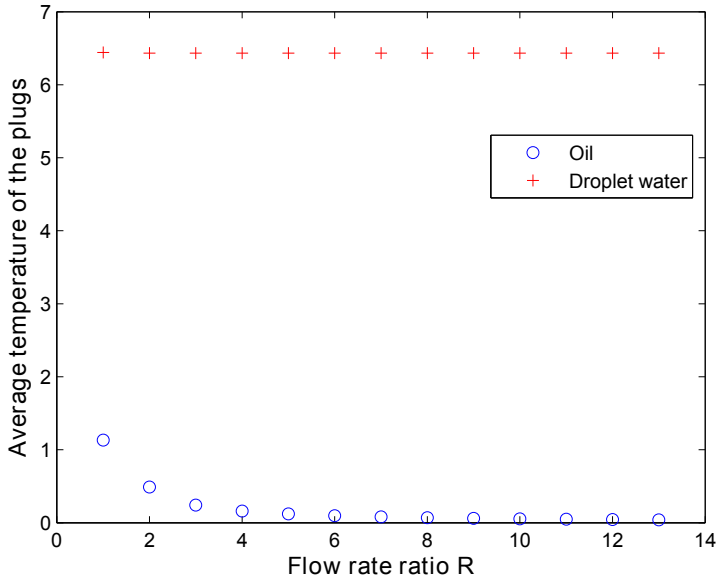

Figure E.2: Average temperature of the oil plug as a function of the flow rate ratio R

Introducing the T_G from expression E.3 in equation 4.61 and then rearranging gives:

$$\frac{\overline{T_{CC}}}{dt} = \frac{\phi(t)}{\rho C_p(1+R)} - \frac{hS}{\rho C_p}(\overline{T_{CC}(t)} - T_p) \tag{E.3}$$

$$\Phi(t) = \frac{\phi(t)}{(\rho_G C_{pG} V_G)(1+R)} \tag{E.4}$$

Applying equation E.4 to the estimated source Φ in figure E.1, then multiplying the source by $(\rho_G C_{pG} V_G)(1+R)$, it is possible to estimate the correct injected source, as shown in figure 4.24.

The heat source estimated using the equivalent homogeneous profiles is significantly corrected by the weighting contribution of the flow rate when the L_{lim} boundary layer of the oil is taken into account. Because the oil plug length increases when the R ratios are increased, the droplet heat sink is limited by the boundary layer of the oil L_{lim}.

The relative error is estimated between the injected heat source ($S_{\texttt{injected}}$) and the estimated heat source ($S_{\texttt{estimated}}$) based on the following expression.

$$Res = \frac{S_{\texttt{injected}} - S_{\texttt{estimated}}}{S_{\texttt{injected}}} * 100 \tag{E.5}$$

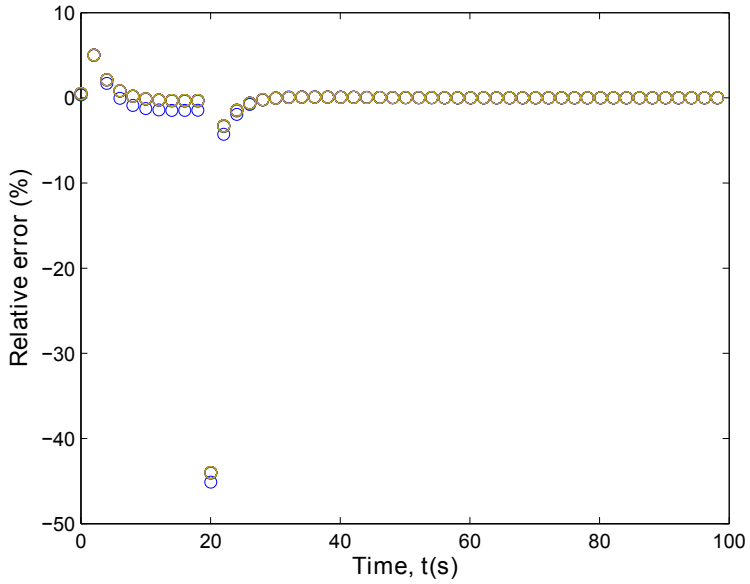

Figure E.3: The relative errors (%) are calculated between the injected heat source (the dashed line in figure E.1) and estimated heat source profiles based on the CC component, as illustrated in figure E.1

Finally, the relative errors between the sources profiles (injected and estimated) are calculated and plotted in figure E.3 and E.4. The relative error illustrated in figures E.3 for a given step function when the flow rate ratios are varied exhibits error at the beginning and end points of source estimation that posses very different orders of magnitude (5 and 50 %, respectively). The error observed indicates that the estimated shape of the source is not symmetric.

The residuals illustrated in figure E.4 demonstrate that when the heat sources are estimated from the droplet profiles, the estimation error is less than 1%. In contrast, when the heat sources are estimated from the equivalent homogeneous profiles (CC), the error is approximately 6%. From a practical point

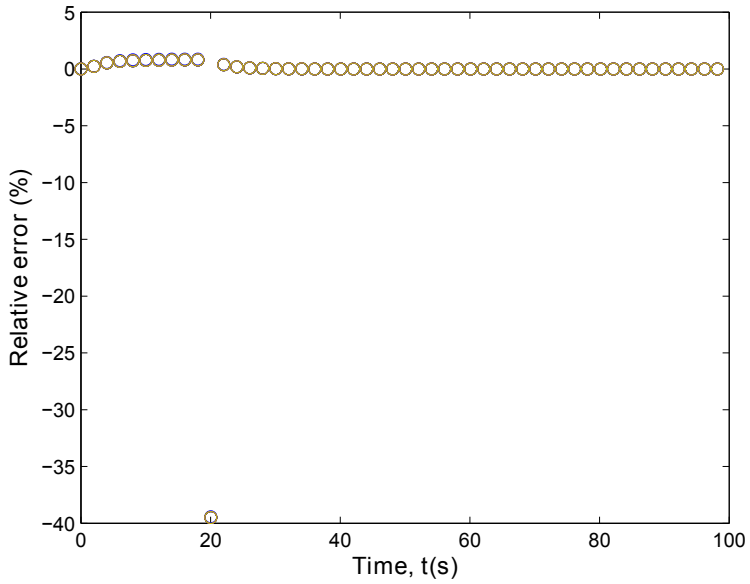

Figure E.4: The relative errors (%) are calculated between the injected heat source (the dashed line in figure 4.25) and estimated heat source profiles based on the droplet profile, as illustrated in figure 4.25

of view, it is easier to work with the CC profiles; working with the equivalent homogeneous medium (CC) is faster in terms of data processing and in terms of the simplicity of image processing. In contrast, processing only the droplet profiles leads to very accurate estimations but requires complex image processing techniques to obtain accurate droplet profiles. Heat source estimation enables the estimation of the chemical reaction enthalpies. To estimate the kinetics of a given chemical reaction, the source profiles in figure 4.24 are integrated over time, thus very good agreement between the input power and the estimated power can be observed, as shown in figure E.5.

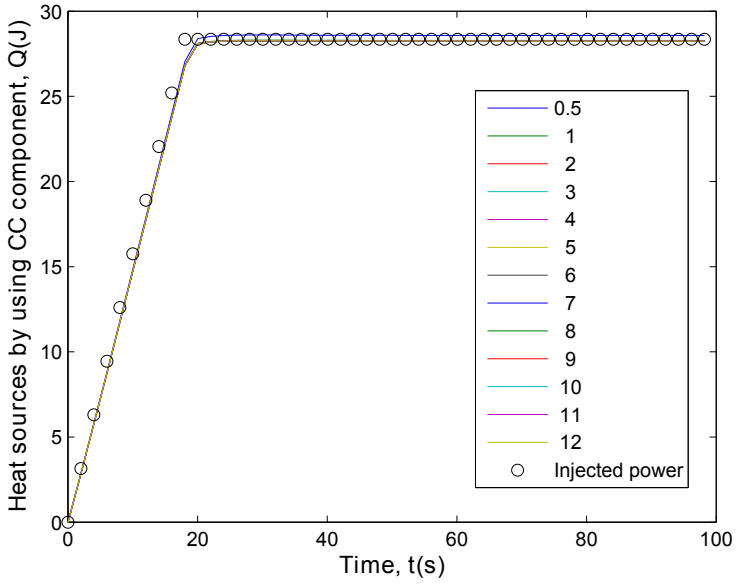

Figure E.5: The integrated source over time is illustrated with black dots and the integrated source over time is presented based on the CC component for each droplet flow at a given R.

When the source profiles in figure 4.25 are integrated over time, good agreement between the input power and estimated power can be observed, as shown in figure E.6. In this case, the integral shapes over time for the input and estimated sources are nearly identical, while the integral values are exactly the same.

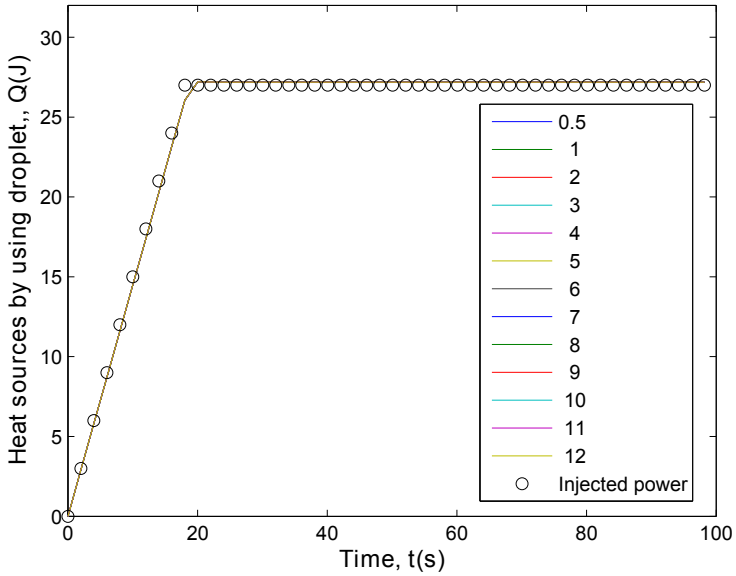

Figure E.6: The integrated source over time is illustrated with black dots and the integrated source over time is presented based on the droplet profiles for each droplet flow at given R.

The sources integrated over time demonstrate that the estimations of the enthalpies (heat source) and kinetics (integrated source) of the reactions can be carried out with this methodology. Now, we analyze the influence of noise on the estimations generated.

Appendix F

Appendix

Next, we test the influence of induced noise on the heat source profile estimations. The profiles are generated with the developed analytical solutions, to which 5% noise has been added. Then, as previously shown, source estimation from the continuous component (CC) is performed by applying equation E.4. Additionally, the droplet estimation is obtained by applying equation 4.58.

In figure F.1, the CC heat source profiles with noise added are shown. Here, it should be noted that the defaults concerning the shape of the source, as observed in figure 4.24, are drowned in the noise. In contrast, when the same level of noise is added to the droplet profiles, no influence is observed, either in terms of the shape or the estimation, as illustrated in figure F.2.

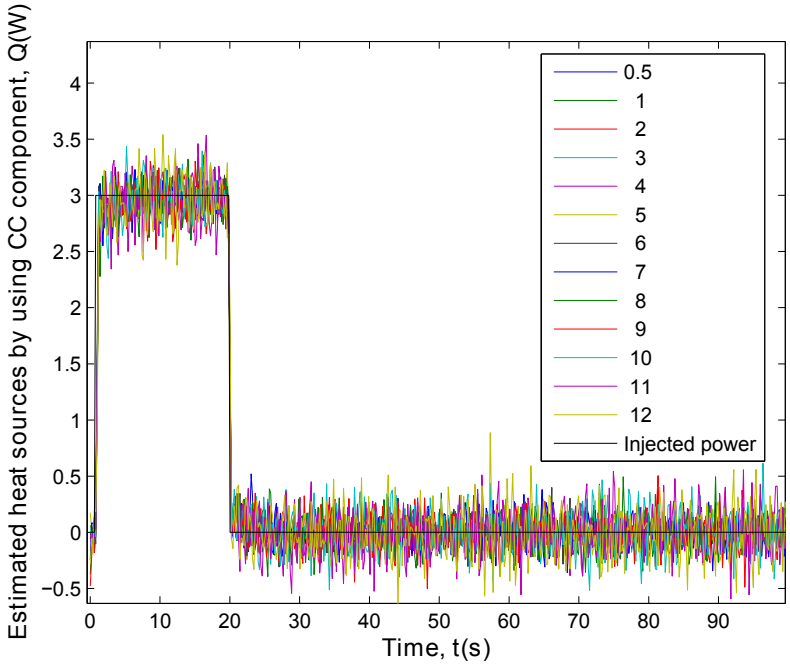

Figure F.1: Injected power over time (the black dashed lines) and the estimated power based on the equivalent homogeneous profiles (CC) at different flow rate ratios (R) over time (the solid lines) after the addition of noise.

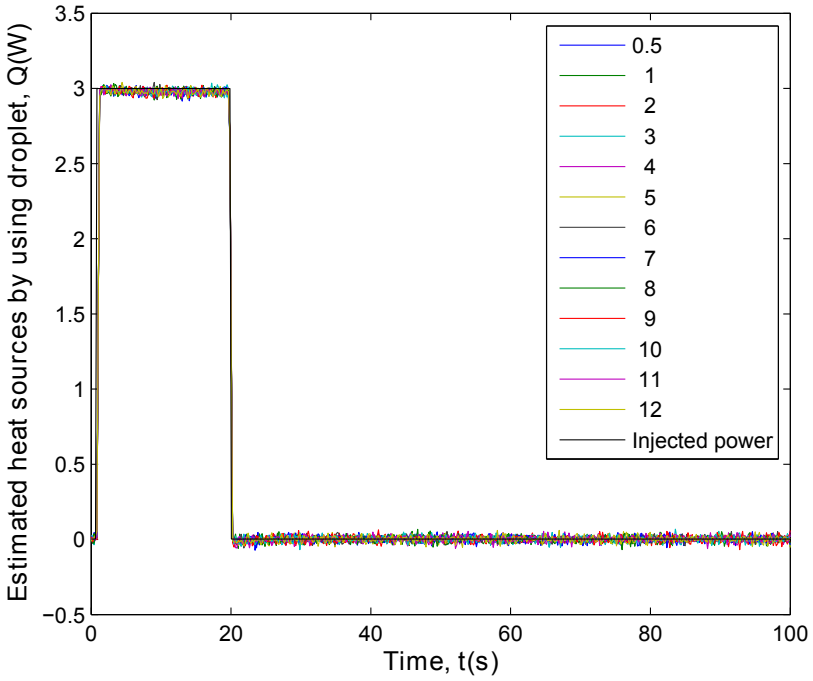

Figure F.2: Injected power over time (the black dashed lines) and the estimated power based on the droplet profile at different flow rate ratios (R) over time (the solid lines) after the addition of noise.

The relative errors between the sources profiles (injected and estimated) are calculated and plotted in figure F.3 and F.4. When the flow rate ratios are varied, the relative errors illustrated in figure F.3 for a given step function exhibit a dispersed error of approximately 15%.

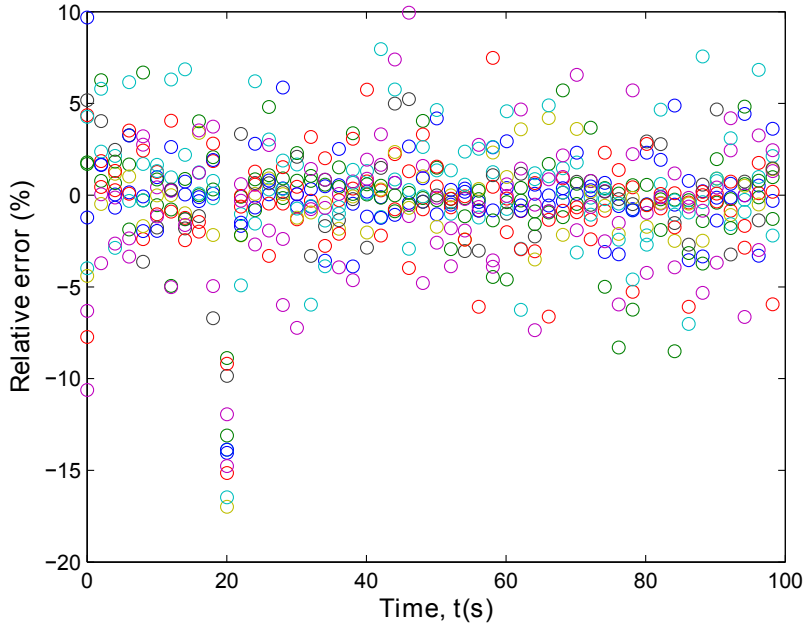

Figure F.3: The relative errors (%) are calculated between the injected heat source (the solid black line in figure F.1) and the estimated heat source profiles based on the droplet profile, as illustrated in figure F.1

The residuals illustrated in figure F.4 demonstrate that when the heat sources are estimated from the

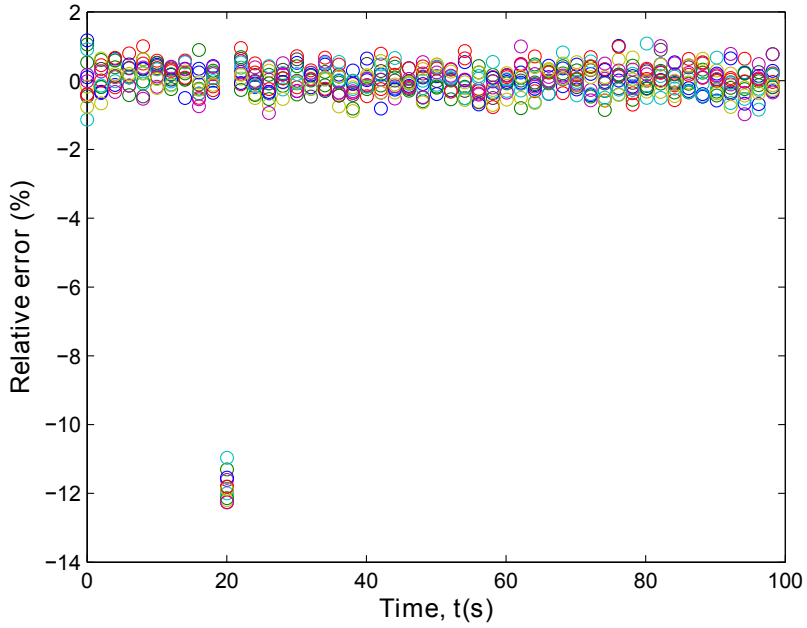

Figure F.4: The relative errors (%) are calculated between the injected heat source (the solid black line in figure F.2) and the estimated heat source profiles based on the droplet profile, as illustrated in figure F.2

droplet profiles, the estimation error is less than 2%. In contrast, when the heat sources are estimated from the equivalent homogeneous profiles (CC), the error is approximately 10%.

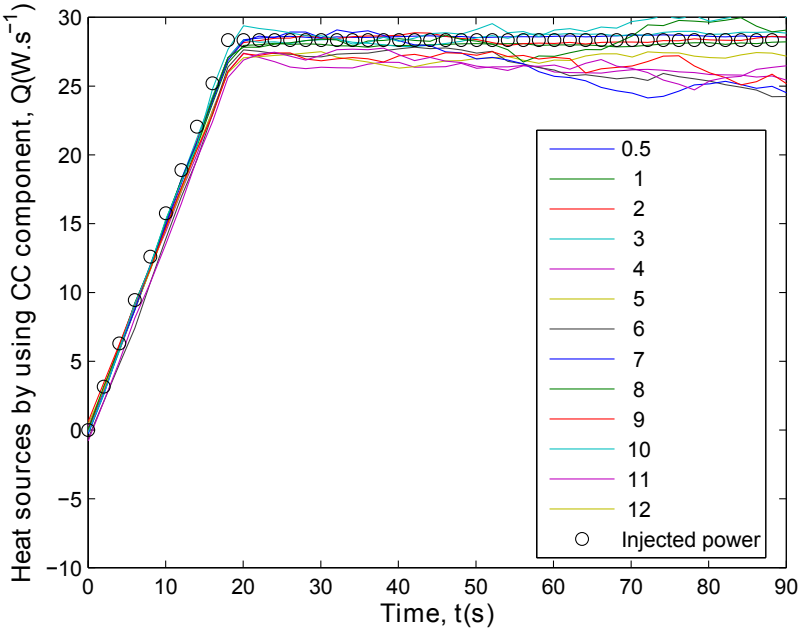

Figure F.5: The integrated source over time illustrated with black dots and the integrated noisy source CC profiles over time based on the droplet profiles for each droplet flow at a given R.

In figure F.5, the integrated noisy heat source profiles from the CC (from figure F.1) as functions of time are plotted. Very good agreement between the input power and the estimated source can be seen at short time scales. However, at long time scales, the estimated profiles are scattered. In contrast,

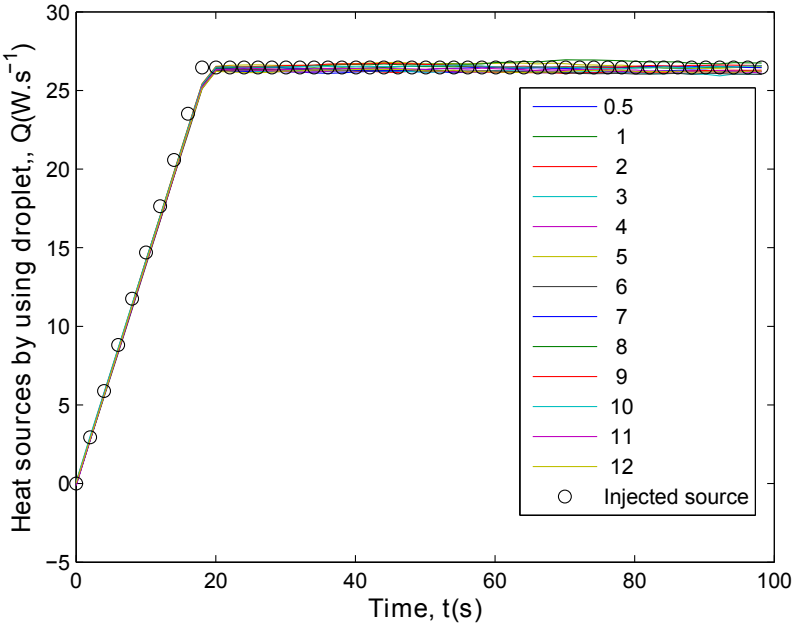

Figure F.6: The integrated source over time illustrated with black dots and the integrated noisy source droplet profiles over time based on the droplet profiles for each droplet flow at a given R.

the integrated noisy heat source profiles illustrated in figure F.6, which have been estimated from the droplet heat source profiles, are shown to be in good agreement with the integrated injected source profiles.

The integrated sources over time after the addition of noise demonstrate that the kinetics can be estimated using this methodology.

Appendix G

Appendix

The model used to estimate the thermal properties

$$H = \frac{h_p S}{\left(\rho C_p V\right)^* U} \tag{G.1}$$

The heat exchange surface (S) is considered to be a cylinder, which represents the droplet and the oil plug length (L_T), as well as the length of the period. Additionally, h_p gives the parietal heat exchange coefficient between the period and the bulk. The $\left(\rho C_p V\right)^*$ term is described by the mixing law governing the flow, that is, the composition of the droplet or oil. U is the mean velocity.

$$H = \frac{h_p \pi d L_T}{\left(\rho C_{pG} L_G + \rho C_{pH} L_H\right) S_{in} U} \tag{G.2}$$

The volume can be rewritten as $S \cdot L$, where S_{in} is the interfacial heat exchange surface between the phases, i.e., a circle that is described by the inner diameter of the tubing. The mean speed U can be rewritten as $U = Q_T / S_{in}$ of the total flow ratio divided by the flowing section, which is also imposed by the inner diameter of the tubing.

$$H = \frac{h_p \pi d L_T S_{in}}{\left(\rho C_{pG} L_G + \rho C_{pH} L_H\right) S_{in} Q_T} \tag{G.3}$$

Elimination S_{in},

$$H = \frac{h_p \pi d L_T}{\left(\rho C_{pG} L_G + \rho C_{pH} L_H\right) Q_T} \tag{G.4}$$

Introduction of the following relations:

$$L_T = L_G + L_H \; ; \; \alpha = \frac{L_G}{L_H} \; ; \; L_T = L_H(1+\alpha) \tag{G.5}$$

$$K = \frac{\left(\rho C_p\right)_G}{\left(\rho C_p\right)_H} \tag{G.6}$$

Applying the previous relations (equation G.5 and G.6) to equation G.4 :

$$H = \frac{h_p \pi d L_H (1+\alpha)}{Q_T (\rho C_p)_H L_H (1+\alpha K)} \tag{G.7}$$

Elimination L_H:

$$H = \frac{h_p \pi d (1+\alpha)}{Q_T (\rho C_p)_H (1+\alpha K)} \tag{G.8}$$

Introduction of the following relation:

$$K_0 = \frac{h_p \pi d}{Q_T \left(\rho C_p\right)_H} \tag{G.9}$$

Applying the previous relation in equation G.9 to equation G.8 :

$$H = K_0 \frac{(1+\alpha)}{(1+\alpha K)} \tag{G.10}$$

With:

$$u = \frac{1}{1+\alpha} \tag{G.11}$$

Equation G.10 can be rewritten as:

$$\frac{1}{H} = \frac{1-K}{K_0} u + \frac{1}{K_0} \tag{G.12}$$

Presented in section 5.1.2.2 as:

$$\frac{1}{H} = S \cdot u + O \; with: \; S = \frac{1-K}{K_0} \; ; \; O = \frac{K}{K_0} \tag{G.13}$$

The equations G.12 and G.13 are written as a linear relation $y = mx + b$. To estimate the thermo-physical properties from the experiments, it is necessary to plot the relation $1/H$ versus u, as shown in figure G.1.A. Then, it is possible to establish other relations between the constant m, which determines the slope and the total flow, as observed in figure G.1.B, where the term b is constant and determines the point at which the line crosses the y-axis and the total flow, as observed in figure G.1.C.

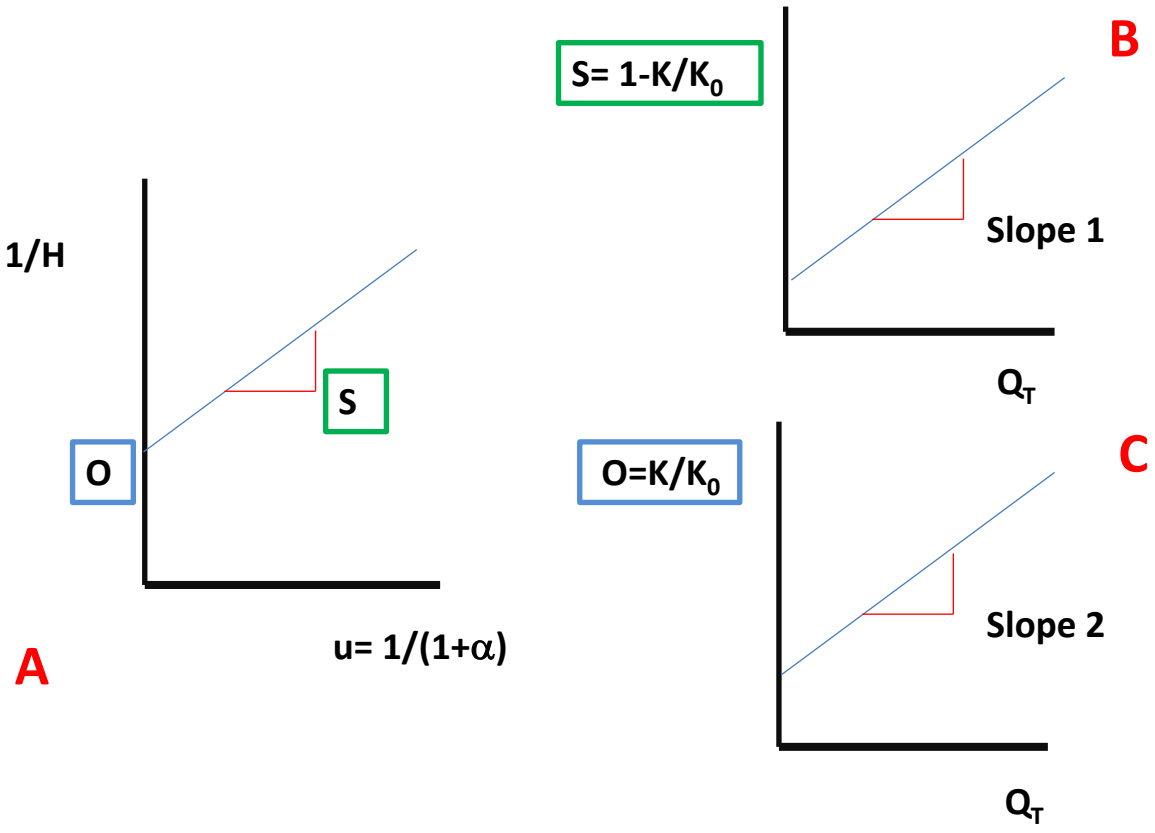

Figure G.1: Ratio of the slopes

From the schematized relation in figure G.1.B, the slope is defined as:

$$Slope1 = \frac{1-K}{K_0}\frac{1}{Q_T} \tag{G.14}$$

Description of slope 1:

$$Slope1 = \frac{\left(\rho C_p\right)_H - \left(\rho C_p\right)_G}{\left(\rho C_p\right)_H} \frac{Q_T \left(\rho C_p\right)_H}{h_p \pi d} \cdot \frac{1}{Q_T} = \frac{\left(\rho C_p\right)_H - \left(\rho C_p\right)_G}{h_p \pi d} \tag{G.15}$$

From the schematized relation in figure G.1.C, the slope is defined as:

$$Slope2 = \frac{K}{K_0} \frac{1}{Q_T} \tag{G.16}$$

Description of slope 2:

$$Slope2 = \frac{\left(\rho C_p\right)_G}{\left(\rho C_p\right)_H} \frac{Q_T \left(\rho C_p\right)_H}{h_p \pi d} \cdot \frac{1}{Q_T} = \frac{\left(\rho C_p\right)_G}{h_p \pi d} \tag{G.17}$$

Finally, it is possible to calculate the ratio of both slopes:

$$\frac{S}{O} = \frac{Slope1}{Slope2} = \frac{\left(\rho C_p\right)_H - \left(\rho C_p\right)_G}{h_p \pi d} \frac{h_p \pi d}{\left(\rho C_p\right)_G} \tag{G.18}$$

Then, rearranging gives:

$$\frac{S}{O} = \frac{Slope1}{Slope2} = \frac{\left(\rho C_p\right)_H - \left(\rho C_p\right)_G}{\left(\rho C_p\right)_G} \tag{G.19}$$

Followed by rearranging again gives:

$$\frac{S}{O} = \frac{1}{K} - 1 \tag{G.20}$$

$$K = \frac{1}{1 + \frac{S}{O}} \tag{G.21}$$

Appendix H

Appendix

UV-vis spectroscopy

Ultraviolet-visible spectroscopy or spectrophotometry (UV-vis) refers to the technique of absorption spectroscopy or reflectance spectroscopy carried out in the ultraviolet-visible spectral region. This means the approach uses light in the visible and adjacent (near-UV and near-infrared (NIR)) ranges. Absorption or reflectance in the visible range directly affects the perceived color of the chemicals involved in a reaction. Additionally, molecules undergo electronic transitions in this region of the electromagnetic spectrum.

We used an Aventes^{TM} spectrophotometer in this work. The principle of this instrument relies on the measurement of the absorbance of colored solution of varying concentration. When the solution is concentrated, the color is usually darker; therefore, the solution absorbs more light. Applying the Beer-Lambert Law, it is possible to develop a calibration curve. The spectrometer should preferably be calibrated to either the wavelength of absorbance of the sample or that of neighboring wavelengths in the case of signal saturation problems.

The calibration step is essential to establish the relationship between the measurements of absorbance and concentration. The quantitative measurement of the evolution of solution concentration during the production of diiodine is based on the normal diatomic form of iodine (I_2). This reaction was performed between potassium iodide (KI) and sodium persulfate ($Na_2S_2O_8$), described as follows:

$$2KI + Na_2S_2O_8 \longrightarrow I_2 + 2SO_4^{2-} + 2K^+ + 2Na^+$$

$$I^- + I_2 \rightleftharpoons I_3^-$$

The redox reaction was studied by UV-vis spectroscopy under two configurations, (i) a batch configuration with magnetic agitation and (ii) underflow online analysis within the droplets.

The I_3^- is colored (yellow) and absorbs in the violet region (the complementary color on the elementary color wheel). It is important to note that the maximum absorption of I_3^- occurs at 362 nm. However, the signal at this wavelength is too intense, so we selected the wavelength of 415 nm to avoid detector saturation.

Batch configuration with magnetic agitation

The experimental set-up is schematized in figure H.1. The batch container is placed inside the opaque cell. The reaction takes place in this cell, which is agitated with a magnetic stirrer. As the reaction proceeds, a continuous light is emitted by the source, which allows the reaction evolution to be monitored based on the absorbance as a function of time. The monitored data are managed by the spectrometer software, Avasoft.

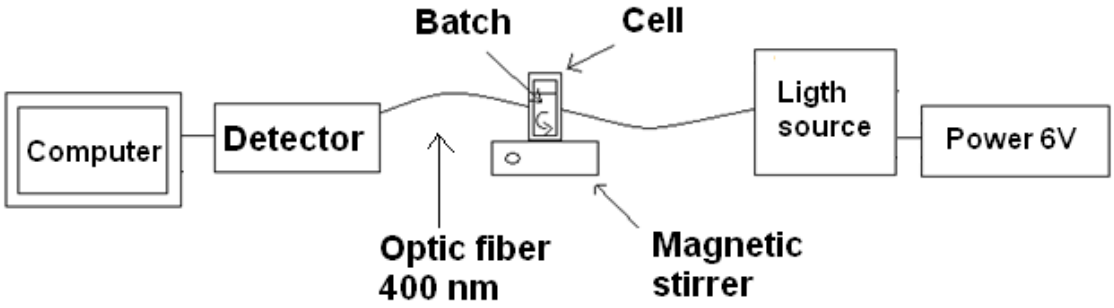

Figure H.1: Experimental set-up for the batch spectroscopic analysis

- **Calibration**

Several conditions must be respected to ensure an accurate estimation of the calibration curve. First, potassium iodide (KI) must be introduced in excess, to increase the solubility of iodine (I_2) and avoid the precipitation of iodine crystals. Accordingly, it has been found that the ratio between the concentrations of C_{KI} and $C_{Na_2S_2O_8}$ must be equal to or greater to 3,000. Moreover, the concentration of KI must be less than or equal to 1 $mol.L^{-1}$, and the concentration of $Na_2S_2O_8$ is determined according to the chosen ratio. The calibration solutions were prepared using the concentrations summarized in table H.1 and are illustrated in figure H.2.

sample	$C_{Na_2S_2O_8}$, (mol.L^{-1})	Volume $Na_2S_2O_8$, (ml)	C_{KI}, (mol.L^{-1})	Volume KI, (ml)
1	0.8 x10^{-4}	1.6	0.24	9.6
2	0.6 x10^{-4}	1.2	0.18	7.2
3	0.4 x10^{-4}	0.8	0.12	4.8
4	0.2 x10^{-4}	0.4	0.06	2.4
5	0.1 x10^{-4}	0.2	0.03	1.2

Table H.1: Summary of the experimental concentrations and volumes used for the calibration

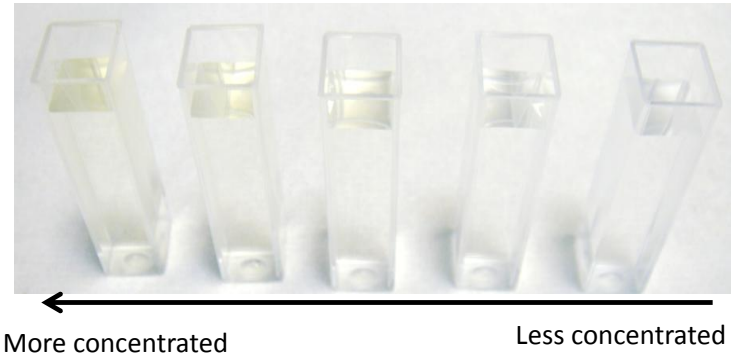

Figure H.2: Range of standard solutions used to make the calibration curve at a ratio of 3,000

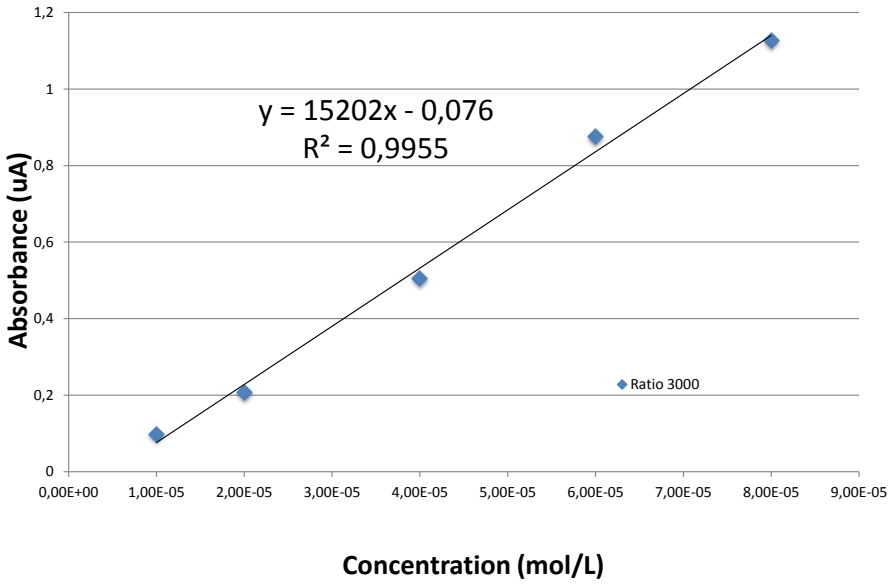

Figure H.3: Concentration of I_2 as a function of the absorbance

- **Kinetics**

To investigate the kinetics of the reaction, sample 4, as described in table H.1, was studied as a function of time.

It is important to note that the reaction reaches 100% conversion after 4 hours. For a total volume of 2.8 *mL*. inside a batch reactor, the residence time (t_{res}) needed to achieve a conversion of 100% is described by:

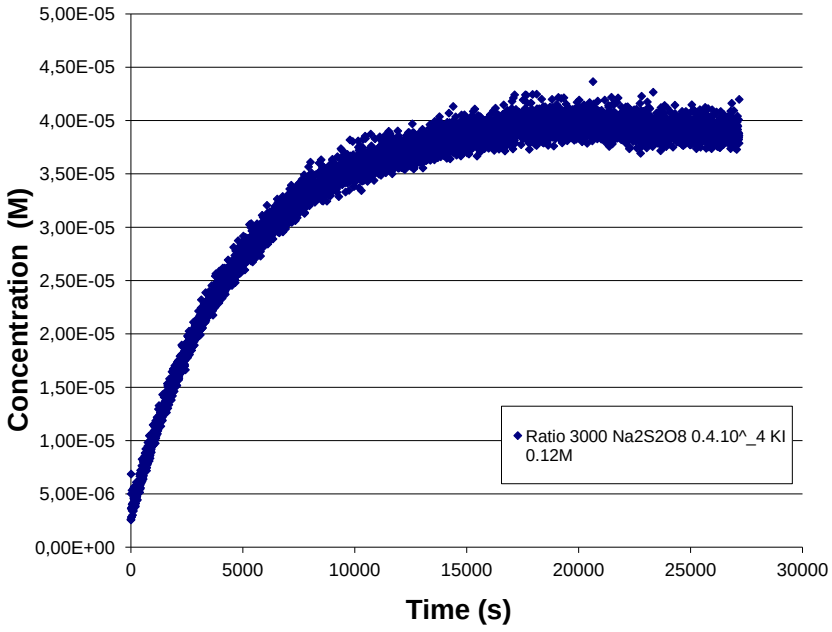

Figure H.4: Evolution of the concentration of I_2 as a function of time

$$t_{res} = \frac{VC_{lim0}}{M_{lim0}} \tag{H.1}$$

where V is the volume of the reactor, C_{lim0} is the initial concentration of the limiting reactant, and M_{lim0} is the molar flow of the limiting reactant. It should be noted in equation H.1 that the residence time to reach 100% conversion is approximately 4 hours and that this curve is proportional to the volume analyzed (2.8 mL) in the batch reactor.

Underflow online analysis within the droplets

Here, online spectroscopy analysis was performed directly on the millifluidic system. The droplet flow rate was 10 $ml.h^{-1}$, with a flow rate ratio between the droplet and the oil of R=2. Both reagents were added into the droplets by syringe pumps operated at the same flow rates $Q_{Na_2S_2O_8} = Q_{KI}$. The absorbance was measured as a function of time at different positions along the reactor, specifically, approximately every 5 cm. The flow was analyzed when steady state had been reached, i.e., when the correspondence between space and time can be applied. Thus, each measurement at a given position corresponds to a reaction time. Moreover, the absorbance was measured by using a reflexion probe, which is an optical fiber operated in a UV-vis reflection mode as a spectrometer (spectrometer AVANTES avaspec 3648; AVANTES source AvaLight-DHS). The transmission-reflection probe is based on the following principle. The incident beam from the probe passes through the tubing

containing the droplet flow, then hits the reflective brass surface, and returns to the probe, where it is transmitted to the detector and then analyzed by the spectrometer software, Avasoft. The experimental set-up is illustrated in figure H.5.

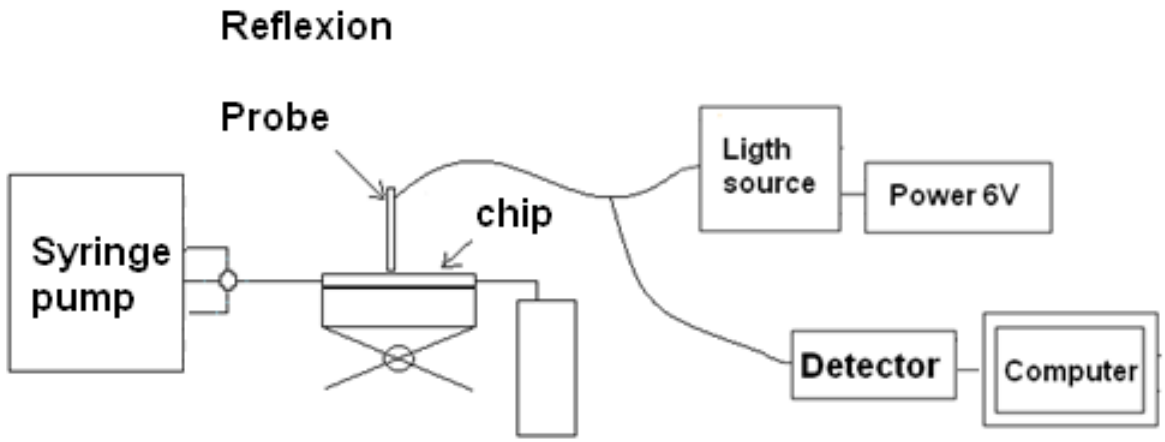

Figure H.5: Experimental set-up for the spectroscopic online analysis

In figure H.6, a raw signal at an example position is shown. Periodic variations in the absorbance can be observed. This variation identifies the transition of the droplets. It is important to mention that the white background is derived from the PTFE tubing filled with oil.

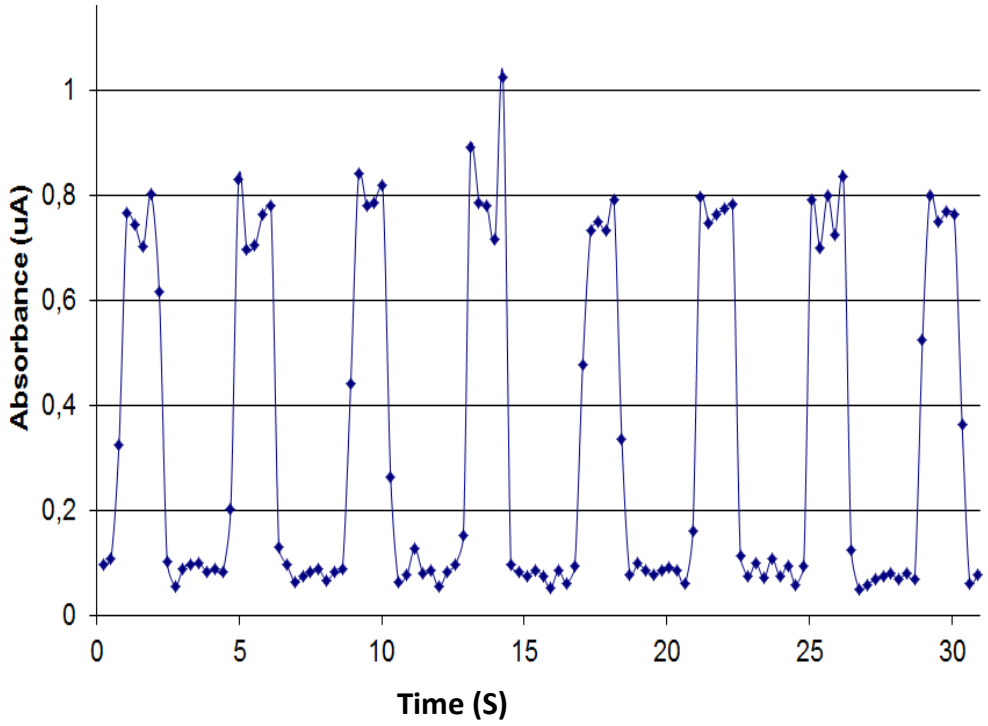

Figure H.6: Raw signal data obtained at a given position along the brass serpentine chip

- **Calibration**

The calibration curve for the droplet flow in the millifludic system must be developed. To optimize the signal acquisition of the droplets, it is necessary to adjust the acquisition parameters. The acquisition rate was fixed to 5 ms, and signal averaging was performed every 10 acquisitions to improve the signal-to-noise ratio.

The calibration curve was obtained by generating a droplet flow. The droplets were composed of a standard solution of diluted iodine in a solution of KI, prepared to obtain the desired concentrations, as summarized in table H.2. The calibration coefficient was then determined (see figure H.7) and enabled the determination of the concentration over time for the reaction at a ratio of 3,000.

sample	C_{I_2}, (mol.L^{-1})
1	0.34 x10^{-4}
2	0.67 x10^{-4}
3	1 x10^{-4}
4	1.35 x10^{-4}
5	1.69 x10^{-4}

Table H.2: Summary of the experimental concentrations and volumes used for the calibration

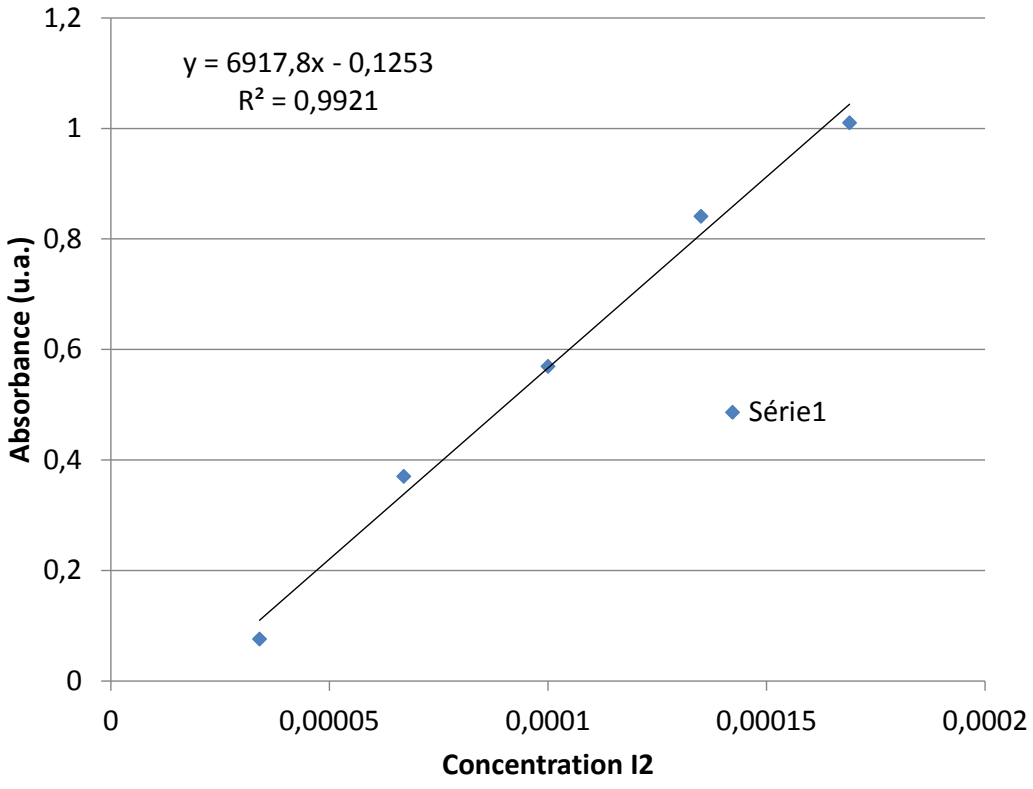

Figure H.7: Concentration of I_2 as a function of the absorbance

- **Kinetics**

To investigate the kinetics of the reaction, sample 4, as described in table 7, was studied as a function of time. Thus, the concentration of each reactant is the same as that previously shown for the kinetics

study batch analysis $C_{Na_2S_2O_8}$ = 0.2$x10^{-4}$ M and C_{KI} = 0.06.

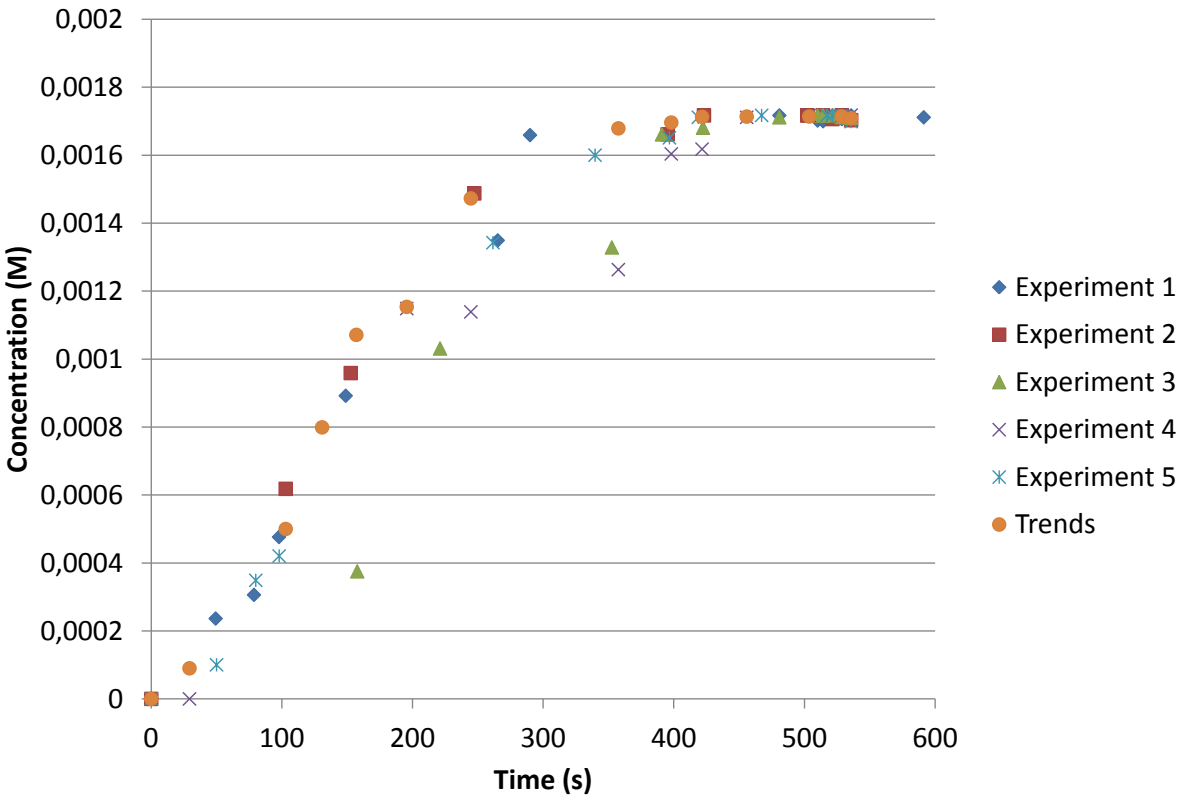

Figure H.8: Evolution of the concentration of I_2 as a function of time

Bibliography

[1] Helen Song, Delai L Chen, and Rustem F Ismagilov. Reactions in droplets in microfluidic channels. *Angewandte chemie international edition*, 45(44):7336–7356, 2006.

[2] K. F. Jensen. Microchemical systems for discovery and development. *Ernst Schering Foundation symposium proceedings*, (3):57–76, 2006.

[3] M. T. Kreutzer, F. Kapteijn, J. A. Moulijn, and J. J. Heiszwolf. Multiphase monolith reactors chemical reaction engineering of segmented flow in microchannels. *Chemical Engineering Science*, 60(22):5895–5916, 2005. Cited By (since 1996):192.

[4] Y. S. Muzychka and M. M. Yovanovich. Laminar forced convection heat transfer in the combined entry region of non-circular ducts. *Journal of Heat Transfer*, 126(1):54–61, 2004. Cited By (since 1996):53.

[5] D. Lakehal, G. Larrignon, and C. Narayanan. Computational heat transfer and two-phase flow topology in miniature tubes. *Microfluidics and Nanofluidics*, 4(4):261–271, 2008. Cited By (since 1996):29.

[6] P. . Lee and S. V. Garimella. Thermally developing flow and heat transfer in rectangular microchannels of different aspect ratios. *International Journal of Heat and Mass Transfer*, 49(17-18):3060–3067, 2006. Cited By (since 1996):123.

[7] P. A. Walsh, E. J. Walsh, and Y. S. Muzychka. Heat transfer model for gas-liquid slug flows under constant flux. *International Journal of Heat and Mass Transfer*, 53(15-16):3193–3201, 2010. Cited By (since 1996):18.

[8] A. R. Betz and D. Attinger. Can segmented flow enhance heat transfer in microchannel heat sinks. *International Journal of Heat and Mass Transfer*, 53(19-20):3683–3691, 2010. Cited By (since 1996):17.

[9] Z. Che, T. N. Wong, and N. . Nguyen. Heat transfer enhancement by recirculating flow within liquid plugs in microchannels. *International Journal of Heat and Mass Transfer*, 55(7-8):1947–1956, 2012. Cited By (since 1996):4.

[10] G. Hetsroni, A. Mosyak, E. Pogrebnyak, and Z. Segal. Heat transfer of gas-liquid mixture in micro-channel heat sink. *International Journal of Heat and Mass Transfer*, 52(17-18):3963–3971, 2009. Cited By (since 1996):10.

[11] D. M. Fries, S. Waelchli, and P. Rudolf von Rohr. Gas-liquid two-phase flow in meandering microchannels. *Chemical Engineering Journal*, 135(SUPPL. 1):S37–S45, 2007. Cited By (since 1996):23.

[12] L. Tadrist. Review on two-phase flow instabilities in narrow spaces. *International Journal of Heat and Fluid Flow*, 28(1 SPEC. ISS.):54–62, 2007. Cited By (since 1996):52.

[13] P. Urbant, A. Leshansky, and Y. Halupovich. On the forced convective heat transport in a droplet-laden flow in microchannels. *Microfluidics and Nanofluidics*, 4(6):533–542, 2008. Cited By (since 1996):14.

[14] Patrick Tabeling. *Introduction la microfluidiques*. Belin, 8, rue Frou 75278 Paris Cedex 06, France, 1 edition, 2003.

[15] S.F. Kandlikar, S. Garimella, D. Li, S. Colin, and M.R. King. *Heat Transfer and fluid flow in minichannels and microchannels*. Elservier, The boulevard, Lanford Line Kidlington Oxford, UK, 1 edition, 2006.

[16] Oliver Geschke, Henning Klank, and Pieter Tellemann. *Microsystem engineering of lab-on-a-chip devices*, volume 258. Wiley Online Library, 2004.

[17] Flavie Sarrazin. *Two phase microreactors for fast process design*. PhD thesis, Transferts, dYnamique des Fluides, EnergEtique et Procedes, 2006.

[18] Kamholz A.E., Weigl B.H., Finlayson B.A., and Yager P. Quantitative analysis of molecular interaction in a microfluidic channel: the t-sensor. *Analytical Chemistry*, 71:5340–5347, 1999.

[19] Ismagilov R.F., Stroock A.D., Kenis P.J.A., Whitesides G., and Stone H. Experimental en theoretical scaling laws for transverse diffusive broadening in two-phase laminar flows in microchannels. *Applied Physics Letter*, 76:2376–2378, 2000.

[20] Yager P. Transverse diffusion in microfluidic systems. *Lab on a Chip - Miniaturisation for Chemistry and Biology*, 3(1):115–150, 2003.

[21] Culbertson C. T., Jacobson S. C., and Ramsey J. M. Diffusion coefficient measurements in microfluidic devices. *Talanta*, 56(2):365373, 2002.

[22] Jean-Baptiste Salmon, Armand Ajdari, Patrick Tabeling, Laurent Servant, David Talaga, and Mathieu Joanicot. In situ raman imaging of interdiffusion in a microchannel. *Applied physics letters*, 86(9):094106–094106, 2005.

[23] Stroock A. D., Dertinger S. K. W., Ajdari A., Mezic I., Stone H. A., and Whitesides G. M. Chaotic mixer for microchannels. *Science*, 295:648–651, 2002.

[24] Knight J.B., Vishwanath A., Brody J.P., and Austin R.H. Hydrodynamic focusing on a silicon chip: mixing nanoliters in microseconds. *Phys Rev Lett*, 80:3863–3866, 1998.

[25] A Mehdizadeh, SA Sherif, and WE Lear. Numerical simulation of thermofluid characteristics of two-phase slug flow in microchannels. *International Journal of Heat and Mass Transfer*, 54(15):3457–3465, 2011.

[26] Thomas A Franke and Achim Wixforth. Microfluidics for miniaturized laboratories on a chip. *ChemPhysChem*, 9(15):2140–2156, 2008.

[27] AS Utada, El Lorenceau, DR Link, PD Kaplan, HA Stone, and DA Weitz. Monodisperse double emulsions generated from a microcapillary device. *Science*, 308(5721):537–541, 2005.

[28] Charles N. Baroud, Francois Gallaire, and Remi Dangla. Dynamics of microfluidic droplets. *Lab Chip*, 10:2032–2045, 2010.

[29] Mathieu Joanicot and Armand Ajdari. Droplet control for microfluidics. *Science*, 309(5736):887–888, 2005.

[30] Galder Cristobal, Jean-Philippe Benoit, Mathieu Joanicot, and Armand Ajdari. Microfluidic bypass for efficient passive regulation of droplet traffic at a junction. *Applied physics letters*, 89(3):034104–034104, 2006.

[31] Shelley L. Anna, Nathalie Bontoux, and Howard A. Stone. Formation of dispersions using "flow focusing" in microchannels. *Applied Physics Letters*, 82(3):364–366, 2003.

[32] Thomas B Jones, M Gunji, M Washizu, and MJ Feldman. Dielectrophoretic liquid actuation and nanodroplet formation. *Journal of Applied Physics*, 89(2):1441–1448, 2001.

[33] Junghoon Lee, Hyejin Moon, Jesse Fowler, Thomas Schoellhammer, and Chang-Jin Kim. Electrowetting and electrowetting-on-dielectric for microscale liquid handling. *Sensors and Actuators A: Physical*, 95(2):259–268, 2002.

[34] S. Jakiela, S. Makulska, P. M. Korczyk, and P. Garstecki. Speed of flow of individual droplets in microfluidic channels as a function of the capillary number, volume of droplets and contrast of viscosities. *Lab on a Chip - Miniaturisation for Chemistry and Biology*, 11(21):3603–3608, 2011. Cited By (since 1996): 5.

[35] Adeline Perro, Celia Nicolet, Julie Angly, Sebastien Lecommandoux, Jean-Francois Le Meins, and Annie Colin. Mastering a double emulsion in a simple co-flow microfluidic to generate complex polymersomes. *Langmuir*, 27(14):9034–9042, 2010.

[36] Shingo Okushima, Takasi Nisisako, Toru Torii, and Toshiro Higuchi. Controlled production of monodisperse double emulsions by two-step droplet breakup in microfluidic devices. *Langmuir*, 20(23):9905–9908, 2004.

[37] Utada A.S., Chu L.Y., Fernandez-Nieves A., Link D.R., Holtze C., and Weitz D.A. Dripping, jetting, drops, and wetting: The magic of microfluidics. *MRS Bull*, 32:702–707, 2007.

[38] Pierre Guillot, Armand Ajdari, Julie Goyon, Mathieu Joanicot, and Annie Colin. Droplets and jets in microfluidic devices. *Comptes Rendus Chimie*, 12(1):247–257, 2009.

[39] Miguel A Herrada, Alfonso M Gañán-Calvo, Antonio Ojeda-Monge, Benjamin Bluth, and Pascual Riesco-Chueca. Liquid flow focused by a gas: jetting, dripping, and recirculation. *Physical Review E*, 78(3):036323, 2008.

[40] J. W. Coleman and S. Garimella. Characterization of two-phase flow patterns in small diameter round and rectangular tubes. *International Journal of Heat and Mass Transfer*, 42(15):2869–2881, 1999. Cited By (since 1996):230.

[41] P. . Lee and S. V. Garimella. Thermally developing flow and heat transfer in rectangular microchannels of different aspect ratios. *International Journal of Heat and Mass Transfer*, 49(17-18):3060–3067, 2006. Cited By (since 1996):122.

[42] Samuel Marre, Cyril Aymonier, P Subra, and Emmanuel Mignard. Dripping to jetting transitions observed from supercritical fluid in liquid microcoflows. *Applied Physics Letters*, 95(13):134105–134105, 2009.

[43] Nicolas Lorber, Flavie Sarrazin, Pierre Guillot, Pascal Panizza, Annie Colin, Bertrand Pavageau, Cindy Hany, Patrick Maestro, Samuel Marre, Thomas Delclos, et al. Some recent advances in the design and the use of miniaturized droplet-based continuous process: Applications in chemistry and high-pressure microflows. *Lab on a Chip*, 11(5):779–787, 2011.

[44] Helen Song, Joshua D Tice, and Rustem F Ismagilov. A microfluidic system for controlling reaction networks in time. *Angewandte Chemie*, 115(7):792–796, 2003.

[45] Helen Song, Michelle R Bringer, Joshua D Tice, Cory J Gerdts, and Rustem F Ismagilov. Experimental test of scaling of mixing by chaotic advection in droplets moving through microfluidic channels. *Applied Physics Letters*, 83(22):4664–4666, 2003.

[46] Metin Muradoglu and Howard A Stone. Mixing in a drop moving through a serpentine channel: A computational study. *Physics of Fluids*, 17:073305, 2005.

[47] Hakan Dogan, Selman Nas, and Metin Muradoglu. Mixing of miscible liquids in gas-segmented serpentine channels. *International Journal of Multiphase Flow*, 35(12):1149–1158, 2009.

[48] F. Sarrazin, K. Loubiere, L. Prat, C. Gourdon, T. Bonometti, and J. Magnaudet. Experimental and numerical study of droplets hydrodynamics in microchannel. *AIChE Journal*, 52(12):4061–4070, 2006. Cited By (since 1996): 34.

[49] Joshua D Tice, Adam D Lyon, and Rustem F Ismagilov. Effects of viscosity on droplet formation and mixing in microfluidic channels. *Analytica Chimica Acta*, 507(1):73–77, 2004.

[50] Issam Mudawar and Morris B Bowers. Ultra-high critical heat flux (chf) for subcooled water flow boilingi: Chf data and parametric effects for small diameter tubes. *International Journal of Heat and Mass Transfer*, 42(8):1405–1428, 1999.

[51] Satish G Kandlikar. High flux heat removal with microchannelsa roadmap of challenges and opportunities. *Heat Transfer Engineering*, 26(8):5–14, 2005.

[52] Issam Mudawar. Assessment of high-heat-flux thermal management schemes. *Components and Packaging Technologies, IEEE Transactions on*, 24(2):122–141, 2001.

[53] D. Brutin and L. Tadrist. Destabilization mechanisms and scaling laws of convective boiling in a minichannel. *Journal of Thermophysics and Heat Transfer*, 20(4):850–855, 2006. Cited By (since 1996):6.

[54] Axel Günther, Saif A Khan, Martina Thalmann, Franz Trachsel, and Klavs F Jensen. Transport and reaction in microscale segmented gas–liquid flow. *Lab on a Chip*, 4(4):278–286, 2004.

[55] Andrew D Griffiths and Dan S Tawfik. Miniaturising the laboratory in emulsion droplets. *Trends in biotechnology*, 24(9):395–402, 2006.

[56] Jingtao Wang, Jin Zhang, and Junjie Han. Synthesis of crystals and particles by crystallization and polymerization in droplet-based microfluidic devices. *Frontiers of Chemical Engineering in China*, 4(1):26–36, 2010.

[57] Klavs F Jensen. Microreaction engineeringis small better? *Chemical Engineering Science*, 56(2):293–303, 2001.

[58] Rebecca R Pompano, Weishan Liu, Wenbin Du, and Rustem F Ismagilov. Microfluidics using spatially defined arrays of droplets in one, two, and three dimensions. *Annual Review of Analytical Chemistry*, 4:59–81, 2011.

[59] Pascal Panizza, Wilfried Engl, Cindy Hany, and Rénal Backov. Controlled production of hierarchically organized large emulsions and particles using assemblies on line of co-axial flow devices. *Colloids and Surfaces A: Physicochemical and Engineering Aspects*, 312(1):24–31, 2008.

[60] W Engl, M Tachibana, P Panizza, and R Backov. Millifluidic as a versatile reactor to tune size and aspect ratio of large polymerized objects. *International journal of multiphase flow*, 33(8):897–903, 2007.

[61] Rawad Tadmouri, Marta Romano, Loic Guillemot, Olivier Mondain-Monval, Régis Wunenburger, and Jacques Leng. Millifluidic production of metallic microparticles. *Soft Matter*, 8(41):10704–10711, 2012.

[62] Nicolas Lorber, Bertrand Pavageau, and Emmanuel Mignard. Droplet-based millifluidics as a new miniaturized tool to investigate polymerization reactions. *Macromolecules*, 43(13):5524–5529, 2010.

[63] Wilfried Engl, Masatoshi Tachibana, Annie Colin, and Pascal Panizza. A droplet-based high-throughput tubular platform to extract rate constants of slow chemical reactions. *Chemical Engineering Science*, 63(6):1692–1695, 2008.

[64] K. Olivon and F. Sarrazin. Heterogeneous reaction with solid catalyst in droplet-flow millifluidic device. *Chemical Engineering Journal*, (0):–, 2012.

[65] Don L DeVoe. Thermal issues in mems and microscale systems. *Components and Packaging Technologies, IEEE Transactions on*, 25(4):576–583, 2002.

[66] Li Shi, Choongho Yu, and Jianhua Zhou. Thermal characterization and sensor applications of one-dimensional nanostructures employing microelectromechanical systems. *The Journal of Physical Chemistry B*, 109(47):22102–22111, 2005.

[67] P. Monk and I. Wadso. A flow micro reaction calorimeter. *Acta Chemica Scandinavica*, 22(1):1842–1852, 1968.

[68] J Michael Köhler and Martin Zieren. Chip reactor for microfluid calorimetry1. *Thermochimica Acta*, 310(1-2):25–35, 1998.

[69] Omar Mokrani, Brahim Bourouga, Cathy Castelain, and Hassan Peerhossaini. Fluid flow and convective heat transfer in flat microchannels. *International Journal of Heat and Mass Transfer*, 52(5):1337–1352, 2009.

[70] Roland Bavière, Michel Favre-Marinet, and Stéphane Le Person. Bias effects on heat transfer measurements in microchannel flows. *International journal of heat and mass transfer*, 49(19):3325–3337, 2006.

[71] Bertrand MARTY. *Conception, realisation et mise en oeuvre d une plateform d instrumentation thermique pour des applications microfluidiques*. PhD thesis, Ecole Doctorale: Genie Electrique, Electronique, Telecommunications, 2009.

[72] Houssein Ammar, Bertrand Garnier, Hervé Willaime, Fabrice Monti, Hassan Peerhossaini, et al. Thermal analysis of chemical reactions in microchannels using highly sensitive thin-film heat-flux microsensor. *Chemical Engineering Science*, 2013.

[73] David Hamadi, Bertrand Garnier, Herve Willaime, Fabrice Monti, and Hassan Peerhossaini. A novel thin-film temperature and heat-flux microsensor for heat transfer measurements in microchannels. *Lab on a Chip*, 12(3):652–658, 2012.

[74] Guilhem Velve Casquillas, F Bertholle, M Le Berre, S Meance, Laurent Malaquin, Jean-Jacques Greffet, and Yong Chen. Thermo-resistance based micro-calorimeter for continuous chemical enthalpy measurements. *Microelectronic Engineering*, 85(5):1367–1369, 2008.

[75] K Wang, YC Lu, HW Shao, and GS Luo. Measuring enthalpy of fast exothermal reaction with micro-reactor-based capillary calorimeter. *AIChE Journal*, 56(4):1045–1052, 2010.

[76] C. Hany, H. Lebrun, C. Pradere, J. Toutain, and J.C. Batsale. Thermal analysis of chemical reaction with a continuous microfluidic calorimeter. *Chemical Engineering Journal*, 160(3):814–822, 2010. Cited By (since 1996):6.

[77] M. Schneider and F. Stoessel. Determination of the kinetic parameters of fast exothermal reactions using a novel microreactor- based calorimeter. *Chemical Engineering Journal*, 115(1-2):73–83, 2005. Cited By (since 1996):5.

[78] Christophe Pradere, Mathieu Joanicot, Jean-Christophe Batsale, Jean Toutain, and Christophe Gourdon. Processing of temperature field in chemical microreactors with infrared thermography. *Quantitative InfraRed Thermography Journal*, 3(1):117–135, 2006.

[79] C. Hany, C. Pradere, J. Toutain, and J.C. Batsale. A millifluidic calorimeter with infrared thermography for the measurement of chemical reaction enthalpy and kinetics. *Quantitative Infra Red Thermography*, 5(2):211–219, 2008. Cited By (since 2008):10.

[80] C. Pradere, C. Hany, J. Toutain, and J. . Batsale. Thermal analysis for velocity, kinetics, and enthalpy reaction measurements in microfluidic devices. *Experimental Heat Transfer*, 23(1):44–62, 2010. Cited By (since 1996):7.

[81] CA Balaras and AA Argiriou. Infrared thermography for building diagnostics. *Energy and buildings*, 34(2):171–183, 2002.

[82] E-C Oerke, P Fröhling, and U Steiner. Thermographic assessment of scab disease on apple leaves. *Precision Agriculture*, 12(5):699–715, 2011.

[83] MY Tay, MC Tan, W Qiu, and XL Zhao. Lock-in thermography application in flip-chip packaging for short defect localization. In *Electronics Packaging Technology Conference (EPTC), 2011 IEEE 13th*, pages 642–646. IEEE, 2011.

[84] VL Hunt, Gary D Lock, Simon G Pickering, and A Keith Charnley. Application of infrared thermography to the study of behavioural fever in the desert locust. *Journal of Thermal Biology*, 36(7):443–451, 2011.

[85] KP Möllmann, N Lutz, and M Vollmer. Thermography of microsystems. *Inframation proceedings, ITC*, 104:07–27, 2004.

[86] J Antes, D Boskovic, H Krause, S Loebbecke, N Lutz, T Tuercke, and W Schweikert. Analysis and improvement of strong exothermic nitrations in microreactors. *Chemical Engineering Research and Design*, 81(7):760–765, 2003.

[87] Pyshar Yi, Aminuddin A Kayani, Adam F Chrimes, Kamran Ghorbani, Saeid Nahavandi, Kourosh Kalantar-zadeh, and Khashayar Khoshmanesh. Thermal analysis of nanofluids in microfluidics using an infrared camera. *Lab on a chip*, 12(14):2520–2525, 2012.

[88] Naoto Kakuta, Katsuya Kondo, Atsushi Ozaki, Hidenobu Arimoto, and Yukio Yamada. Temperature imaging of sub-millimeter-thick water using a near-infrared camera. *International Journal of Heat and Mass Transfer*, 52(19):4221–4228, 2009.

[89] Yassine Rouizi, Denis Maillet, Yves Jannot, and Isabelle Perry. Inverse convection in a flat mini-channel: towards estimation of fluid bulk temperature distribution with infrared thermography. In *Journal of Physics: Conference Series*, volume 395, page 012070. IOP Publishing, 2012.

[90] Olivier Fudym, Christophe Pradère, and Jean-Christophe Batsale. An analytical two-temperature model for convection–diffusion in multilayered systems: application to the thermal characterization of microchannel reactors. *Chemical engineering science*, 62(15):4054–4064, 2007.

[91] J Haber, MN Kashid, N Borhani, J Thome, U Krtschil, A Renken, and L Kiwi-Minsker. Infrared imaging of temperature profiles in microreactors for fast and exothermic reactions. *Chemical Engineering Journal*, 2012.

[92] Jean-christophe Batsale, Christophe Pradere, Bertrand Pavageau, Cindy Hany, and Jean Toutain. Method and facility for determining at least one parameter of a physical and/or chemical transformation, November 2010.

[93] A. Rogalski. Quantum well photoconductors in infrared detector technology. *Journal of Applied Physics*, 93(8):4355–4392, 2003. Cited By (since 2003):130.

[94] W. Minkina and S. Dudzik. *Infrared Thermography Error and Uncertainties*. Wiley Sons, Czestochowa University of Technology, Poland, 1 edition, 2009.

[95] Wikimedia Foundation. Phage lambda: Thermal conductivity, June 2013.

[96] Cindy Hany. *Developpement de methodes thermiques pour la caracterisation de reactions chimiques en microfluidique*. PhD thesis, Ecole doctorale des sciences chimiques, 2009.

[97] Piotr Garstecki, Howard A. Stone, and George M. Whitesides. Mechanism for flow-rate controlled breakup in confined geometries: A route to monodisperse emulsions. *Phys. Rev. Lett.*, 94:164501, Apr 2005.

[98] Galder Cristobal, Laurence Arbouet, Flavie Sarrazin, David Talaga, Jean-Luc Bruneel, Mathieu Joanicot, and Laurent Servant. On-line laser raman spectroscopic probing of droplets engineered in microfluidic devices. *Lab Chip*, 6:1140–1146, 2006.

[99] J. Illingworth and J. Kittler. A survey of the hough transform. *Computer Vision, Graphics and Image Processing*, 44(1):87–116, 1988. Cited By (since 1996):718.

[100] Duda Richard O. and Hart Peter E. Use of the hough transformation to detect lines and curves in pictures. *Communications of the ACM*, 15(1):11–15, 1972. Cited By:1514.

[101] C. Hansen and S. R. Quake. Microfluidics in structural biology: Smaller, faster... better. *Current opinion in structural biology*, 13(5):538–544, 2003. Cited By (since 1996):129.

[102] R. L. Hartman and K. F. Jensen. Microchemical systems for continuous-flow synthesis. *Lab on a Chip - Miniaturisation for Chemistry and Biology*, 9(17):2495–2507, 2009. Cited By (since 1996):145.

[103] A. M. Nightingale, S. H. Krishnadasan, D. Berhanu, X. Niu, C. Drury, R. McIntyre, E. Valsami-Jones, and J. C. Demello. A stable droplet reactor for high temperature nanocrystal synthesis. *Lab on a Chip - Miniaturisation for Chemistry and Biology*, 11(7):1221–1227, 2011. Cited By (since 1996):20.

[104] P. Gao, S. Le Person, and M. Favre-Marinet. Scale effects on hydrodynamics and heat transfer in two-dimensional mini and microchannels. *International Journal of Thermal Sciences*, 41(11):1017–1027, 2002. Cited By (since 1996):87.

[105] S. Luciani, D. Brutin, C. Le Niliot, L. Tadrist, and O. Rahli. Boiling heat transfer in a vertical microchannel: Local estimation during flow boiling with a non intrusive method. *Multiphase Science and Technology*, 21(4):297–328, 2009. Cited By (since 1996):6.

[106] S. Luciani, D. Brutin, C. Le Niliot, O. Rahli, and L. Tadrist. Flow boiling in minichannels under normal, hyper-, and microgravity: Local heat transfer analysis using inverse methods.

Journal of Heat Transfer, 130(10), 2008. Cited By (since 1996):12.

[107] H. J. Lee and S. Y. Lee. Heat transfer correlation for boiling flows in small rectangular horizontal channels with low aspect ratios. *International Journal of Multiphase Flow*, 27(12):2043–2062, 2001. Cited By (since 1996):127.

[108] G. Hetsroni, M. Gurevich, A. Mosyak, E. Pogrebnyak, R. Rozenblit, and L. P. Yarin. Boiling in capillary tubes. *International Journal of Multiphase Flow*, 29(10):1551–1563, 2003. Cited By (since 1996):19.

[109] R Byron Bird, Warren E Stewart, and Edwin N Lightfoot. *Transport phenomena*. Wiley. com, 2002.

[110] Horvath C., Solomon B.A., and Engasser J.M. Measurement of radial transport in slug flow using enzyme tube. *Ind. Eng. Chem. Fundam*, 12(4):431–439, 1973. Cited By:1514.

[111] D. Lakehal, G. Larrignon, and C. Narayanan. Computational heat transfer and two-phase flow topology in miniature tubes. *Microfluidics and Nanofluidics*, 4(4):261–271, 2008. Cited By (since 1996):28.

[112] R. Scardovelli and S. Zaleski. Direct numerical simulation of free-surface and interfacial flow. *Ann. Review Fluid Mech.*, **31**:567–603, 1999.

[113] J.M. Delhaye. Jump conditions and entropy sources in two-phase systems. local instant formulation. *Int. J. Multiphase Flow*, **1**:395–409, 1974.

[114] I. Kataoka. Local instant formulation of two-phase flow. *Int. J. Multiphase Flows*, **12**(5):745–758, 1986.

[115] J. Toutain, J. . Battaglia, C. Pradere, J. Pailhes, A. Kusiak, W. Aregba, and J. . Batsale. Numerical inversion of laplace transform for time resolved thermal characterization experiment. *Journal of Heat Transfer*, 133(4), 2011.

[116] J.V. Beck and K. Arnold, editors. *Parameter Estimation in Engineering and Science*. Wiley Sons, University of Michigan, 1 edition, 1977.

[117] Joseph Lee Rodgers and W Alan Nicewander. Thirteen ways to look at the correlation coefficient. *The American Statistician*, 42(1):59–66, 1988.

[118] Lide D.R., editor. *Handbook of Chemistry and Physics*. CRC Press, Ohio, 72 edition, 1991-1992.

[119] Hartmuth C Kolb, MG Finn, and K Barry Sharpless. Click chemistry: diverse chemical function from a few good reactions. *Angewandte Chemie International Edition*, 40(11):2004–2021, 2001.

[120] Brian Gold, Nikolay E Shevchenko, Natalie Bonus, Gregory B Dudley, and Igor V Alabugin. Selective transition state stabilization via hyperconjugative and conjugative assistance: Stereoelectronic concept for copper-free click chemistry. *The Journal of organic chemistry*, 77(1):75–89, 2011.